UNIVERSITY OF STRATHCLYDE
DEPARTMENT OF PHYSICS

Investigating Relativistic Transparency: Absorption and Propagation of High-Intensity Laser Pulses in Plasma

by

Antonio Lofrese

in partial fulfilment of the requirements for the degree of Doctor of Philosophy in Physics

2024

Copyright Declaration

This thesis is the result of the author's original research. It has been composed by the author and has not been previously submitted for examination which has led to the award of a degree.

The copyright of this thesis belongs to the author under the terms of the United Kingdom Copyright Acts as qualified by University of Strathclyde Regulation 3.50. Due acknowledgement must always be made of the use of any material contained in, or derived from, this thesis.

Signed:

Date:

Abstract

This thesis reports on experimental and numerical investigations of the interaction of intense laser pulses ($> 10^{18}$ Wcm^{-2}) with ultra-thin (micro and nanometre scale) foils undergoing expansion and relativistic self-induced transparency. Laser energy absorption and propagation physics is explored to enhance our understanding of how intense laser light interacts with foils in the relativistic transparency regime. This interaction regime is important for the laser-driven generation of high-energy particles such as electrons and ions and for generating x-rays and γ-rays and gigagauss magnetic fields. Aspects of such interactions have immense significance in realising numerous envisioned potential applications that include their use as an driver for inertial fusion and in proton therapy for cancer treatment, while offering valuable insights into underlying fundamental physics. Control of the laser-plasma interaction physics is important for the development of these potential applications.

The work reported in this thesis focuses on laser energy absorption and propagation in dense plasma. This involves an in-depth examination of the relativistic self-focusing phenomena and identifies the critical parameters that can be manipulated to enhance or control this. The work is organised into two primary investigations. The first study presents diagnostic methods used to characterise the degree of laser energy absorption in overdense and relativistically transparent plasmas. To begin, the scaling of absorption with peak laser intensity for targets that remain opaque during the interaction was investigated using diagnostic techniques developed specifically for these measurements. The results demonstrate a strong agreement with previously published data. Measurements were conducted to examine how absorption varies in targets undergoing Relativistic Self-Induced

Transparency (RSIT) and the impact of this process on the laser pulse propagation. It is found that for targets exhibiting significant transmission of the laser light, the measurements are strongly dependent on the particular design of the diagnostic tools used. This effect can be corrected by modifying the design of the instrument. The result point to a significant degree of collimation of the transmitted laser light.

The second focuses on numerical investigation of the underpinning physics, including relativistic self-focusing effects during the propagation of a intense laser pulses in relativistically transparent plasma. PIC simulations were performed with increasing complexity to investigate the underlying physics. It is found that the two most important factors that influence the absorption and propagation of the beam are the focal position of the pulse and the expansion of the plasma. The combination of these two parameters can influence the laser pulse propagation and produce a less divergent pulse far from the target. This study carries significant implications for fundamental comprehension, the advancement of applications, and for refining experimental procedures.

Acknowledgements

The work reported in this thesis was made possible thanks to assistance and support from several individuals and entities that have contributed to the realisation of this academic milestone. Foremost, my deepest gratitude goes to my PhD supervisor, Prof. Paul McKenna, for granting me the chance to undertake this research project, whose mentorship has been the lighthouse guiding me through the intricate seas of my research. The unwavering support, intellectual guidance, and encouragement provided the foundation upon which this thesis stands. I will forever appreciate his faith in me and the chance he provided, as it has proven to be one of the most fulfilling experiences in both my personal and professional journey. Secondly, thanks must go the the second pillar of my thesis, Dr. Ross Gray, for his insightful guidance and unparalleled dedication throughout my academic journey. His supervision has been a source of inspiration, shaping not only my research but also fostering my personal and career development. Without his daily guidance and input, a significant portion of the work in this thesis would not have been finished. I have been truly fortunate to have had the privilege of learning from his expertise and am profoundly grateful for the impact he has had on my academic pursuits. I would also like to express my gratitude to Dr. Martin King for guiding and assisting me in all matters related to simulations and for his contributions to my work. I extend my sincere thankfulness to Dr. Robbie Wilson for his motivation of thinking critically about my own work and his emphasis on recognising potential weaknesses which cultivated in me a heightened sense of responsibility. For the enjoyable moments shared especially during experiments, for fostering a sense of inclusion within the team and for his belief in my potential, which has been a constant source of inspiration. Thanks to Dr. Timothy Frazer for his unconditional help in the English-proof and for his meticulous review of drafts of this entire thesis. His valuable input and insightful suggestions have significantly enriched the content and quality of this thesis. Moreover, I extend heartfelt thanks to Prof. McKenna, and Drs. Gray, King, Wilson and Frazer for their academic insights and meticulous review. Their constructive feedback has undoubtedly elevated the quality of this work. I additionally thank my colleagues, both past and present; Sam, Zoe, Matthew D., Jonathan, Alana, Matthew A., Jesel. Each of them has played a significant role in shaping my PhD experience, and, last but not least; Ewan and Jack for their collective support and fellowship have enriched my research endeavours, making this academic pursuit all the more rewarding. I would like to thank the entire team at GSI Helmholtz Centre for Heavy Ion Research in Darmstadt for their invaluable contributions that have made the research presented here not only feasible but also enriched with collaborative efforts.

Finally, I must thank my parents, Angela and Mimmo, and my sister, Mariagrazia, whose steadfast support has been the bedrock of my journey. Their love, encouragement, and understanding have been my pillars of strength throughout this undertaking. A special acknowledgement is reserved for my mother, whose influence on both my life and this project continues to resonate even in her absence.

Role of Author

The author of this thesis conducted the analysis and interpretation of experimental and simulation data, leading to novel insights into the underlying physics. This work was carried out under the guidance of Prof. Paul McKenna and involved collaboration with fellow group members. The author played a significant role in planning and executing the experiment outlined in this thesis, including conducting measurements and analysing both experimental and simulated data. The simulations showcased in this thesis were executed under the supervision of Dr. M. King and subsequently scrutinised by the author for comprehensive analysis.

Chapter 4: The experiment was set up by Dr. R. Wilson and Dr. R.J Gray where the author participated in the implementation of all diagnostics during the experimental setup phase. The author developed the analysis method for the main diagnostic, as well as performing the analysis itself. The absorption values presented were calculated by Dr. R. Wilson and S. Williamson, all other experimental results presented were analysed by the author.

Chapter 5: The comprehensive analysis of both experimental data and 2D PIC simulations has been conducted by author supported by Dr M. King. Dr. M. King executed a substantial portion of the 2D PIC simulations, with collaborative planning involving both the author and Dr. R.J Gray. This collaborative effort ensured a robust examination of the experimental and simulation data, contributing to the depth and validity of the findings presented.

List of Figures

Chapter 1

Introduction

The subject of this thesis centres on investigation of the interaction of an ultra-intense laser pulse with dense plasma. Since the advent of the laser, in 1960 [1], and with the progress made in laser technology over the years, great interest has developed in the study of the behaviour of matter under extreme conditions. Laser light possesses numerous characteristics, such as temporal coherence, a monochromatic spectrum and a high degree of collimation, that make it well-suited for both driving and diagnosing physical processes.

Over the last fifty years, the maximum attainable laser intensity has increased by many orders of magnitude, facilitated by various technological developments. The introduction of Q-switching in 1961 [2], made it possible to create pulses with high energy beyond a kilo-Joule. The development of mode-locking in 1964 [3] enabled laser pulses with ultra-short pulse lengths, down to picoseconds. Subsequently, the development in 1985 of chirped pulse amplification (CPA) [4] then enabled short pulse durations while avoiding limitations of optical damage in the laser chain. Ultimately, this approach opened up the experimental investigation of laser-plasma interactions with relativistic intense laser pulses ($\mathrm{I}_L > 10^{18}$ Wcm^{-2}) with short pulse durations (< 1 ps) which is the subject of this thesis.

Figure 1.1 offers a depiction of the technological advances throughout the years since the first laser demonstration, indicating with the different regimes of laser-plasma interactions.

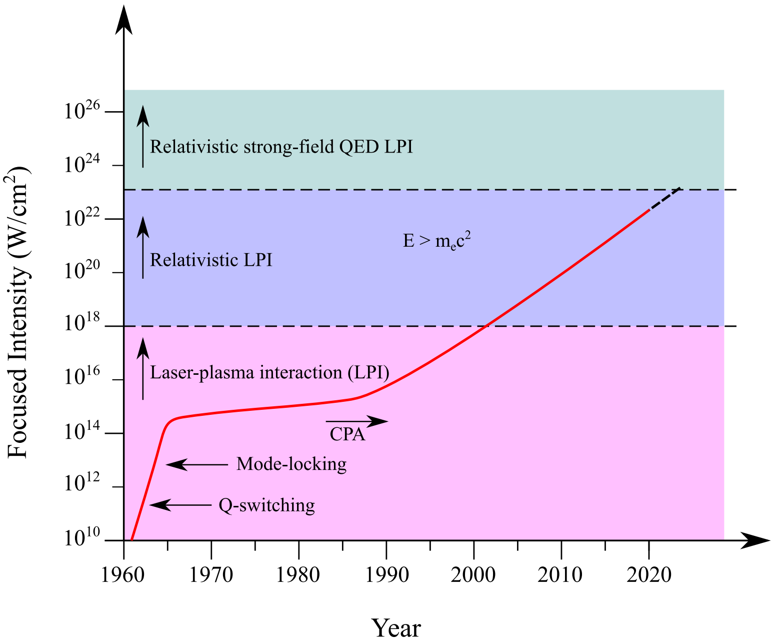

Figure 1.1: Evolution of peak laser intensity as a function of time since the first demonstration of the laser in 1960, indicating the three distinct laser-plasma interaction (LPI) regimes for laser light with wavelength approximately equal to 1 micron.

With such development and using focusing optics it is possible to produce optical pulses which, when they irradiate matter, can generate plasma. The phenomena that occur during relativistic laser-plasma interactions have been thoroughly investigated, such as the generation of strong magnetic and electric fields (on the order of MG and TV/m) [5], high energy photons (X-rays and gamma rays) [6][7] and sources of energetic particles (electrons, ions and neutrons) [8].

In the realm of relativistic laser-plasma interactions, one of the fundamental mechanisms that has captured significant attention is target normal sheath acceleration (TNSA) [9]. This mechanism, where a relativistically intense laser pulse ($> 10^{18}$ Wcm^{-2} for a laser wavelength of around 1 μm) induces plasma on the front surface of a target foil, and accelerates plasma electrons to sufficient energy that a significant proportion propagate through the foil, creating an electric field at the rear surface that accelerates ions.

With increasing laser intensity, and particularly for ultrahigh intensities ($> 10^{21}$ Wcm^{-2}), the radiation pressure exerted by the laser pulse assumes a more prominent role in the interaction, accelerating electrons inward and generating a strong electric field in the laser focus area. This, in turn, leads to the acceleration of ions through radiation pressure acceleration (RPA) [10]. Both TNSA and RPA mechanisms can operate concurrently in the same interaction, giving rise to a hybrid ion acceleration scheme known as TNSA-RPA [11]. The potential application of the resulting novel source of energetic ions [12][13], has ignited a surge of interest and exploration. Currently, many studies are focused on applications to inertial confinement fusion schemes [14], or for medical applications such as proton oncology [15] and medical imaging [16]. However, being able to control and optimise these sources is a significant challenge for the scientific community, which must develop new understanding and new methodologies to in order to develop useful radiation sources. Considerable advancement has been made toward this goal in the past few years, and certain desired applications are now materialising.

Advancements in laser intensity and thin foil target fabrication have propelled this field into a novel phase, featuring phenomena known as Relativistic Self-Induced Transparency (RSIT) transition regime. This transition is made possible through the intricate interplay of various physical processes, such as ionisation, heating and expansion of initially ultrathin foil targets. RSIT manifests when the relativistic mass of electrons, oscillating in response to laser light, reaches a threshold where the plasma frequency drops below the laser frequency. This transformative process results in the initially opaque ultrathin foil becoming transparent during the interaction, thereby enabling the transmission of the remaining laser light [17]. The residual portion of the laser pulse propagating through the target gives rise to various phenomena that can significantly influence particle acceleration. The energetic particle beams generated through laser-driven particle acceleration mechanisms in the RSIT regime offer possibilities for creating secondary sources of particles and radiation with potential applications in a myriad of fields, including medical oncology [18, 19, 20, 21].

Beyond the fields of surgery and chemotherapy, radiotherapy emerges as a fundamental and cutting-edge strategy in the comprehensive management of cancer. Radiotherapy employs ionising radiation to damage the atoms within the tissues it penetrates, with the aim of destroying cancer cells. Considering that all tissues are typically vulnerable to radiation-induced harm, the primary constraint in radiotherapy lies in limiting damage to the healthy tissues adjacent to the tumor. Typically this incidental damage occurs as a result of the energy distribution of x-rays within the body, where the highest dose of x-rays is administered on the surface of the patient and diminishes exponentially as the depth increases. An alternative treatment approach that resolves this problem is to use energetic particles such as protons or heavier ion species, often referred to as hadron therapy. Unlike conventional radiotherapy where photons are used, hadron therapy, sometimes called particle therapy, is a comprehensive term employed to describe the treatment of tumors using external irradiation with accelerated hadronic particles and it exploits the trend of energy loss of charged particles in matter as a function of depth, the so-called Bragg peak, which allows energy to be deposited extremely precisely at a given depth, thus minimising damage to surrounding healthy tissues. Initially suggested by Wilson in 1946 [22], proton therapy was recognised at the first treatment centres at the Lawrence Berkeley Laboratory, in 1954 [23]. Currently, proton energies needed to treat tumours located deep within the body (typically in the range of 200-250 MeV) can only be attained using conventional particle accelerators. These facilities are often large scale, require significant radiation shielding and are costly to build and operate. Hence, there is a interest for potentially more cost-effective and compact sources of the proton and ions essential for tumour therapy.

Significant recent progress in the field of laser-driven ion acceleration has been made. The characteristics of beams of ions accelerated by laser pulses differ from those produced by conventional accelerators as they contain multiple ion species and have extremely short pulse durations. This results in a radiation pulse with orders of magnitude higher dose rates, potentially with a greater therapeutic effectiveness compared to X-rays [24][25]. It was shown in Powell *et al.* [26] that when the solid target becomes relativistically transparent during the interaction, a plasma jet is formed at the back of the target where the electrons trapped inside are directly accelerated by the laser pulse, transmitted through the target, resulting in enhanced proton energy, while in Higginson *et al.* [27] an increased achievable ion energies (exceeding 94 MeV) and conversion efficiencies through a hybrid scheme of TNSA-RPA, boosted by relativistic transparency, was demonstrated. Moreover, to make laser-driven protons suitable for health applications, there will be a need for significant enhancements in the attainable beam properties, such as the particle energy spectrum and the beam focusability. These improvements are essential to ensure precise energy delivery to the tumour while minimising harm to adjacent healthy tissues. To accomplish this, a more comprehensive understanding is essential regarding the underlying physics during the RSIT process as the target evolves. The work reported in this thesis focuses on this.

1.1 Thesis outline

This thesis reports on the experimental and numerical investigation of the physics underpinning laser-solid interactions within ultra-high intensity regime focusing on investigation of laser absorption as a function of target thickness. In particular a detailed study on relativistic self-focusing effects during the propagation of a high intensity laser pulse with ultra-thin foils undergoing relativistic transparency is presented. A description of each of the chapters which form this thesis are presented as follows:

- In **Chapter 2** the underlying fundamental theory of laser-plasma interactions is introduced. This is crucial for defining and understanding the key processes addressed in the research chapters of this thesis. The chapter begins with a description of the basic electromagnetic principles, followed by a detailed description of the fundamental concepts that define the nature of plasma, a discussion of relativistic self-induced transparency and, finally, relevant ion acceleration mechanisms.

- In **Chapter 3** an overview of the experimental and numerical methodologies applied in this thesis are provided, encompassing the technology essential for producing ultraintense short-pulse laser systems, experimental set-ups and diagnostics employed. In the final section of this chapter, the numerical methods used in this thesis to simulate laser-plasma interactions are introduced.

- In **Chapter 4** an investigation of laser pulse energy absorption by an ultrathin foil undergoing relativistic self induced transparency as a function of target thickness is presented. Results of experimental and numerical investigations, exploring the use of diagnostics, such as integrating spheres and scattering screens, to diagnose the underpinning physics of RSIT are reported. Furthermore, the limitations of these diagnostics in the case where there is significant transmitted laser light is examined.
- In **Chapter 5** an exploration into the complex interplay of factors influencing laser energy divergence and residual absorption in the RSIT regime is reported, involving an in-depth examination of the relativistic self-focusing phenomena that occur when a high-intensity laser pulse propagates through dense plasma.
- In **Chapter 6** an overview of the outcomes and the analysis of the conclusions presented in chapters 4 and 5 is supplied. Future possibilities and the potential steps to be taken are also addressed and examined.

Chapter 2

Underpinning physics concepts of laser-solid interactions

2.1 Introduction

The study of intense laser interactions with solid density plasma encompasses numerous disciplines in physics, from the field of photonics defining the behaviour of high-intensity lasers, to atomic and plasma physics which enables the study of the electrical and magnetic properties of materials. In order to gain useful insights into the physics behind these phenomena it is important to understand the fundamental processes of laser-plasma physics relevant to this thesis, which is the focus of this chapter.

The theories that define the nature of the laser pulse itself will be introduced starting from basic electromagnetic principles, such as Maxwell's equations, where we will define the fundamental properties of electromagnetic radiation that allow us to describe its behaviour. Subsequently we will analyse what happens when an electromagnetic wave (EM) interacts with a single charged particle such as an electron, as this is the most fundamental interaction involved in laser-matter studies. A detailed description of the fundamental concepts that define the nature of plasma will be given before proceeding to examine the more complex processes when plasma is exposed to electromagnetic radiation. The mechanisms of laser energy absorption in the plasma will then be presented, with the implications this has in the system, such as the heating of electrons within the plasma. Finally we will examine various mechanisms by which it is possible to accelerate charged particles to energies on the order of MeV through a laser-solid interaction, where some of the potential applications for energy production and medical applications will be introduced. Additional information regarding the concepts discussed in the upcoming sections can be found in various existing sources, such as the works of Kruer [28], Gibbon [29] and Macchi [30].

2.2 Electromagnetic radiation

To describe the behaviour and nature of plasma, as well as its interaction with light, it is helpful to review some basic electromagnetic theories; including Maxwell's four equations which describe the generation of electric and magnetic fields and how they relate to each other, and the Lorentz force equation for a charged particle in an electromagnetic field.

Since ancient times, the observation of natural phenomena has led to the discovery of the existence of mechanical actions of attraction and repulsion between electrified bodies, as well as between magnetised bodies. Faraday was convinced that all the forces of nature were connected in some way. Consequently he believed that electricity and magnetism were not separate, but were instead two different manifestations of the same fundamental phenomenon. This conviction prompted Oersted to look for this connection between electricity and magnetism by discovering that the electric current circulating in a conductor exerts a force on a nearby magnet, thus publishing in 1820, a pamphlet showing that they were in fact closely related [31] [32].

Furthermore, Faraday knew that his new hypotheses had a scope that went far beyond the simple question of electricity and how those ideas could be traced back to a general conception of matter, thus starting a search for the effects of electricity on polarised light. Unfortunately Faraday did not have sufficient mathematical and physical knowledge to develop a theory of electromagnetic waves, but in 1873, the Scottish physicist James Clerk Maxwell formulated his electromagnetic field theory, *On Physical Lines of Force* [33]. According to this theory, even in a vacuum, variable electric fields produce magnetic fields and vice versa, thus leading to the description of light as an electromagnetic wave. A few years later Maxwell's equations were reduced to four equations by Oliver Heaviside [34] [32], which we recognise today in their differential form;

$$\nabla \cdot \mathbf{E} = \frac{\rho}{\varepsilon_0} \tag{2.1}$$

which represent the Gauss' law for Electric field generation, where $\mathbf{E}$ is the electric field, ρ is the charge density and ε_0 is the electric permittivity of free space, while ∇ is the vector differential operator, defined as $\nabla = (\partial/\partial x, \partial/\partial y, \partial/\partial z)$ in three dimensional Cartesian space;

$$\nabla \cdot \mathbf{B} = 0 \tag{2.2}$$

defined as Gauss' law for Magnetic field generation, with $\mathbf{B}$ the magnetic field and $\partial/\partial t$ the temporal derivative;

$$\nabla \times \mathbf{E} = -\frac{\partial \mathbf{B}}{\partial t} \tag{2.3}$$

the Faraday-Maxwell equation or known as Electromagnetic Induction, and finally;

$$\nabla \times \mathbf{B} = \mu_0 \mathbf{J} + \mu_0 \varepsilon_0 \frac{\partial \mathbf{E}}{\partial t} \tag{2.4}$$

described as the Ampere-Maxwell equation, where $\mathbf{J}$ is the current density and μ_0 the magnetic permeability of free space.

The first two equations describe the electric and magnetic fields and concern the existence of charges that produce them; in particular, the first describes the electric field generated by stationary charges, according to Coulomb's law, while the second equation establishes that there are no isolated magnetic poles, unlike for electric charges, but that the north pole of a magnet is always connected to a south pole. Maxwell's third equation expresses the Faraday-Newman law of electromagnetic induction, which states that a time-varying magnetic field produces an electric field. And finally the last equation states that any current generates a magnetic field, both a direct current and a time-varying electric field.

From the point of view of Newtonian dynamics, the law describing the interactions of the electric field and the magnetic field on electrically charged particles was explained by the Dutch physicist Hendrik Lorentz around 1890. This law states that in the presence of a electromagnetic field, **E** and **B**, a particle of charge q and speed **v** is subject to a force, called the Lorentz force, equal to;

$$\mathbf{F}_L = q(\mathbf{E} + \mathbf{v} \times \mathbf{B}) \tag{2.5}$$

In this thesis we will refer to electromagnetic waves as solutions to homogeneous Maxwell equations, therefore it will be useful to reformulate these equations in the absence of charges or currents.

For a given vector field, **A**, by taking the vector identity; $\nabla\times(\nabla\times\mathbf{A}) = \nabla(\nabla\cdot\mathbf{A})$ - $\nabla\ ^2\mathbf{A}$ we can reformulate the Faraday-Maxwell equation;

$$\nabla \times (\nabla \times \mathbf{E}) = \nabla \times \left(-\frac{\partial \mathbf{B}}{\partial t}\right) = \nabla(\nabla \cdot \mathbf{E}) - \nabla^2 \mathbf{E} \tag{2.6}$$

if we assume the electromagnetic wave propagation is in vacuum, the charge ρ and current density **J** will both be 0, thus we can eliminate the term $\nabla(\nabla\cdot\mathbf{E})$. Substituting the Gauss' law for electric field (Eq. 2.1) in 2.4 and swapping the differential operation for the magnetic field, we obtain the wave equation;

$$\nabla^2 \mathbf{E} = \frac{1}{c^2}\frac{\partial^2 \mathbf{E}}{\partial t^2} \tag{2.7}$$

This describes a wave that propagates in vacuum at a speed $c = 1/\sqrt{\epsilon_0 \mu_0} \simeq 3 \times 10^8$ ms^{-1}, known as the speed of light. One solution to this equation is;

$$\mathbf{E} = E_0 \hat{\mathbf{e}}_x e^{[i(\mathbf{k},\mathbf{z} - \omega t)]} \tag{2.8}$$

where E_0 is the amplitude of the electric field, $\hat{\mathbf{e}}_x$ represent the unit vector describing the direction of the field in the x-plane, $\mathbf{k}$ is the wave vector with magnitude $k = \frac{\omega}{v}$, while $\mathbf{z}$ and ω are, respectively, the propagation direction and the angular frequency, and finally t is time.

There is an expression of identical form for the magnetic field $\mathbf{B}$, substituting the previous solution (Eq. 2.8) into Faraday-Maxwell equation (Eq. 2.3);

$$\mathbf{B} = B_0 \hat{\mathbf{e}}_y e^{[i(\mathbf{k},\mathbf{y}-\omega t)]} \tag{2.9}$$

By replacing these two solutions for the electric and magnetic field in the Maxwell's equations we find;

$$i\mathbf{k} \cdot \mathbf{E} = 0 \quad \text{and} \quad i\mathbf{k} \cdot \mathbf{B} = 0 \tag{2.10}$$

These show that the electric and magnetic fields are orthogonal to each other and that both oscillate perpendicular (transverse) to the direction of propagation of the wave. Finally;

$$i\mathbf{k} \times \mathbf{B} = \frac{-i\omega}{c^2}\mathbf{E} \Rightarrow |\mathbf{B}| = \frac{|\mathbf{E}|}{c} \tag{2.11}$$

which states that the electric field strength is c times greater than the magnetic field. As we will see later this is the reason why during a laser-matter interaction, an electron in the presence of an electromagnetic wave will primarily be subject to the action of the electric field, while movement induced by the magnetic field can be neglected, unless the speed of the electron reaches relativistic values and in this case we should also consider the action of the B field.

If we substitute the solution (Eq. 2.8) into the wave equation (Eq. 2.7) we can obtain the dispersion relation that describes the propagation of the light in the vacuum;

$$kc = \omega \tag{2.12}$$

being a linear relationship between the angular frequency and the wave vector, both the phase (v_ϕ) and the group velocity (v_g) will have equal value, of c;

$$\frac{\omega}{k} = \frac{d\omega}{dk} = c \tag{2.13}$$

where $\omega/\mathrm{k} = v_\phi$ and $\mathrm{d}\omega/\mathrm{dk} = v_g$. This relationship holds when the electromagnetic wave travels in a vacuum, but as we shall observe subsequently, when an EM wave travels through a plasma, this relationship will not always be true.

2.3 High power laser pulses

Before attempting to understand how laser light interacts with a plasma, it is useful to introduce some parameters that will often be mentioned in this thesis. In laser-matter interactions, short high-intensity pulses are used where "short" refers to the time duration of the laser pulse, typically on the order of tens of femtoseconds or picoseconds, while "high intensity" describes pulses with peak values greater than 10^{18} Wcm^{-2}.

These laser pulses usually display Gaussian-like spatial and temporal profiles as shown for the PHELIX laser used in this study [35] and therefore this discussion focuses on these profiles. The temporal profile is typically described by the pulse duration, which is the full width half maximum (FWHM) of the Gaussian pulse envelope. The spatial extent of the focal spot can be described by the focal spot size, ϕ_L. This parameter has been shown to have a significant effect on the physics of laser-solid interactions [36] [37]. The generation of a focal spot, i.e. the region that interacts with the solid target, is typically achieved through the use of an off-axis parabolic mirror (OAP) which acts to focus the laser pulse to a small, micron-scale, region. The spot size may be defined by the spot waist parameter which represents the radius where the intensity drops to $1/e^2$ of its peak value. A focal spot of this shape is referred to as diffraction limited, with a diameter

$2\omega_0$ defined as;

$$2\omega_0 = 1.22\frac{\lambda_L f}{D} \tag{2.14}$$

where λ_L is the laser wavelength, f is the focal length of the optic and D is the diameter of the collimated beam prior to the focusing optic. To describe the minimum focal spot size that can be achieved, a dimensionless quantity is usually used, that represents the ratio between the focal length and the diameter of the beam, denoted as F/#, and it describes how quickly a pulse focuses, a lower number denoting quicker focusing.

Another important parameter to the focal spot characterisation is represented by the encircled energy, often referred to as EE. This is a measure of energy contained within the central region of the focal spot, i.e. the area used to defined the spot size, where a high quality focal spot results in a higher encircled energy, typically the values of this energy fall in the range of 20-40%. A reduction in spot encircled energy may result from poor optimisation of, or damage to, the focusing optic or aberrations in the pulse wavefront caused from thermal effects for instance. The OAP mirror is particularly sensitive to the aberrations, which in this work typically cause the values of EE to be ~30% (see for example the measurements for the PHELIX laser reported in [35]). The EE is determined by measuring the distribution of the focal spot, and calculating the ratio of the integrated pixel counts within the FWHM area to the integrated counts of the entire spot.

Another key parameter used to characterise the pulse focal spot spatial evolution is the Rayleigh range, defined mathematically as follows;

$$z_R = \frac{2\pi\omega_0}{\lambda_L} \tag{2.15}$$

This represents the distance from the beam waist (i.e. smallest radius) to where the beam radius is increased by a factor of $\sqrt{2}$.

Finally, an additional key laser parameter is the optical polarisation of the pulse. This represents the orientation of the electric field oscillation in a plane perpendicular to the propagation direction. If during propagation the orientation changes at each point in space, then the pulse is said to be unpolarised, i.e. if a wave propagates along a z-axis direction, the oscillation of the electric field can have orientation only in the x,y plane. Linear polarisation can be classified into s- or p- polarisation where the plane of polarisation is orientated perpendicular or parallel to the plane of incidence, respectively. Specifically, the p-polarisation describes the electric field orientated in the plane of incidence, while the other describes the electric field orientated perpendicular to this plane. Circular polarisation, on the other hand, is characterised by two electromagnetic waves that are perpendicular to each other of equal amplitude, 90° out of phase. When the two perpendicular electromagnetic waves do not have equal amplitude, then they described as having elliptical polarisation. The polarisation forms described above are illustrated in figure 2.1.

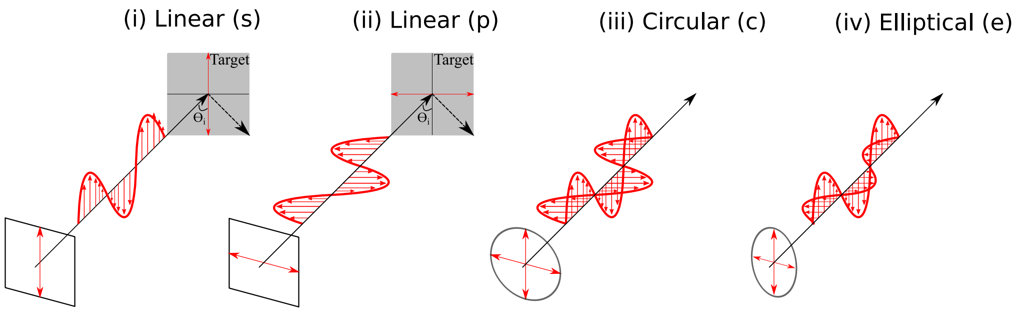

Figure 2.1: Illustration depicting the direction of the electric field of an EM wave relative to its direction of propagation, for (a) linear s-polarisation, (b) linear p-polarisation, (c) circular polarisation and (d) elliptical polarisation. In scenarios (i) and (ii), an interaction target is irradiated to each field at an incident angle of θ_i, facilitating the differentiation between s and p polarisation.

2.4 Plasma Physics

2.4.1 Definition of Plasma

The state of matter know as plasma was first observed in the laboratory by William Crookes in 1879, using a vacuum glass tube for the study of cathode rays and electron properties. The rarefied gas inside the tube subjected to a high potential between an anode and cathode had released electric discharges. The gas had been transformed into a new state, the so-called fourth state of matter. It was the American Irving Langmuir who introduced the word plasma in 1928 in the article *"Oscillations in Ionised Gases"*, [38], borrowing it from the ancient Greek term $\pi\lambda\alpha\sigma\mu\alpha$, which means "moldable substance", to describe a "region containing a charge of ions and electrons".

Differing from the three classic states of matter (solid, liquid and gaseous) which are abundant on our planet, the presence of plasma on Earth is quite rare, despite constituting 99.9% of the visible matter in the universe; from the interior of stars, interstellar space, solar wind, auroras, ionosphere and lightning, all of which are made of plasma. In addition to these natural forms, plasmas are produced in the laboratory for specific purposes, such as neon tubes, electric arcs, radio frequency discharges for industrial applications, up to high temperature plasmas for controlled nuclear fusion research and laser generated plasmas. Therefore the plasma state requires a definition of its own. In a simplified first approximation it could be defined as an ionised gas, made up of charged particles and is globally neutral, in the sense that the total electric charge is zero.

The classic definition of plasma is as follows: *"A plasma is a quasi-neutral gas of charged and neutral particles which exhibits collective behaviour"* where the term *"quasi-neutral"* indicates that the charges present inside the plasma are able to shield the effect of other charges that are added, i.e. if a test charge were inserted, the electrons would form a cloud around this charge in such a way that beyond a certain distance the field of the inserted charge would be null. *"Collective behaviour"* indicates that inside the plasma, although the charged particles are not bound to each other, their motion generates electromagnetic fields which thus influence the behaviour of the other charges through long-range Coulomb interactions. Thus any motion of a charged particle in the plasma affects and is affected by the fields created by other charged particles. Thus a plasma is a many-body system of particles whose physical behaviour is strongly influenced by the presence of charges and requires a description that takes into account both the electromagnetic nature and the dynamics of the particles.

To have a more detailed understanding of this definition it is advisable to introduce two physical quantities which determine some macroscopic properties: the Debye length and the plasma frequency. Having a large number of free charges, plasmas tend to shield external disturbances. Therefore, if there is a positive ion locally, an electron cloud forms around it, which tends to shield this external disturbance. For this reason, the size of the Coulomb interaction inside a plasma is greatly reduced, for example compared to the case of a rarefied gas. The electron density around an ion, assuming the Maxwell-Boltzmann distribution is valid, is;

$$n_e(r) = n_{e0} e^{\frac{eV(r)}{K_B T_e}} \tag{2.16}$$

where $n_e(r)$ is the local electron density around the ion, *V(r)* is the local potential of the plasma, k_B the Boltzmann constant and T_e is the electron temperature. Expanding the exponential to the first order and rewriting the expression for the local charge density, ρ, as;

$$\rho(r) = en_{i0} - en_{e0}\left(1 + \frac{eV(r)}{k_B T_e}\right) \tag{2.17}$$

and neglecting the agitation of the ions;

$$\rho(r) = -\frac{e^2 n_{e0} V(r)}{k_B T_e} \tag{2.18}$$

If we insert this expression in the Poisson equation, rewrite it in polar coordinates around the ion and rename n_{e0} with n_e we obtain;

$$\frac{\partial^2 \mathbf{V}}{\partial r^2} = \frac{e^2 n_e V(r)}{k_B T_e \varepsilon_0} \tag{2.19}$$

with the solution;

$$V(r) = V_0 e^{-\frac{r}{\lambda_D}} \tag{2.20}$$

Debye length is defined as;

$$\lambda_D^2 = \frac{k_B T_e \varepsilon_0}{e^2 n_e} \tag{2.21}$$

The result translates into the fact that if a test charge is placed within the plasma, q, the plasma creates a cloud of space charge which reduces the Coulomb electric potential until the single charge effect is cancelled over distances greater than λ_D, which takes the name of Debye length. At distances greater than the Debye length, only the collective effects are measured and not those of the individual charges. It can be seen that the Debye length decreases as the electron density increases (because more electrons are available for shielding), and increases as the temperature increases (since the mobility of the charges increases). For Debye shielding to function effectively, there needs to be a sufficient quantity of electrons to shield a test charge, and these electrons must exist within a defined Debye sphere, with a sphere radius λ_D. In the Debye sphere, the average number of electrons contained is defined as;

$$N_D = \frac{4}{3} n_e \pi \lambda_D^3 \tag{2.22}$$

When the number of electrons within this sphere is greater than one, $N_D \gg 1$, the plasma is capable of screening any local charge imbalances. To be effective there must be a sufficient number of electrons inside the Debye sphere where the particles exhibit collective behaviour, while for $N_D \ll 1$, binary collisions between the particles are the dominant physical phenomenon. For a typical plasma at critical density and a temperature of 1 keV, the number of electrons would be equal to 1.7×10^3.

Another aspect related to the physical nature of plasma concerns the oscillations of electrons within the plasma. Already previously introduced by Langmuir, when an electron moves in the presence of an ion, an electric field is created which involves the attraction of both, with the aim of restoring neutrality. As a consequence of this force the electron will undergo an acceleration moving at a sustained speed which will exceed the that of the ion. The presence of the ion will constrain the dynamics of the electron again and it will find itself oscillating around this equilibrium position at a frequency, defined as the plasma or Langmuir frequency. The electron motion can be described starting from Gauss's law for the generation of the electric field in one dimension;

$$E = \frac{\rho}{\varepsilon_0} = -\frac{en_e\delta_x}{\varepsilon_0} \tag{2.23}$$

where δ_x is the displaced distance from initial position. The equation of motion of the electron will be governed by the Lorentz force (Eqn. 2.5), where neglecting the term $\mathbf{v}\times\mathbf{B}$ (as will be explained in detail below), and using Newton's second law, we obtain;

$$\mathbf{F} = -e\mathbf{E} = m_e\frac{d^2\delta_x}{dt^2} = -e\mathbf{E} \tag{2.24}$$

by substituting the expression of the electric field (Eqn. 2.23) in the previous expression and rearranging, we obtain the equation of motion for the electron in the plasma as;

$$\frac{d^2\delta_x}{dt^2} + \frac{e^2n_e\delta_x}{\varepsilon_0 m_e} = 0 \tag{2.25}$$

where;

$$\frac{d^2\delta_x}{dt^2} = a = -\frac{e^2n_e\delta_x}{\varepsilon_0 m_e} \tag{2.26}$$

which represents the harmonic oscillation equation, with $a = -\omega^2\delta_x$, ω is the oscillation frequency and therefore the electron will oscillate around its rest position with harmonic motion at frequency;

$$\omega_p = \sqrt{\frac{e^2n_e}{\varepsilon_0 m_e}} \tag{2.27}$$

The frequency of electron plasma oscillations is crucial when determining the dynamics of laser-plasma interaction, above all used as a reference to distinguish the plasma from any ionised gas, with the necessary condition that the frequency of the plasma must be greater than its collisional frequency, $\omega_P > \omega_C$, which represents the average time of the collisions which take place inside an ionised gas.

2.4.2 Laser Induced Ionisation Processes

After introducing in the previous section the key parameters that are involved in a laser-matter interaction considered in this thesis, we can start examining the mechanisms underlying how a solid target is transformed into plasma through the interaction with an intense laser pulse. For this transformation to occur, a sufficient number of electrons bound to the atom must be freed. This process is called ionisation, where an electron is stripped from the outer to the inner most atomic orbital, the atom is transformed into a positive ion, and the electron is moved away to a distance where there is negligible electrostatic interaction between the electron and the ion, defined as the ionisation potential, I_P.

Considering Bohr's atomic model, which is a good approximation in the case of atomic hydrogen, the mean radius of the electron's orbit around the nucleus in its ground energy state is defined by the Bohr radius, a_B, as;

$$a_B = \frac{4\pi\varepsilon_0\hbar^2}{m_e e^2} \tag{2.28}$$

where $\hbar$ is the reduced Planck's constant, and the Bohr radius is $a_B = 0.053$ nm. If we assume that both the nucleus and the electron act as point charges, the Bohr radius can be used in Coulomb's law to obtain the magnitude of the electric field holding the electron to the nucleus, E_a;

$$E_a = \frac{e}{4\pi\varepsilon_0 a_B^2} \tag{2.29}$$

which has a value of $E_a \simeq 5.1 \times 10^9$ Vm^{-1}. In this way it is possible to determine the intensity of the laser necessary to strip the electron from the atom;

$$I_a = \frac{\eta c \varepsilon_0}{2} E_a^2 \tag{2.30}$$

where η is the refractive index of the propagation medium, and in the case of vacuum propagation ($\eta = 1$) the intensity becomes $I_a \simeq 3.5 \times 10^{16}$ Wcm^{-2}. This means that any laser pulse with this intensity or greater will succeed in ionising the hydrogen atom. Figure 2.2 (a) shows a schematic of single photon ionisation mechanism. However, ionisation also occurs for lower intensities due to other mechanisms that will now be described.

2.4.3 Multi-photon ionisation

In our research, the laser used has a near infrared wavelength, of central value λ_L = 1053 nm (see section 3.3 for more details), where a single photon at this wavelength has an energy of 1.2 eV. If we use hydrogen as an example, which has an ionisation potential, U_H, of 13.6 eV, direct ionisation by single photon absorption would not be possible, but would take at least 12 photons to overcome the ionisation potential of the hydrogen atom. This process, which was predicted theoretically by M. Goeppert-Mayer in 1931 [39], is called multi-photon ionisation (MPI) where the atom absorbs enough photons to release an electron. The final energy of a free electron produced by this mechanism is given by;

$$E_f = (n + s)\hbar\omega_L - U_I \tag{2.31}$$

where n is the number of photons with collective energy U_I, s is the number of additional photons absorbed and ω_L is the laser frequency. Figure 2.2 (b) shows a sketch depicting this process.

2.4.4 Tunnelling Ionisation

Another ionisation mechanism that becomes important for high laser intensities is the tunnelling effect. The Coulomb potential from an atom can be described as:

$$V_x = \frac{1}{4\pi\varepsilon_0}\frac{Ze^2}{|x|} - eE(T)x \tag{2.32}$$

where Z is the atomic number, x the distance from the charged particle and E represents the time dependent electric potential due to the incident laser. The second term suppresses the Coulomb potential of the atomic nucleus, allowing the electron to escape the atomic potential through the potential barrier, known as the tunnelling ionisation.

To quantitatively distinguish the tunnelling regime from the multi-photon ionisation process a key parameter known as the Keldysh parameter, γ_K, may be used. This allows us to compare the ionisation energy, E_{ion} with the classical ponderomotive potential, ϕ_{pond};

$$\gamma_K = \sqrt{\frac{E_{ion}}{2\phi_{pond}}} \tag{2.33}$$

where ϕ_{pond} is described as;

$$\phi_{pond} = \frac{e^2E^2}{4m_e\omega_L^2} \tag{2.34}$$

for the tunnelling effect to be dominant the γ_k must be $\ll 1$, here the potential of the laser pulse is so high as to suppress the potential experienced by the electron from the nucleus. On the contrary when $\gamma_k \gg 1$ the potential of the laser is not sufficient to suppress the barrier and the dominant mechanism is the multi-photon effect. When the laser intensities are higher, $I_L > 10^{14}$ Wcm^{-2}, the potential barrier connecting the bound electrons can be completely suppressed by a laser potential so that the electrons are free, and this mechanism is known as barrier suppression ionisation. Figures 2.2 (c) and (d) show a depiction of these mechanisms.

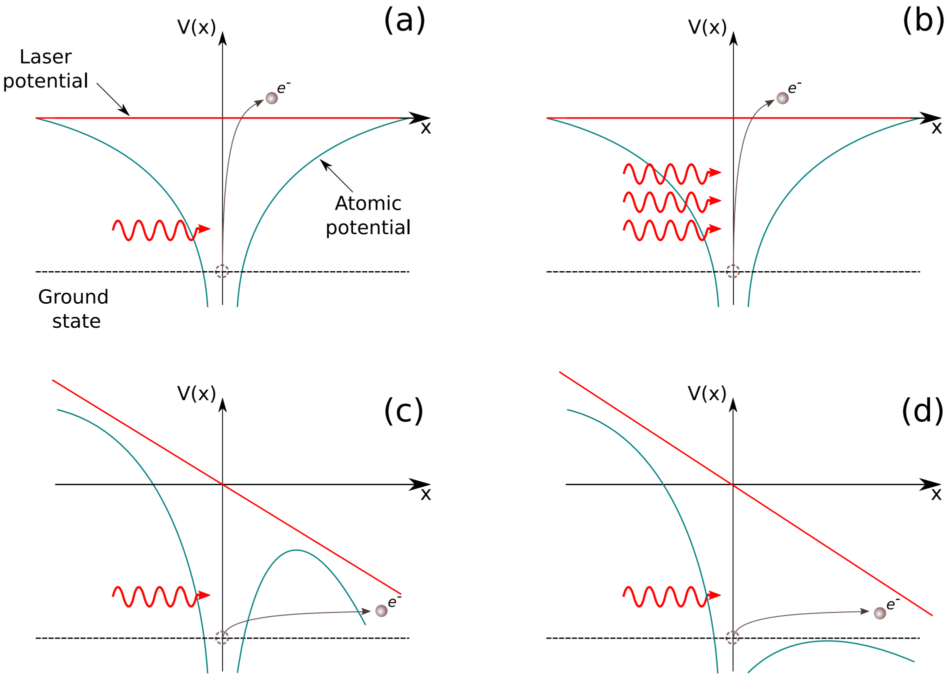

Figure 2.2: Illustration of the ionisation processes relevant to the laser-solid interactions discussed in this section. The black dotted lines represent the unperturbed Coulomb potential, blue the unperturbed Coulomb potential, and red the incident laser potential. (a) single photon ionisation, where the red arrow indicates the photon that is absorbed by the atom. (b) multi-photon ionisation, multiple photons provide the electron with enough energy to escape the atomic potential and with the red arrows representing an absorbed photon. (c) Tunnelling ionisation, where the decrease of the atomic potential barrier by the laser field increases the probability of the electron tunnelling effect. (d) Barrier suppression ionisation, in which the barrier is completely suppressed and the electron is liberated from the nucleus.

2.5 Laser interaction with solid density plasma

In this section we will describe the basic theory of electromagnetic wave propagation through plasma by examining the various mechanisms of energy absorption from a laser pulse to electrons, but first it is useful to consider the simplified case of the interaction of a strong, infinite plane wave with a single electron.

2.5.1 Single electron motion in an EM field

Compared to ions, electrons are preferentially accelerated due to their lower mass, and so the motion of the ions will be neglected. As described earlier, the force experienced by an electron is described by the Lorentz equation;

$$F_L = \frac{d\mathbf{p}}{dt} = -e(\mathbf{E} + \mathbf{v} \times \mathbf{B}) \tag{2.35}$$

with $\mathbf{p} = \gamma \mathrm{m}_e \mathbf{v}$, and where $\gamma = \sqrt{1 + p^2/m_e c^2}$ is the Lorentz factor. For simplicity we consider the motion of the electron in a non-relativistic regime, to begin, where only the influence of the electric field is considered. For an electric field given by $|\mathbf{E}| = E_0 \mathrm{sin}(\omega t)$, equation 2.35 can be re-written as;

$$F_L = m_e \frac{d\mathbf{v}}{dt} = -eE_0 \sin(\omega t) \tag{2.36}$$

This electric field will cause the electron to oscillate with a velocity of;

$$v_{osc} = \frac{eE_0}{m_e \omega} \cos(\omega t) \tag{2.37}$$

Therefore, an electron which is initially at rest in the presence of the electric field will begin to oscillate perpendicular in the electric field direction, oscillating at the frequency of the electromagnetic field. Equation 2.37 defines the quiver velocity and from this, the maximum velocity achieved by the electron can be seen to be $v_{max} = eE_0/m_e\omega$.

It can be observed from equation 2.35 that the vector product between the velocity of the electron and the action of the magnetic field leads to a resultant force that acts to push the electron in the direction of propagation of the electromagnetic wave, but for non-relativistic velocities, the action of the magnetic field can be neglected since from equation 2.11 it turns out to be a factor of c times smaller than the electric field. Therefore the electron will only be subject to the presence of the electric field by oscillating in its polarisation direction.

At this point it is useful to define a key parameter to characterise the regime of motion of the electrons;

$$a_0 = \frac{eE_0}{m_e c \omega} \tag{2.38}$$

where a_0 is the normalised vector potential, and is commonly used to express the magnitude of an electric field during laser-solid interaction. When $a_0 \ll 1$, the electric field is dominant in determining the electron motion and the magnetic field contribution may be neglected. However higher intensity laser fields are used, then $a_0 > 1$ and electron velocities will reach a significant fraction of the speed of light, and thus relativistic effects must be considered. It is also often useful to define the Poynting vector;

$$\mathbf{S} = \frac{1}{\mu_0}\mathbf{E} \times \mathbf{B} \tag{2.39}$$

which describes the energy flux associated with the propagation of electromagnetic fields. If we consider a linearly polarised wave, where the electric and magnetic fields can be respectively described as $\mathbf{E}$=$E\sin(\omega t$ - $kz)$ and $\mathbf{B}$=$B\sin(\omega t$ - $kz)$, using equation 2.11 and recalling that $\varepsilon_0 = 1/(c^2\mu_0)$, the intensity I may be found by averaging over one laser period, as;

$$I = \langle S \rangle = \frac{\varepsilon_0 c E_0^2}{2} \tag{2.40}$$

The intensity of light required to accelerate electrons to relativistic velocities can then be related to the normalised light amplitude by rearranging equation 2.38 in terms of electric fields, $E_0 = (a_0 m_e c\omega)/e$, and then substituting accordingly;

$$I_L = \frac{a_0^2}{\lambda_L^2}\frac{(2\pi)^2 m_e^2 c^5[\mathrm{cm}]\varepsilon_0[\mathrm{Fcm}^{-1}]}{2e^2} \tag{2.41}$$

while expressing c and ε_0 in non-SI units, thus enabling the constant terms to be expressed as 1.37×10^{18} Wcm^{-2}. Therefore the transition to relativistic effects occurs when the product of the laser intensity and wavelength squared (known as the laser irradiance) meets the condition $I\lambda^2 > 1.37\times10^{18}$ Wcm$^{-2}\mu$m^2.

For laser irradiances above this, electron velocities will approach a significant fraction of the speed of light. In this scenario, relativistic effects, such as the increase in electron mass, will occur. Therefore, it is necessary to correct the electron momentum by the Lorentz factor, $\gamma = 1/(1$ - $(v/c)^2)^{1/2}$, accordingly, p

$= \gamma m_e c$. In addition, these relativistic velocities mean that the $\mathbf{v}\times\mathbf{B}$ term in the Lorentz force equation begins to be important, given that the magnitude of the $e(\mathbf{v}\times\mathbf{B})$ component is now on the same order as $e\mathbf{E}$. In this case, electrons experience simultaneously a force in the direction of the electric field and another force in the longitudinal direction due to the $\mathbf{v}\times\mathbf{B}$ term. The resultant two velocities in the perpendicular, $v^{(1)}$, and longitudinal, $v^{(2)}$, directions are included in the Lorentz's force equation as:

$$m_e \frac{d(v^{(1)} + v^{(2)})}{dt} = -e(\mathbf{E} + (v^{(1)} + v^{(2)}) \times \mathbf{B}) \tag{2.42}$$

By solving this equation, the velocities and positions in the perpendicular and longitudinal plane are determined as follows [30]:

$$\begin{cases} v^{(1)}(t) = a_0 c \cdot \sin(\omega t)\hat{y} & \Rightarrow \quad y(t) = -a_0 \dfrac{c}{\omega} \cdot \cos(\omega t) \\ v^{(2)}(t) = \dfrac{a_0^2 c}{4} \cdot \cos(2\omega t)\hat{z} & \Rightarrow \quad z(t) = -\dfrac{a_0^2 c}{8\omega} \cdot \sin(2\omega t) \end{cases} \tag{2.43}$$

These two equations show that in a relativistic regime:

- The perpendicular velocity and trajectory, $v^{(1)}$, scales with a_0, while the longitudinal velocity, $v^{(2)}$, scales with ${a_0}^2$.
- The perpendicular velocity and trajectory, $v^{(1)}$, oscillates once per laser period (at 1ω), while the longitudinal velocity, $v^{(2)}$, oscillates twice per laser frequency (at 2ω).

2.5.2 The ponderomotive force

In the previous section, the effect of an infinite plane wave on an electron was described. In reality, however, a laser pulse, such as those employed in this thesis, typically has a Gaussian temporal and spatial profile with finite spatial dimensions and temporal duration. Typically, in the non-relativistic case, in a homogeneous field at each cycle of oscillation of the electromagnetic wave the electron returns to its initial point, i.e. it will oscillate around its equilibrium point, having an average cyclical oscillation energy described by the ponderomotive potential;

$$U_P = -\frac{e^2}{2m_e {\omega^2}_L}\langle E^2\rangle \tag{2.44}$$

where $\langle E^2\rangle$ is the cycle averaged electric field squared. The spatial gradient of the ponderomotive potential defines the so-called ponderomotive force, defined by Gibbon [29], and described in detail in references [40][41]. This may be expressed mathematically as the mean cycle of the position and velocity of the electron;

$$F_P = -\frac{e^2}{2m_e {\omega^2}_L}\nabla\langle E^2\rangle \tag{2.45}$$

The ponderomotive force ejects particles from regions where the electric field is higher. The force imposed on an electron oscillating at the laser frequency at the turning point of the oscillation into a larger field amplitude is greater than that imposed at the point turning with a lower field.

In the relativistic regime the ponderomotive force is defined as $\mathbf{F}_P$ = -$m_e c^2 \nabla\gamma$ and the ponderomotive potential is given by;

$$U_P = -m_e c^2(\gamma - 1) \tag{2.46}$$

As can be seen from equation 2.46, the ponderomotive force does not depend on the sign of the charged particle. Consequently it will push any type of particle (positive or negative) in the same direction, i.e. away from a region of strong electric field. In the case of plasma, positive particles include protons and heavier ions which being much heavier than electrons, will be less affected by this force.

2.5.3 EM propagation in plasma

In the previous section, the simple case of the motion of a single electron in the presence of an electromagnetic wave was examined. However this does not reflect the various processes that occur when an electromagnetic wave interacts with a system of charged particles and therefore with plasma. We consider the propagation of laser light in a plasma by using the wave equation including the charge density, $\mathbf{J} \neq 0$, since the wave propagates in the presence of charged particles, and assuming the quasi-neutrality, $\rho = 0$, equation 2.7 becomes;

$$\nabla^2 \mathbf{E} - \frac{1}{c^2}\frac{\partial^2 \mathbf{E}}{\partial t^2} - \mu_0 \frac{\partial \mathbf{J}}{\partial t} = 0 \tag{2.47}$$

By setting $\partial/\partial t$ = -$i\omega$, ∇ = ik and $\mathbf{J}$=-$n_e e\mathbf{v}$, we can calculate the dispersion relation when the electromagnetic wave propagates in a plasma as;

$$\omega_L^2 = c^2 k_0^2 + \omega_P^2 \tag{2.48}$$

This relationship highlights how the plasma frequency will alter the EM wave propagation. From this expression it is possible to obtain two distinct parameters; the phase velocity, $v_p = \omega/k$, and the group velocity, $v_g = d\omega/dk$;

$$v_p = \sqrt{c^2 + \frac{\omega_P^2}{k^2}} \tag{2.49}$$

$$v_g = \frac{c^2}{\sqrt{c^2 + \frac{\omega_P^2}{k^2}}} \tag{2.50}$$

At this point it can be seen from the equation 2.48, that when the frequency of the laser and the plasma are equal, $\omega_L = \omega_P$, the EM wave can no longer propagate in the plasma but is absorbed or reflected. This condition is usually expressed in terms of plasma density, so by substituting in equation 2.27, and by setting the frequency of the laser equal to the plasma frequency, the critical density may be defined as follows;

$$n_c = \frac{m_e \varepsilon_0 \omega^2}{e^2} \sim 1.1 \times 10^{21} \lambda_{\mu m}^2 [cm^{-3}] \tag{2.51}$$

Plasma in which the electron density is lower than n_c, is defined as underdense, where the frequency of the propagating EM wave, ω_L, is greater than the plasma frequency, ω_P. In this region, as the frequency of the EM wave increases, its phase and group velocity will tend to c, as showed in figure 2.3. On the other hand, when $n_e > n_c$, the plasma is defined as overdense, the electrons forming the plasma will oscillate at frequencies higher than the oscillations of the EM wave acting to screen the field. At the critical density surface, the pulse will not be entirely reflected. Instead, the electric field will penetrate into the plasma within a certain depth known as the skin depth, $l_s = c/(\omega_P^2 \text{ - } \omega^2)^{1/2}$, which defines the distance over which the electric field decays to 1/e of it's amplitude into the overdense plasma. See figure 2.3 for an illustration of these concepts.

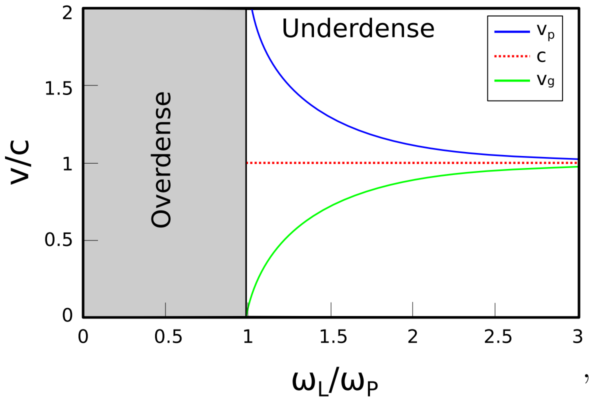

Figure 2.3: Group (solid green line) and phase (solid blue line) velocity of a wave propagating through the plasma as a function of its frequency normalised to the plasma frequency. When $\omega_L/\omega_P > 1$ the plasma is underdense, on the contrary when the $\omega_L/\omega_P < 1$ it is defined as overdense. While at the interface between the two regions, the group velocity tends to 0 and the phase velocity tends to infinity.

Reflection of the laser pulse at the critical density surface is only valid when the pulse is normally incident i.e. $\theta = 0°$. Consequently, it is crucial to formulate an expression that describes the density at which the laser is reflected for higher angles, taking θ into account. To attain this, it is useful to define the refractive index of the plasma, which we can derive from the dispersion relation (equation 2.48) as;

$$\eta = \sqrt{1 - \frac{\omega_P^2}{\omega_L^2}} \tag{2.52}$$

This equation shows that when the laser frequency is lower than the plasma frequency, the refractive index becomes imaginary, making it physically impossible for light to continue propagating through the plasma.

2.6 Laser induced plasma expansion

After introducing and discussing the mechanisms on how an intense laser pulse can generate a plasma, it becomes important to delve into the dynamics and characteristics of the plasma formed on the front surface of the target.

The atomic potential is significantly influenced by the number of protons in the nucleus. A higher proton count results in a stronger nuclear charge, generally enhancing the attraction between the nucleus and the electrons. However, for outer shell electrons in larger atoms, the binding energy is typically lower due to their increased distance from the nucleus. Consequently, when a short pulse laser irradiates a solid density target with a main peak intensity exceeding 10^{18} Wcm^{-2}, the less intense light arriving before the main peak can still be sufficient to ionise the target. This ionisation occurring through multi-photon ionisation or tunnel ionisation, as discussed in section 2.4.2, leads to the formation of a pre-plasma. The spatial extent of this pre-plasma affects several aspects in the dynamics of laser-plasma interactions, and therefore we need parameters to characterise it. The expanding front surface plasma travels at a speed approximately equal to the local sound speed, c_s, expressed as;

$$c_s = \sqrt{\frac{k_B Z^*(T_e + T_i)}{m_i}} \tag{2.53}$$

where k$_B$ is Boltzmann's constant, Z^* the ionisation state, T_e is the plasma electron temperature, T_i the plasma ion temperature and m_i is the ion mass. Inside the plasma, free electrons exert a thermal pressure which causes the plasma to expand with an approximately exponential density profile that decreases with increasing distance from the initial position of the target surface. This density profile may be defined by;

$$n_e(z) = n_0 exp\left(-\frac{z}{L_s}\right) \tag{2.54}$$

where n_0 is the targets initial electron density, z is the distance from the initial target surface and L_s is the so-called density scale length, i.e. the distance at which the density drops to 1/e of the initial density n_0. The density scale length is an important parameter in laser-solid interactions since it can greatly influence the interaction dynamics, especially the absorption of laser energy to plasma electrons [42][43]. Using the sound speed, c_s, and the duration of the laser pulse, τ_L, the scale length can be estimated as;

$$L_s = c_s \tau_L \tag{2.55}$$

2.7 Absorption mechanisms

As we saw in the previous section an electron cannot experience a net energy gain when irradiated by a plane wave electromagnetic field in a vacuum, known as the Lawson-Woodward theorem [44] [45], i.e. the electron gains no net energy while oscillating in the field, as any energy gained will be transferred back to the laser during the second half of a pulse cycle. The assumptions imposed by the Lawson-Woodward theorem determine that (i) the electron must be highly relativistic, (ii) there must be no static magnetic and electric fields present, (iii) the interaction region must be infinite, (iv) the non linear effects are neglected, (v) and occurs in a vacuum, with no boundaries present. In a more realistic scenario, such as in laser-plasma interactions, the conditions imposed by Lawson-Woodward theorem are no longer valid due to the laser beam being focused with a finite temporal and spatial profile. During the interaction, a series of mechanisms can occur due to the presence of the plasma itself and allow for net energy gain to electrons. In general, two main categories of mechanisms can be distinguished, by which the plasma can absorb energy from the laser: collisional and collisionless absorption mechanisms.

Collisional processes are based on the heating of electrons by the laser pulse where the electrons experience a binary collision with the ions of the plasma, to which they transfer energy, in a process called inverse bremsstrahlung, before the laser is able to recover it. This process is dependent on the mean free path of the electrons, which is less than the extent of the plasma. It is found that the collisional regime of the absorption mechanisms dominates for high electron densities and for intensities up to 10^{15} Wcm^{-2}. Collisional absorption therefore plays an important role in heating the pre-plasma which initially forms from the lower intensity laser pulse preceding the main pulse.

For higher laser intensities, such as the laser pulses studied in this thesis, collisionless absorption processes become dominant and occurs when the electron oscillations are so large that the electron is pushed beyond the critical density surface that it is no longer affected by the laser field and thus gain energy. There are several absorption mechanisms and the most important ones will be described in the following sections.

2.7.1 Resonance absorption mechanism

One of the most relevant collisionless absorption mechanisms in laser-solid interactions is resonance absorption. In the general case, this occurs when a non-relativistic p-polarised laser pulse (with $a_0 \ll 1$) is incident at a non-zero angle of incidence with respect to the target surface, with the component of the electric field parallel to the density gradient of the pre-plasma, i.e. parallel to the normal vector of the target surface. There will be a region where the electric field excites oscillations in the plasma electrons, at the laser frequency ($\omega_P = \omega_L$), i.e. at critical surface. This is illustrated in figure 2.4, where the linearly polarised laser is incident at an oblique angle, θ. The angle incidence is necessary to allow the laser pulse to drive the electrons in the direction of the electric field, parallel to the normal of the target, beyond the critical surface where the laser decays evanescently resulting in the electrons escaping the electric field due to the reduced restoring force.

An important aspect to consider concerns the condition of oblique incidence which can influence the propagation of the laser pulse due to the presence of non-uniform pre-plasma which forms during the rising edge of the pulse and extends into the vacuum on the front surface of the target. This happens when opposite edges of the pulse pass through differing plasma densities and, consequently, different refractive indices, which results in the laser being turned before it reaches the critical surface. We can use the dispersion relation to examine this behaviour, from equation 2.48 we can include the angle of incidence by modifying the vector k transversal to the density gradient such that $k_y = (\omega_L/\mathrm{c})\sin\theta$. We obtain the new dispersion relation:

$$\omega_L^2 = \omega_P^2 + k_x^2 c^2 + \omega_L^2 sin^2\theta \tag{2.56}$$

which highlights how the vector k_x changes continuously in the presence of the density gradient and that the reflection occurs when $k_x \leq 0$.

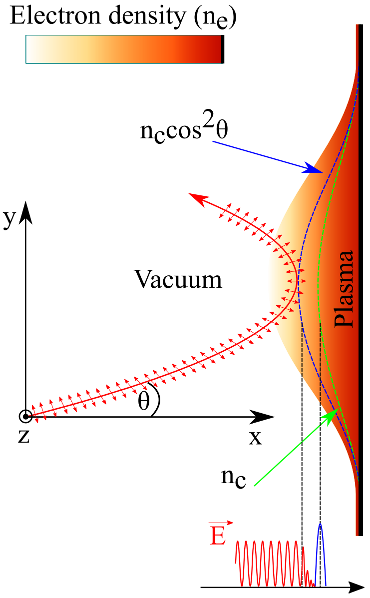

Figure 2.4: Illustration depicting the resonance absorption mechanism: the p-polarised laser pulse, with an electric field oriented parallel to the plasma density gradient, interacts with the target at an incidence angle, θ. The EM wave therefore interacts obliquely with the plasma and when it reaches the surface of critical density it is reflected, where $\omega_L = \omega_P$. Beyond this surface the electrons are accelerated into the target.

For a specific incidence angle, the portion of laser energy absorbed by this mechanism, f_{abs}, is characterised by the Denisov function, ξ [46], such that: $f_{abs} \propto \xi$ exp (-2/3 ξ^3), where $\xi = (kL_s)^{1/3}\sin\theta$. Resonant absorption is most efficient for incidence angles ranging from oblique to nearly parallel [29], since relatively long density scale length plasma ($\sim L_s \gg \lambda_L$) is required. Consequently, the portion of the laser field that reaches the critical density decreases as the angle increases. The relationship between laser incidence angle and absorption was documented by Friedberg *et al.* [47], showing that an angle of $\theta \approx 23°$ resulted in maximum absorption at $L_s = 10\lambda_L/2\pi$. Resonance absorption will be dominant at laser intensities in the range 10^{12} to 10^{17} Wcm^{-2}, while for higher intensity values other absorption mechanisms predominate due to the onset of relativistic effects.

2.7.2 Vacuum heating mechanism

The second relevant collisionless absorption mechanism to consider is vacuum heating, also known as Brunel heating or not-so-resonant absorption. This mechanism is very similar to resonant absorption, and occurs when a p-polarised laser pulse interacts with a sharp density gradient ($L_s \ll \lambda_L$) present on the front surface of the plasma involving the injection of electrons into the plasma. In this condition, the plasma scale length is less then the electron amplitude of the electron transverse oscillation in the laser electric field. During the first half cycle of the propagating wave electrons are pulled into the vacuum, and then in the second part of the cycle these electrons are accelerated into the plasma by the same field with a laser field oscillation rate $v \simeq eE/m_e\omega_L$. At this point the amplitude of the electron's oscillation will carry it beyond the critical surface where the field evanescently decays resulting in a minor restoring force, and the electrons will thus carry off an energy transfer from the laser into the plasma after each laser period. In simulations conducted by Gibbon and Bell [48], it was observed that electrons could undergo multiple oscillations between the vacuum and the underdense plasma prior to their injection beyond the critical surface. Typically this mechanism is optimised for large angles of incidence, as reported in [47], which maximises the electric field component perpendicular to the plasma density gradient. Unlike the resonance absorption, in vacuum heating the spatial extent of the pre-plasma is less than the amplitude of the transversal oscillation of the electron in the laser electric field and becomes dominant for laser intensity $> 10^{16}$ Wcm^{-2}. Figure 2.5 depicts this absorption mechanism.

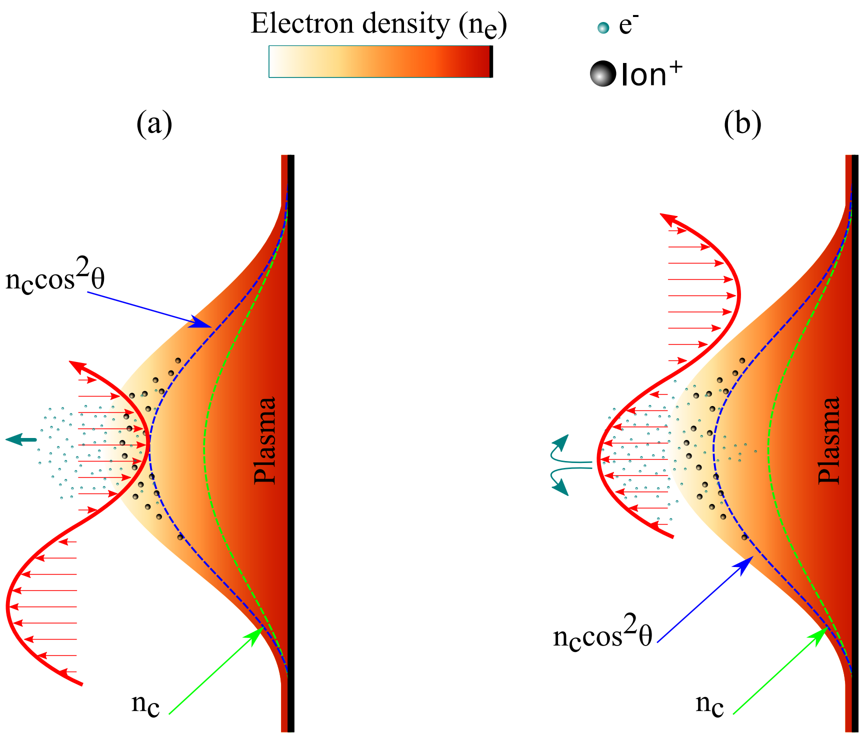

Figure 2.5: Schematic illustration of the vacuum heating absorption mechanism. (a) the p-polarised laser pulse interacts with the plasma, on a relatively steep density gradient. In the first half period of the wave, where its electric field is able to expel electrons from the plasma into vacuum, while in (b) the second half of the laser period, the electric field, having the opposite direction, accelerates the electrons back into the plasma and beyond the critical density surface. Here the electric field of the laser decays evanescently and the electrons no longer feels the restoring force and accelerated behind the critical surface gaining energy.

2.7.3 Relativistic J×B heating mechanism

When the intensity of the laser fields is relativistically intense (as in the investigations presented in this thesis), the **v**×**B** component of the Lorentz force becomes comparable in magnitude to the electric field component. The effect of the magnetic induction field, **B**, cannot be neglected and the electron is driven at a frequency of $2\omega_L$ along the propagation axis of the laser. Electrons moving in the direction of the laser propagation will be subjected to a force which can be expressed as:

$$\mathbf{F}_P = -\frac{e^2}{4m_e\omega_L^2}\nabla\langle E^2\rangle\left(1+\frac{1-\epsilon^2}{1+\epsilon^2}cos(2\omega_L)\right) \tag{2.57}$$

This force is responsible for the energy absorption mechanism called **J**×**B** heating. Studying this relationship we see that the first term in the equation corresponds to the ponderomotive force term, while the second term contains the oscillatory component $2\omega_L$ which makes the electrons oscillate at twice the laser frequency and drives them beyond the critical plasma surface. The direction of the force reaches a maximum twice per cycle: once in the first half and again in the second half. Specifically, the cross product (-**v** × -**B**) and (**v** × **B**) results in a force which is pointing in the same direction (into the target). In the first half of the cycle, the force is (-**v** × -**B**), and in the second half, it is (**v** × **B**). This can also be seen in equation 2.43. Hence, electrons are injected twice per cycle. This mechanism is illustrated in figure 2.6.

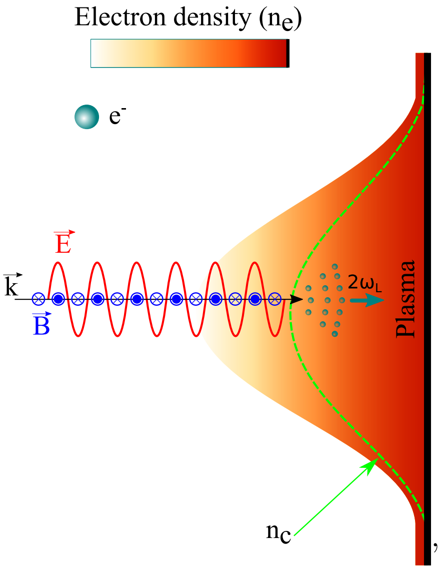

Figure 2.6: Illustration of the **J**×**B** heating mechanism. The incident laser pulse pushes electrons at twice the laser frequency beyond the critical surface, along the laser k-vector.

2.8 Properties of laser-generated electrons

The previous sections have described the mechanisms by which laser energy can be transferred to plasma electrons, often referred to as “fast” or “hot” electrons. The spectral and propagation characteristics of these fast electrons are of fundamental importance for numerous laser-solid interaction theories of interest, such as the acceleration of ions and the generation of x-rays, therefore it is necessary to present a description in order to have a deeper understanding of laser-solid interactions.

2.8.1 Fast electron spectrum and temperature

The collisionless absorption mechanisms explored in the previous section, leads to a certain fraction of electrons being heated in the laser field to temperatures much higher than the average plasma temperature. The energy gained by the population of fast electrons may be stochastic and that averaging over these energies, in the non-relativistic regime, leads to a Maxwell-Boltzmann distribution [49] described by the function;

$$f(E_f) = N_f \sqrt{\frac{4E_f}{\pi(k_B T_f)^3}} exp\left(-\frac{E_f}{k_B T_f}\right) \tag{2.58}$$

where N_f the total number of fast electrons and E_f is the fast electron energy. In reality, the collective effects that impact overall absorption can lead to deviations from the ideal single-temperature Maxwell-Boltzmann distribution. As the plasma heats up and $k_B T_e$ nears or surpasses $m_e c^2$, the increasing relativistic mass of electrons must be considered by including the γ factor, and the distribution changes to a Maxwell-Jüttner distribution;

$$f(\gamma) = \frac{\gamma^2 \beta}{\theta K_2(1/\theta)} exp\left(-\frac{\gamma}{\theta}\right) \tag{2.59}$$

where $\beta = v/c$, $\theta = k_B T_e / m_e c^2$, and K_2 is the modified Bessel function of the second kind. In figure 2.7 the energy spectrum distribution of the injected electrons is shown.

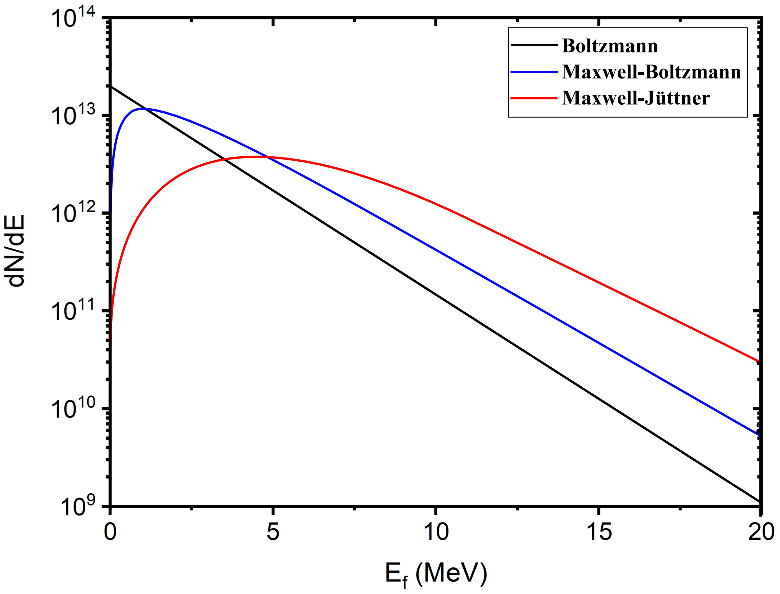

Figure 2.7: Energy spectra for three distinct fast electron distributions. The Boltzmann distribution (represented by black data) is included for comparison with the two fast electron energy distributions, defined as dN/dE = $N_f e^{E_f/K_b T_f}$.

The mean kinetic energy of the fast electron energy distribution is typically defined using a temperature, $k_B T_f$, which has been observed to rise in proportion to laser intensity, or more precisely, with irradiance, $I_L \lambda^2{}_L$. There have been various proposed scalings with irradiance, with various approximations developed taking into account varying laser parameters [50] [51], and all agree that increasing laser irradiance leads to an increase in fast electron temperature. In the relativistic regime, the most commonly cited electron temperature scaling as function of laser intensity is often referred to as 'Wilks scaling' [52], and is given by:

$$k_B T_f = m_e c^2 \left(\sqrt{1 + \frac{I_L \lambda_L^2}{1.37 \times 10^{18}}} - 1 \right) \tag{2.60}$$

This represents an analytically derived equation for the variation in electron temperatures when a relativistic laser pulse interacts with a solid density target at a normal incidence. Describing the properties of fast electrons within the target has been notably challenging because of the presence of powerful electrostatic fields that confine the majority of fast electrons within the target, with only a minor portion managing to exit into the vacuum. Therefore determining electron temperature typically relies on indirect techniques, such as the detection of x-ray emissions originating from the target [53], or by measuring the population of electrons that manage to escape, i.e., those not confined within the target [54].

2.8.2 Fast electron transport

The population of relativistic electrons has a kinetic energy greater than the electron rest mass energy ($E_f > m_e c^2$) and typically have a peak current on the order of mega-amperes (MA). Such high currents generate enormous induced magnetic fields, as noted by Alfvén [55], which will act to inhibit the propagation of the electron beam. The current limit above which electrons can no longer propagate, commonly referred to as the Alfvén limit (I_a), can be estimated as;

$$I_A \cong \frac{4\pi}{e\mu_0} p \tag{2.61}$$

where p is the electron momentum. If we consider a 1 MeV electron beam, this current limit is calculated to be 47.5 kA, which is several orders of magnitude lower than the predicted MA fast electron currents. Therefore, there must be some other effect that allows the electron current to exceed the Alfven limit. This limit is circumvented when considering the net current flowing inside the target. When the fast electrons, $\mathbf{j}_f$, are generated within the plasma, a space charge separation field is induced due to this displacement of charges, and this field attracts a spatially localised current from the target in the opposite direction to $\mathbf{j}_f$. This secondary current is referred to as the return current, $\mathbf{j}_r$, which consists of a larger number of lower temperature electrons, acting to balance the net current. This balance is typically expressed as;

$$\mathbf{j}_f + \mathbf{j}_r \approx 0 \tag{2.62}$$

However, perfect current neutrality is not obtained since the return current does not exactly spatially overlap the fast current, thus giving rise to the formation of magnetic fields and other beam instabilities, which can have important effects on the dynamics of the fast electron beam while it propagates. The electric field can be described by Ohm's law as:

$$\mathbf{E} = \eta_e \mathbf{j}_r \tag{2.63}$$

where η_e is the plasma resistivity, and the magnetic field may be expressed via Faraday's law as:

$$\frac{\partial \mathbf{B}}{\partial t} = -\nabla \times \mathbf{E} = \nabla \times (\eta_e \mathbf{j}_r) \tag{2.64}$$

$$\nabla \times \mathbf{B} = \mu_0(\mathbf{j}_f + \mathbf{j}r) \tag{2.65}$$

If the current is not neutralised then the net current is;

$$\mathbf{j}_f + \mathbf{j}_r = \frac{\nabla \times \mathbf{B}}{\mu_0} \tag{2.66}$$

$$\mathbf{j}_r = -\frac{\nabla \times \mathbf{B}}{\mu_0} - \mathbf{j}_f \tag{2.67}$$

$$\frac{\partial \mathbf{B}}{\partial t} = -\nabla \times \left(\frac{\eta_e}{\mu_0}\nabla \times \mathbf{B} - \eta_e \mathbf{j}_f\right) \tag{2.68}$$

$$\frac{\partial \mathbf{B}}{\partial t} = -\nabla \times \left(\frac{\eta_e}{\mu_0}\nabla \times \mathbf{B}\right) + \nabla \times (\eta_e \mathbf{j}_f) \tag{2.69}$$

For plasma conditions present within the target the η_e/μ_0 term can be approximated to 1, and the equation becomes;

$$\frac{\partial \mathbf{B}}{\partial t} = -\nabla \times (\eta_e \mathbf{j}_f) \tag{2.70}$$

$$\frac{\partial \mathbf{B}}{\partial t} = \eta_e(\nabla \times \mathbf{j}_f) + \nabla \eta_e \times \mathbf{j}_f \tag{2.71}$$

From equation 2.71 it can be seen that the first term on the RHS of the relation, $\eta_e(\nabla \times \mathbf{j}_f)$, describes the generation of the magnetic field due to the variation of the current density associated with the fast electron beam. The current density present on-axis decreases as the radial distance from the central axis of the beam increases; a magnetic field is thus created which exerts a radial force directed inwards which, by pinching the beam, reduces its divergence. Furthermore, within the beam there are local electron density modulations, which leads to the generation of magnetic fields which acts to increase the current density in regions where the density is already high, and this leads to filamentation of the beam [56] and subsequently to a possible beam breakup. The second term in the equation 2.71 describes the evolution of the magnetic fields that are generated due to resistivity gradients inside the plasma, resulting, for example, from temperature variations. The current density of the fast electrons is higher on-axis than that of the returning electrons which is more collisional, leading to increased heating on-axis, falling off towards the edges of the beam. This temperature variation will influence the resistivity, leading to the generation of magnetic fields. These induced magnetic fields will act to push or pull the fast electrons away from or towards the axis of propagation, which results in an expansion or pinching of the beam. These two terms acting together complicate the evolutionary behaviour of the fast electron beam for the entire duration of the propagation.

2.9 Onset of relativistic induced transparency

As described in section 2.5.3, an electromagnetic wave with a frequency lower than the plasma frequency cannot propagate through the plasma since the refractive index is imaginary. The development of relativistically intense lasers ($\mathrm{I}_L > 10^{18}$ Wcm^{-2} at wavelengths $\lambda_L = 1$ μm) has made it possible to obtain relativistic effects which influence the propagation of the pulse when it interacts with the plasma. As the intensity of the laser increases, the mass of the electrons is relativistically increased by the Lorentz factor, γ, which makes them heavier than the classical description. Therefore, we have to correct the critical plasma density from equation 2.51 to;

$$n_e' = \frac{\gamma m_e \varepsilon_0 \omega_L^2}{e^2} = \gamma n_c \tag{2.72}$$

In the chapter 2.5.3, overdense plasma was described as a plasma with a frequency higher than the laser frequency, and in terms of critical density this can be rewritten as $n_e > n_c$. Since the Lorentz factor is influenced by the kinetic energy of the electrons governed by the intensity of the laser, if this intensity is sufficient high, there will be a precise value that satisfies $n_e < n\text{'}_c$. At that point, the overdense plasma will become relativistically underdense, enabling laser propagation further into the plasma than would be possible without the influence of relativistic effects. This process is known as relativistically induced transparency (RIT). Therefore, it is evident that transparency occurs for an initially overdense target with the condition $n_e < n\text{'}_c$, and for currently achieveable laser intensities, this may occur through a combination of two mechanisms: i) due to an increasing electron Lorentz factor and/or ii) target expansion due to thermal and electrostatic pressure (i.e. decreasing the plasma density). This combination of mechanisms is often referred to as relativistic self-induced transparency (RSIT). The main phases of the RSIT process are depicted in figure 2.8, which are:

1. During the interaction with solid target, the rising edge of the laser pulse will rapidly ionise the material and generate plasma, which will expands due to thermal pressure and its density will decrease exponentially at the front surface of the target. The majority of the plasma maintains the condition $n_e > n_c$ and will remain overdense in this initial phase of the interaction, see figure 2.8

2. A portion of the leading edge of the pulse will be reflected back at the plasma density $n_e = n\text{'}_c$, while, the rest of the laser pulse possesses an intensity significant enough to exert substantial radiation pressure on the plasma electrons, leading to their accumulation and the formation of a region with remarkably high electron density localised around that electron density surface and the electron kinetic energies reach relativistic values.

Nevertheless, due to the heightened electron density, the condition $n_e < n'_c$ is not yet fulfilled at this point in the interaction, see figure 2.8

3. In the last stage, γ will increase until the laser pulse reaches its peak intensity during the interaction. Concurrently, as the plasma expands, the condition $n_e < n'_c$ will occur and the remaining part of the laser pulse will be able to propagate through the relativistically underdense plasma.

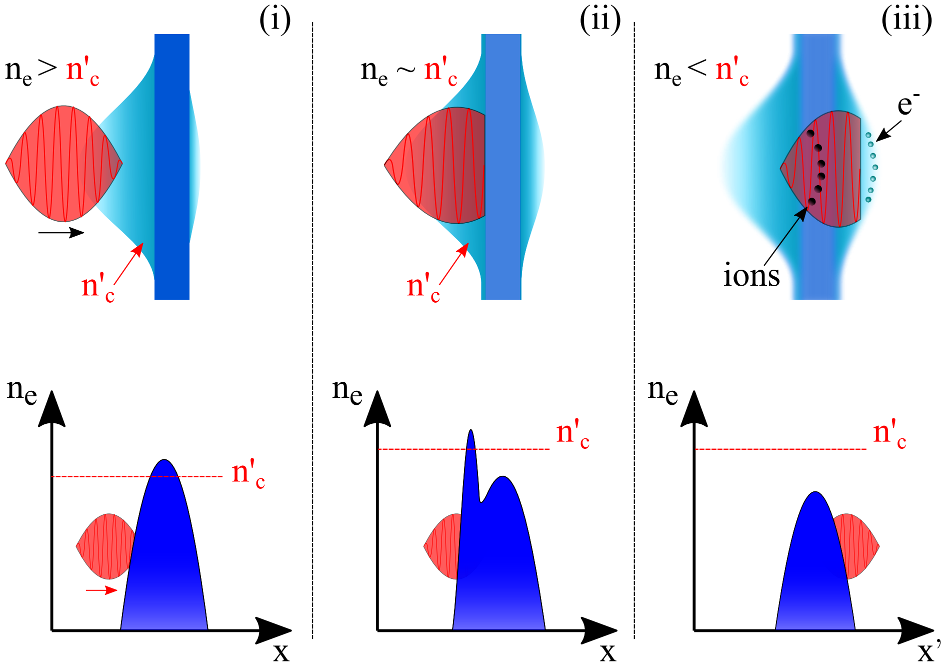

Figure 2.8: Scheme of the RIT process phases: (i) Initially the laser irradiates the target on the leading edge of the pulse, heating the electrons and the target begins to expand. (ii) Subsequently the higher intensity region of the laser pulse acts by pushing forward the electrons of the plasma from the front surface via the ponderomotive force into the critical density surface region, where the electron density in front of the laser also increases, while most of the target falls below the critical density. (iii) At this point, due to the expansion, the electron density continues to decrease below the critical density while the latter increases, and the laser can volumetrically interact with the plasma electrons.

If we consider aluminium targets (such as those used in this thesis), irradiated with a laser pulse at a wavelength of 1 μm the initially opaque target will become relativistically transparent if the intensity reaches values greater than 8×10^{23} Wcm^{-2}, which is several orders of magnitude higher than those provided by the laser employed in this thesis. For this reason, the target expansion is generally required for transparency to occur.

For targets thicker than the skin depth (i.e., where $l \gg l_s$), the leading edge of the pulse will be reflected from the critical surface, causing a sudden increase of the electron density within the skin depth. Therefore, this rise in density will delay the initiation of RSIT at the beginning of the pulse and it will only manifest when the laser reaches a level of intensity that causes both target expansion and electron heating. While for a thin target, one of the conditions for which relativistic transparency can occur is via laser radiation-driven compression of the target electron layer to a thickness less than the skin depth (l_s), $l<l_s$. In this scenario, the skin depth has to be corrected following the electron density increasing during radiation compression. This leads to an increase in the plasma frequency, thereby reducing the skin depth. However, given that the relativistically corrected skin depth, l_s' $= \sqrt{\gamma} l_s$, has a dependence on the Lorentz factor, this process also occurs around the peak of the pulse, and this condition [17] is reached when;

$$a_0 > \pi \frac{n_e}{n_c} \frac{l}{\lambda} = \zeta \tag{2.73}$$

The actual parameter which controls the onset of the relativistic transparency for thin targets is the areal density $n_e l$, since the other parameters, n_c and λ, are intrinsic to the incident laser. The equation 2.73 was employed by Macchi *et al.* [57] to derive a formalism for the target reflectivity, R, in relation to ζ:

$$R \simeq \begin{cases} \zeta^2/(1+\zeta^2) & \text{for } a_0 < \sqrt{1+\zeta^2} \\ \zeta^2/a_0 & \text{for } a_0 > \sqrt{1+\zeta^2} \end{cases} \tag{2.74}$$

This relation shows that when a_0 is significantly greater than 1, $a_0 \gg 1$, the reflection coefficient diminishes to lower levels, leading to increased transmission. As a result, the condition $a_0 > \zeta$ can be employed as a threshold for approximating the onset of relativistic transparency for thin targets.

The RSIT process results in numerous profound impacts on the interaction between high-intensity short-pulse lasers and solid-density plasmas. Experiments [58][59] over the past few years have demonstrated a noteworthy increase in the maximum proton energies within the relativistic transparent regime. In 3D particle-in-cell simulations [60], it has been demonstrated that the underdense plasma produced can also function as a polariser or a wave plate to alter the pulse polarisation. Furthermore, the potential to deliver laser energy deeper into the classically overdense plasma enhances the feasibility of the inertial confinement scheme for the fast ignition concept [61][62].

2.10 Laser-driven particle acceleration

In the previous sections, we have seen the concepts of accelerating charged particles such as electrons via intense optical pulses, but have ignored the motion of ions due to their mass being significantly higher than that of electrons. In current laser-plasma interactions, direct acceleration of ions is not yet feasible, as peak laser intensities higher than 10^{24} Wcm^{-2} are required. To accelerate heavy particles, other physical processes are therefore exploited where fields are generated sufficiently strong so as to overcome the inertia of the ions.

The first proposal for accelerating ions by means of plasmas was presented in the 1950s, [63], but interesting results on the application on such began to be obtained only in the 1990s thanks to the CPA technique, which will be introduced in section 4.2, which made possible sufficiently high laser intensities. In the last three decades, the acceleration of ions from lasers has thus been the subject of in-depth investigations mainly due to the possible applications in the energy production, medical applications and industrial fields, and a considerable amount of theoretical and numerical work has been conducted in order to better understand the underlying physical processes. A number of acceleration mechanisms have been proposed, some of which have been experimentally demonstrated capable of accelerating ions to energies of several tens of MeV. In principle, these mechanisms occur during collisionless absorption processes where the plasma electrons create space charge fields with gradients of acceleration of several TV/m, which drive the ion acceleration at energies higher than 100 MeV [27] [64] [65].

In subsequent sections, information on the primary mechanisms of ion acceleration driven by short-pulse lasers will be reported.

2.10.1 Target normal sheath acceleration

The most widely explored mechanism in the framework of laser-driven ion acceleration is known as target normal sheath acceleration (TNSA), first experimentally demonstrated and reported in Snavely*et al.* [9], Hatchett *et al.* [66] and Clark *et al.* [67], and subsequently theoretically examined by Wilks *et al.* in 2001 [68]. In this mechanism, a relativistically intense laser pulse ($> 10^{18}$ Wcm^{-2}) irradiates a solid density target foil. The thickness of the target is on the order of many microns, which allows it to remain opaque to the laser pulse throughout the interaction. The front surface of the irradiated target undergoes ionisation due to lower intensity light preceding the main pulse with subsequent expansion of the plasma. At this point, the main pulse interacts with the plasma and is partially absorbed via the various electron heating mechanisms described in the section 2.7. The fast electron beam generated on the front surface propagates inside the target until it reaches the rear surface creating a sheath field as a consequence of electron accumulation at the rear surface of the target since there is no return current to draw beyond this region and therefore only those electrons with sufficient energy manage to escape. The population of these electrons on the back surface is confined by Coulomb forces which results in the generation of a strong electrostatic sheath field, on the order of TVm^{-1}, which reflects electrons still generated by the laser back into the target [69]. These electrons recirculating within the target induce a similar sheath field on the front surface, further reflecting the electrons towards the rear of the target and could gain additional energy from the laser pulse, resulting in an extended re-circulation or refluxing process [37]. The refluxing of these electrons has a very important impact, in that it increases the duration of the TNSA acceleration process [70]. As a result of the lateral dispersion of fast electrons while passing through the target, a sheath field will develop on the rear surface, with a lateral spatial expansion [71] [72] [73]. The longitudinal spatial extent of the rear surface sheath field is determined by the Debye length of the sheath electron population, which can be expressed as:

$$\lambda_{D,Sheath} = \sqrt{\frac{\varepsilon_0 k_B T_e}{e^2 n_{e,sheath}}} \tag{2.75}$$

where $n_{e,sheath}$ is the electron density of the sheath. The extension is typically on the order of a few microns for electron temperatures in the MeV range and electron density, n_e, on the order of 10^{19} cm^{-3}. The transverse spatial extent of the sheath, known as sheath area, depends on the divergence of the electron beam and its temporal evolution on the back of the target. The size of the sheath area can be estimated through:

$$S_{Sheath} = \pi(r_0 + d \cdot \tan\theta)^2 \tag{2.76}$$

where r_0 is the radius of the laser focal spot, d is the target thickness and θ is the divergence angle of the electron beam. The sheath field that forms in this region is extremely strong (on the order of TVm^{-1}) and can be estimated as;

$$E_S \approx \frac{k_B T_e}{e \lambda_D} \tag{2.77}$$

This electric field is able to ionise contaminants on the rear surface of the target [74] [75], and to rapidly accelerate them longitudinally, up to energies of tens of MeV. This accelerated ion beam comes from a layer of the target which forms on the rear surface and is characterised by a number of ion species consisting of hydrocarbons and water vapour present in the atmosphere and deposited on the target surface. In figure 2.9 a schematic of this process is presented.

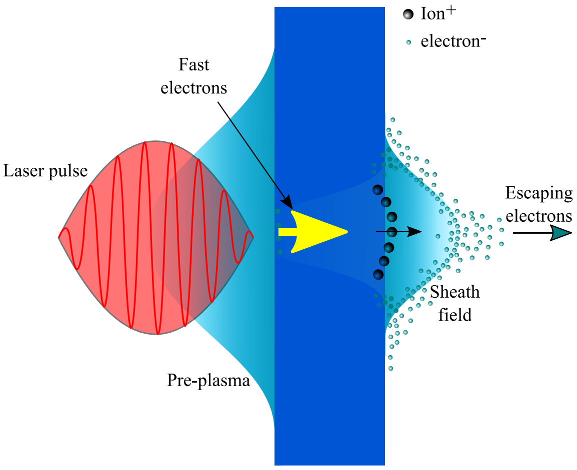

Figure 2.9: Diagram of the principle of the target normal sheath acceleration mechanism (TNSA). The laser pulse irradiates the front surface of the target, forming a plasma and hot electrons which propagate through the target. Some of the electrons that reach the back surface manage to escape, while the rest build up a strong sheath field that accelerates ions from the back surface of the target.

The ions generated from the rear surface layer are accelerated based on their charge-to-mass ratio (q/m). All ions, including protons (which have the highest q/m ratio) accelerate for as long as the field is present. Once the protons are generated, they screen the heavier ions from the sheath field, which results in less acceleration efficiency. However, ions, despite their lower q/m ratio, still experience some degree of acceleration and are observed alongside protons. Typically, a TNSA ion beam has a broad thermal ion energy distribution with a sharp maximum energy cut-off which depends on the driving electron temperature and density where the maximum proton energy achievable is closely linked to the peak laser intensity [76] [77], through the temperature and density of the generated electrons during the interaction.

The beam of accelerated ions exhibits a divergence that increases at lower particle energies due to the fact that the spatial profile of the electron density distribution forming the accelerating sheath is typically Gaussian in nature which is strongest on-axis and decays transversely. Moreover, the ion paths are perpendicular to the local orientation of the sheath where the resultant divergence varies along the evolving gradient of the sheath's transverse profile, and the ions are accelerated at angles normal to the sheath, thus the ion divergence is energy dependent [71].

2.10.2 Radiation pressure acceleration

Another promising laser-driven ion acceleration mechanism explored in recent years is radiation pressure acceleration (RPA). This mechanism dominates in interactions with thin targets (micron-nanometer scale) at ultra-high intensity laser ($> 10^{21}$ Wcm^{-2}) [78][79][80]. It is based on the momentum carried by an electromagnetic wave which is transferred to the plasma when it is reflected. As a result, the EM wave will exert a pressure on the surface which can be expressed as:

$$P_{rad} = (1 + R - T)\frac{I_L}{c} = (2R + A)\frac{I_L}{c} \tag{2.78}$$

where where R is the reflectivity coefficient, T is the transmission coefficient and A is the absorption coefficient. In order to conserve energy, the condition $R + T + A = 1$ must always be true. For intense laser pulses, this pressure can be high enough to counteract the rapid decompression of the target plasma. The intense laser pulse will directly accelerate electrons as soon as the radiation pressure exceeds the thermal pressure, the displacement of these electrons creates an intense charge separation field that subsequently accelerates ions. Unlike in TNSA, where the ions are accelerated from the back surface of the target, in the RPA mechanism the acceleration is driven from the front surface by photon pressure. In the case of a circularly polarised laser pulse as it interacts with the target, the front surface can be seen as a reflector moving at a speed $v = \beta\ c$, the surface reflectivity, $R(\omega$'), is a function of laser frequency in a moving frame, defined such that the target surface is at rest. Since radiation pressure is an invariant quantity, the pressure in the laboratory frame and rest frame can be expressed as:

$$P_{rad} = P'_{rad} = \frac{2I_L}{c} R(\omega)' \frac{1 - \beta}{1 + \beta} \tag{2.79}$$

The relationship between the incoming ω' and reflected ω frequencies is due to the relativistic Doppler effect, described as:

$$\omega' = \omega\sqrt{\frac{1-\beta}{1+\beta}} \tag{2.80}$$

By measuring the spectral shift of the reflected laser light, the Doppler shift can be used to determine the recession velocity of the critical plasma surface [81].

In the RPA model, two regimes are generally considered, Hole-boring (HB) and Light-sail (LS). Both undergo a recession of the frontal surface of the target, in the case of hole-boring, the laser pressure compresses the target, deforming the front surface and steepening the density profile. Here only a small fraction of the electrons of the plasma undergoes acceleration induced by the radiation pressure which then determines the acceleration of the ions from the front surface of the target. In the light-sail mechanism, however, the intense laser pulse accelerates the full region contained in the focal spot volume of the target, the compressed electron layer is pushed forward during hole boring reaching the target rear side whilst the laser light is still present. For the remainder of the laser pulse interaction light sail mode of RPA occurs. For ultra thin targets, the transition from hole boring to light sail mode happens very quickly and therefore the light sail mode dominates. In figure 2.10 a schematic of the two processes for RPA is shown.

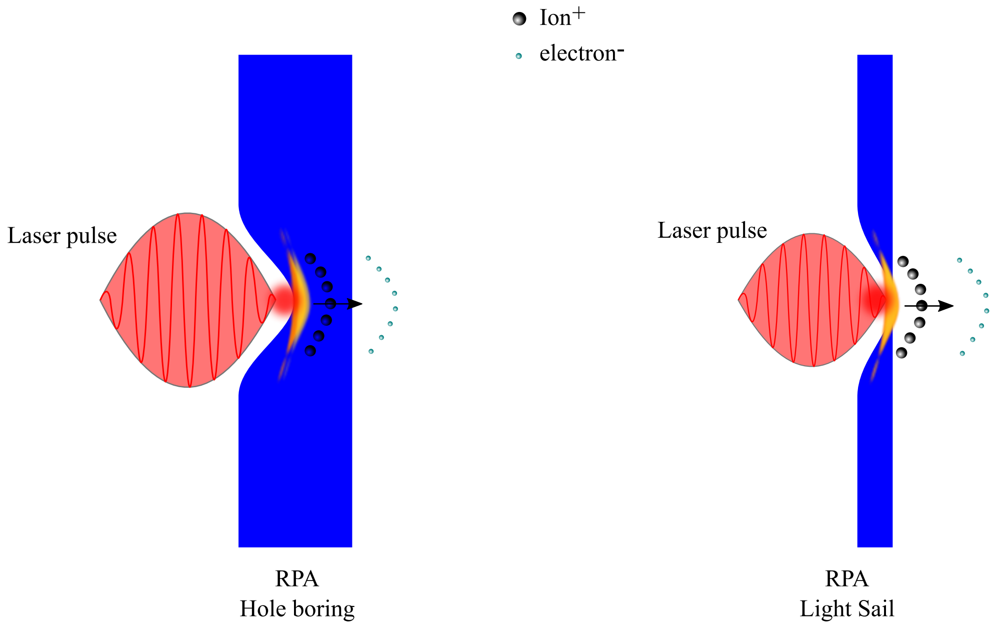

Figure 2.10: Diagram illustrating the different physical conditions present during (a) RPA - Hole Boring and (b) RPA - Light Sail.

2.11 Summary

From this chapter, it is clear that the interaction between a high intensity laser pulse with a solid density target is complex, involving numerous physical processes in rapid succession. We have discussed this physics, starting from the basics of the motion of single charged particles in an EM field and the definition of plasma, building up to discussion of the production mechanisms of highly energetic ion beams and other phenomena which are still being investigated. A solid foundation in this underpinning physics is essential to enable the understanding of the novel experimental techniques used, and the subsequent analysis performed, in the following chapters.

Chapter 3

Methodology: Lasers, diagnostics and simulations

In the previous chapter, the fundamental physics underpinning the interaction of intense laser pulses with solid density matter was explored. However, it is equally necessary to understand how these experiments are conducted, in terms of the laser systems employed, the diagnostics used to measure aspects of the interactions and the numerical codes implemented to help model and interpret the experimental measurements.

In this chapter we will describe the techniques employed in some of the high-power laser systems and experimental target areas in which laser-solid interaction experiments are performed. A description of the techniques used to generate high intensity, focused laser pulses will be provided, along with a description of the techniques used in this thesis to diagnose the interaction of such pulses with solid-density targets. In the final section of this chapter, the numerical methods used in this thesis to simulate laser-solid interactions will be introduced.

3.1 Properties of a short pulse, high intensity laser

In the context of studying the interaction between a linearly polarised, high-power laser pulse and dense plasma, a number of laser parameters have a significant impact on the interaction dynamics. Within this section, we will consider aspects of temporal intensity contrast and the characteristics of the laser focal spot, which are key parameters when seeking to understand laser-solid interactions.

3.1.1 High power laser technology

One of the most important aspects to review is the structure of high-power laser systems, typically located at large national science and technology facilities. These facilities, located around the globe, are centres of excellence for scientific research in the field of high power laser science and applications.

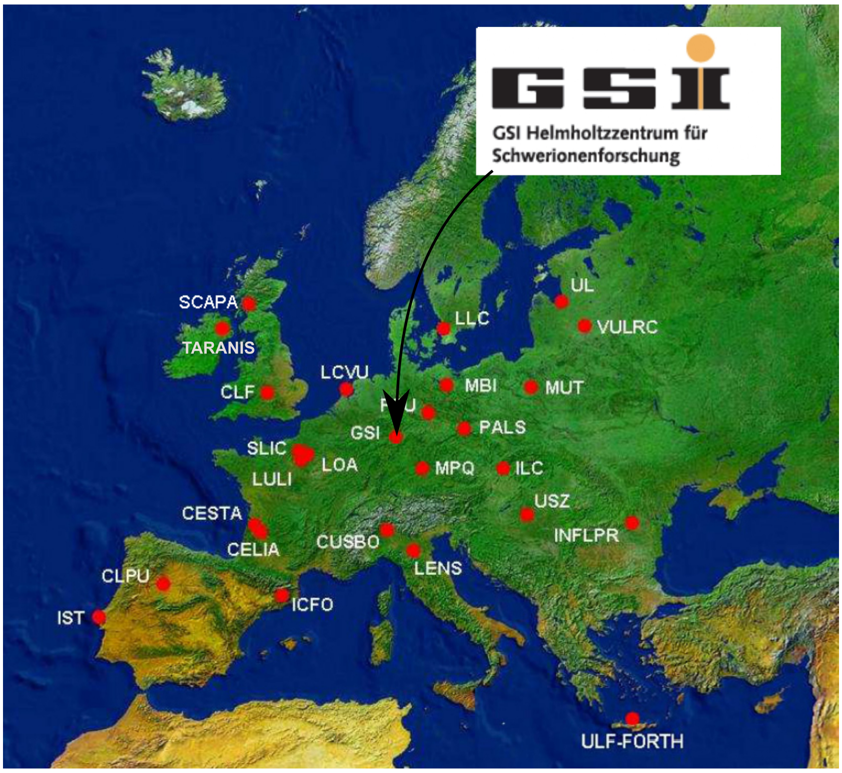

Figure 3.1: Map showing the location of some high intensity laser facilities in Europe [82], identifying the PHELIX laser system at GSI, Darmstadt (Germany), used in this thesis.

In the UK, there are facilities dedicated to scientific innovation and discovery, as shown in figure 3.1. The Central Laser Facility at STFC Rutherford Appleton Laboratory (RAL) is one of the world's leading laser facilities, enabling experimental applications of physics. The research performed there includes the acceleration of particles to high energies with a view to applications such as proton radiotherapy, inertial confinement fusion and the generation of betatron x-rays for high contrast imaging. The Scottish Centre for the Application of Plasma-based Accelerators (SCAPA), based at the University of Strathclyde, primarily focuses on the development and application of laser-driven particle and radiation sources. Additionally, the Terawatt Apparatus for Relativistic And Non-linear Interdisciplinary Science (TARANIS), installed in the Centre for Plasma Physics at the Queen's University Belfast, supports a wide ranging science program, including laser-driven particle acceleration, x-ray lasers and high energy density physics experiments. Among the various facilities present in Europe there is the PHELIX laser system based at the GSI Helmholtz Centre for Heavy Ion Research in Germany, a large-scale accelerator facility for heavy ions, where research activities are developed oriented towards research materials, plasma physics, biophysics and nuclear medicine. In particular, the PHELIX laser was used to carry out the measurements reported in this thesis and will be described in more detail later in this chapter.

3.1.2 Chirped pulse amplification

The fundamental technology behind the generation of the high-power laser pulses used in these facilities is the technique of chirped pulse amplification (CPA) which has revolutionised the field of high-energy laser physics. This technique, developed by Gérard Mourou and Donna Strickland in 1985 [4], who the 2018 Nobel Prize in Physics for their research, enables the creation of ultra-short, high energy laser pulses, thus allowing experimental investigations of high intensity laser plasma interactions in the relativistic regime. Increasing laser power and peak intensity has been one of the most important problems facing laser science and technology since the invention of the laser in the early 1960s [1]. Q-switching and mode-locking techniques [2][83], developed in the 1960s, pushed peak powers into the MW to GW range and thus made the discovery of basic nonlinear optical effects possible. The nonlinear optical response of a material can be described by introducing an intensity dependent refractive index term $\eta_2 I$ in addition to the conventional refractive index at low intensities of η_0 as shown below:

$$\eta = \eta_0 + \eta_2 I \tag{3.1}$$

where η is the total refractive index, while η_2 (cm^{2}W^{-1}) is a material-dependent non-linear index coefficient. As described in the previous chapter, ultrashort pulse lasers typically have a transverse profile whose intensity can be approximately described with a Gaussian function and when they propagate through a medium at sufficiently high intensities, a change in refractive index is obtained, the edges of the beam (with less intensity) move faster than the centre of the pulse (which has greater intensity) causing a focusing effect. Nonlinear optical effects are often quantified using a parameter known as the B-integral, which describes the phase (ϕ) that accumulates after the pulse has propagated a distance L through an optical medium:

$$\phi = \frac{2\pi}{\lambda} \int_0^L \eta \, dz \tag{3.2}$$

$$\phi = \frac{2\pi}{\lambda} \int_0^L \eta_0 \, dz + \frac{2\pi}{\lambda} \int_0^L \eta_2 I(z) \, dz \tag{3.3}$$

where the second term of the phase is known as the B-integral;

$$B = \frac{2\pi}{\lambda} \int_0^L \eta_2 I(z) \, dx \tag{3.4}$$

This may result in filamentation or self-focusing of the beam, considerably increasing the potential for damage to the optics within the system. The CPA technique allows high final laser intensities to be achieved while keeping the intensity of the laser pulse low during the amplification process by temporally stretching the pulse to a much longer duration (for example via a pair of diffraction gratings) in order to reduce the peak power to a level below which non-linear effects and optical damage in the amplifier gain medium occur. This allows the pulse to be safely amplified through the optical amplification chain, frequently through several phases. Finally, the pulse is then re-compressed (again via a grating pair) to a duration similar to the duration of the input pulse. A pulse duration increase of approximately 10^3 to 10^5 times can be attained, stretching a femtosecond or picosecond seed pulse into a duration on the scale of nanoseconds. The stages of this process are shown below in figure 3.2:

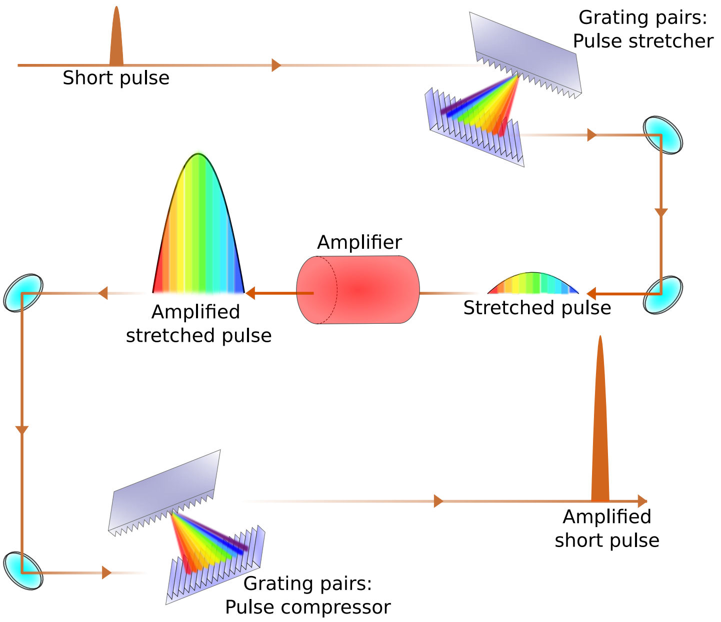

Figure 3.2: Principle of chirped pulse amplification: the initial short pulse from the oscillator is temporally stretched through a grating to reduce its intensity suitable for amplification. The amplified pulse, with higher energy, is then temporally compressed back to near its original duration.

3.2 Laser pulse amplification

In this section we will explore the main amplification schemes used within the CPA technique, namely regenerative and multi-pass amplification, where both involve propagation of the seed pulse through an optically pumped gain medium. In the process of regenerative amplification [84], the laser pulse is injected into an optical cavity containing the gain medium, where it crosses multiple times until the energy stored in the amplifying medium is extracted. Figure 3.3 shows the optical configuration scheme of a regenerative amplifier.

The scheme is based initially on having the stretched laser pulse injected through a polariser, followed by a half waveplate, the latter is set at an angle of

45° with respect to the input polarisation, thus rotating polarisation angle by 90°. Next, a Faraday rotator will again rotate the polarisation by an amount depending on the length of the rotator, the strength of the applied external magnetic field, and the Verdet's constant of the material. After the Faraday rotator, the pulse passes through a second polariser set to reflect or transmit light based on the polarisation state. On reflection, the input pulse propagates through a Pockels cell where by applying a specific voltage, the cell will behave like a quarter waveplate. The pulse will leave the Pockels cell with circular polarisation, where the direction of rotation will be reversed by reflection from the cavity mirror. Subsequently, when the pulse makes its second pass through the Pockels cell, it will have a polarisation state of 90°, and will be transmitted through the polariser. This will enable the pulse to propagate through to the gain medium. To allow the pulse to exit the cavity, the voltage across the Pockels cell is reduced to zero, so there is no polarisation rotation and the laser pulse can be reflected back via the input optics.

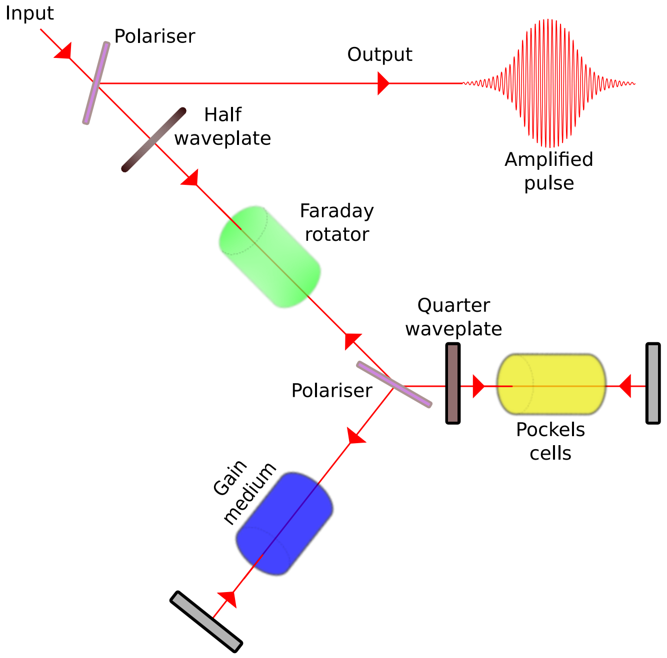

Figure 3.3: Simple schematic showing the main components and arrangement of a basic regenerative amplifier.

The multi-pass amplification technique is one of the most widely used CPA-based technologies, the basic concept is that the incoming laser pulse is propagated through a series of mirrors which enable the pulse to make many geometrically separated passes through an optically pumped gain medium. These amplifiers contain a number of mirrors which direct the signal beam path such that they make multiple passes, through the gain crystal, with slightly different angular directions in order to keep the beams corresponding to the different passes spatially separated, see figure 3.4. The alignment of this system can become quite complex because in order to have a large number of passages one is often forced to use beam directions which do not always lie on the same plane. Multi-pass amplifiers are typically set up to be the final amplification stage in the CPA laser chain, as the single pass gain can be set relatively high compared to a regenerative amplifier as the beam passes through a minimal number of optics where B-integral could be a problem. The substantial difference from a regenerative amplifier is that the latter can be considered as a special type of multipass amplifier, where the multiple passes are not arranged via the geometric optical path, but with an optical switch.

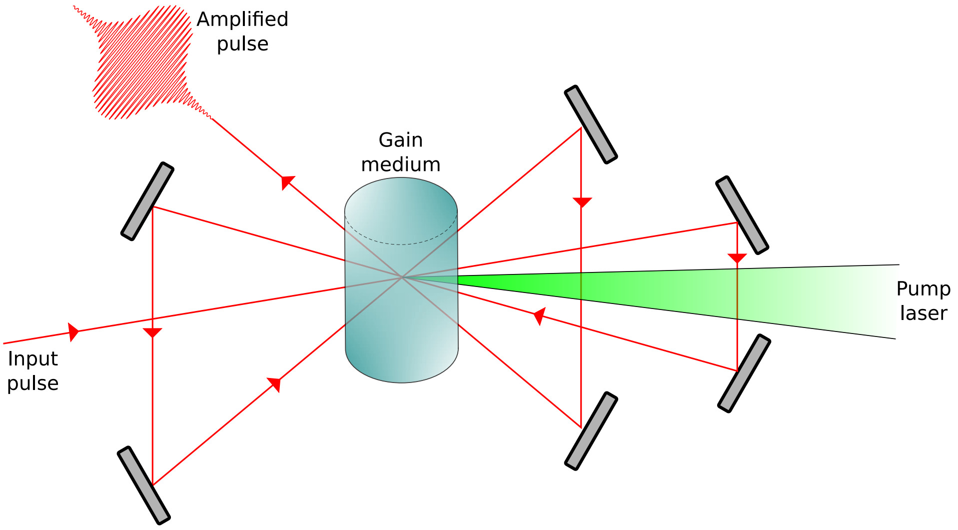

Figure 3.4: Schematic of typical multi-pass amplifier arrangement employed in a CPA scheme.

3.2.1 Laser pulse temporal intensity contrast

An inherent challenge when using the amplification techniques described in the previous section, results from the amplification of all light produced by the laser gain medium, which results in a non-ideal temporal intensity profile. In addition to the main pulse, there is a degree of lower intensity light which exists preceding, and following, the main pulse. This typically comprises of a pedestal formed by amplified spontaneous emission (ASE), which can be up to several nanoseconds in duration. Also, light immediately before the main pulse can be produced by phase errors in the stretcher, resulting from imperfections in the optical elements and alignment issues. These errors introduce phase shifts and scattering, leading to the temporal broadening at the base of the pulse. Figure 3.5 illustrates a schematic representation of a pulse, with each of these issues. Inside the resonant cavity, the pump energy supplied by an external source excites the electrons within the medium's atoms from a low energy level to a higher one, invoking a process termed a population inversion. Here the electrons, after a characteristic time, will spontaneously decay emitting radiation in all directions, with a spectrum related to the width of the line of the decay transition. In most laser amplifiers, the ASE level and is determined by the output control systems employed in the amplifier stages (such as Pockel's cells), typically preceding the arrival of the main pulse by a few nanoseconds.

Although the level of ASE tends to be many orders of magnitude lower than the peak intensity, for high intensity laser pulses where peak intensities reach values greater than 10^{18} Wcm^{-2}, the ASE would be able to act on a target for a relatively long duration and with sufficient intensity to cause significant ionisation and expansion of the plasma prior to the arrival of the main pulse. The relationship between the main pulse intensity and the ASE intensity is termed "laser temporal-intensity contrast" and plays a significant role in influencing plasma conditions / expansion prior to the arrival of the main laser pulse [85][86]. Figure 3.5 illustrates an example laser temporal intensity pulse profile compared with the idealised case.

Furthermore, when a laser pulse travels through a medium, reflections can produce post-pulses. If a post-pulse is generated within the duration of the stretched main pulse ($\sim$ ns), it can interfer with the main pulse and modulate its spectral intensity. This modulated spectrum, in turn, modulates the refractive index of the medium, which affects the phase of the main pulse. Consequently, a pre-pulse can be generated after pulse recompression. The intensity of this pre-pulse increases with the square of the B-integral, as the phase modulation from non-linear effects becomes more pronounced. An example of this is also shown on the schematic in figure 3.5. These pre-pulses may occur tens to hundreds of picoseconds before the main pulse with peaks extending above the level of the ASE pedestal. These can be remedied by utilising wedged optics into the laser system, preventing back-surface reflections from propagating throughout the entire laser chain. In addition, it is important to consider that a laser pulse can exhibit significant uncompensated dispersion, occurring temporally close to the main pulse (typically within tens of picoseconds), resulting in a temporal broadening of the main pulse.

High power laser facilities frequently implement various strategies to enhance the temporal intensity contrast. Optical parametric amplification (OPA) can be utilised to enhance the intensity of the stretched pulse while minimising the spontaneous emission generated. This procedure functions by simultaneously transmitting a laser pulse through a crystal material along with a pump pulse of higher frequency. When phase matching conditions are appropriately met, typically through the crystal's birefringence, the photons of the pump pulse are converted to the photons of the main pulse undergoing amplification, and this process also generates a third component of photons, a so-called idler wave, which frequency is determined by the energy gap between the photons of the pump and the main pulse.

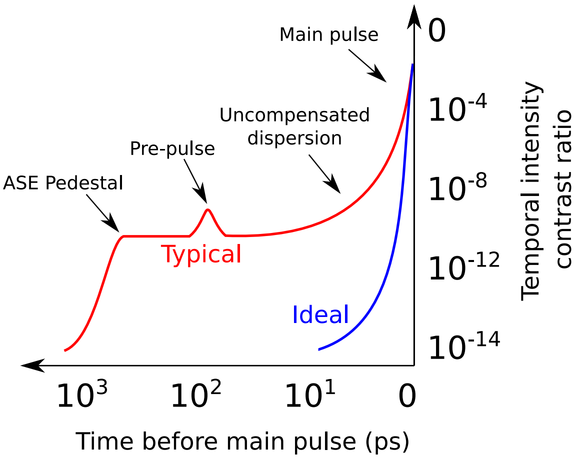

Figure 3.5: Illustration of realistic laser temporal profile (moving from right to left) with laser pedestal (ASE), and the prepulse before the main pulse compared with the idealised case

Typically this method operates with the CPA technique and is known as optical parametric chirped pulse amplification (OPCPA) [87]. As previously mentioned, the primary benefit of this approach for high-power laser systems in laser-plasma experiments lies in its enhancement of temporal intensity contrast. Parametric amplification takes place only when both the pump and main beam are present, and when they are temporally synchronised, the amplification of the laser pedestal is diminished compared to the main pulse profile. In addition, the level of heating in a parametric amplifier is decreased in comparison to a laser amplifier because of the limited coupling of laser photons to the crystal structure. Consequently, these systems can be operated at higher repetition rates.

Another frequently used method to improve laser contrast, is the use of plasma mirrors [88]. Usually, a plasma mirror (PM) is a flat glass slab with an anti-reflective coating to minimise the reflection of the low intensity section of the incoming focusing pulse. With the increasing intensity profile of the pulse, the front surface of the glass will start to undergo ionisation, which will lead to the formation of an overdense plasma region acting to reflect the remainder of the pulse. As a consequence, only the reflected portion, isolated from the preceding lower-intensity light, will interact with the target.

3.2.2 Focal spot size and and encircled energy

There are several methods to maximise the peak intensity of a laser pulse, namely compressing the pulse to a shorter pulse duration, increasing the pulse energy or by focusing the pulse to a smaller focal spot size. The focal spot size is an important parameter that plays a key role not only in influencing the laser intensity but can also profoundly affect the physics of laser-plasma interaction. Therefore, understanding the focal spot size and quality is essential for calculating the peak intensity achieved in the interaction and comprehending the fundamental physics involved. The focal spot size is typically optimised during the target alignment process before every target shot through the use of an off-axis parabolic (OAP) mirror. A focusing mirror is required instead of a lens due to the high intensity of the incident pulse, which would cause damage to the lens due to non-linear optical effects, and a resultant decrease in the quality of the wavefront.

To characterise the focal spot, two essential parameters are employed, the spot size (ϕ_L) and the encircled energy (EE) within an area of diameter ϕ_L. The size is defined by the spot waist parameter which represents the radius where the intensity drops to $1/e^2$ of its peak value. A focal spot of this size is referred to as diffraction limited, with a diameter $2\omega_0$ defined as:

$$2\omega_0 = 1.22\frac{\lambda_L f}{D} \tag{3.5}$$

where λ_L is the laser wavelength, f is the focal length of the optic and D is the diameter of the collimated beam prior to the focusing element. For a given focusing optic and laser wavelength, a dimensionless quantity called the F-number is usually used to describe the focusing properties of the beam, it represents the ratio between the focal length and the diameter of the beam, denoted as $F/\# = f/D$.

Another important parameter to the focal spot characterisation is the encircled energy. This is a measure of energy contained within the central region of the focal spot, i.e. the area used to defined the spot size, where a higher quality focal spot results in a higher encircled energy, typically the values of this energy fall in the range of 20-40%.

Another key parameter used to characterise the pulse focal spot spatial evolution is the Rayleigh range, defined mathematically as follows:

$$z_R = \frac{\pi {\omega_0}^2}{\lambda_L} \tag{3.6}$$

This represents the distance from the beam waist (i.e. smallest radius) to where the beam radius is increased by a factor of $\sqrt{2}$. The target must be placed within the Rayleigh range in order to achieve the maximum on-target intensity. The figure 3.6 shows a schematic of idealised Gaussian beam.

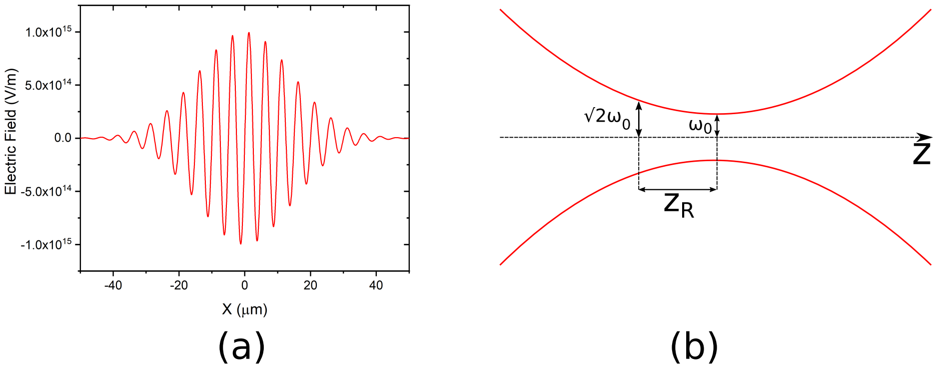

(a) (b)

Figure 3.6: (a) Idealised Gaussian beam of the type used in laser plasma interactions. (b) Schematic of focusing Gaussian beam.

3.3 GSI PHELIX laser

As mentioned, the laser system employed for the work presented in this thesis was the Petawatt High-Energy Laser for Heavy Ion Experiments (PHELIX), located at the GSI facility near Darmstadt in Germany [89]. A schematic of the PHELIX laser structure is depicted in figure 3.7. PHELIX is a versatile laser system based on an Nd:Glass structure, operating at a central wavelength of 1053 nm, which uses two frontends (in the nano and femtosecond order), a preamplifier and a main amplifier. The femtosecond frontend generates, through a laser oscillator, short pulses at a frequency of 76 MHz with a duration of 100 fs and energies around 4 nJ. The pulse is either pre-amplified by an ultra-fast optical parametric amplifier (uOPA) or it simply passes through the uOPA without any amplification where the total gain is provided by the subsequent amplifiers.

Subsequently, an adjustable pulse stretcher is used in the amplification scheme based on the CPA technique, where the pulse is stretched, amplified and re-compressed again. The pulse is then gradually enlarged to a maximum exit beam diameter of 70 mm to keep the fluence within safe limits. After this, the stretched pulse is amplified by two titanium-doped sapphire regenerative amplifiers, producing pulses with typical output energies of 30 mJ. The beam then enters the main amplification stage, passing twice through a series of five flash-lamp pumped Nd:glass amplifier heads, which can produce a maximum pulse energy of up to 250 J. After the pulse compressor, the beam is guided towards the target chamber under vacuum. Subsequently, an f/1.5 off-axis parabola (OAP) is used to focus the laser pulse to a minimum ideal spot size of 1.2 μm. However, due to beam aberrations affecting the focal spot quality, the actual Gaussian intensity distribution achieved was approximately $\phi_L = 5$ μm (FWHM).

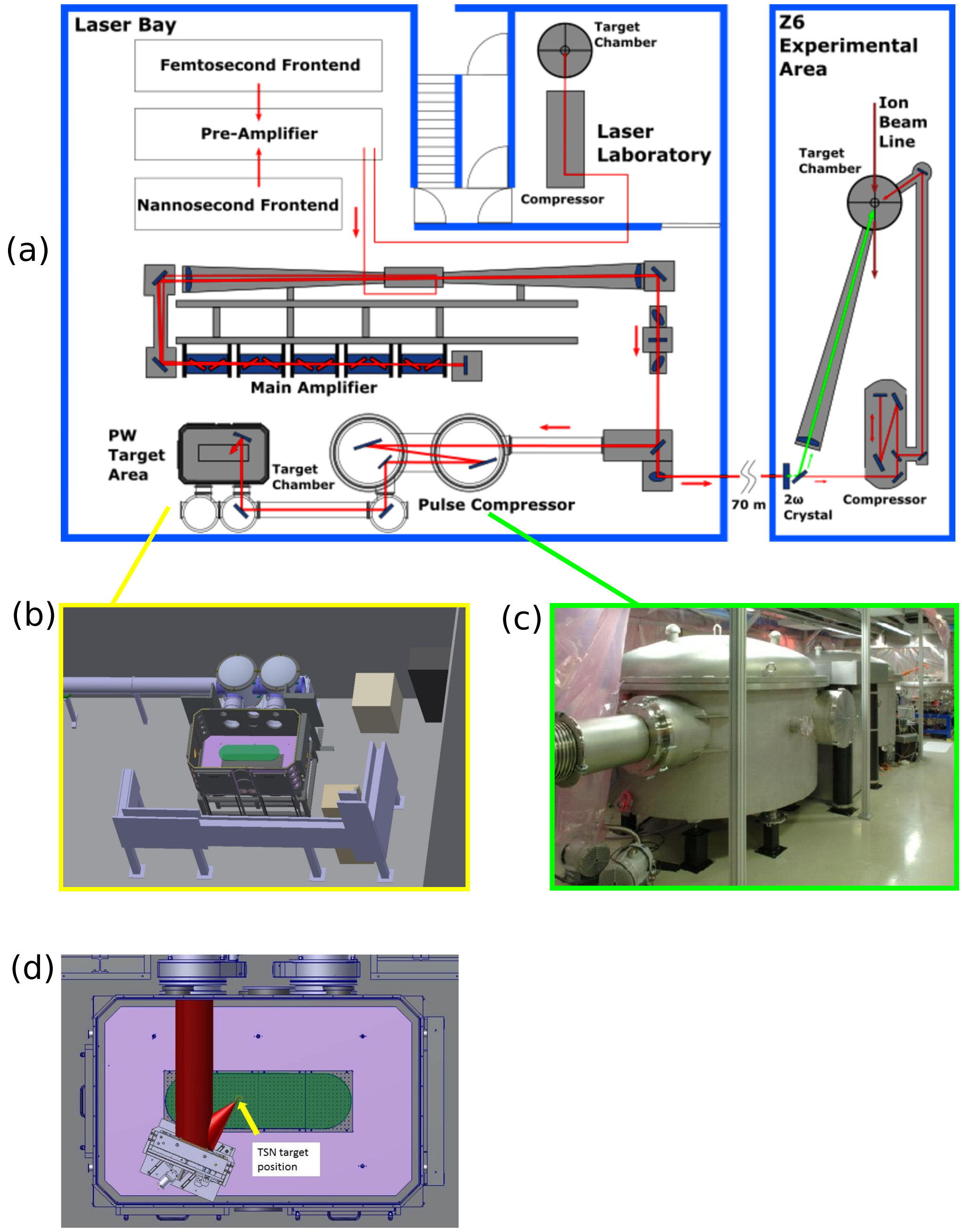

Figure 3.7: Overview of the PHELIX laser system and interaction area [90], with (a) a schematic diagram of the laser system and the target area, (b) the layout of the interaction chamber, (c) an image of the pulse compressor, (d) example of a target position.

3.4 Optical diagnostic techniques

In the previous chapter, the fundamental physics underlying the interaction of intense laser pulses with plasma was discussed. Since this thesis reports experimental investigations involving these interactions, a detailed description of the diagnostic techniques used in the experimental campaign conducted is necessary. In this section the main diagnostic techniques used to obtain the results presented in the following chapters will be discussed.

3.4.1 Integrating Sphere

Quantification of laser energy absorption during a laser-solid interaction may be achieved through a variety of techniques designed to characterise laser light that is not absorbed, i.e. light that is reflected, scattered, and transmitted by the target. One of the main devices used for the investigation reported in this thesis is an integrating sphere, a diagnostic tool used to quantify the components of scattered light. This technique has been employed since the early 1900s [91] for various experiments, the oldest application concerning the measurement of the total geometric luminous flux of electric lamps [92] where the light emission of different types of lamps was compared. This technique was also used to measure the total reflectivity or transmittance from diffuse or scattering materials [93], and more recently to investigate the absorption of laser energy in plasma [94].

The device itself is a hollow sphere, with the diameter maximised for a given flux of scattered light, as too small of a diameter would cause optical damage to the surface of the sphere. The surface of the inner cavity is coated in a highly reflective, diffusely scattering material, so as to uniformly distribute the light signal around the sphere and to ensure that the radiation exchange between two points is independent of the viewing angle and the distance between the points. This device is shown in figure 3.8

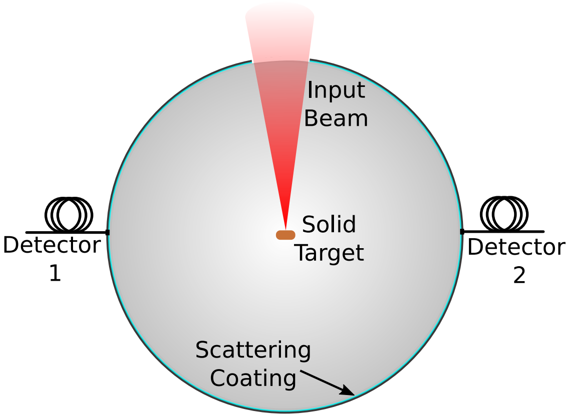

Figure 3.8: Schematic of the basic principle of an integrating sphere operating on a laser-solid interaction investigation with laser light entering and irradiating the solid target placed inside.

Laser light enters the sphere via an aperture and is incident on the target. It is then scattered in all directions. The brightness of the light emitted from / scattered by the target is described by its radiance L, which is represented by the flux density per unit solid angle:

$$L = \frac{\Phi}{\pi A_S} \frac{p}{1 - p(1 - f)} \tag{3.7}$$

where Φ is the amplitude of the light introduced to the sphere, A_S is the surface area of the inner cavity, p is the reflectivity coefficient of the wall coating, and f the port fractional area with respect to A_S. The distribution of radiance within an actual integrating sphere will depend on the distribution of the incident flux, the geometry of the sphere including the location of the apertures present which lead to light loss, and the reflectivity distribution function for the sphere coating. The selection of the sphere's coating material can make a significant difference in the brightness produced for a given sphere design, even a small change in reflectivity could significantly alter the sphere's radiance. The coatings used in a laser-plasma context are typically highly reflective at over 95% for wavelengths ranging from 350 nm to 1350 nm and are typically made of magnesium oxide and barium sulphate [95]. Finally, to reduce the absorption and dispersion of light, the objects used inside the sphere are manufactured using plastic materials as the Polytetrafluoroethylene (PTFE), commonly known as Teflon. In this way the spatial uniformity of the sphere itself is optimised. Another aspect of this device that should not be overlooked is the effect of target debris produced during the interaction, which can alter the sphere's ability to act in an integrating manner i.e. the debris could cause light to be preferentially reflected in a particular direction, resulting in unequal spectrometer responses. The overall reflectivity will be altered and the durability degraded when used repeatedly, therefore it becomes very important to monitor the build-up of debris over the course of an experiment, and take measures to minimise the effect of debris on the sphere.

Coupled to the sphere, optical spectrometers were used to detect the scattered light. They are widely employed in scientific research, industry, and various applications and generally consist of an entrance slit, a diffraction grating or prism, focusing optics, and a detector. The slit regulates the amount of light entering the spectrometer in order to control the spectral resolution. Subsequently, there is a system of mirrors which direct light onto a diffraction grating, which splits the light into its constituent wavelength components. These are directed onto a detector which measures the spatial distribution of the light from the grating. A schematic of a spectrometer is shown in the figure 3.9.

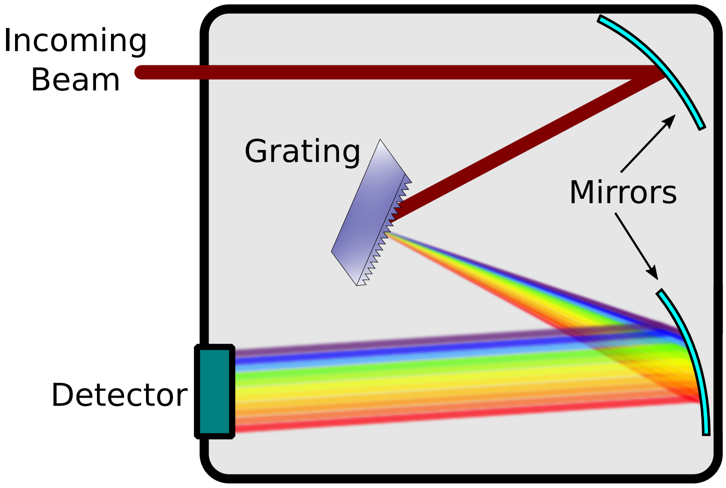

Figure 3.9: Schematic of a spectrometer with the three main components: the entrance slit which allows the incoming beam to enter, the grating acting as a dispersive element to split the light into its constituent wavelengths and finally the detector that captures the light and measures the intensity as a function of wavelength.

3.4.2 Backscattered and transmitted light quantification

Another primary diagnostic used for the work presented in this thesis were scatter screens. A scatter screen is an instrument whose surface is made of specular reflecting paint, such as Spectralon, so that the incident light is dispersed equally in all directions. In this way, the apparent brightness is independent of the observer's viewing angle. Figure 3.10 shows a scatter screen setup used during the experimental campaign.

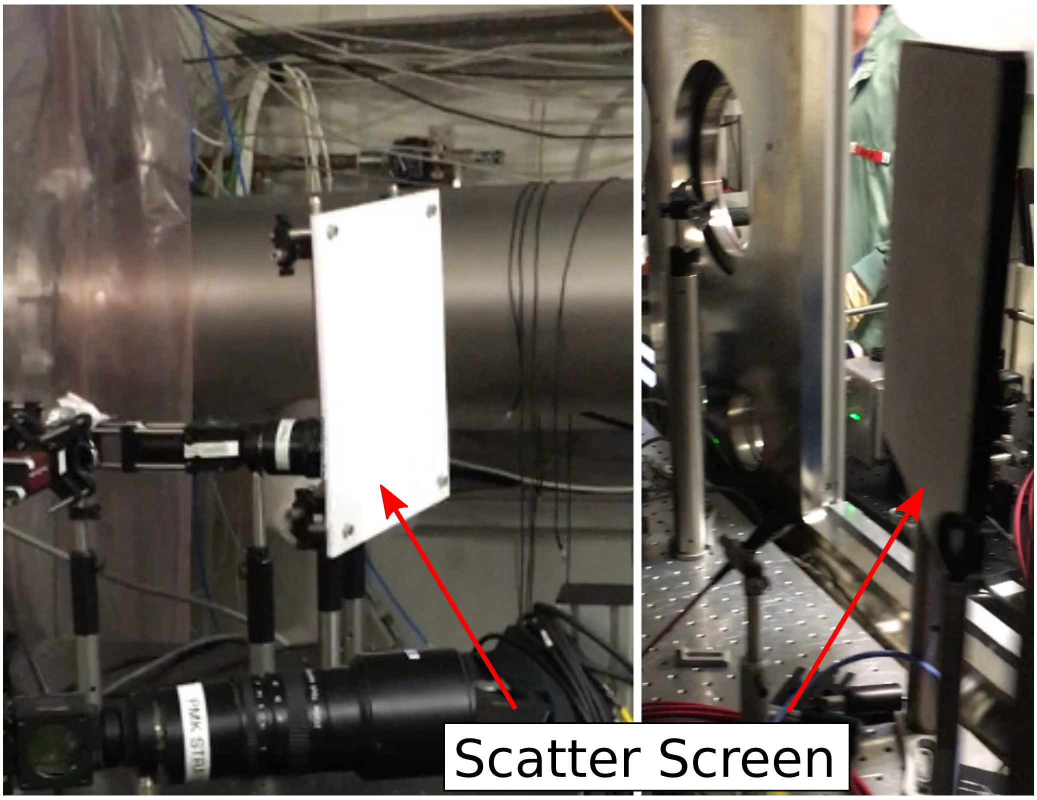

Figure 3.10: Photographs of the scatter screens used to quantify the energy content of backreflected and transmitted laser light.

From the PTFE screen, the scattered light is measured by a detection system consisting of a CCD (Charge-Coupled Device) camera, which transforms a light signal into a digital electronic signal. In this thesis, two scatter screens were used, a transmission screen placed behind the target rear surface to quantify the transmitted target light through the target and a backscatter screen placed behind the final dielectric turning mirror before the focusing off-axis parabolic mirror, to measure the un-absorbed laser light reflected back up the beamline from the target front surface.

3.4.3 Neutral density filters

Neutral density (ND) filters, have been used for some optical components in order to avoid both damage to the components and to avoid saturation of the detected signal. ND filters are a type of optically dark filter which consist of a thin film optical coating, applied to a plastic or glass substrate. The coating can be optimised for specific wavelength ranges allowing reduction in the intensity of the wavelengths that propagate through them where the optical density power, *OD*, transmitted through the filter can be calculated as:

$$OD = \log_{10}\left(\frac{T}{100}\right) \tag{3.8}$$

where T is the transmission of the filter. The OD value is characterised for a specific wavelength to be attenuated which is typically characterised for 555 nm (the value quoted by the manufacturer). As our experiment employs a 1054 nm wavelength laser, it becomes important to characterise the response of the filter at this wavelength. In figure 3.11, the transmission percentage as a function of wavelength for different ND filters is shown.

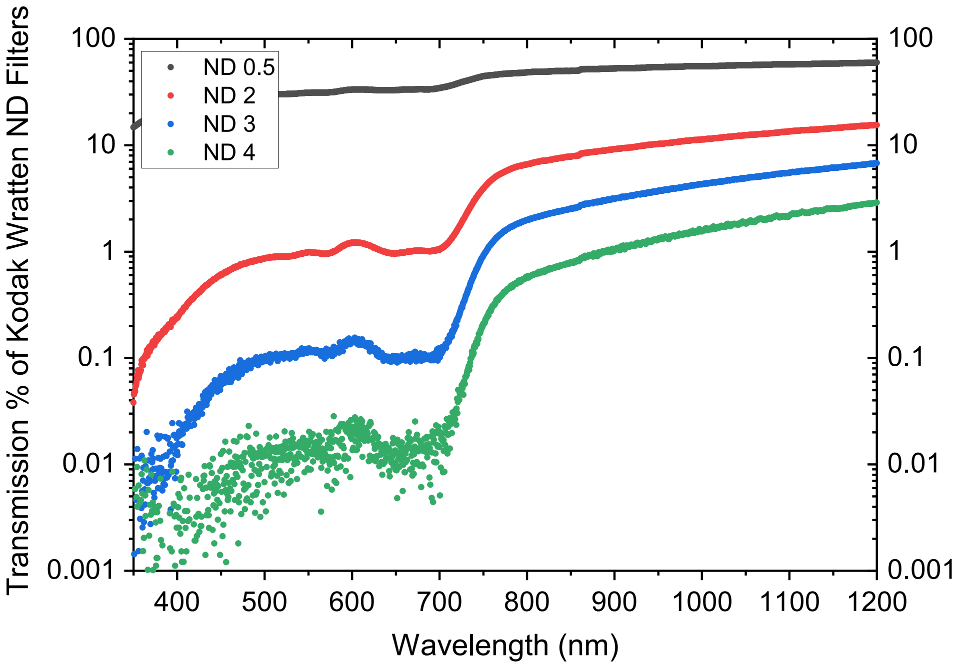

Figure 3.11: Transmission % of Kodak Wratten ND filters as a function of the wavelength of the transmitted light.

3.5 Numerical Methods

The large number of parameters influencing intense laser-solid interactions, and the highly non-linear nature of these interactions, makes analytical solutions to many laser-plasma scenarios impossible.

High performance computing techniques can help solve this problem through the use of numerical simulations. These tools, based on the design of models of real systems, implement simulation algorithms that allow the motion of the particles involved and their collective behaviour resulting from the electromagnetic fields generated by the particles themselves in motion, to be modelled in an accurate way.

A particular simulation method employed to aid in the understanding of the experimental results presented in chapter 5 is the particle-in-the-cell (PIC) approach, the principle of which will be discussed in the next section.

3.5.1 Particle-in-cell simulations: EPOCH

PIC simulations can be applied to different branches of physics, but are usually associated with the study of plasma. The idea behind PIC simulations is relatively simple: simulate the motion of the plasma and calculate all the macroscopic quantities (such as charge density, temperature, etc.), starting from the position and speed of the particles.

A comprehensive description of a plasma is achieved through kinetic theory, which seeks to explain the macroscopic properties of a plasma by considering the motion of each individual particle [96][97]. This description begins with a density functional, $N = N(\mathbf{x},\ \mathbf{v},\ t)$, which represents the collection of all positions of a single particle in 6D phase space, and is given by;

$$N(\mathbf{x}, \mathbf{v}, t) = \sum_{k=1}^{N} \delta(\mathbf{x} - \mathbf{X}_k)\delta(\mathbf{v} - \mathbf{V}_k) \tag{3.9}$$

where $\mathbf{X}_k$ and $\mathbf{V}_k$ are the position and velocity coordinates of particle k, and δ is the Dirac delta function, which is non-zero only when $\mathbf{x} = \mathbf{X}_k$ and $\mathbf{v} = \mathbf{V}_k$. The evolution of the density function is described by a continuity equation called the Klimontovich equation [98]. This equation presumes the conservation of the number of particles (i.e. no collisions that serve as sources or sinks), and is expressed as follows;

$$\frac{\partial N_s}{\partial t} + \mathbf{v} \cdot \nabla N_s + \frac{q_s}{m}(\mathbf{E}^m + \mathbf{v} \times \mathbf{B}^m) \cdot \nabla_v N_s = 0 \tag{3.10}$$

where q_s represents the charge of the species and ∇_v denotes the gradient with respect to the velocity vector. The Klimontovich equation describes each particle's position and velocity over time, but this level of detail is unnecessary for understanding macroscopic plasma properties and is as difficult to solve as an N-body problem. To simplify, a distribution function $f_s = f_s(\mathbf{x},\ \mathbf{v},\ \mathrm{t})$ is used, representing the number of particles in a phase space volume $\Delta\mathbf{x}\Delta\mathbf{v}$ around $(\mathbf{x},\ \mathbf{v})$ at a given time. The number of particles in this volume can change over time, causing fluctuations in electromagnetic fields. By averaging over all configurations with the same distribution, this results in the kinetic equation;

$$\frac{\partial f_s}{\partial t} + \mathbf{v} \cdot \nabla f_s + \frac{q}{m}(\mathbf{E} + \mathbf{v} \times \mathbf{B}) \cdot \nabla_v f_s = -\frac{q}{m}\langle(\delta\mathbf{E} + \mathbf{v} \times \delta\mathbf{B}) \cdot \nabla_v \delta N\rangle \tag{3.11}$$

where $\langle\rangle$ represents an ensemble average, and this procedure removes the variable components of the fields, $\langle\delta\mathbf{E}\rangle = 0$. The Vlasov equation (Eqn. 3.11) furnishes a kinetic portrayal of plasma through the evolution of the distribution functions describing averaged quantities. Nonetheless, given that the distribution function is a 6D quantity (involving three position and three velocity coordinates), solving the Vlasov equation demands considerable computational resources, and would require prohibitively long simulation times. PIC codes tackle this issue by discretising the distribution function into finite elements known as macro-particles [99]. Each macro-particle represents a group of particles that behave uniformly, whose dynamics are described according to the Lorentz force, and since no collisions are included, they are free to move through each other without changing shape and/or rotating. The system of equations that delineates the movement of the macro-particles and the corresponding fields is formulated as follows;

$$\frac{d\mathbf{x}}{dt} = \mathbf{v} \tag{3.12}$$

$$\frac{d\mathbf{u}}{dt} = \frac{q}{m}(\mathbf{E} + \mathbf{v} \times \mathbf{B}) \tag{3.13}$$

where $\mathbf{u} = \gamma\mathbf{v}$, such that $\gamma = (1 + (\mathrm{u/v})^2)^{1/2}$, and;

$$\frac{\partial\mathbf{B}}{\partial t} = -\nabla \times \mathbf{E} \tag{3.14}$$

$$\frac{\partial\mathbf{E}}{\partial t} = c^2\nabla \times \mathbf{E} - \frac{\mathbf{j}}{\varepsilon_0} \tag{3.15}$$

To compute the current density, $\mathbf{j}$, the particle positions are interpolated onto a grid. The macro-particle's shape (or weight) indicates the influence of the particle distributed across local grid positions. The particle flux across the grid determines the current density, which is then utilised to calculate the electric and magnetic fields. This is accomplished using the Finite Difference Time Domain (FDTD) technique, allowing for simultaneous determination of both fields within the same time step. Commencing at time step n, the fields are defined as:

$$\frac{\mathbf{E}^{n+1/2} - \mathbf{E}^{n}}{\Delta t/2} = c^2 \nabla \times \mathbf{B}^{n} - \frac{\mathbf{j}^{n}}{\varepsilon_0} \tag{3.16}$$

$$\frac{\mathbf{B}^{n+1/2} - \mathbf{B}^{n}}{\Delta t/2} = -\nabla \times \mathbf{E}^{n+1/2} \tag{3.17}$$

where, $\mathbf{E}_{n+1/2}$ and $\mathbf{B}_{n+1/2}$ are the electric and magnetic fields calculated between simulation timesteps, t_n and t_{n+1}, due to the motion, and current density, j_n, associated with particles at t_n. The components of the electric and magnetic fields are stored on the vertices and edges of a Yee grid [100] and are reinserted into the Lorentz force equation to move the macro-particles to new positions at the next simulation time step, t_{n+1}. The macro-particle velocity in each cell is centred using a Boris algorithm [101], and the particle flux generates a current density at this time step, creating electromagnetic fields that are calculated at the next half time step, $t_{n+3/2}$. These fields then move the macro-particles to new positions at the subsequent time step, t_{n+2}, resulting in a repetitive cycle for each simulation time step. Figure 3.12 shows a flowchart representing the PIC algorithm.

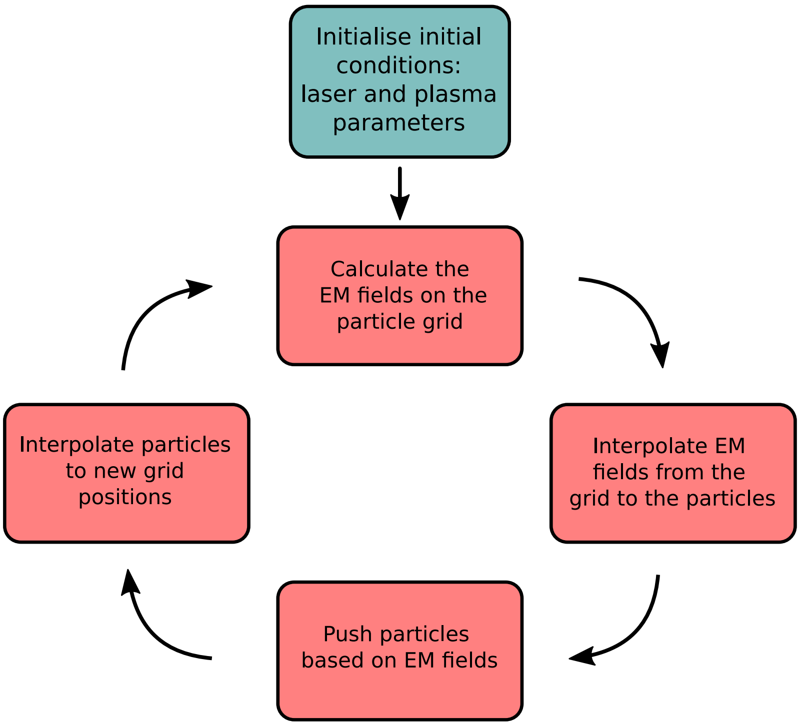

Figure 3.12: Flowchart of the steps of the particle-in-cell coding process (PIC) algorithm involved in simulating a plasma system.

Chapter 4

Investigating the effect of the RSIT on laser absorption in ultra-intense laser-solid interactions

In this chapter an investigation of total energy absorption in ultra-thin foils undergoing relativistic self induced transparency (RSIT) is presented. We report the results of experimental and numerical investigations, exploring the use of diagnostics such as integrating spheres and scattering screens, to diagnose the underpinning physics of RSIT. Furthermore, the limitations of these diagnostics in the case where there is significant transmitted laser light are examined.

4.1 Introduction

The study of laser energy absorption has been a topic of great interest since the early investigations of laser-plasma physics and it continues to be today one of the most difficult areas to understand. Absorption strongly depends on almost all interaction parameters, such as laser intensity [102], angle of incidence [103], laser polarisation [104] and density scale length of the target plasma [105], to name a few. Energy coupling mechanisms such as resonance absorption, vacuum heating and $\mathbf{J} \times \mathbf{B}$ acceleration (as detailed in section 2.7), also depend on these interaction parameters.

Understanding absorption therefore requires knowledge of how these parameters play a part in the complex dynamics behind laser energy coupling in relativistic laser foil interactions. Understanding the laser energy coupling efficiency is fundamental to almost all topics in intense laser-plasma interactions, such as in the acceleration of high-energy charged particles, inertial confinement fusion schemes and laboratory astrophysics. The large number of theoretical studies and experimental investigations in this field contribute to a better understanding of these complex interactions.

To improve our understanding of interactions in the relativistic regime, it is necessary to make experimental measurements of laser absorption using suitable diagnostic techniques. We employed a number of diagnostic tools in our investigation, including an integrating sphere, developed by our group specifically for these measurements. It will be shown that in the target transition from opaque to relativistically-induced transparency to the intense laser light, the properties of the transmitted laser pulse are modified resulting in optical damage to the integrating sphere. This is verified by the results obtained with a transmission screen diagnostic used to measure the unabsorbed energy, and gives us key insight into the underpinning physics, which will be explored in the next chapter. This investigation has important consequences not only for the fundamental understanding of absorption in plasma undergoing RSIT, but also for the development of future experimental diagnostics and methodologies.

4.2 Review of relevant literature

Ultrashort and high intensity laser pulse energy absorption in solid targets has been explored in several works, such as D. F. Price *et al.* [106], which provided an experimental determination of the energy absorption and an indirect measure of dense plasma electrical conductivity for intensities exceeding 10^{13} Wcm^{-2}. Laser absorption studies have also been performed for other types of dense target, such as dense spray ethanol droplets, as reported in E.T.Gumbrell *et al.* [107], using an Ulbricht sphere (an integrating sphere) to quantify the laser energy diffusely scattered from the droplets. The same diagnostic tool was also employed in the work reported by Borghesi *et al.* [95], where they irradiated aluminium targets with pulses of intensity up to 10^{17} Wcm^{-2}, varying laser incidence angle and polarisation.

One of first direct measurements of total absorption in relativistic regime was reported in Ping *et al.* [108]. They present the first direct measurements of total absorption of short laser pulses (150 fs), at 800 nm laser wavelength, with energy up to 20 J, demonstrating an intensity dependent scaling of laser absorption, and an enhanced absorption at I $\geq 1\times10^{20}$ Wcm^{-2}, reaching 60% for near-normal incidence and 80% - 90% for 45° incidence. This study, and others, were also used in Davies [109] to develop an empirical model that describes the absorption energy as a function of laser irradiance:

$$f_{ABS} = \left(\frac{I_L\lambda^2}{3.37\times10^{20}[\mathrm{Wcm^{-2}\mu m^2}]}\right)^P \tag{4.1}$$

where P is a fitting parameter. This is an empirically derived formula, useful for modelling data with irradiance values for $I_L\lambda^2$ from 3×10^{18} to 2.3×10^{20} Wcm$^{-2}\mu$m^2, matching the intensity range used in our experiment. This was subsequently used in Levy *et al.* [110] to develop a theoretical model that establishes upper and lower bounds on laser coupling for relatively thick solid density targets. These bounds constrain nonlinear absorption mechanisms across the petawatt regime, forbidding high absorption values at low laser power and low absorption values at high laser power.

Although these results demonstrate that the absorption depends strongly on the laser intensity from the variation of the pulse energy, further studies have been conducted to understand the complex dynamics underlying the absorption mechanism, as reported in Gray *et al.* [37]. This investigation confirmed the previously published scaling of absorption with intensity by variation of laser pulse energy, but also showed that focal spot size variation to alter the peak intensity results in a slower scaling. This difference occurs because the focal spot size and the pulse duration are sufficiently large and the electron beam divergence is sufficiently small to enable the recirculating population of electrons, within the foil between the sheath fields formed on the target surfaces, to interact multiple times with the laser pulse at the target front surface [69][70].

The previously reported investigations have been expanded to study the absorption in relativistic interactions of intense laser pulses with targets that remain opaque during the interaction [111][112]. Further studies have been carried out in laser-solid interactions during transitions from surface- to volume-dominated relativistic interactions as reported in Williamson *et al.* [113], where the foils undergo relativistic induced transparency. These first measurements report a peak of absorption of 80% at an optimum thickness of 380 nm, just above the threshold for relativistic transparency.

4.3 Experimental method

The investigation presented in this chapter involved an experiment carried out at GSI Helmholtz Centre for Heavy Ion Research in Germany, where the high power PHELIX laser (details of which are given in section 3.4) was used to generate high-intensity linearly polarised (S-polarised) laser pulses, which were incident at 0° along the target normal axis onto aluminium foils with thicknesses ranging from 20 nm to 6 μm. The targets were positioned using a magnifying microscope objective imaging system, with an alignment reference laser of the same central wavelength as the PHELIX main beam.

The peak laser intensity was $(5\pm1)\times10^{19}$ Wcm^{-2} with a (5 ± 1) μm focal spot (FWHM) diameter. Plasma mirrors were not employed and the laser intensity contrast was measured to be 10^{12} at 1 ns and 10^{4} at 10 ps prior to the main pulse. The total laser energy absorption was measured using three diagnostics, which are: (i) an integrating sphere used to quantify the degree of unabsorbed laser light scattered from the target, (ii) a transmission screen placed behind the target rear surface, i.e. behind the sphere, to quantify the transmitted target light and (iii) a back-scatter screen positioned behind the final dielectric turning mirror before the focusing off-axis parabolic mirror, to measure the unabsorbed laser light reflected back up the beamline from the target front surface.

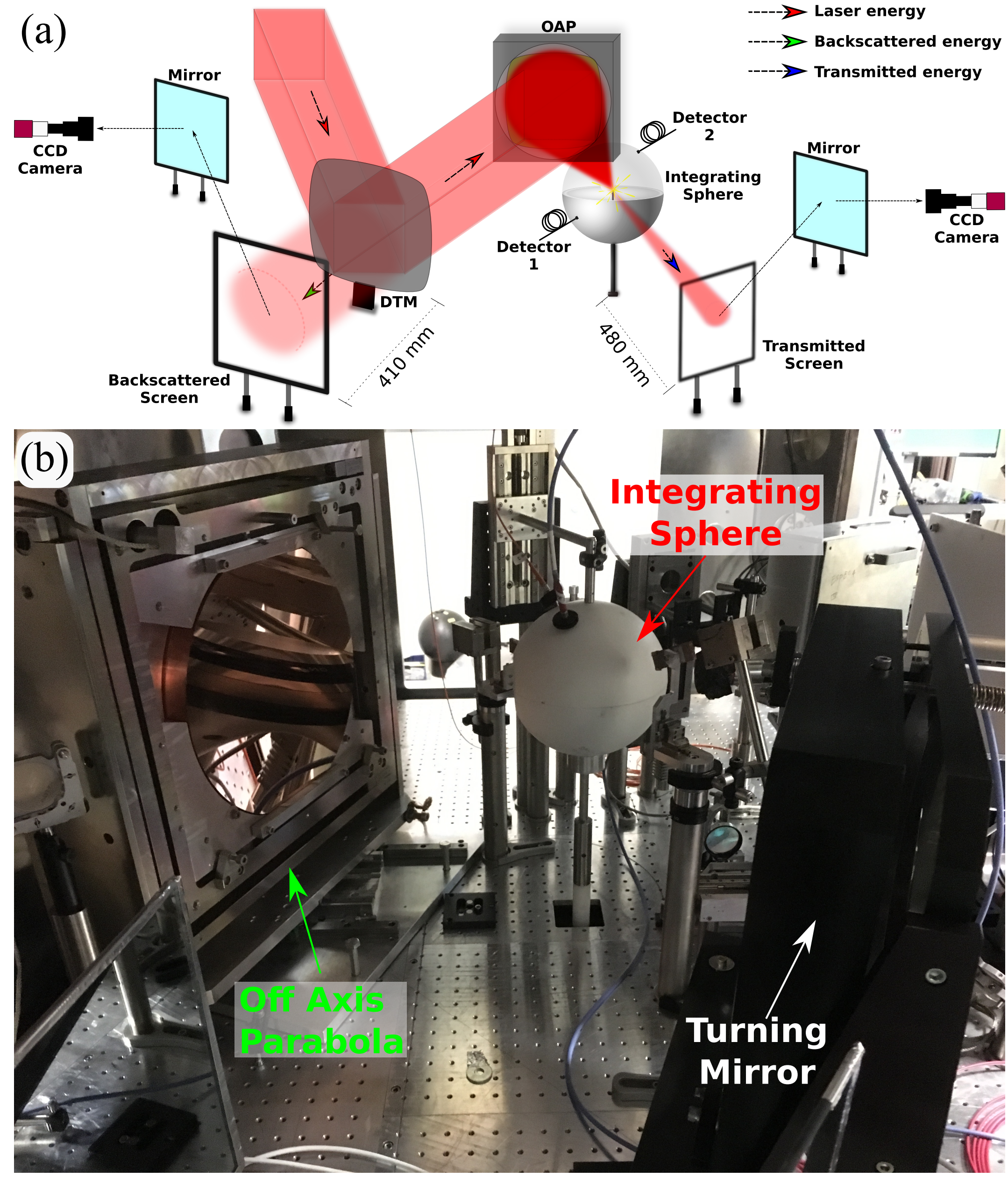

Figure 4.1: (a) Schematic configuration of the experimental setup to quantify the degree of laser energy absorbed during a laser-solid interaction with the main diagnostics used in this investigation, which are an integrating sphere, and screens for back-scattered and transmitted laser light. (b) A photo of the experimental arrangement inside the interaction chamber at GSI, with the integrating sphere in the closed configuration.

A common technique to quantify the laser energy absorbed by the target is to measure all the components of the light that are not absorbed, based on the following energy balance equation:

$$E_{ABS} = E_{IN} - E_{BS} - E_{TR} \tag{4.2}$$

where E_{IN} is the laser energy incident onto the target, E_{BS} is the back-scattered energy, E_{TR} is the transmitted and diffusely scattered light, and finally E_{ABS} is the laser energy absorbed by the target.

The laser energy in the sphere, which includes the transmitted and diffusely laser light, was determined by measuring the spectrum of light in the sphere obtained by means of two optical (Avantes) spectrometers, connected to the sphere via optical fibres. Optical spectrometers are typically used [108] for the purpose of measuring the spectral characteristics of light, such as intensity, wavelength, and energy distribution. Unlike traditional setups constrained by angular acceptance restrictions, the signal is calibrated within the integrating sphere. This setup allows for the accurate calculation of energy even when light enters from various angles, ensuring comprehensive and precise analysis across the spectrum. Using two spectrometers enables cross-verification of signals, ensuring accurate and consistent measurements. Ideally, the signals obtained should be identical or very close. Consistent readings from both instruments confirm the reliability of the data, ensuring it is not compromised by instrument-specific errors. Neutral density filters between fibres and sphere are used to avoid the possibility of optical damage. The energy measured in the sphere was then compared with the transmitted light through the sphere onto a scattering screen placed in the laser propagation direction. The back-scattered light leaves the sphere through the entrance aperture (70 mm in diameter), and is collected by the off-axis parabolic mirror, directing it back along the laser path. A diffuse scatter screen was used to capture the leak through the final turning mirror, which has a small percentage transmission (~0.1% at 1054 nm), and was imaged using a CCD camera filtered for 1054 nm light (1ω). Figure 4.1 displays a schematic of the experimental set-up indicating the position of each diagnostic.

4.4 Calibration of diagnostic tools

Once the set-up was completed, all diagnostics were calibrated to enable a direct measure of the absorbed energy. A schematic of the calibration process for each diagnostic is shown in figure 4.2.

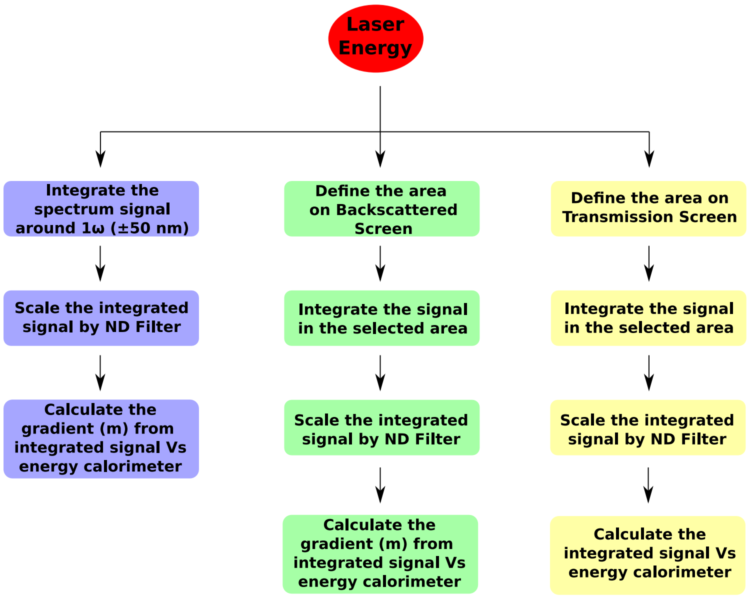

Figure 4.2: Flowchart illustrating the calibration step for each diagnostic tool, sphere calibration in purple while back-scattered and transmitted energy calibration in green and yellow, respectively.

In particular, we measured the throughput of the beamline, i.e. the ratio between the laser energy measured prior to the compressor and the energy on target, obtained using a calorimeter placed in front of the sphere. Consequently, knowing how much energy enters the sphere, we irradiated the walls of the sphere by a known low energy laser pulse (on the order of mJ), and the resultant spectrometer measurements were integrated over ± 50 nm with respect to the central wavelength of the laser light, over which the spectrum drops to the background level. An example of the sphere calibration is shown in the figure 4.3(a).

The calibration of the input energy to the sphere signal, as previously mentioned, was obtained through the use of two optical spectrometers, connected via optical fibres and suitably filtered, via 2 mm apertures at 50° above the equator on the top of the sphere (60° anti-clockwise along the equator from the incoming laser axis) and 45° below the equator, on the bottom of the sphere (120° clockwise with respect to the laser axis). The calibration of input pulse energy to sphere signal for the two spectrometers is shown in figure 4.3(b).

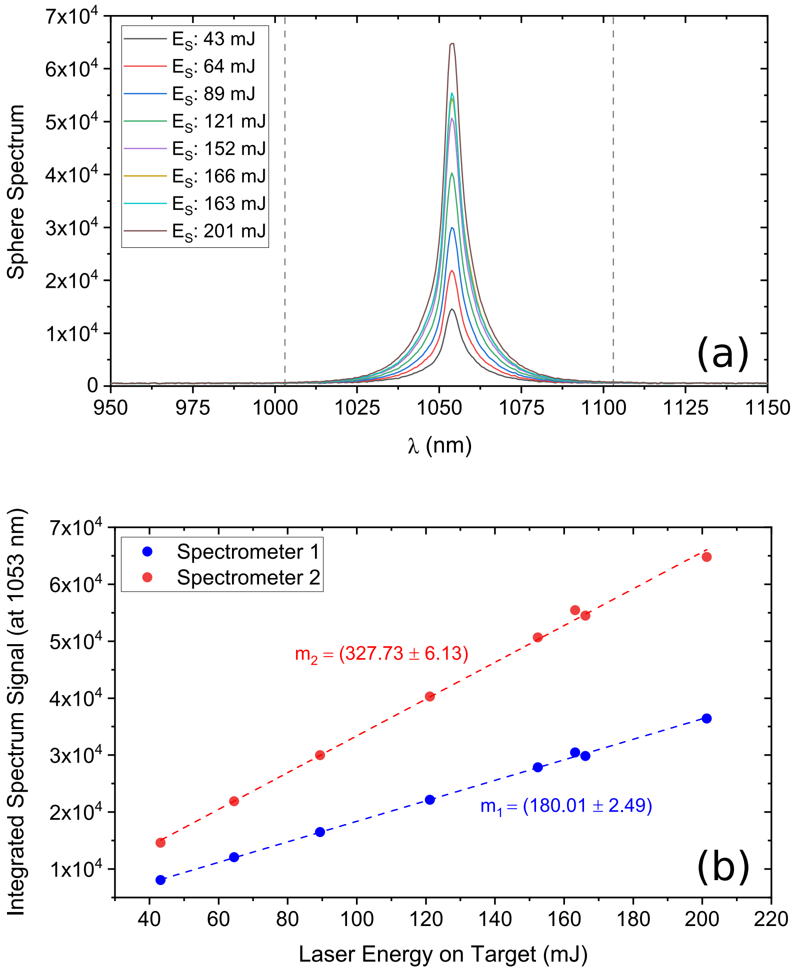

Figure 4.3: (a) Example of sphere spectrum calibration for different shots integrated around central wavelength of the laser ± 50 nm (dashed grey lines). (b) Energy response integrated at 1053 ± 40 nm for the sphere calibration with each optical spectrometer. Spectrometers 1 and 2 are the spectrometers connected from the top and the bottom of the sphere, respectively.

As mentioned, to complete the absorption measurement, we need to calculate the unabsorbed light component that leaves the sphere through the entrance aperture and irradiates the scatter screen. To calibrate this, a 2” sample of the main interaction beam was taken and split to two equal components, one 50% component is directed to an energy calorimeter and the other to the scattering screen. Then, the scatter screen was imaged using a camera filtered for the fundamental laser wavelength (1054 nm), see figure 4.4. Separately calibrating and measuring the back-scattered energy and the energy in the sphere ensures that changes in the fraction of the light which leaves the sphere (due to changes in the fraction of light backscattered from the target) do not impact the measurement of the total absorption. At higher intensities, the divergence of the backscattered light may vary due to critical surface deformation and propagation in the preplasma. However, if the divergence increases, the light will now be collected on the integrating sphere allowing the total backscattered signal to continue to be accounted for in the absorption measurement.

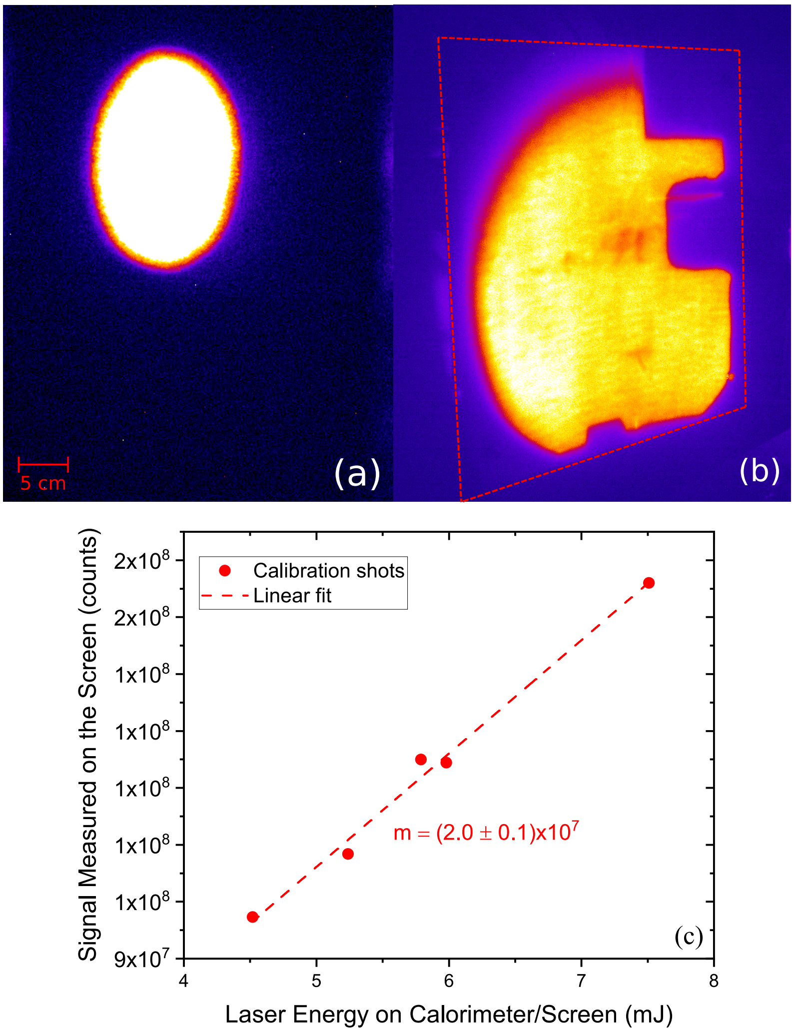

Figure 4.4: Scattering screen calibration: (a) and (b) are respectively the back-scatter and the transmission screens imaged using CCD cameras. The dashed red line (in b) denotes the edge of the transmission screen. (c) Energy response curve from back-scatter calibration shots.

To perform the calibration of the transmission screen a CCD camera was placed on the roof of the chamber to image the transmission screen. In figure 4.5, the imaging system used during the experiment is shown.

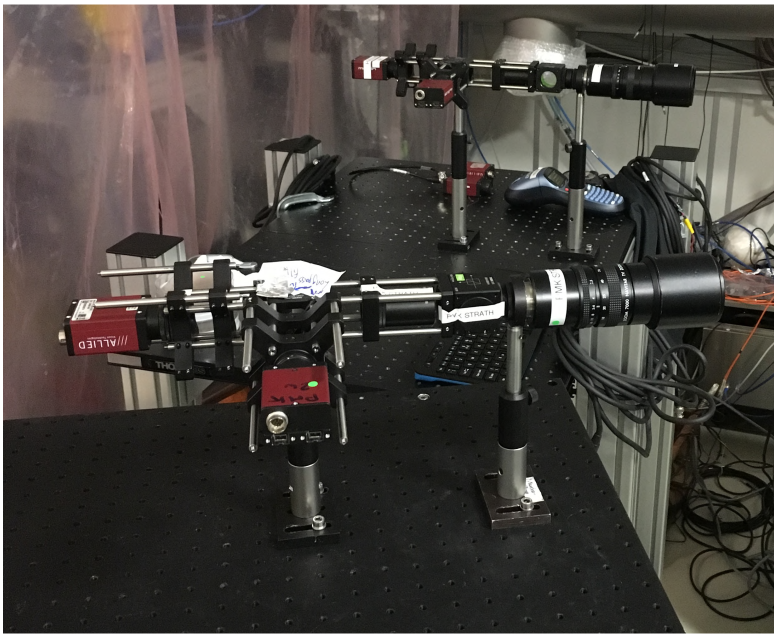

Figure 4.5: Photograph of the dual-wavelength imaging system employed to measure the light signal incident on the scatter screens.

The laser energy absorption during the laser-solid interaction was determined via the process illustrated in figure 4.6.

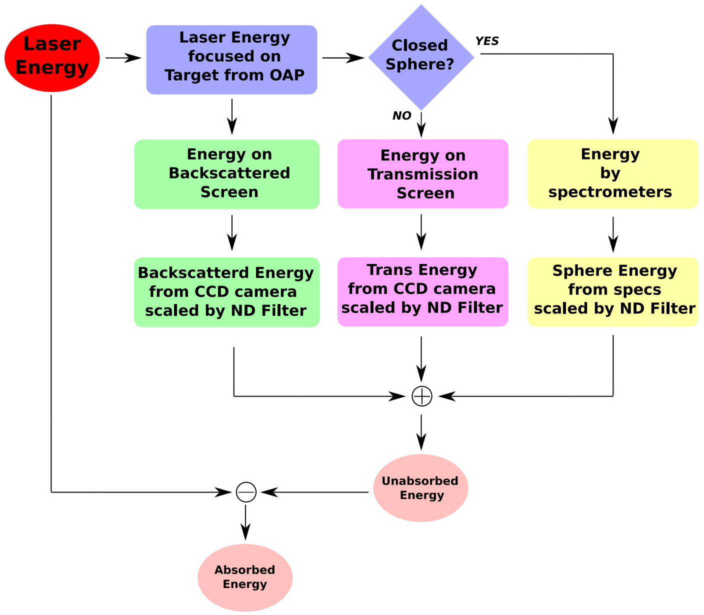

Figure 4.6: Flowchart illustrating the steps of the diagnostic tools to measure the energy absorbed.

4.5 Absorption measurements in the overdense regime

In this section, results from the experimental investigation of the total absorbed energy are presented initially for relatively thick (micron-scale) targets that remain overdense throughout the interaction and subsequently for thinner (nanometre-scale) targets that undergo RSIT during the interaction.

The study starts with investigating the scaling of absorption for a similar target thickness (6 μm) to the investigations reported in Ping *et al.* [108], Gray *et al.* [37] and Williamson *et al.* [113] in order to compare and test our methodology. The laser pulse was focused using an off-axis parabolic mirror, and the pulse energy was varied from 30 to 110 J. Aluminium targets, 6 μm thick, were placed within the integrating sphere at the focus of the laser pulse. Targets of such thickness do not exhibit RSIT and remain opaque throughout the laser interaction.

In this first analysis related to the scaling of the absorption with intensity (by varying the input laser energy), the sphere response is characterised by measuring the signal scaled by the attenuation factor of the neutral density filters used, and converting into energy using the calibrations discussed previously. Several neutral density filters were stacked to obtain a customised optical density, thus avoiding the saturation of the optical sensors by attenuating large amounts of energy. As shown in figure 4.7, the signal of diffusely scattered laser light is quantified by summing the internal counts from both spectrometers.

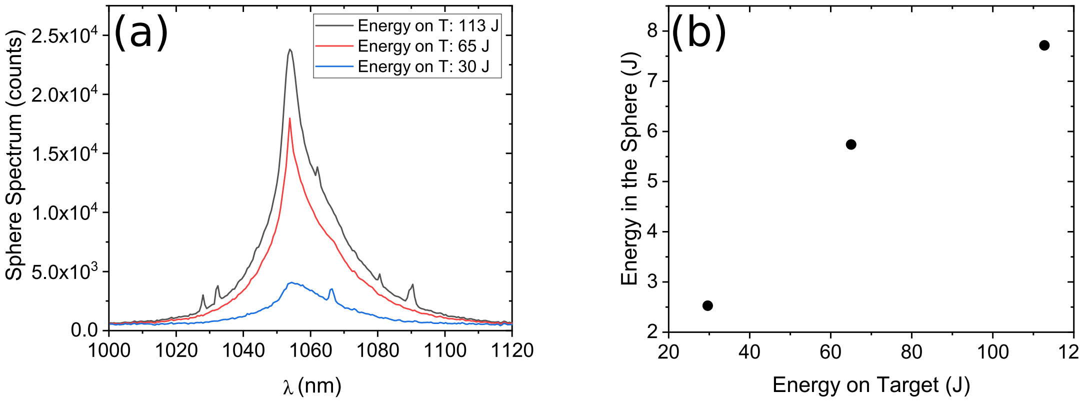

Figure 4.7: (a) Spectrum measured from the optical spectrometers connected to the top and the bottom of the sphere for a range of different energy on targets. (b) Energy response from the sphere for different energy on targets.

In addition, the unabsorbed laser light back-reflected from the target onto the back-scatter screen was measured, as shown in figure 4.8.

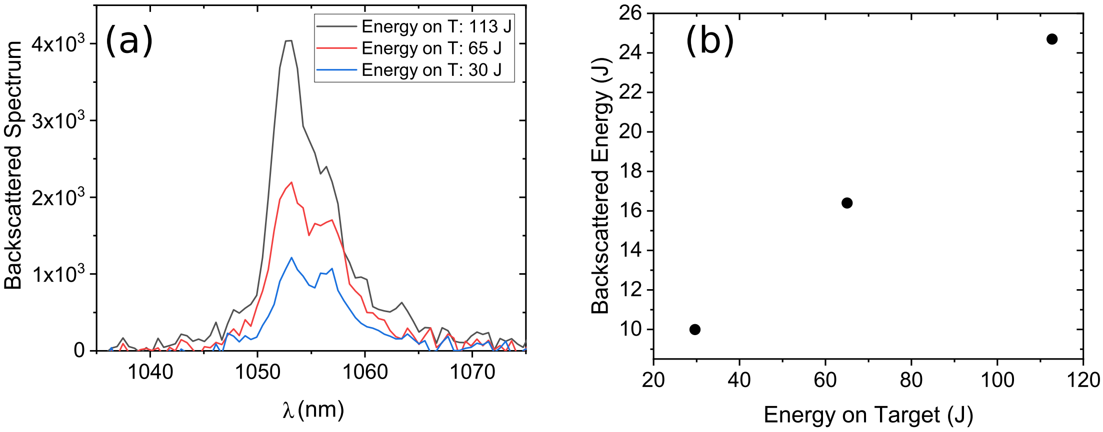

Figure 4.8: (a) Back-reflection spectrum measured for a range of different energy on target. (b) Back-reflected energy as a function of energy on target.

Finally, through the combination of measurements of the energy in the sphere and the light -back-reflected from the target, the total laser energy absorption is determined. Due to the coating of the turning mirror, only a small fraction of the back-reflected light is transmitted onto the screen. As a result, the calculated laser energy absorption value is strongly dependent on the precision and accuracy of the instrument used to quantify the energy and therefore a range of values close to the high reflectivity of the mirror was defined. For the absorption measurement for targets that do not undergo RSIT, the same reflectivity value reported in Gray *et al.* was used for this experiment, which produced absorption results that were in the same range as reported in Gray *et al.*.

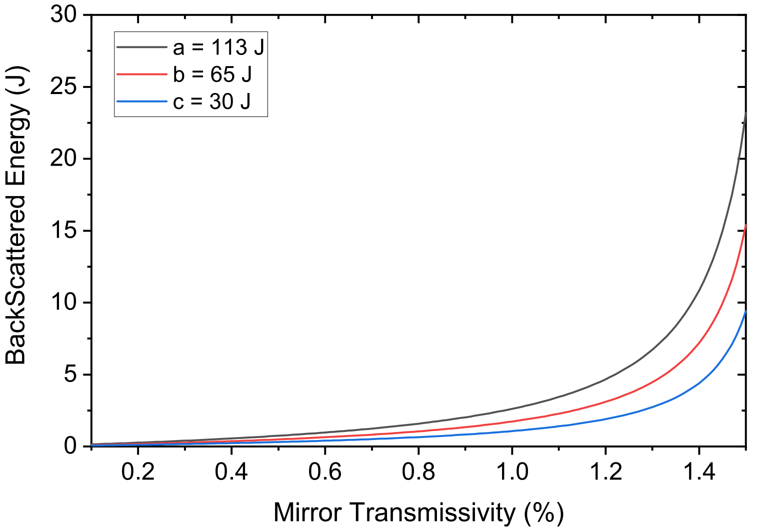

Figure 4.9: Example back-scattered energy as a function of the final turning mirror transmission at 1054 nm, where a, b and c have laser energies of 113 J, 65 J and 30 J, respectively. The target in all cases is a 6 μm thick aluminium foil.

In this way, it was possible to define a threshold value of reflectivity for the turning mirror, of 99.90%, which was then used in the calculation of absorption in the subsequent analysis. As can be seen from figure 4.9, the values of the back-scattered energy varies rapidly as soon as the chosen transmission percentage threshold is exceeded, and quantifying the accuracy in the experimental instrumentation is fundamentally important.

The resulting scaling of the absorption for a 6 μm thick target, that remains opaque (does not undergo RSIT), is shown in figure 4.10. To assess these measurements in context of the values presented in Gray *et al.* [37], we analyse our data using the Davies' empirical model for fractional absorption, as described in equation 4.1, which takes into account the findings provided by Gray *et al.* and others. The key finding highlighted in this study is a strong agreement between the measurements of fractional absorption with the results in Gray *et al.* and those of the Davies fit function, as a function of laser irradiance.

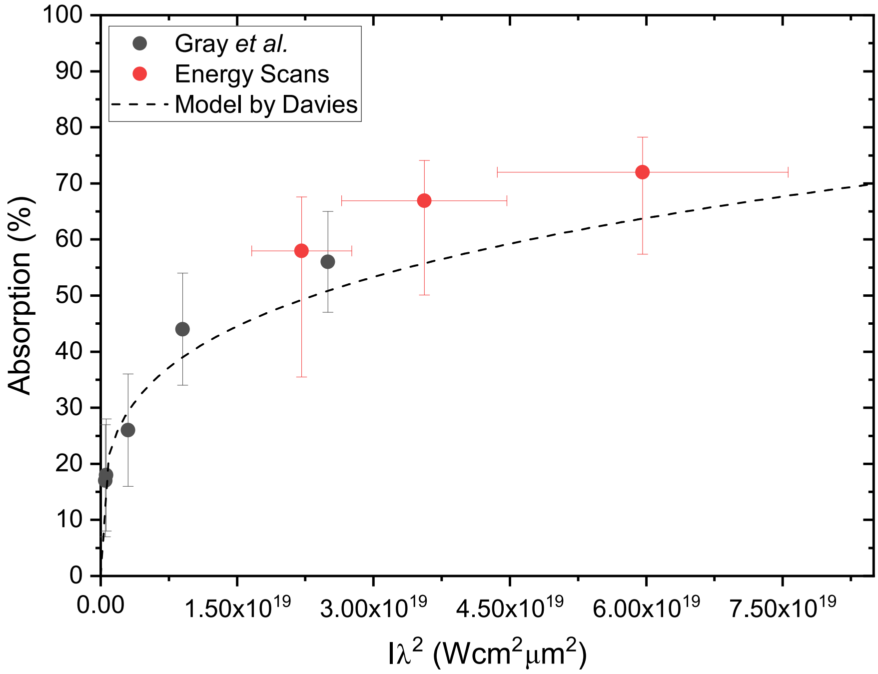

Figure 4.10: Total laser energy absorption as a function of laser irradiance, where the red circles correspond to a thick target, $L = 6$ μm, varying energy from 30 to 110 J, while the black circles are data from Gray *et al.*, and the dotted line is the empirical model derived by Davies, as shown in Eq. 5.1 with the fitting parameter P=0.26 ± 0.02.

Additionally, this final study demonstrated how the equipment used in the experiment and the methodology developed for this investigation proved to work in the analysis of this regime. In the next section we will see how this methodology will be applied to targets undergoing RSIT.

4.6 Absorption measurement for targets that undergo RSIT

The next stage in our investigation is to measure the total laser absorption in the transparency regime, by using ultra-thin foils of thickness between 20 nm and 200 nm. Unlike in the previous sections, measurements were made when the sphere was both opened and closed, allowing the transmitted light to exit the sphere and be detected by the diffuse scatter screen. Absorption measurements were made with the closed sphere configuration as discussed previously, by summing the components of unabsorbed light. In the open sphere configuration, the total energy absorption was calculated considering also the transmitted component measured using the transmission screen.

Williamson *et al.* [113] report the first measurements of energy absorption for intense laser-foil interactions in the transition from a surface-dominated to a volumetric-dominated regime, by varying the target thickness from 20 μm to 77 nm. In thicker targets, the fast electrons were reported to be largely trapped within the target by the longitudinal sheath fields formed at the target front and rear, causing the electrons to re-circulate, while the laser pulse is present. Thus the majority of the electron energy is contained within the overdense region. The energy absorption was shown to vary slowly, with a peak value of 80% observed for a target thickness of 380 nm. This is an increase of ∼10% with respect to the thicker target results reported in Gray *et al.* [37], and corresponds to the thinnest target that does not become relativistically transparent during the interaction, i.e. the target expands during the interaction such that the peak density is near (but remains higher than) the relativistically corrected critical density. Thinner targets, down to 20 nm, were also explored in 2D PIC simulations, and it was found that the absorption decreases by ∼30% for the thinnest case, as a result of RSIT occurring very early in the interaction.

In this section we compare the total absorption measurements with the experimental results presented in Williamson *et al.* [113], including very thin targets, and also compare with the simulation outcomes reported in Williamson *et al.*.

As can be seen from figure 4.11(a), there are differences in the absorption scaling with target thickness than the results reported in Williamson *et al.* [113]. Specifically, from the Williamson *et al.* results, for ultrathin targets a decrease is expected due to the early onset of transparency, leading to higher transmission through the target and reduced coupling efficiency. This is not observed to the same extent in the present results, and so we investigated the source of this discrepancy. For this reason, the energy values measured from the sphere and on the transmission screen for the same target thicknesses were compared. This shows that for the thinnest targets investigated (20 and 40 nm), there is an inconsistency in the measurement as the energy measured by the sphere is less than the energy on the transmission screen. This is not physically possible as the energy of the sphere is the sum of the scattered and transmitted energy, and so the energy in the sphere should always be greater than the energy measured on the transmission screen. From figure 4.11 (b), when we look at unabsorbed energy, for 20 and 40 nm-thick targets, the energy in the sphere and on the transmission screen do not match. In contrast, for thicker targets such as the 100 nm case, when the transmission is very low, there is much better agreement, and the sphere and the transmitted energy calculation give the same response. This means that the transmitted light could be responsible for this apparent discrepancy.

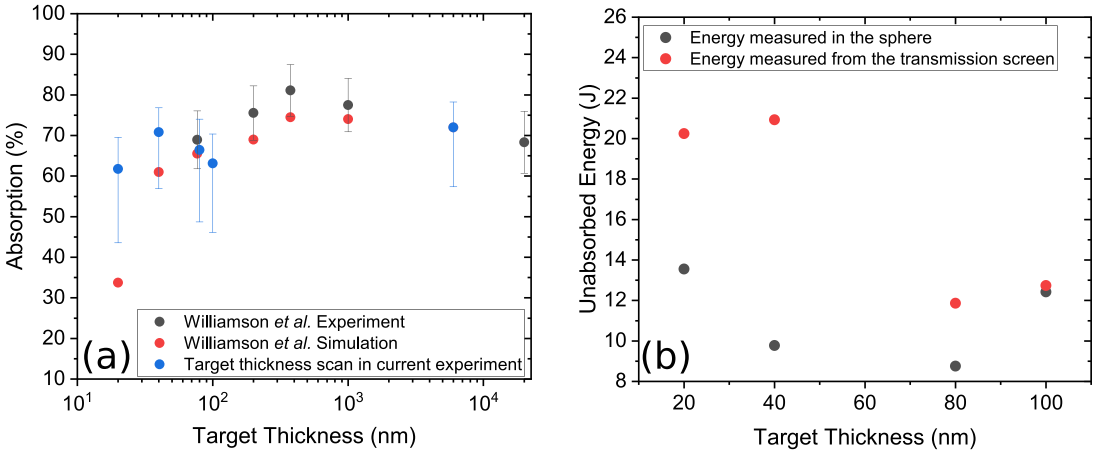

Figure 4.11: (a) Comparison of the percentage of the laser energy absorption as a function of target thickness. The black and the red circles are, respectively, the experimental data and simulations from Williamson *et al.*, while the blue data refer to the new data from this study. (b) Light components not absorbed by the plasma, as a function of target thickness. The black dots are the energy measured using the sphere while the red dots correspond to the energy measured using the diffuse transmission screen.

To understand this unexpected scaling of absorption, we explored several potential sources of this discrepancy. A plausible explanation could be inaccuracies in the calibration of the neutral density filters positioned between the fibres and the sphere or a leak of energy from the sphere, providing a source of escaping, undetected energy. Alternatively, this could be explained by possible damage to the scattering surface inside the sphere, resulting in a degradation of its ability to measure light scattered from or transmitted through the target during the irradiation of the thinnest targets (the calibration may no longer be valid).

We investigated possible explanations relating to a substantial decrease in energy measured by the sphere, first considering the amount of energy not accounted for, which is approximately 50%, given by the difference in the values measured using the sphere and using the transmission screen. A potential explanation is the presence of a possible gap around the equator, if the two hemispheres are not joined properly (i.e. lined up), from which would result in a quantity of energy not measured by the sphere. This involves calculating the size of the gap in the vicinity of the two hemispheres, determining the dimensions through an area ratio between that of the gap and that of the beam on the surface of the sphere. This measurement was made possible by knowing the size of the beam on the transmission screen and assuming a reasonable gap height between the hemisphere, h, of a few mm. We started by measuring the F-number of the transmitted light, $F = \frac{\ell}{D}$, where ℓ is the distance between the target and the transmission screen, and D is the diameter of the beam on the transmission screen.

We calculated the area of the beam on the sphere, as $A_2 = \pi(\frac{r}{2F})^2$, assuming the same F-number. Then we measured the difference between the sphere area, A_2, and the gap area, $A_1 = \frac{hr}{F}$, where r is the sphere radius and imposing this ratio equal to the amount of energy lost, i.e. equal to 50%. From this calculation it was possible to derive that a gap of approximately 15 mm would be required to enable sufficient light to escape the sphere to account for the missing energy in the experimental measurements. A gap of this size is not feasible in the experiment. These calculations were also performed for realistic gap sizes, with h equal to 2 and 3 mm for area A_1. The calculated leaded energy results are shown in figure 4.12. This would also be sensitive to the directionality of the light within the sphere, i.e. the highly directional nature of the transmitted component.

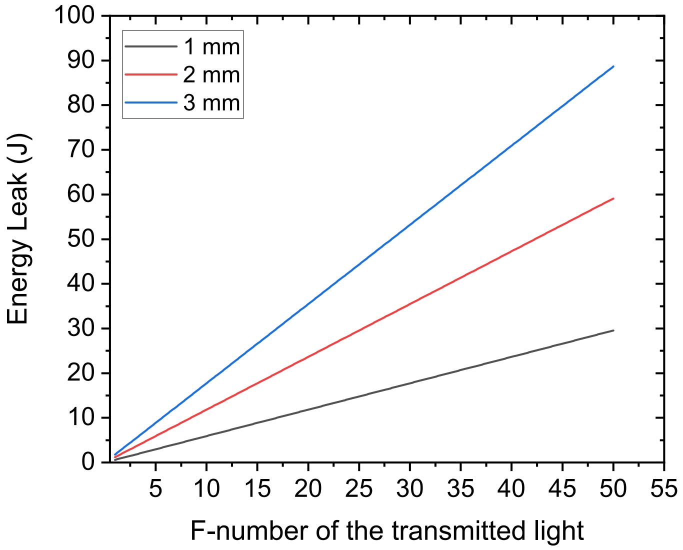

Figure 4.12: Loss of energy from the sphere as a function of F-number of the laser light transmitted through the target, for gap size h equal to 1 mm, 2 mm and 3mm.

Another possible explanation for the measured difference in energy is the use of number of low value ND filters (typically between 6 and 7 pieces of ND) layered together to effectively form a large combined ND value. This was due to the availability of ND filters during the time-limited experiment. The energy of the scattered and transmitted light in the sphere was calculated by scaling the signal with the characterised ND filters, in particular between the sphere and the optical fibres in order to avoid saturation or damage to the optical components. The attenuation of these filters is strongly wavelength dependent, and so it's important to characterise the response of the ND filters at the central wavelength of the particular laser used. Therefore we found a calibration between the quoted ND value, at 500 nm, and the true ND value, at 1053 nm. In this way, it was possible to determine the true ND for the range of filters used over the course of the experiment. For example, for relatively thick targets that do not undergo RSIT during the interaction, we used a stack of seven ND filters to attenuate the signal. The uncertainty in the measurement of the true ND value was found to be 0.003. A correction of this order is not consistent with the amount of energy unaccounted for by the sphere.

In this last case we used the ND filter wavelength calibration equation to calculate the optical density of a ND=7.0 filter, made up of three ND=2.0 filters and one ND=1.0 filter layered together, and considering that these being plastic, we assume that they have a reflection on both surfaces of 4%. We also have to take into account the numerous surfaces that can cause reflections in a stack of ND filters since this could change the overall effective 'ND' value.

Taking measurements for the stack of ND using a spectrophotometer, the measured difference was just over half a Joule, so we conclude it is still too low to account for the observed energy discrepancy.

A final and more plausible explanation for the energy discrepancy is found by exploring the spectrum of light measured by a spectrometer connected to the sphere to detect any other harmonics generated during the experiment. Here we placed 'short-pass' filters in front of the fibres, in order to block/attenuate the strong 1ω signal present in the integrating sphere and measure the higher harmonics (between 200 and 800 nm).

The results presented in figure 4.13(a) show that for targets that do not undergo RSIT, distinct spectral lines are measured throughout the spectrum, as shown in figure 4.13(b) and (c), which are normalised to the maximum signal. These lines correlate exactly with spectral emission lines of barium which is the dominant component of the coating on the internal surface of the sphere. In figure 4.13 the barium emission lines are represented by dashed lines. By plotting the position of each peak of the measured spectrum against the wavelengths of the spectral emission lines of barium, and applying a linear fit, as shown the figure 4.14, a strong correlation is found, with an R^2=0.99, indicating a near perfect fit.

These findings indicate that the beam size undergoes changes as the targets become relativistically transparent to the intense laser light. We analysed its dimension through the use of another diagnostic tool. As previously discussed, a transmission screen was placed behind the rear surface of the target, to quantify the laser light transmitted through the target. In the transition to the RSIT regime, as shown in figure 4.15, the diameter of the transmitted laser pulse measured when using ultra-thin targets is approximately 10 cm, a factor of three smaller than the beam measured during calibration without a target present. Thus the divergence of the laser pulse after focus is altered as it propagates through the relativistically transparent plasma, and it becomes more collimated. This results in an increase in intensity on the inner surface of the sphere, damaging the scattering surface and reducing the energy coupling into the spectrometers. The detection of barium emission lines are produced as a result of this optical damage.

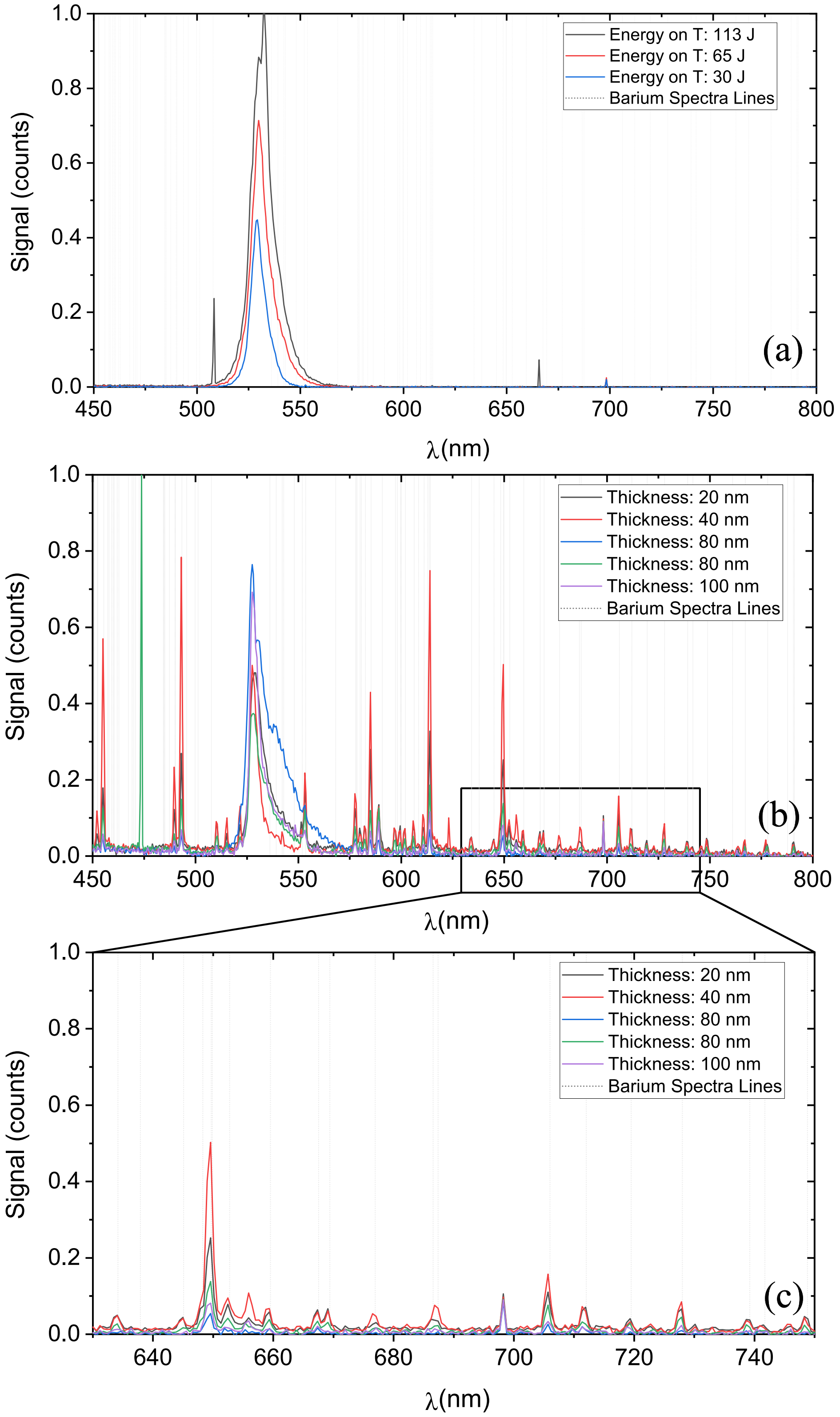

Figure 4.13: Measured back-scattered optical spectrum for: (a) targets that remain opaque to the laser beam; and (b) targets undergoing RSIT. The dashed lines mark the positions of Barium spectra lines. (c) Back-scattered spectrum for manometer-scale-thickness targets zoomed in the range between 640 and 750 nm and normalised at peak value for the same range. The barium emission spectrum was taken from the NIST Atomic Spectra Database.

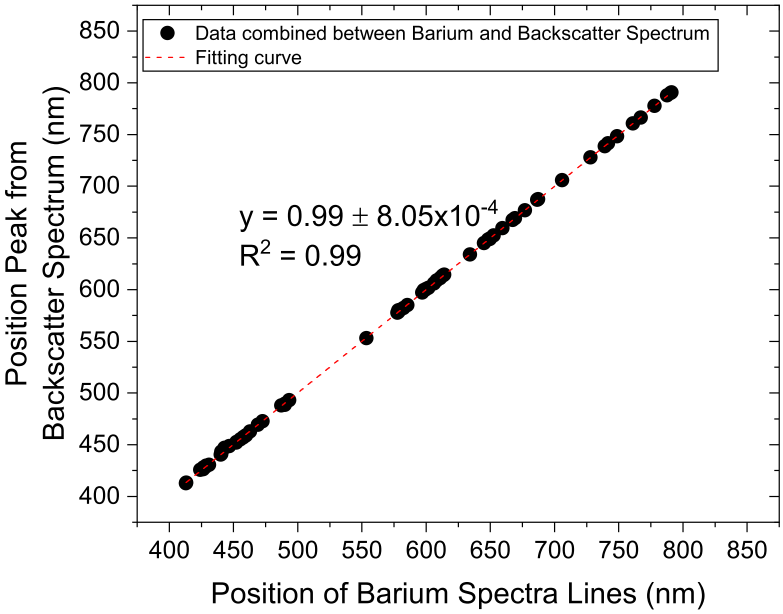

Figure 4.14: Position of the peaks of the spectrum (for thin target) as a function of the position of the Barium spectral lines. The strong correlation confirms the original of the peaks as arising from barium emission from the coating on the inner surface of the hemisphere.

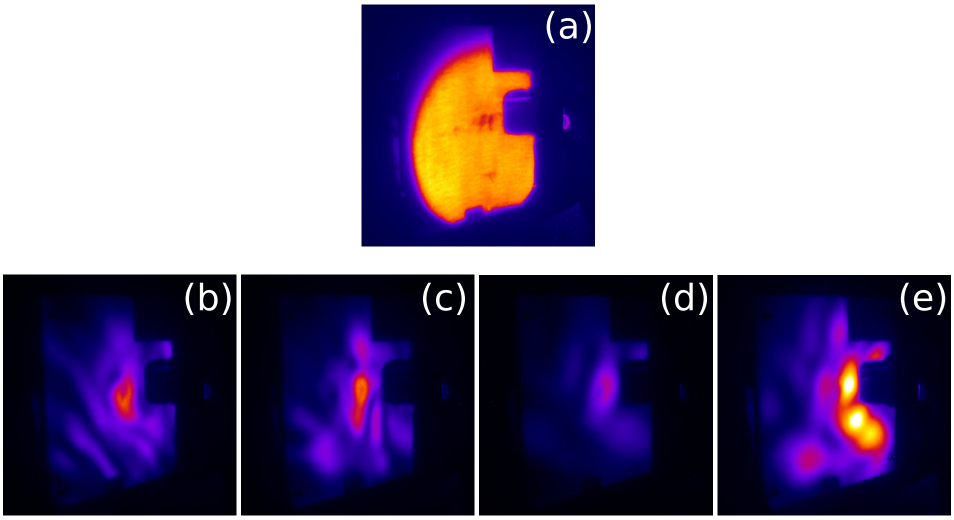

Figure 4.15: Example images of laser beam as measured on the transmission screen. (a) Beam size with no target or plasma present. (b) to (e) The transmitted laser beam size through 20, 40, 80 and 100 nm-thick targets, respectively.

Despite this, it was possible to quantify the amount of unmeasured energy for targets (20 nm and 40 nm) where a significant portion of the laser light propagates through the target, by adding the energy measured by the sphere for targets that do not undergo RSIT (6 μm).

The measured absorption, corrected for the missing energy, as a function of target thickness in the range 20 nm to 20 μm is plotted in figure 4.16. Better overall agreement is observed with the trends reported in Williamson *et al.* [113], The simulations reported only considered limited target expansion (less than 1 μm) which may explain the discrepancy at 20 nm. The implications of this expansion are later analysed in next chapter.

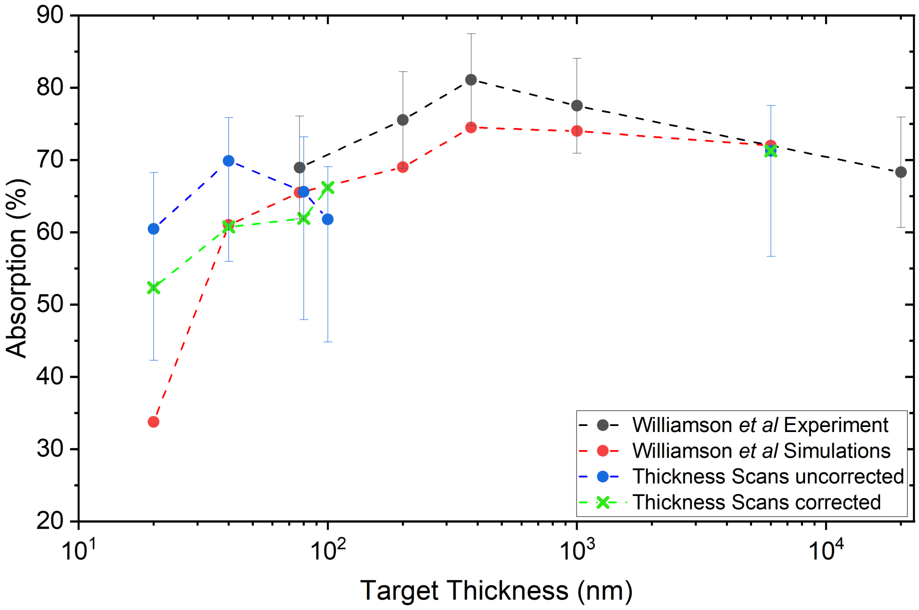

Figure 4.16: Comparison of the total laser energy absorption with the experimental and simulation data reported in Williamson *et al.* [113], as a function of target thickness. The blue and green circles represent the absorption values considering the energy measured from the sphere (i.e. uncorrected) and the energy estimated from the transmission diffuse screen (i.e. corrected), respectively.

The missing energy within the sphere depends on the extent of the damage to the inner surface, coated by a thin layer of barium sulphate. The energy is absorbed and re-emitted in the form of line emission. This damage has had an effect on the quality of the sphere's operation, particularly in the regime where the targets are very transparent, as the transmitted light becomes very collimated, increasing the transmitted energy density on the sphere wall and altering the diagnostic response. The sphere was designed to work for the specific F-number of the off-axis parabolic mirror used in the PHELIX target area. Due to the range of target thicknesses used, this was not an issue in the experiment reported in

[113]. These results show that despite using the same diagnostic setup, optical damage only occurred for targets undergoing substantial RSIT early in the pulse, which resulted in strong collimation of the transmitted light through the greatly expanded plasma.

In the experiment, we based our approach on the assumption of best focus; however, it is important to acknowledge that variations in the focal position may play a significant impact on the results. This potential influence will be thoroughly examined in the next chapter.

4.6.1 Conclusions

In this chapter, the diagnostic tools used to characterise the degree of laser energy coupling to overdense and relativistically transparent plasmas, during an intense laser-solid interaction, have been explored. First, the scaling of absorption with peak laser intensity for targets that remain opaque during the interaction was investigated using diagnostic techniques developed specifically for these measurements, which includes an integrating sphere and the diffuse scatter screens to quantify the energy components of the laser light not absorbed by the target plasma. We find energy scaling results that are comparable to those reported in Ping *et al.* [108] and Gray *et al.* [37], giving us confidence in the diagnostic approach used.

Additionally, measurements were made on the scaling of energy absorption with targets that undergo RSIT. We have seen that ultrathin targets that expand and undergo relativistic transparency early in the interaction have a high degree of laser light transmission and so a high energy on the back inner surface of the sphere. We also find that the transmitted laser light is much less divergent than the light focused onto the target. The enhanced laser energy density on the inner wall of the sphere causes breakdown of the diffuse scattering coating and as a results, the sphere calibration changes - it is not able to correctly diagnose the energy inside it. Taking into account the amount of unmeasured energy, better agreement was found with results reported in Williamson *et al.*, where the absorption decreases as the targets become very thin.

Despite the difficulties encountered, such as the breakdown of the sphere in the case of ultra-thin targets, the integrating sphere in combination with the other diagnostic tools made it possible to achieve a good measurement of laser energy absorption absorption. These results have shown that in the transition to a regime for which the targets are relativistically transparent, the light becomes highly collimated. To measure the energy absorption such that the sphere coating is not damaged, it would be necessary to use a sphere with a dimension larger than the focal length of the parabola. However, the off-axis focusing angle of the parabola used to focus the light onto the target limits the overall sphere radius. These challenges may however be overcome by modifying the design of the integrating sphere, through the addition of a hole within the sphere that allows the laser light that is transmitted through the target to propagate without damaging the internal surfaces. This would allow the absorbed energy to be determined in a regime where there is a high degree of transparency.

Fully understanding the resultant optical properties of the laser light propagation through the relativistically transparent plasma is a complex topic, which will be explored in detail in the next chapter.

Chapter 5

Self focusing of intense laser light in relativistic transparent plasma

5.1 Introduction

In the previous chapter, to measure and characterise the laser transmission in nanometer scale targets, the main diagnostic instruments employed were the integrating sphere and the scatter screens, while the mean laser intensity was kept to its maximum attainable value of 1×10^{19} Wcm^{-2}. This revealed a strong change in the size of the beam of transmitted light. To better understand the behaviour of the laser pulse as it propagates through the plasma, it is useful to investigate the most significant factors that lead the laser pulse to self-focus and defocus. This will give insight into the role the laser and plasma parameters play in the laser propagation behaviour.

This chapter reports on an investigation into these phenomena in intense laser-plasma interactions via a detailed study of the relativistic self-focusing effects during the propagation of a high-intensity laser pulse in a relativistically transparent plasma. It will be demonstrated that the variation in the focus position with respect to the target front surface and target expansion will be the main driving mechanisms that will influence the pulse propagation.

5.2 Overview

In the preceding chapter the discussion was centred on investigation of laser-energy coupling in plasma which showed that laser energy absorption in thick targets scales exponentially for increasing intensity, which is in good agreement with the previously reported findings in this relativistic regime [108][37]. The increasing absorption rate is demonstrated to be more pronounced in the thinnest targets, just above the threshold for relativistic transparency [113], and when the RSIT is achieved the total absorption energy decreases.

As previously discussed, in the transition to the RSIT regime the divergence of the laser pulse after focus is altered as it propagates through the relativistically transparent plasma. It is found to become more collimated. To understand and characterise this process and its implications on the absorption dynamics when the laser-solid interaction undergoes RSIT, it is necessary to analyse in detail the range of parameters involved in the propagation of the laser pulse. The propagation of a Gaussian laser pulse in vacuum is usually determined by diffraction, i.e. when the pulse with a planar wave front tends to have the lowest divergence as it approaches the focus of a Gaussian beam. This divergence can be reduced or reversed to convergence when there is a radial variation in the refractive index of the medium through which the pulse is propagating, which results in different parts of the wavefront travelling with a different phase velocity. The variation is due to radial variation of the plasma frequency. This can happen due to plasma density variation across the wavefront (due to depletion or density build-up) or, due to preferential heating of the plasma at the centre of the pulse, the relativistic mass increase will be higher than at the edges due to the intensity of the pulse. In our experiment, the measurement of absorption was impacted by strong self focusing and collimation which occurred as the laser propagated through the transparent target. As discussed in the previous chapter, this led to a laser intensity on the walls of the integrating sphere which was greater than its damage threshold, leading to a break down in the measurement.

5.3 Methodology

Previously, it was found that measuring absorption for thin targets (< 200 nm) that undergo RSIT was complicated due to the transmitted light being more intense than expected, although the sphere still proved to be an excellent diagnostic tool for targets that remained opaque. The divergence of the transmitted laser pulse was found to vary greatly when it propagates through a thin target undergoing RSIT with the measured beam displaying filamentary behaviour that impacted upon divergence measurements.

In this chapter, observations and analysis are reported on the variation of the divergence of the laser pulse as it propagates in near-critical density plasma. To understand the complex physics involved in these interactions, it is useful to first develop a 1D analytical model to consider what parameters are important for the self-focusing, ignoring some physical aspects that occur during the propagation such as diffraction effects in the first instance. To further analyse the propagation dynamics occurring in this regime, Particle in Cell (PIC) simulation models are used due to their suitability for predicting the evolution and behaviour of complex laser-plasma interaction systems. Simpler simulation setups will be considered first before increasing the complexity to better understand the physical phenomena that occur.

To determine the resultant beam divergence from the simulations, different analysis methods are developed: the first method consists of finding and following the wavefront of the laser pulse with the maximum peak value of the defined intensity while it propagates through the plasma. Through a Gaussian fitting function, this will enable the evolution of the FWHM (thus the beam radius) which consequently enables measurement of the beam divergence. This method is applied in various scenarios mainly characterised by simulation parameters with different laser intensities and plasma densities. Finally, to conduct higher resolution simulations, a different approach is performed investigating beam divergence behaviour far from the interaction region using the moving window simulation method which simulates the dynamic behaviour over time. The method involves introducing a window that moves or shifts through the simulation domain as the simulation progresses, enables the tracking of beam propagation in an expanded plasma over longer time scales providing a more realistic scenario.

5.4 Analytical model

In order to investigate the dynamics of the laser pulse propagation in the transition to the RSIT regime, a simple Gaussian analytical model was considered for the interaction of the laser pulse with the plasma, in the regime where relativistic self-focusing depends on the plasma density and the power of the laser. To simplify the calculation, the diffraction phenomena is neglected.

At high intensities, the medium rapidly ionises at the initial edge of the pulse, leading to subsequent interaction between the intense pulse and an underdense plasma. The quantity of electrons generated through ionisation at a specific point in the beam path is highly dependent on the local intensity. Consequently, any variation in intensity across the beam profile results in a spatially changing index of refraction. This alteration then affects the propagation of individual rays through the medium, ultimately modifying the beam path. The refractive index of the plasma is given by [114]:

$$\frac{\partial \eta}{\partial r} = \left(\frac{{\omega_p}^2}{8{\omega_L}^2}\right)\frac{\partial a_0^2}{\partial r} \tag{5.1}$$

where a_0 is the amplitude of the normalised vector potential. The variation of beam propagation within a medium undergoing ionisation at relativistic intensities can be addressed by employing the paraxial ray equation for a Gaussian beam:

$$\frac{d^2 r}{dx^2} = \frac{1}{\eta_0}\frac{\partial \eta}{\partial r} + \frac{\lambda^2 r}{4\pi^2 {r_0}^4} \tag{5.2}$$

The initial term on the right-hand side of equation 5.2 represents the contributions from the refractive index gradient, which is assumed to vary quadratically with the distance r from the axis, that is;

$$\eta(r,x) = \eta_0 - \frac{1}{2}\eta_2 r^2 \tag{5.3}$$

The final term in equation 5.2 describes the diffraction of a Gaussian beam, characterised by an intensity variation given by;

$$I(r,x) = I_0 e^{(-r/r_0)^2} \tag{5.4}$$

Using the same formulation and notation as presented in [115], where $r(x)$ denotes the variation of the radius for a specific ray along the beam axis, and the beam radius defined as $r_0(x) = \omega_0(x)/\sqrt{2}$, where $\omega_0(x)$ represents the beam waist. This implies that the intensity at the central point of the beam is connected to the total beam power, P, through the relationship $I_0 = P/(\pi {r_0}^2)$. By employing the relation ${a_L}^2 = (2r_e/\pi mc^3)\lambda^2 I$, where r_e denotes the classical electron radius (r_e = e^2/mc^2), and incorporating the definition of the critical power for self-focusing as $P_c = (2mc^3/r_e)(\omega_L/\omega_p)^2$ [116], and the gradient of the refractive index can be expressed as $\partial\eta/\partial r$ = -$(\lambda^2/\pi^2 {r_0}^4)(P/P_c)r/e$. In this case, we have employed the approximation $[\partial e^{-r^2/r_0^2}/\partial r]_{r\approx r_0}\approx$ -$2r/(e{r_0}^2)$, indicating that the refractive index gradient is evaluated near the radial position $r \approx r_0$. This is to best evaluate the overall beam evolution, which is effectively described by following the ray path at a distance $r = r_0$ from the propagation axis.

Incorporating these results into equation 5.3 and assuming $\eta_0 \approx 1$, the paraxial ray equation for fully ionised plasma is obtained in the form;

$$\frac{d^2 r}{dx^2} = \frac{\lambda^2}{4\pi^2 {r_0}^4}\left(1 - \kappa\frac{P}{P_c}\right) r \tag{5.5}$$

with the position factor κ = 4/e, and P the laser power measured during the experiment.

The solution of the previous equation gives the variation of the beam radius along the propagation, x, in the form:

$$r^2(x) = r_{0,min}^2 \left[1 + \left(1 - \frac{\kappa P}{P_c} \right) \left(\frac{x}{x_{0,min}} \right)^2 \right] \tag{5.6}$$

with $x_{0,min} = 2\pi \mathrm{r}^2{}_{0,min}/\lambda$ which leads to a minimum beam radius of $r_{0,min}$ when P is less than P_c/κ.

The evolution of the laser, through equation 5.4, was calculated considering the size of the beam radius during propagation starting from the best focus, 0 μm. We opted a plasma density range spanning from 0.001 to $0.1n_c$. At the lower limit of $0.001n_c$, the plasma density is sufficiently diminished to approach a vacuum-like state, allowing the laser pulse to traverse the plasma without undergoing significant alterations. Conversely, the upper limit of $0.1n_c$ represents a plasma density sufficient to strongly modify the propagation of the laser pulse, resulting in pronounced self-focusing effects and consequential substantial beam divergence, as will be discussed later. In this way, for different values of homogeneous plasma density, it is possible to determine the minimum value of the beam radius that propagates as it interacts with the plasma, which, acting as a lens, focuses the beam with different degrees of self-focusing. As shown in figure 5.1, the laser pulse shows a stronger focus as the plasma density increases, resulting in a very steep beam profile. As has already been said, the diffraction term has been ignored in this configuration, the phenomena of which would prevent the beam radius from reducing below the wavelength and producing a diffraction pattern in the beam. The analytical model is valid up to the point where the laser pulse self-focuses to the diffraction-limit. At this stage, the model accurately describes the behaviour and characteristics of the laser pulse as it converges. However, beyond this self-focusing point, diffraction effects become significant, altering the behaviour of the laser pulse in ways that the current model does not capture. Since the model does not incorporate the diffraction, its predictions and applicability are limited to the region before diffraction becomes a dominant factor. Therefore, the validity of the model does not extend beyond the self-focusing point, where diffraction effects need to be considered for accurate analysis.

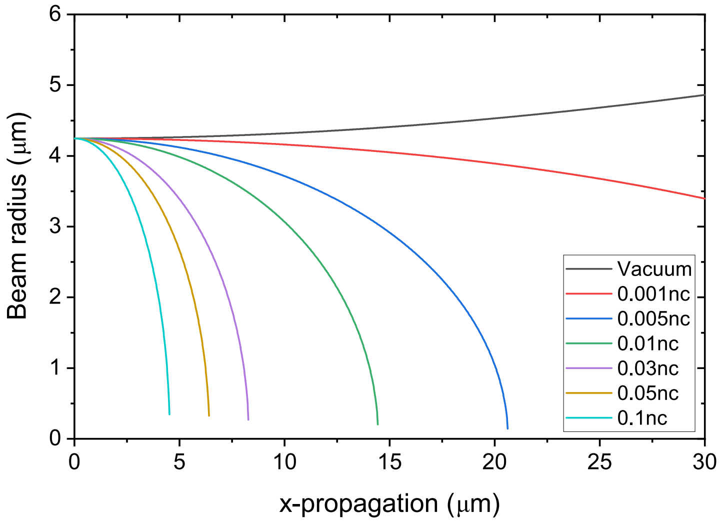

Figure 5.1: Beam radius variation through the Eqn. 5.4 at different plasma densities and laser power $P = 6.71 \times 10^{13}$ W, for which the threshold for self-focusing is achieved, compared with no plasma case (represented by black line), starting from best focus position (0 μm) where the smallest and highest quality focal spot is achieved.

To get useful information on the physics behind these interactions when the laser pulse leaves the plasma, and investigate the effect on the beam divergence, one needs to know a range of important information such as the focusing of the laser pulse, the plasma density and the plasma expansion. This is explored in the following sections.

5.5 PIC Simulations and discussion

5.5.1 Influence of transparency on self-focusing within fully ionised aluminium plasma in the high intensity and short pulse regime

In order to understand and interpret the experimental results, 2D PIC simulations have been performed using the relativistic EPOCH PIC code [117]. To begin, the influence of underdense to near-critical density plasma on the beam propagation was considered. The initial conditions were defined with Al^{13+} ions plasma filling a simulation domain of 60 μm × 30 μm with 3000 × 1500 computational mesh cells corresponding to 20 nm of spatial resolution in the x and y dimensions respectively. The laser was linearly polarised in the y direction with a wavelength of 1.053 μm, focused to a Gaussian intensity distribution with a focal spot FWHM $\phi_L = 5$ μm, corresponding to the spot size achieved experimentally. The focus position is defined as x$_{foc} = 0$ μm, which correspond to the centre of the simulation box in this case. The peak laser intensity was defined as $I = 1{\times}10^{19}$ Wcm^{-2} and a short pulse, starting with short pulse duration, $\tau = 40$ fs, in order to simplify the setup and reducing the number of complex physical processes occurring during the simulation. The simulations were run for a total duration of 300 fs and plasma densities, n_e, ranging from 0.001 to 0.1 n_c. A schematic illustration of this simulation is shown in figure 5.2.

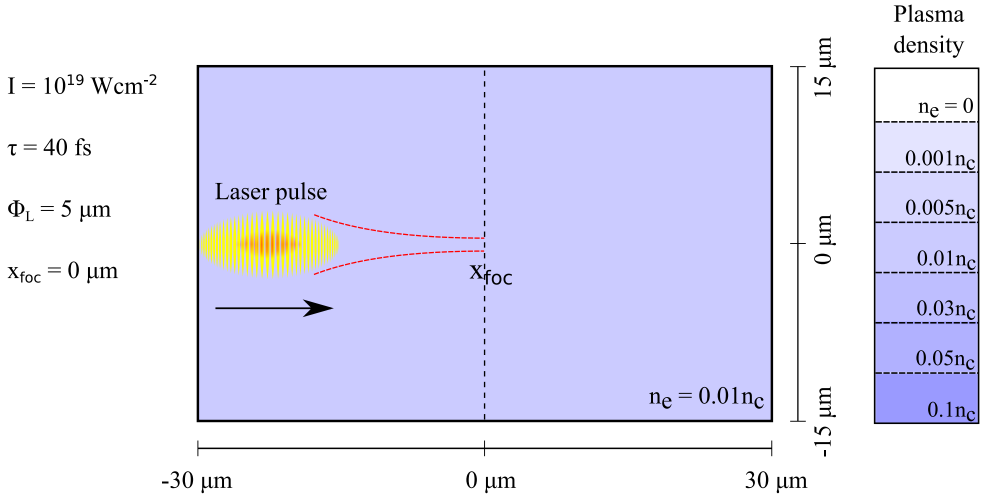

Figure 5.2: Schematic representation of the initial laser-plasma simulations. The high intensity laser pulse is injected from the left-hand boundary and is focused to $x = x_{foc}$, represented by the dashed black line, through a fully ionised plasma. In this example n_e was set to $0.01n_c$. The simulations were performed with the plasma density ranging from 0.001 to $0.1n_c$ and compared to the vacuum case, $n_e = 0$

To observe the impact of the plasma on the beam radius throughout the simulation, a systematic methodology has been implemented. The approach involves the detection and tracking of the peak intensity wavefront of the laser pulse as it propagates through the plasma. For each output, the longitudinal position and the transverse FWHM is measured for this peak wavefront and converted into radius. Repeating this measurement every 12 fs, it is possible to obtain the temporal variation of the beam radius, r, during the interaction.

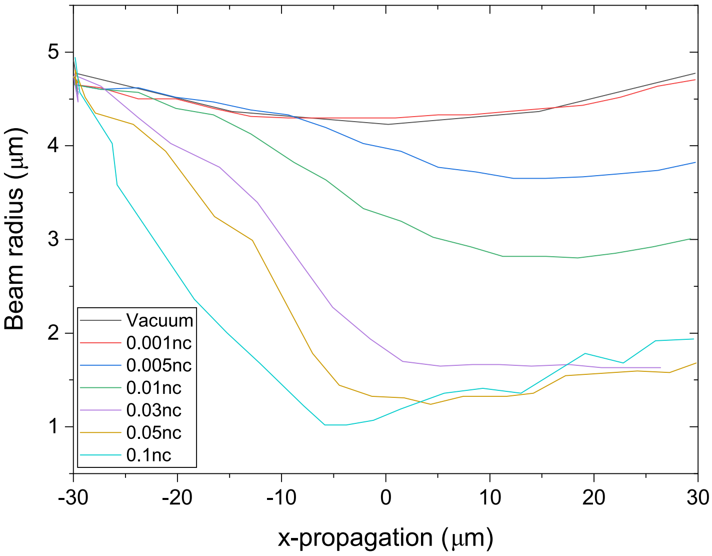

Figure 5.3: EPOCH simulation result: beam radius as a function of peak wavefront position in fully ionised aluminium plasma for different plasma densities. The vacuum case of n_e=0 is shown in black.

The beam radius of the peak wavefront as a function of wavefront position from the PIC simulation is shown in figure 5.3 It can be seen that in the first 30 μm the laser pulse experiences a degree of self-focusing that increases for higher initial densities.

This self-focusing continues and becomes more pronounced up to the region approaching the best focus position, i.e., towards the centre of the box simulation. During the interaction, a ponderomotive channelling effect is created where electrons are ejected from the laser axis due to the ponderomotive force, which pushes them into regions of less intense field (see section 2.5.2). In addition, the relativistic increase in electron mass especially along the laser pulse axis results in the plasma frequency reducing along the propagation axis. At the edges of the beam profile, the plasma frequency is increased due to density build-up. From equation 2.52, the lower the frequency of the plasma the higher the refractive index and vice-versa. In terms of the phase velocity of the pulse this relationship causes the wings of the wavefront to travel faster in the plasma than the peak of the pulse and the laser starts to self-focus in the plasma. These two contributions, due to the ponderomotive expulsion and relativistic self-focusing, becomes significantly stronger at higher densities, likely due to the fact the initial plasma frequency is now higher and when the electrons are expelled, a steeper change in the refractive index is obtained, as shown in figure 5.3. The laser pulse reaches a minimum beam radius approximately equal to 1 μm for the highest density simulated n_e=0.1n_c. In the last 30 μm, the beam begins to expand as the laser propagates towards the end of the simulation, showing a degree of divergence with a slope that increases with the highest plasma density. In the 0.03n_c case, the beam appears collimated over this region after the focal position, due to the degree of self-focusing of the plasma channelling balancing the beam divergence, thus remaining fairly flat during propagation.

In all cases the simulations were performed with the plasma completely filling the simulation box. In the next sections we will analyse the evolution of the laser pulse during its propagation when it leaves the plasma.

5.5.2 Investigation on the evolution of the laser pulse after self-focusing in an underdense plasma

To investigate these changes in beam radius as the pulse leaves the plasma, the plasma was now defined with a finite extent of 25 μm from x=-30 μm to x=-5 μm at different densities, from n_e=0.001 to 0.1n_c, with the remainder of the simulation box as vacuum. The plasma distribution thus defined shows a close resemblance to the conditions that occur in the dynamic scenario of an expanding solid target, in particular in the presence of the vacuum boundary. The simulation domain and number of simulation cells are the same as the previous section. Separate simulations were performed for a pulse durations of τ_L=40 fs and τ_L=100 fs. The figure 5.4 depicts a schematic of the simulation in plasma-vacuum case.

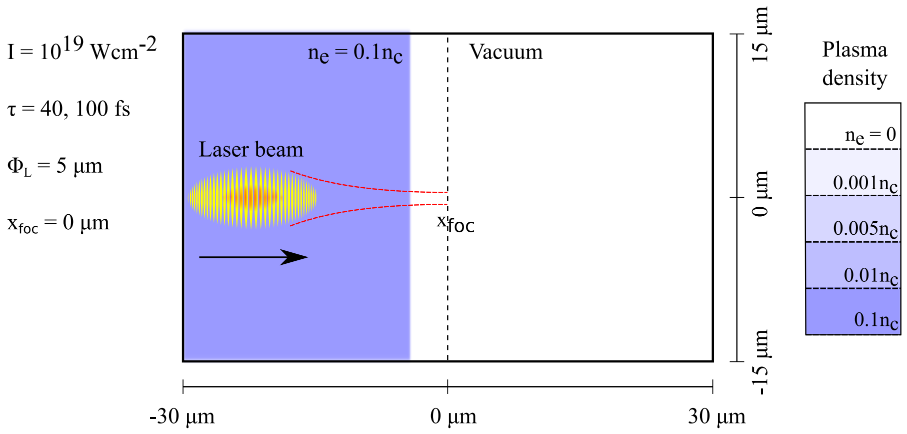

Figure 5.4: Schematic representation of the plasma-vacuum simulation: The plasma extends in x for 25 μm, depicted as the purple region (in the example $n_e = 0.1 n_c$) and the beam is initially focused into the vacuum at $x_{foc} = 0$ μm, represented by white region.

The 2D-PIC simulation results are shown in figure 5.5 where the black line represents the variation of the beam radius for the full plasma shown in figure 5.3, while the red and blue line shows the beam radius as the laser pulse propagates in the plasma and into the vacuum, at pulse duration of 40 fs and 100 fs, respectively.

As in the previous full plasma case, the plasma acts as a lens on the laser pulse, reaching a minimum radius of 1 μm for the highest density value (n_e=0.1n_c), as seen in figure 5.5 (d), but immediately after the focal position the pulse shows increased divergence for higher initial density values. The measurements indicate that there is no appreciable difference in the beam radius evolution for the two different laser pulse durations for n_e $\leq$0.05 n_c, as shown in figure 5.5 from (a) to (c). For the highest plasma density case, n_e=0.1 n_c, the two pulse durations exhibit different behaviour in vacuum. In particular, with τ = 100 fs, towards the end of the propagation, the beam shows a larger divergence compared with shorter pulse duration, τ = 40 fs, see figure 5.5 (d). For short pulse durations, the wavefronts preceding the peak wavefront have significantly lower intensity, resulting in a reduced transverse ponderomotive effect compared to the peak wavefront. This lower intensity is due to the sharper gradient in the intensity profile. In contrast, for longer pulse durations, the intensity gradient is more gradual. As a result, the intensity of the wavefronts in front of the peak is more comparable to that of the peak wavefront. The pondermotive pressure of the light preceding the peak wavefront is intense enough that it expels electrons radially, via the pondermotive force, forming a cavity prior to the peak intensity wavefront. This alters the plasma density experienced by the following wavefronts resulting in an intensity peak in regions relatively distant from the laser axis, see figure 5.6 (c), with the wavefronts becoming more pronounced as the beam moves away from the focal position, and due to the extreme curvature of the wavefront, measurement of the beam radius using the transverse FWHM is not as accurate and that may lead to discrepancies.

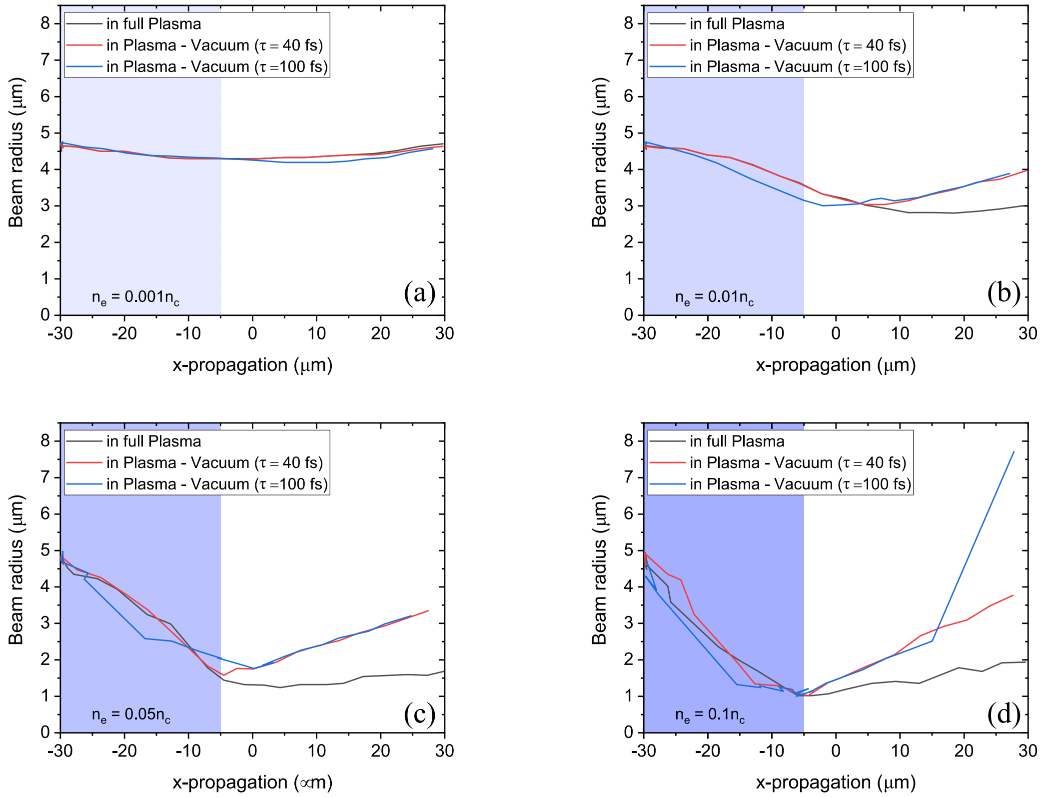

Figure 5.5: Simulation results of the variation of beam radius for different plasma-vacuum densities, (a) $0.001n_c$, (b) $0.01n_c$, (c) $0.05n_c$, (d) $0.1n_c$. The blue and white region represent 25 μm of plasma and 35 μm of vacuum, respectively. The variation of the beam radius in the plasma-vacuum case is shown in red and blue for 40 and 100 fs of pulse duration, respectively, while the beam radius for the previous full plasma simulation is shown in black.

It is observed that the plasma density has a significant influence on the beam propagation behaviour, except for low density values, such as $0.001n_c$, where the laser pulse propagates relatively unperturbed. For higher densities, the plasma acts as a positive focusing lens, which becomes stronger at higher density values.

As soon as the laser pulse leaves the plasma, the beam radius begins to increase, unlike in the previous full plasma case where the self-focusing counteracts the beam expansion. This behaviour is near identical for both pulse durations, 40 and 100 fs, with the exception of the n_e=0.1 n_c case where the divergence increases only towards the end of the propagation. This phenomenon becomes more pronounced as the laser pulse continues to propagate, see the figure 5.6 from (a) to (c), at different plasma density for τ = 40 and 100 fs, and the curvature of the wavefronts increase resulting in less accurate measurement of the beam radius.

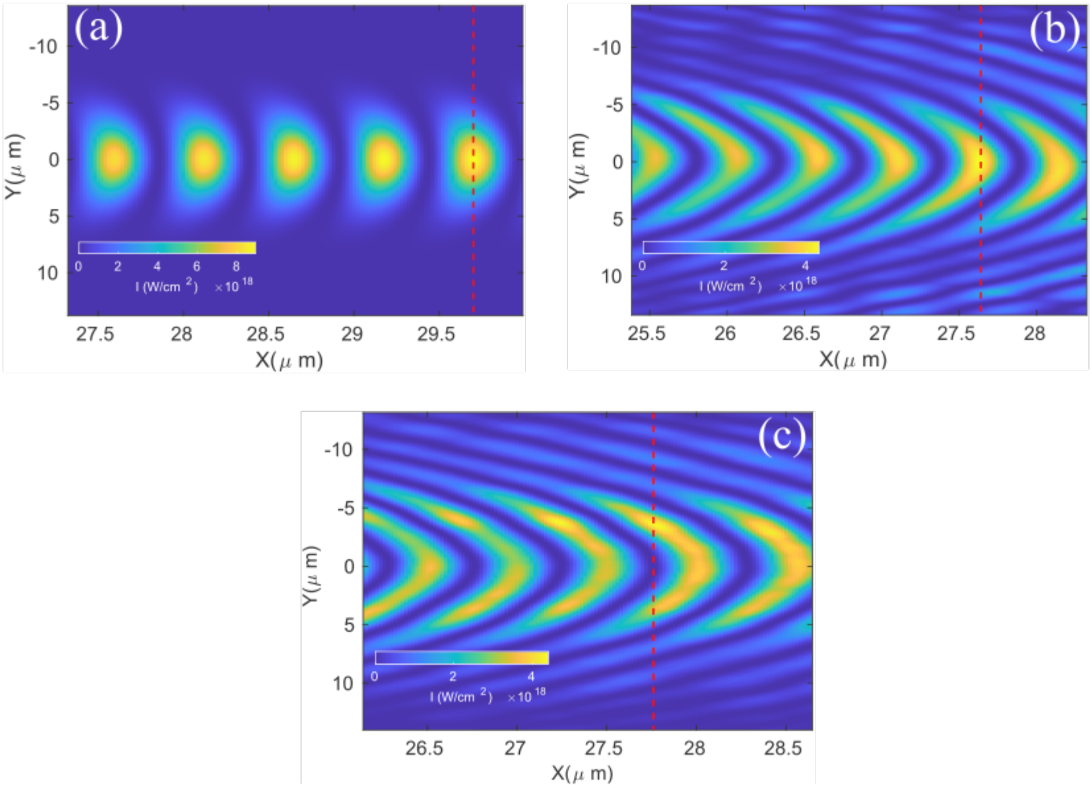

Figure 5.6: Spatial intensity distribution at (a) τ = 40 fs for $0.001n_c$, (b) τ = 40 fs for $0.1n_c$ and (c) with τ = 100 fs for $0.1n_c$. The dashed red lines represents the determined position of the peak intensity wavefront after 300 fs.

5.5.3 Influence of transparency on self-focusing within a Gaussian plasma density profile

A more realistic scenario was considered as the light arriving before the main pulse, although significantly less intense, is still sufficient to ionise the target thus producing an expansion of the plasma which results in a strong longitudinal density gradient in the plasma [118]. To investigate the laser propagation in this case, the plasma density in the simulations is now defined by assuming a 10 nm, solid density aluminium foil is expanded with a 1D longitudinal Gaussian density profile with a variable FWHM, x_F, from 40 μm to 80 μm, reducing the peak density but keeping the overall areal density constant, see the schematic in figure 5.7. The peak densities were $0.01n_c$ and $0.005n_c$ and for the 40 μm and 80 μm expansion cases, respectively. The simulation domain was 120 μm × 30 μm with 3000 × 750 simulation cells. The laser pulse was defined with $I = 1{\times}10^{19}$ Wcm^{-2} and a Gaussian intensity distribution, $\phi_L = 5$ μm of FWHM, which was focused in the middle of the plasma, $x_{foc} = 0$.

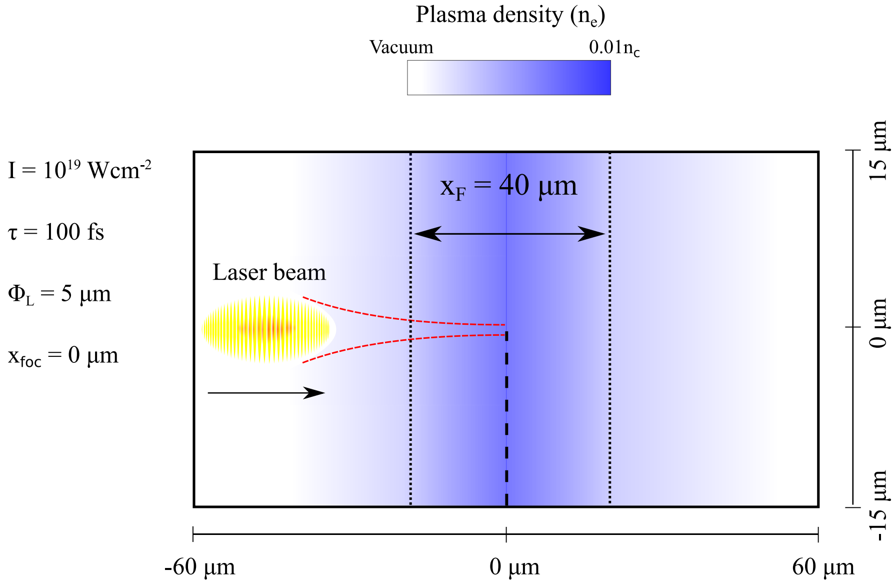

Figure 5.7: Schematic of laser pulse interacting with a plasma with a Gaussian density profile with $x_F = 40$ μm. The beam is focused in the middle of the box indicated by the black dashed line, where the plasma density has the highest value, $0.01n_c$.

The methods developed to determine the beam divergence have been modified in order to improve the accuracy in the measurements. This adjustment became necessary due to an increase in beam divergence, rendering the previous approach inadequate for ensuring accuracy. In particular, we increased the output temporal resolution, from 12 fs to 0.5 fs with a total duration of 600 fs. From the first time step the tracking of the peak of the laser is achieved by taking account of the variation of the group velocity change. The group velocity with which the peak of the pulse travels inside the simulation box is measured by taking into account the plasma density where it is located. By measuring an average of the density around the position of the peak intensity value, it is possible to determine the new plasma frequency and consequently the group velocity with which the pulse travels within the plasma between each output. This ensures the analysis of the same position in the pulse at each output. A diagram of the method to track the wavefront is shown in figure 5.8.

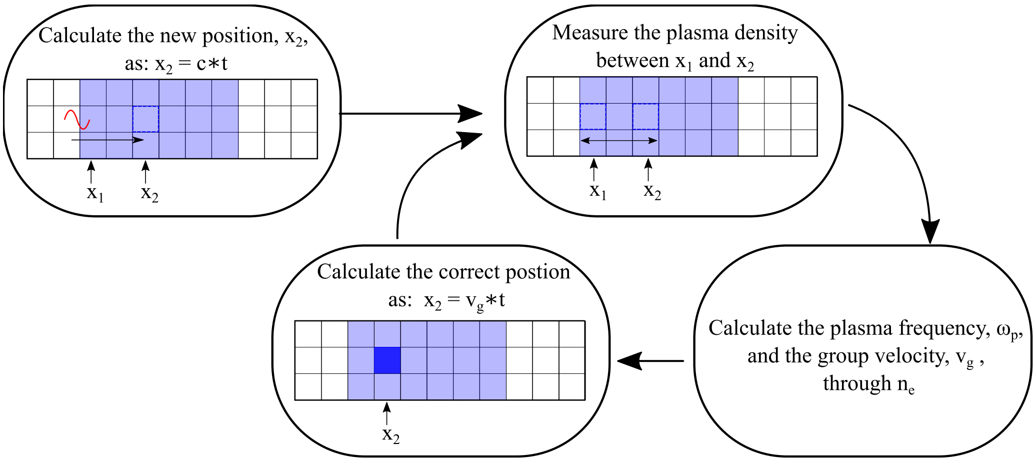

Figure 5.8: Tracking wavefront diagram: (1) At the beginning of the simulation the laser pulse propagates into the vacuum at speed of light, c, moving from x_1 to x_2. (2) As the beam interacts with plasma, the predicted new position, x_2, is measured taking into account the average of n_e between x_1 and x_2. (3) Through n_e, the real laser pulse speed, v_g, is measured. (4) The correct new position, x_2, is calculated through the group velocity, v_g.

In the first instance, the laser pulse propagates through the expanded plasma where it undergoes increased self-focusing as the density increases approaching the initial focus, and after further propagation the pulse starts to diverge as the density reduces, until the end of the box simulation. This can be seen in the figure 5.9, which shows the variation of beam radius as a function of wavefront position for $x_F = 40$ and $60\ \mu$m of FWHM of Gaussian density profile. With increased expansion, $x_F = 60\ \mu$m, after the beam self-focuses and moves into the decreasing density region, the beam radius starts to increase slower than in the $x_F = 40\ \mu$m case. The same behaviour was seen in the previous section where the presence of the plasma reduces the beam divergence compared with vacuum.

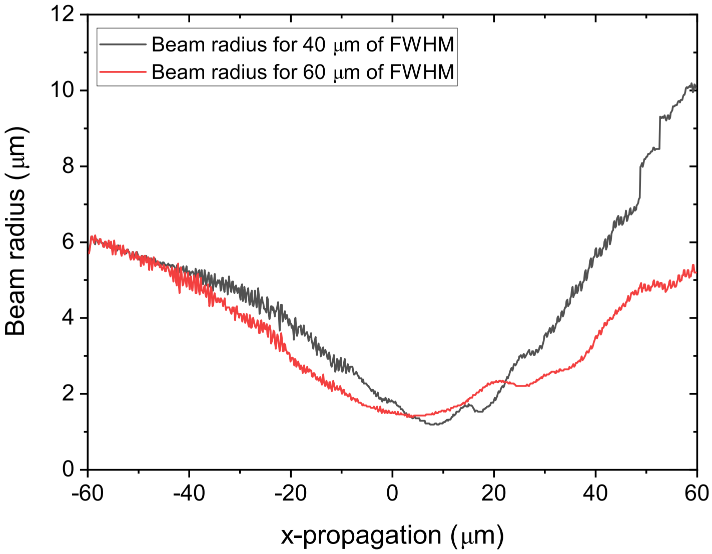

Figure 5.9: Variation of the beam radius curves in a plasma with Gaussian density profile with 40 and 60 μm of FWHM corresponding to blue and red line, respectively.

This increasing self-focusing can be seen through the 2D time-space plots of the tracked laser peak, shown in 5.10 (a) and (c), which represents the transverse profile of beam (in y dimension) corresponding to the propagation of the peak of the pulse through the simulation domain. From the region where the beam is tightly focused, the 2D time-space plots show the formation of beam wings, formed laterally to the main pulse, and more pronounced in the 40 μm case. The wings appear to be symmetrical with respect to the direction of laser propagation, and as for the rest of the pulse, they also propagate with some divergence from the focusing point.

As we can see from the figure 5.10 (b) and (d) the laser pulse propagating through the plasma exerts a radial ponderomotive force on the electrons and creates a low-density plasma channel, in both cases with $x_F = 40$ and $60\ \mu$m.

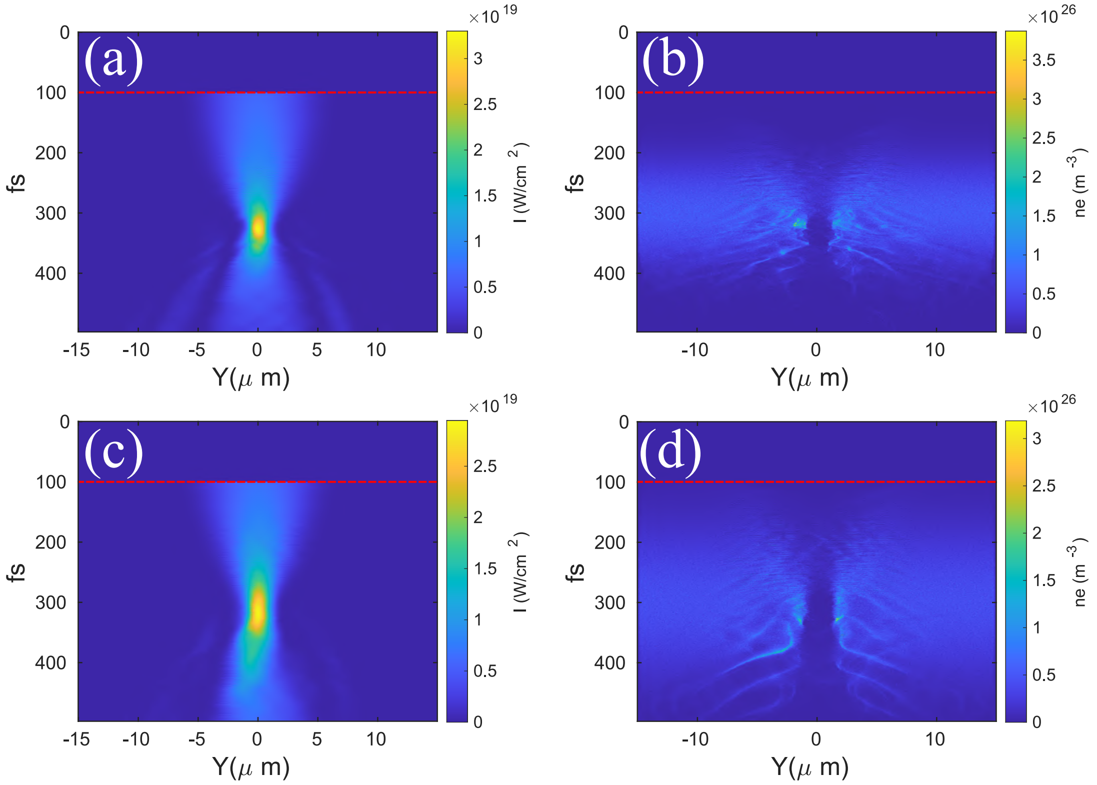

Figure 5.10: (a) and (c) the 2D intensity time-space plot for plasma expansions of 40 and 60 μm of FWHM, respectively. The dashed red line, at t = 100 fs, corresponds to the peak of the laser pulse entering into the simulation box. (b) and (d) the 2D time-space plots for the plasma density sampled at the same position as the intensity for 40 and 60 μm of FWHM, respectively.

The results from these measurements show that with a Gaussian plasma density profile, with the same areal density of an expanded thin foil target, a strong self-focusing of the laser pulse occurs as it propagates towards the initial focal position, where the pulse reaches a minimum size of 2 μm for both 40 μm and 60 μm FWHM. It is observed that for the remaining propagation of the pulse, the divergence angle is reduced for increased plasma expansion and filaments begin to form due to the diffraction of the laser pulse. In the next section we will analyse the divergence of the laser pulse when focused at different focus positions and the effects it has during the interaction with the plasma.

5.5.4 Influence of transparency on positive defocusing in the high intensity and short pulse regime.

To investigate the self-focusing phenomenon observed in the experiment, we explored numerous elementary cases, examining various simple scenarios to understand the underlying dynamics. However, it became apparent that these scenarios were insufficient in capturing the dynamics exhibited in the experimental results. The strong focusing observed resulted in a larger divergence of the beam downstream, contrary to the experimentally detected outcomes. Therefore, it is necessary to consider and explore alternative approaches that could potentially lead to lower divergence as observed experimentally. One such method was to consider an imperfect laser pulse interaction. In the first instance, the pulse is defocused, which in experimental terms would mean a misalignment of the optical components that could lead to an imperfect focus. This potential defocus effect was tested in EPOCH for two different cases: with a Gaussian plasma expansion and with a uniform density slab target.

To increase the focal spot size, the simulations were carried out focusing the beam at a different focal position (x_{foc} = -100 μm) before the centre of the Gaussian density profile of 40 and 60 μm of FWHM, keeping the same laser parameters as before, and to enhance our understanding of the laser pulse evolution, the simulation box was extended to 180 μm × 30 μm and with 4500 × 1500 computational mesh cells for 600 fs of duration and an output temporal resolution of 0.5 fs, see the schematic in the figure 5.11.

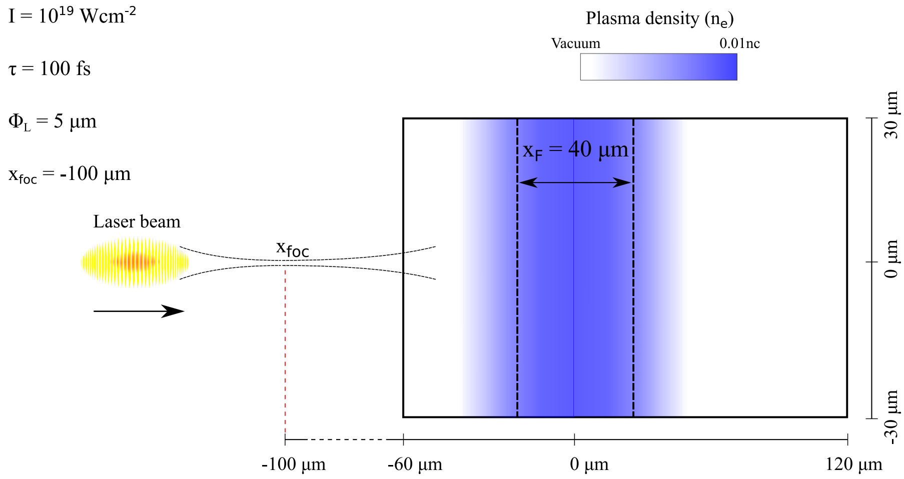

Figure 5.11: Schematic of the laser pulse focused 100 μm before the the peak of plasma density. In the example, the plasma has a Gaussian density profile with 40 μm of FWHM delimited by dashed black lines.

Figure 5.12 shows the evolution of the beam radius for the initially defocused pulse for the two expanded plasma cases. As the laser enters the simulation box, due to the Gaussian nature of the beam, the divergence of the laser pulse increases and for 40 μm of FWHM it continues to grow up to the peak density. For the 60 μm of FWHM case, the divergence grows for the first $\sim$ 25 μm before starting to reduce as the laser pulse interacts with denser plasma. In both cases, after the peak density region, the divergence varies more slowly before beginning to decrease. In the 60 μm of FWHM case, the beam starts to focus from $\sim$ 20 μm to $\sim$ 30 μm after the peak density where it reaches a minimum radius of $\sim$ 3 μm. For 40 μm of FWHM, the beam starts to focus for $\sim$ 20 μm after the peak density exhibiting a minimum radius of less then 6 μm. In figure 5.12 the measurement displays a noise in the simulation output, arising from the formation of filaments due to the diffraction of the laser pulse. This phenomenon occurs approximately 20 μm after the peak density with an increasing beam size of 1 μm before focusing quickly from $\sim$ 40 μm to $\sim$ 60 μm. In both cases, after the self-focusing, the beam radius remains almost constant for $\sim$ 15 μm before starting to grow as the density approaches vacuum.

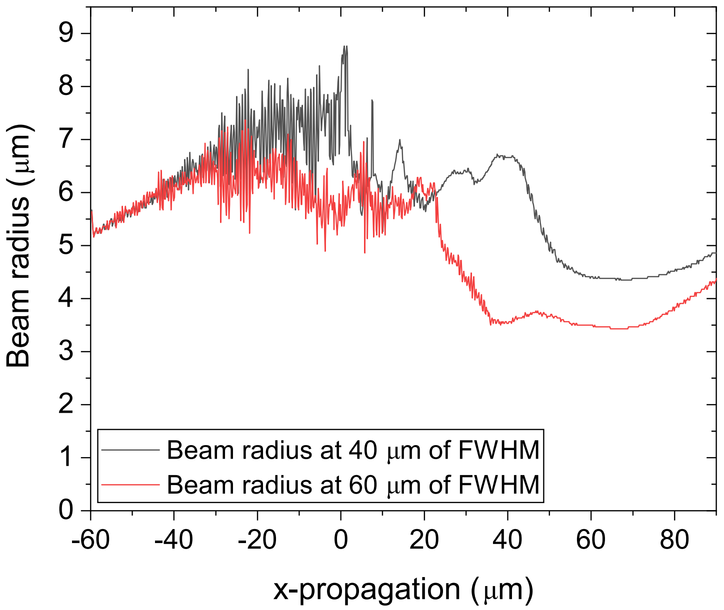

Figure 5.12: Variation of the beam radii for a beam focused 100 μm before the plasma in a Gaussian density profile with 40 μm of FWHM in black line and 60 μm of FWHM in red line.

In each instance, when the laser pulse propagates and interacts with the denser plasma region, thin filaments begin to form and diverge either side of the laser axis as shown by the 2D time-space intensity plots of the tracked wavefront in figures 5.13 (a) and (c). These effects can also be observed in the 2D time-space plots of the electron density, shown in figure 5.13 (b) and (d), where the filaments produce small plasma channels with lower density and begin to refract the laser pulse in the plasma density gradient.

In this scenario, unlike the previous simulations, as the laser pulse is initially defocused, the beam radius grows, reaching a maximum of 7.8 μm near the plasma density peak. Here, as the plasma acts as a lens, the pulse refocuses, resulting in a reduction of the radius of the pulse during propagation. The laser pulse appears to be quite collimated towards the end of the propagation. To better understand how this defocus effect affects beam collimation and its strong self focusing, we performed simulations to test which parameters involved reduce the beam divergence.

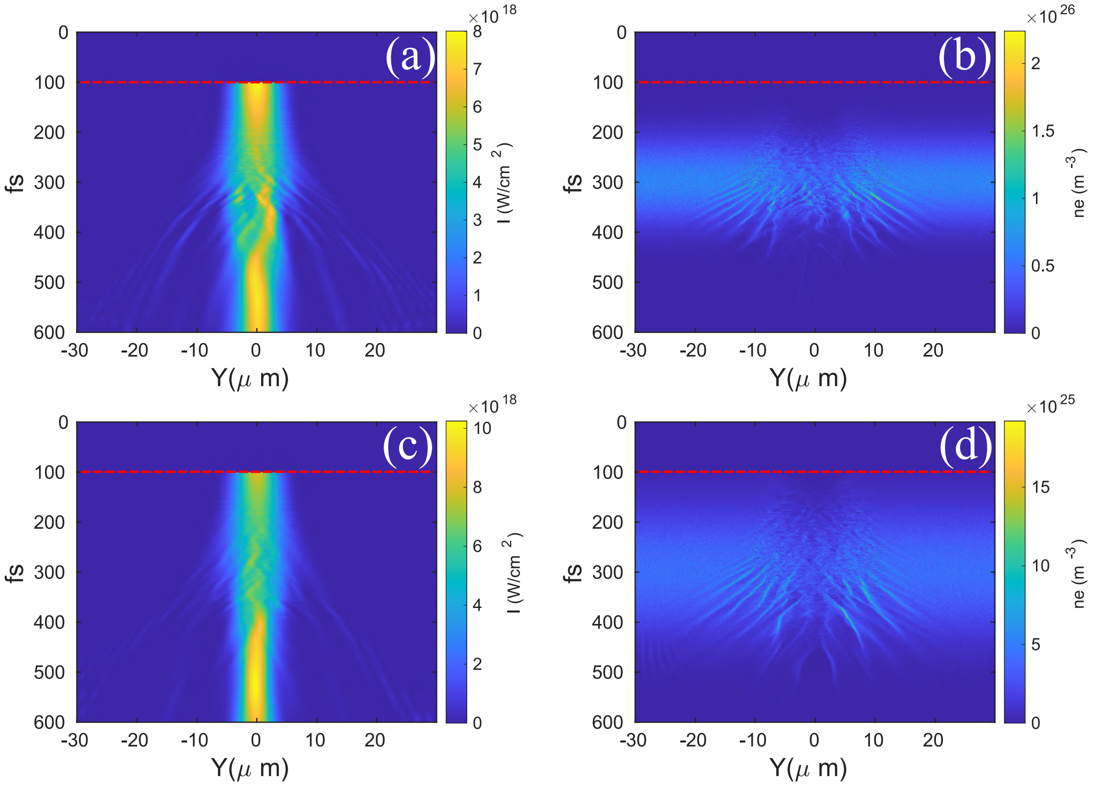

Figure 5.13: (a) and (c) the 2D intensity time-space plot respectively for 40 and 60 μm of FWHM. (b) and (d) 2D time-space plot for the plasma density at 40 and 60 μm of FWHM, respectively.

To understand if the driving mechanism behind this process depends on a large focal spot we will first test the interaction varying the beam spot size through variation of the best focus size and see how the initial beam radius impacts upon the evolution. In particular the laser pulse with $I = 1{\times}10^{19}$ Wcm^{-2}, and Gaussian temporal profile, $\tau = 100$ fs, is focused into the plasma, at focal position, $x_{foc} = 0$ μm. This corresponds to the peak of plasma density, with a larger focal spot, set at 8 μm, the same dimension obtained by focusing the beam 100 μm before the plasma, as used in the previous section. Figure 5.14 shows the evolution of the beam radius as a function of wavefront position with $\phi_L = 8$ μm. Upon the laser entering the simulation box, a consistent pattern emerges: following the self-focusing of the beam and its traversal into the decreasing density region, there is a noticeable rise in the beam radius. This behaviour mirrors the trends observed in the preceding section, where the presence of the plasma reduces the beam divergence reaching a minimum radius of ~ 1.22 μm and then increases.

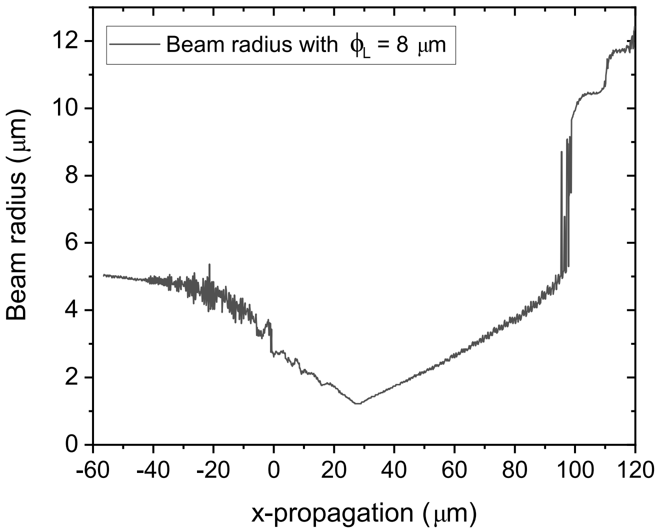

Figure 5.14: Variation of the beam radius in a plasma with Gaussian density profile with $\phi_L = 8\ \mu$m

Examing the figures 5.15 (a) and (b), it can be observed how the laser pulse focuses towards the best focus position near the maximum peak of the plasma density, with $x_F = 60\ \mu$m, and then diverges immediately after until the end of the propagation as we saw in the section 5.5.3. The 2D time-space plots depict the generation of lateral beam wings, emerging laterally to the main pulse as in the figures 5.10 (a) and (b), where in comparison to the defocus scheme with $\phi_L = 5\ \mu$m, as seen in previous section, the divergence does not decrease, it is not influenced by a different focal spot size but seems to depend on a different position of the best focus.

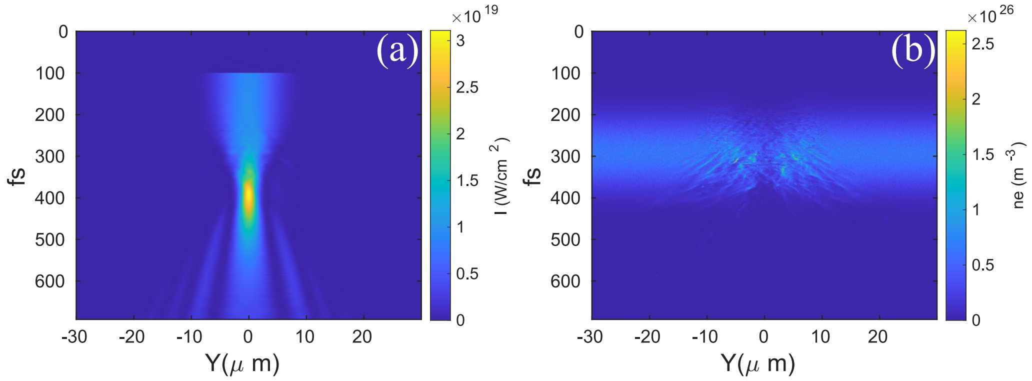

Figure 5.15: 2D time-space plots: (a) and (b) are respectively the beam intensity and density profiles, where the laser pulse with larger focal spot, $\phi_L = 8\ \mu$m, is focused into the plasma.

In order to understand these changing physical processes, further investigations were made considering a different defocus position, the laser beam with I = $1{\times}10^{19}$ Wcm^{-2} and 5 μm FWHM of Gaussian density distribution was focused 100 μm after the density peak of the Gaussian profile, in order for the beam, to focus through the plasma. Once more, figure 5.16 shows how the laser pulse entering the simulation box begins to undergo self-focusing reaching a minimum radius of approximately 1.36 μm after $\sim$ 88 μm of propagation and then immediately begin to diverge.

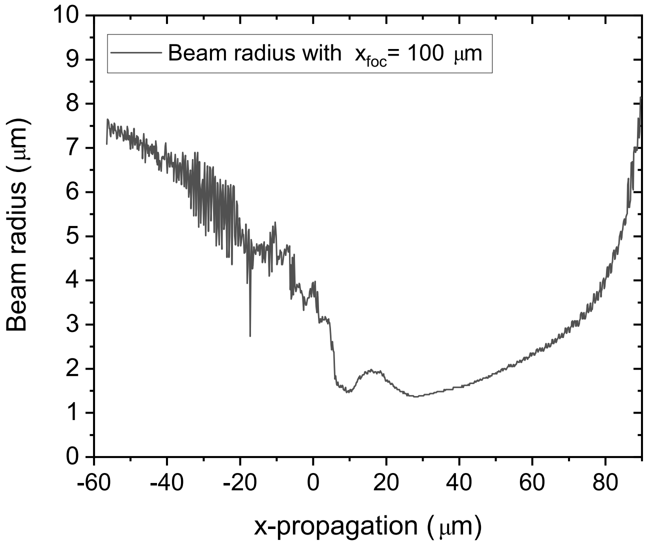

Figure 5.16: Variation of the beam radius in a plasma with Gaussian density profile with x_{foc} = 100 μm

Also from the 2D plot in the figure 5.17 (c) and (d), we can see the laser beam focusing at the best focus achieves its minimum radius to start growing after, showing the increasing divergence as it propagates further, similar to the previous case.

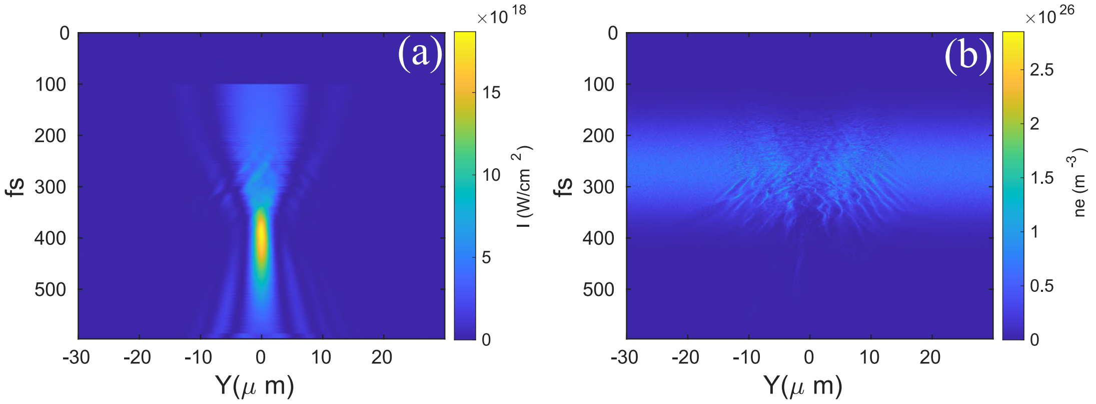

Figure 5.17: 2D time-space plots: (a) and (b) the intensity and density profiles when the laser pulse, with ϕ_L = 5 μm, is focused 100 μm after the density peak.

As we have seen, focusing the beam with a larger focal spot, the pulse presents a divergence which increased immediately after the strong self-focusing, and no beam collimation was observed after the best focus. This could mean that the change in the size of the focal spot does not affect the divergence of the beam, rather it is the focal position that causes a negative divergence, as we have observed in the defocus scheme. Moreover, following the results that the beam was focused after the peak density of the Gaussian profile suggest that the condition for having a collimated beam is that the focal position is before the plasma.

5.5.5 Effect of defocusing on laser pulse propagation in transparency regime for a uniform plasma

In order to simplify the analysis, defocusing the pulse before the plasma (with x_{foc} = -100 μm) was repeated considering a slab plasma profile with different laser intensity values, I=10^{17} to 10^{19} Wcm^{-2}. The plasma was initialised as a 25 μm thick slab of uniform density plasma in a simulation box containing 3500 × 3000 cells, 70 μm × 60 μm. The transverse size of the box simulation was increased by 15 μm to ensure minimal reflection since the reflection of the laser pulse would alter the measurements of the beam size. The plasma was defined with different densities, n_e=0.01 to 0.1n_c. See figure 5.18 for a schematic of these simulations.

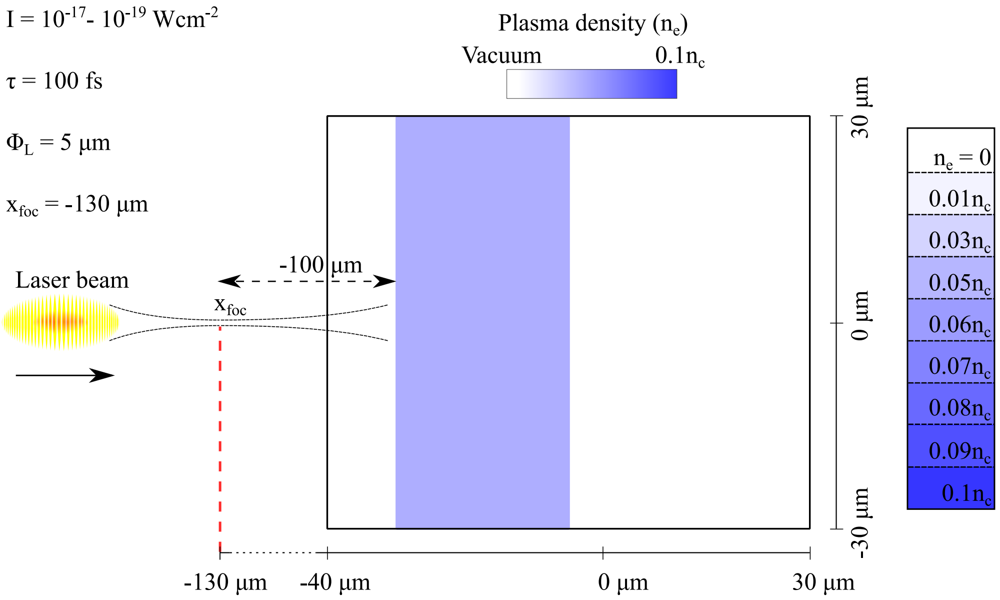

Figure 5.18: Schematic of a laser pulse focused 100 μm before a fully ionised aluminium plasma slab extended for 25 μm. In the example n_e was set to 0.05n$_c$.

The evolution of the intensity profiles in time are shown in figure 5.19 through the 2D plots, where the beam profile with lower densities remains effectively unperturbed as the plasma is not dense enough. Figure 5.19 (a), presents edges of the preceding wavefront, that propagate together with the main pulse with a slight divergence that increases until the end of the simulation. These edges of the preceding wavefront also appear in the vacuum case, mainly due to the Gaussian nature of the beam whose wavefronts tend to curve as it propagates away from the best focus.

For higher density plasma, this response begins to change, in particular already with densities close to 0.03 n_c, shown in figure 5.19 (b), where after 150 fs, multiple filament formation occurs, that start altering the entire propagation, even after propagation into vacuum. Note, these filaments also further perturb the plasma density, as observed in figure 5.20 (b). This process is exacerbated with denser plasma, from (c) to (g) the appearance of the filaments becomes stronger and the main pulse appears to focus towards the end of the simulation. While, for the highest density plasma, 0.1n_c, the laser pulse shows a strong central filament downstream.

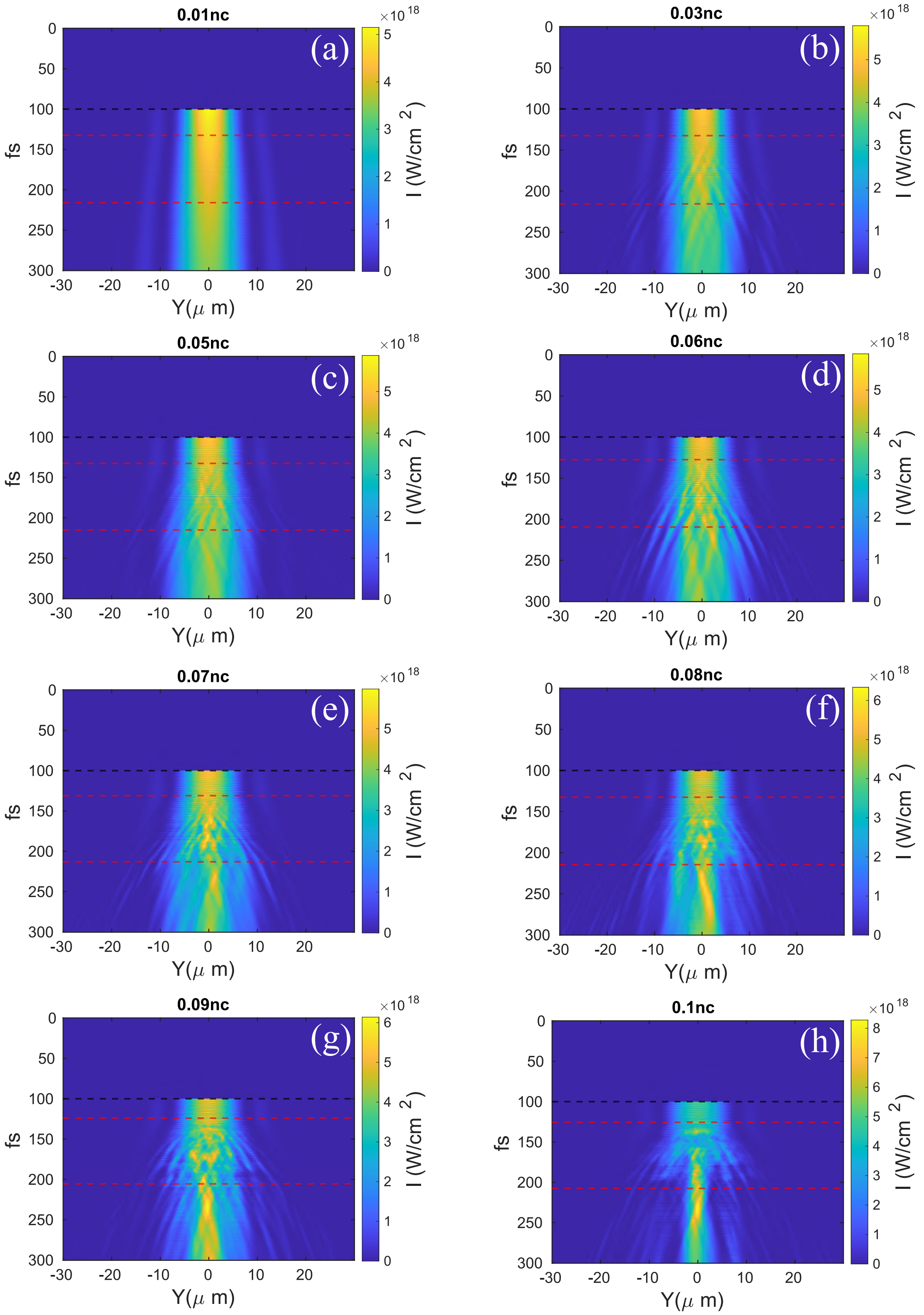

Figure 5.19: Evolution of the intensity profiles in time, with the beam focused 100 μm before the front surface of the target, at different densities as stated above each plot. The dashed red lines represent the start and the end of the plasma and the dashed black line, at t = 100 fs, corresponds to the peak of the laser pulse when enters in the box simulation.

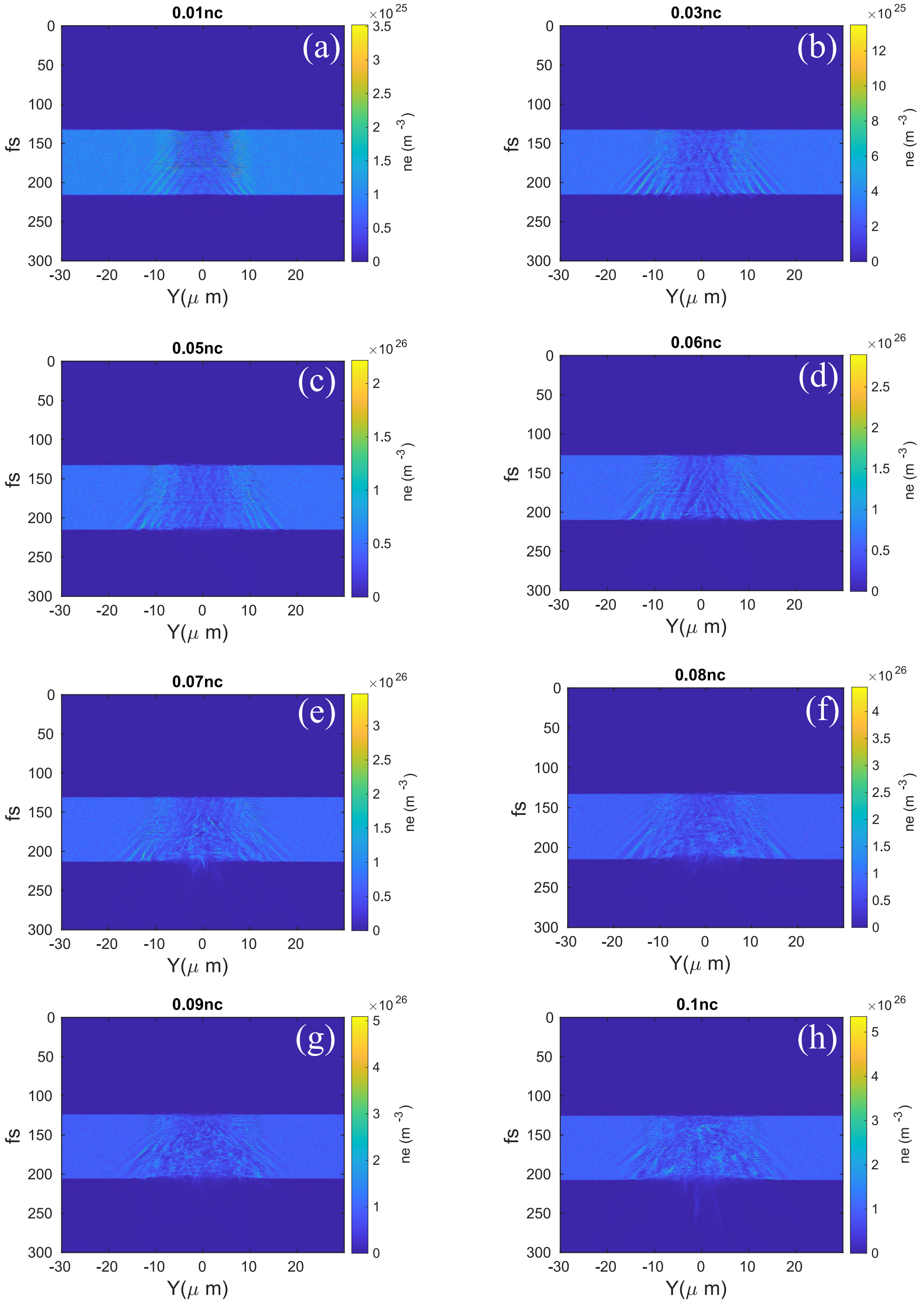

Figure 5.20: Evolution of density profiles in time, with the beam focused 100 μm before the front surface of the target, at different densities as stated above each plot.

The beam divergence was measured after the pulse has left the plasma, specifically, for each output, the transverse intensity of a wavefront, corresponding to the peak of the pulse is measured, and through a Gaussian fitting function it enables the determination of the beam radius. In this way, the data is fit to a Gaussian distribution function to measure the FWHM, converted into beam radius and, by measuring at two points in time, the divergence can be determined. This fitting method is performed at $t_1 = 420$ fs, which corresponds approximate 2 μm after the laser pulse leaves the plasma, and then again at $t_2 = 486$ fs (22 μm after target rear surface). From the two measurements it is possible to determine the radii of the beam at two different points in space, and the divergence is subsequently calculated in the following way:

$$\theta = 2\mathrm{arctan}\left(\frac{r_2 - r_1}{l}\right) \tag{5.7}$$

where r_2 and r_1 are respectively the radii measured in the two different locations of the beam propagation, and l is the distance between them. Two different fitting functions respectively with two different forms of measure of the accuracy of fit are used. In particular, a model where the fitting is done through a mathematical function that fits to the overall Gaussian envelope of the pulse modelling the shape of the data. We call this approach Overall Gaussian Fitting (OGF), which is given by:

$$y_1 = ae^{-\left(\frac{x-b}{c}\right)^2} \tag{5.8}$$

where a is the amplitude, b is the centroid (location) and c is related to the peak width. This fitting function attempts to automatically estimate starting point coefficients for the fitting based on the data provided. The default behaviour of the fit function is to use algorithms to determine initial parameter values, which are the coefficients a, b and c.

The OGF fitting function primarily examines the overall expansion of the laser pulse, providing a measure of the beam's collective expansion. However, this method may not always yield accurate or optimal initial values, especially for complex and noisy data as plasma density increases (as will be shown later) where most of the energy concentrates in a dominant central filament. To address this, a second method has been developed, focusing on the region with this strong central filament and ignoring the secondary filaments. In this approach, the initial values in the fitting function are defined manually. Specifically, the amplitude of the Gaussian component is disregarded, as indicated by;

$$y_2 = e^{-\left(\frac{x-b}{c}\right)^2} \tag{5.9}$$

This second fitting model finds the peak, and based on that fits a Gaussian function around the peak, which hereafter is called Average Peak Gaussian Fitting (APGF). The Gaussian functions that model the data are hown in figure 5.21, OGF and the APGF functions are represented respectively by the green and red line. Both are fit to the data (in dashed blue line) after the target rear surface, when the beam leaves the plasma at t_1 and then at t_2, which correspond to 20 μm of propagation.

Figure 5.21 (a) shows the transverse profile of the wavefront at t_1, for a plasma density of $0.01n_c$. Here, both fitting curves model the data accurately, consistent with the representation of the intensity profile in figure 5.19 (a), where the radius size is around 11 μm.

Filamentary structures begin to appear at low densities, as in the case of $0.03\mathrm{n}_c$. Here the respective peaks of the Gaussian fitting functions differ slightly, leading to a small difference in the size of the beam and consequently varies the divergence angle, 4.9° from OGF and 7.7° through APGF, we can see the variation of both as the density of the plasma varies in the figure 5.22 (a) and (b) respectively. This difference begins to be more pronounced as the plasma density increases, starting from $0.06\mathrm{n}_c$, the modeled radius is no longer the same. As the laser pulse leaves the plasma the difference in beam radius varies from 1.4 μm for $0.06\mathrm{n}_c$ to 2.2 μm for $0.08\mathrm{n}_c$, due to the APGF fit tending to the peak filament as opposed to measuring the overall transverse profile. However, this gap starts decreasing for much higher plasma densities, and goes to zero for the highest plasma density. See the figure 5.21 (h) for the 0.1n_c case, where the fitting functions model the data in the same way and the two curves practically overlap.

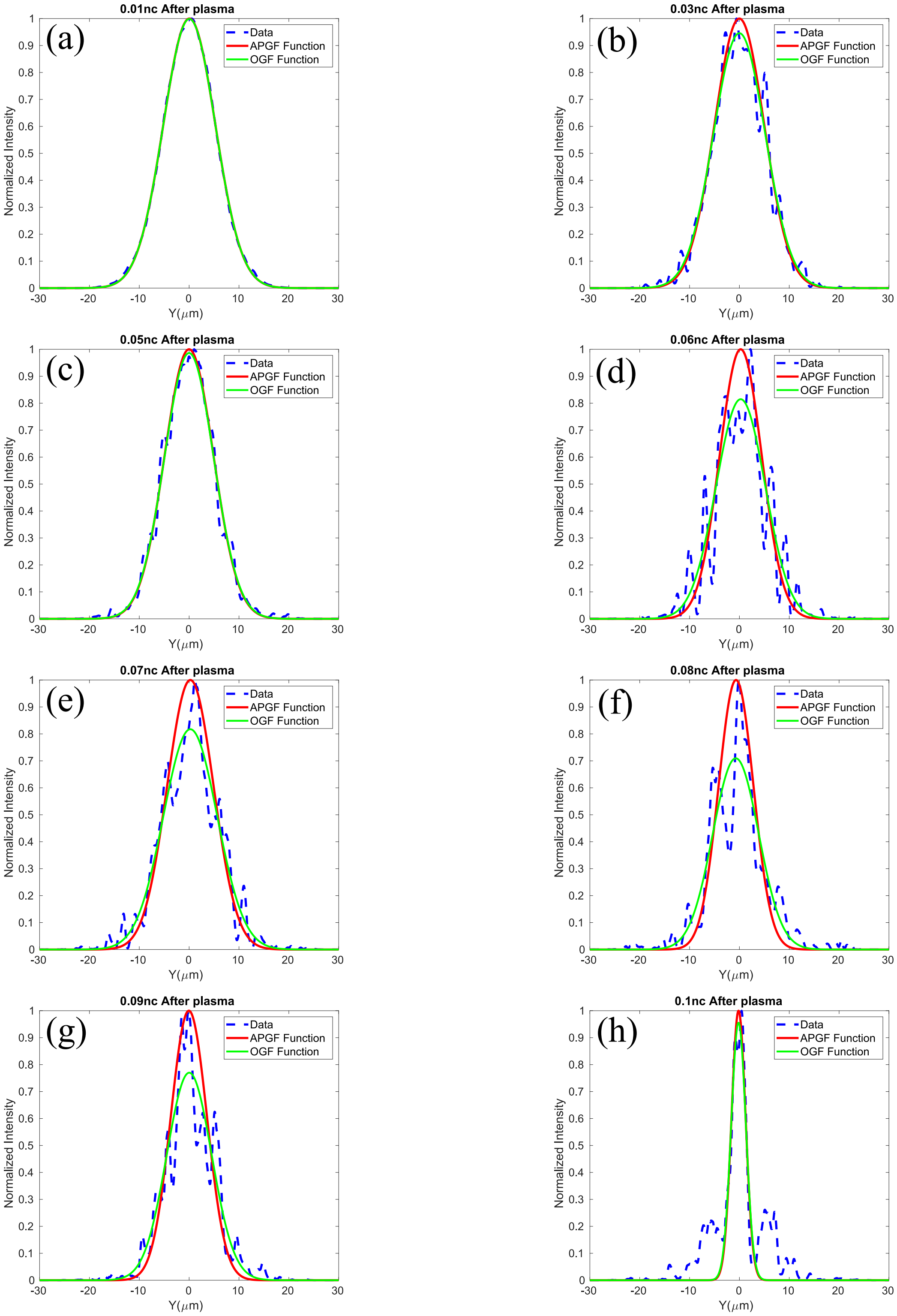

Figure 5.21: Comparing the fitting curves as the beam, with I = 1×10^{19} Wcm^{-2}, leaves the plasma at t_1 = 420 fs, for different plasma density as stated above each plot: the dashed blue line represents the simulation data, the solid red line is the APGF function and the green line is the OGF function.

In terms of divergence, figure 5.22 (b) illustrates a slight collimation of the laser pulse with a change in angle as the plasma density increases, which grows slowly from the 0.6n$_c$ case. This convergence continues for higher density values up to 0.9n$_c$, beyond which the laser pulse seems to undergo strong self-focusing resulting in significant divergence (see the 0.1n$_c$ case), where both fitting functions, OGF and APGF, coincide. As we have seen, during the interaction, the laser beam breaks down into numerous filaments that persist for long distances. This effect becomes more pronounced as the plasma density increases resulting in the formation of more intense filaments that significantly impact the overall behaviour of the laser beam propagation.

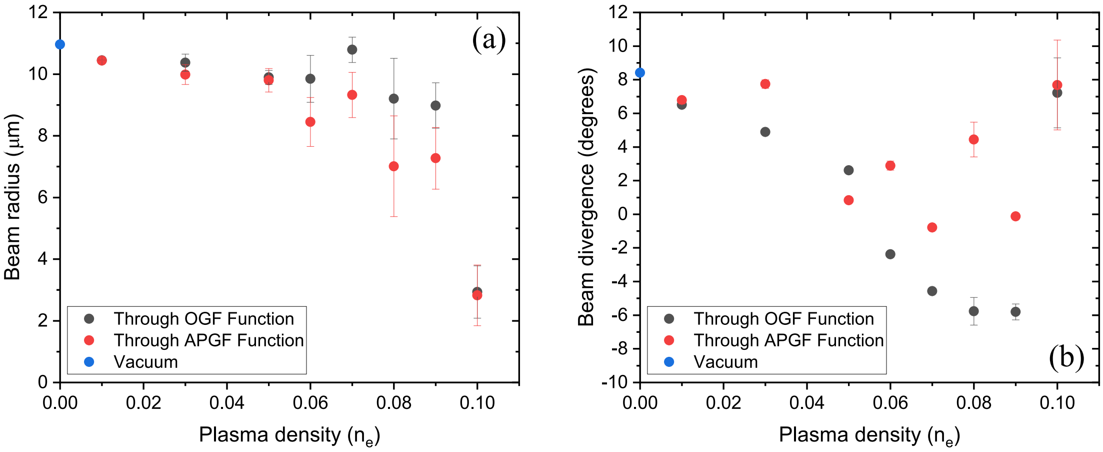

Figure 5.22: Variation for the beam radius (a) and divergence angle (b) based on the two fitting curves with $I = 1\times10^{19}$ Wcm^{-2}.

These simulations were repeated for lower intensity values, starting from $I = 1\times10^{18}$ Wcm^{-2}, for the same initial plasma densities. From the 2D intensity time-space plots shown in figure 5.23, it can be seen how the laser pulse is less subject to perturbations as it propagates unlike the previous case. This is confirmed by the electron density time-space plots shown in figure 5.24, where the plasma does not present modulations due to the generation of the laser filaments.

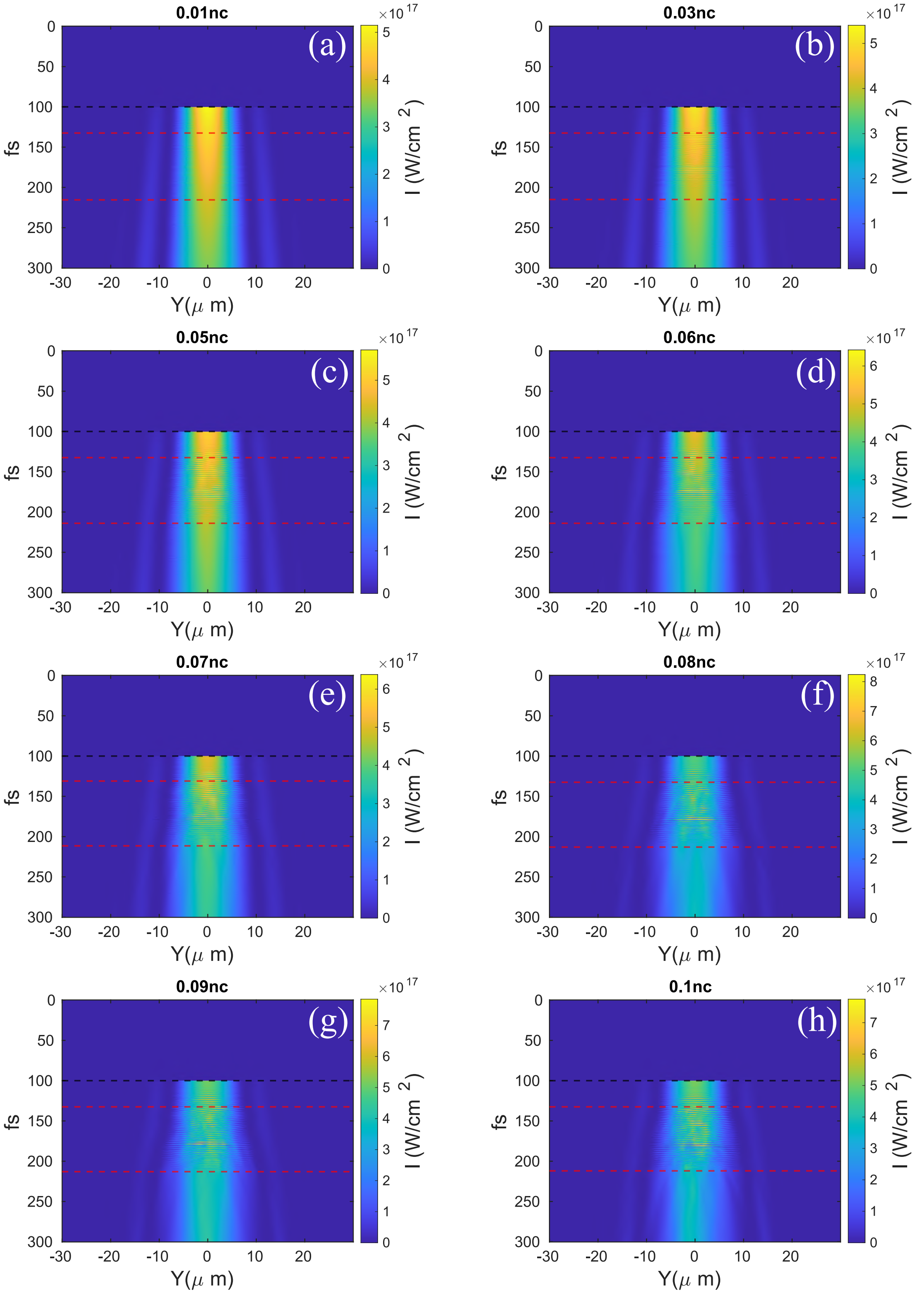

Figure 5.23: Intensity beam profiles for each time step, in defocus beam with slab plasma at different densities stated above each plot, with $I = 1{\times}10^{18}$ Wcm^{-2}.

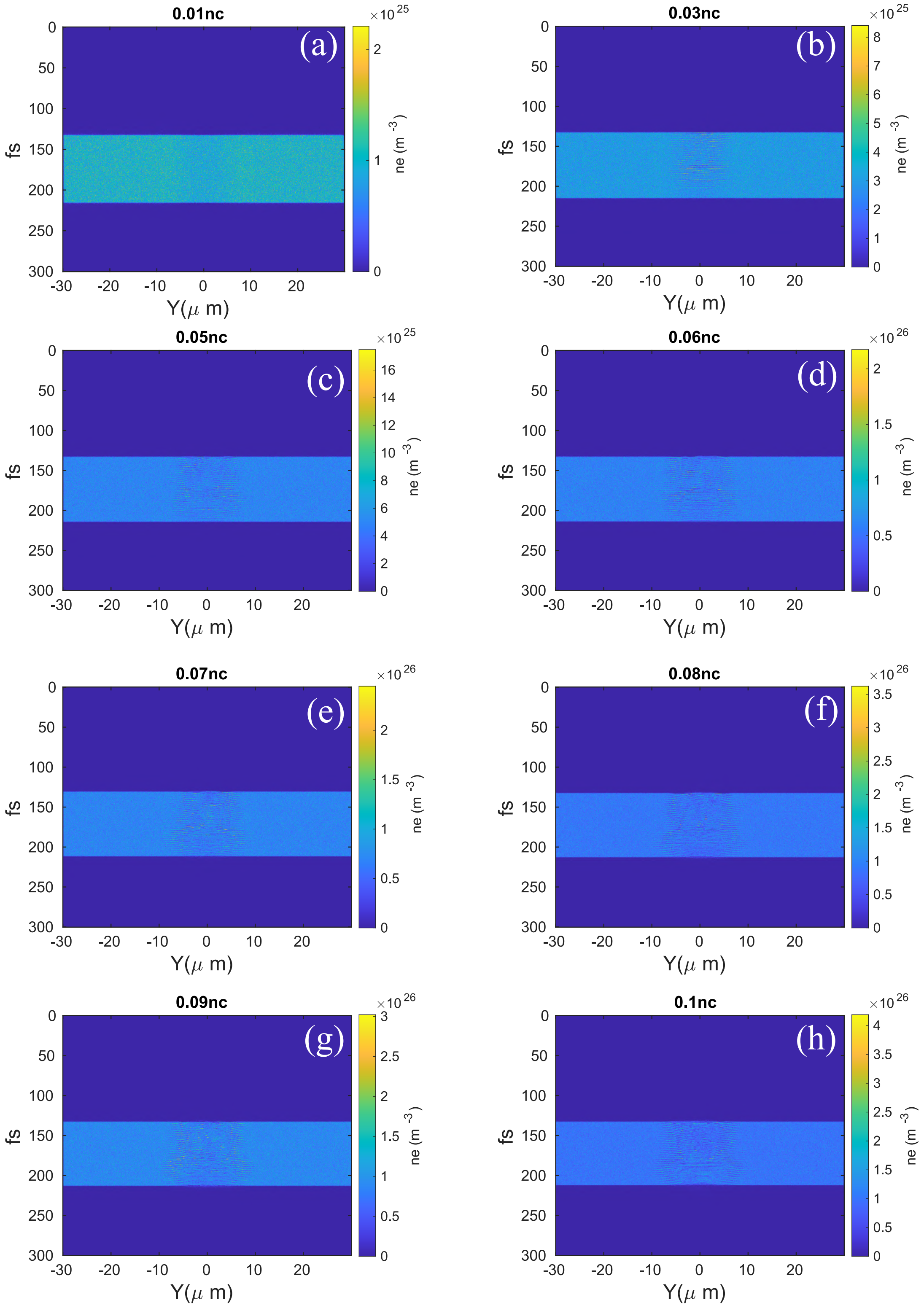

Figure 5.24: Plasma density profiles for each time step, in defocus beam with slab plasma at different densities stated above each plot, with $I = 1{\times}10^{18}$ Wcm^{-2}.

With lower intensity, the two fitting functions correctly model the transverse intensity profile for most of the density values, as can be seen in the figures 5.25(a-h). The effect of the filaments occurred much less and the curves approximately match each other even at the end of the propagation. At lower intensity, the beam radius appears unchanged at low densities as shown in figure 5.26 (a), while as soon as the plasma density becomes greater than 0.05n$_c$, the radius decreases until it reaches a minimum at higher density values. At 0.1n$_c$, differences in the measurements of the beam are again noted through the two fitting functions, although they are much smaller when compared to the case of higher intensities.

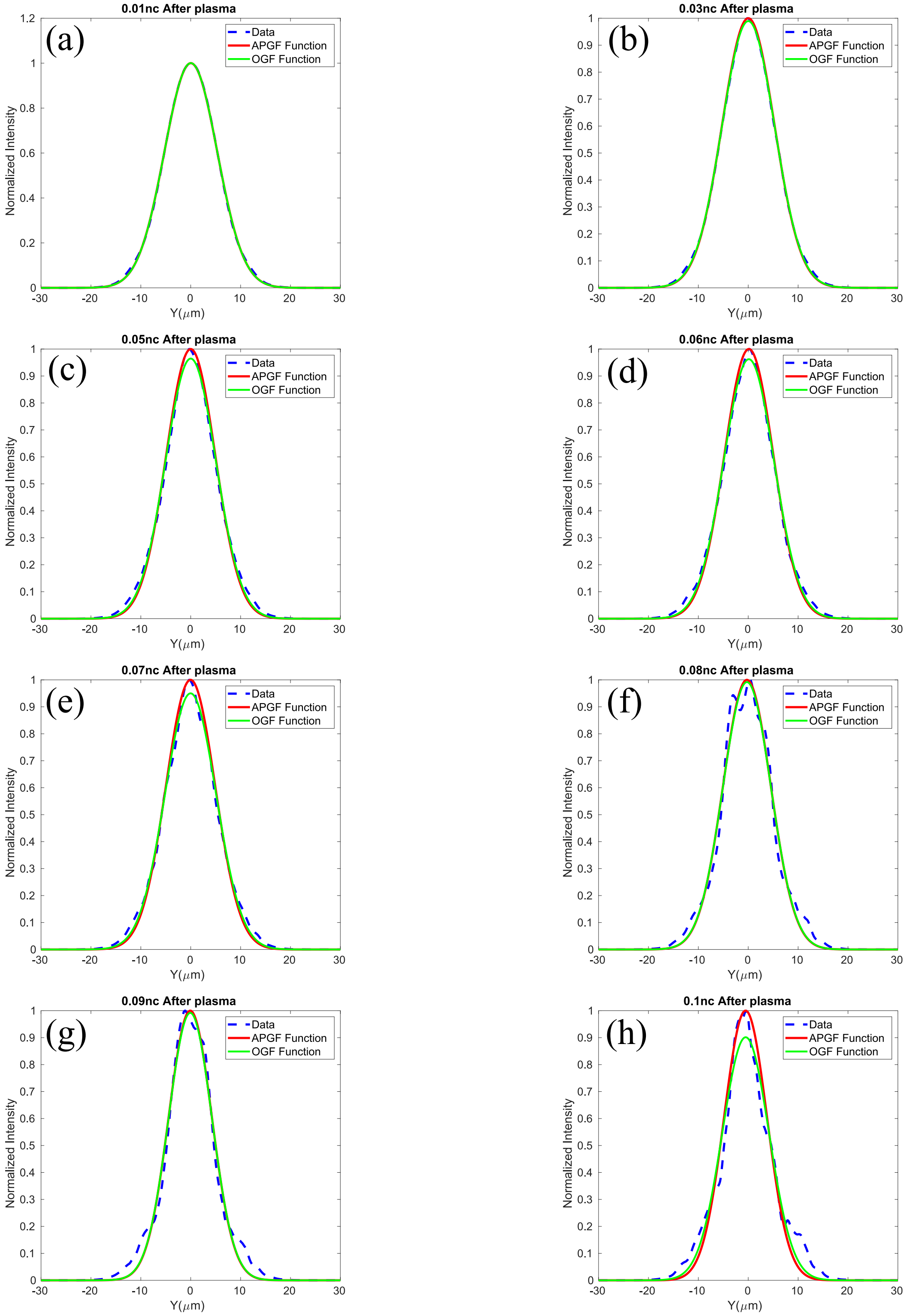

Figure 5.25: Comparing the fitting curves as the beam, with I = 1×10^{18} Wcm^{-2}, leaves the plasma for different plasma density stated above each plot: the dashed blue line represent the data, the solid red line is the APGF function and the green line is the OGF function.

In terms of angle there are no large differences as in the previous case with I

$= 1{\times}10^{19}$ Wcm^{-2}. Using both functions a positive convergence is obtained which grows as the plasma density increases, as shown in figure 5.26 (b). This would suggest that the laser is not intense enough to perturb the plasma in a way that causes a substantial density change such that it strongly focuses the laser pulse and exhibits pronounced divergence as in the previous case with $0.1n_c$. Instead, it presents a constant and continuous convergence even at the highest density value.

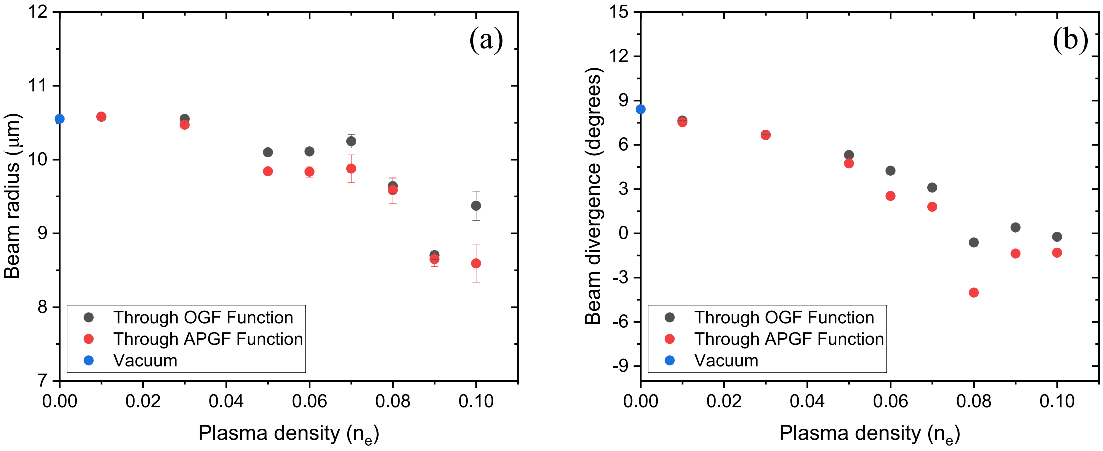

Figure 5.26: Beam radius (a) and divergence angle (b) as a function of plasma density, as determined using the two fitting curves with $I = 1{\times}10^{18}$ Wcm^{-2}.

These simulations were again repeated at an intensity I=10^{17} Wcm^{-2}, where we measured no difference in the propagation of the laser pulse at any plasma density. As figure 5.27 (a) shows, there was little variation in the beam radius and consequently the beam divergence through both the fitting functions as shown in figure 5.27 (b).

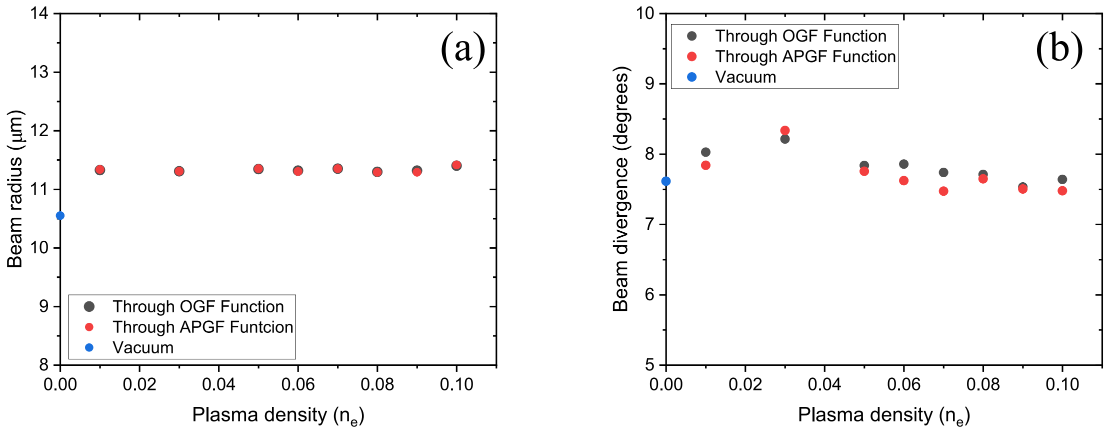

Figure 5.27: Beam radius (a) and divergence angle (b) as a function of plasma density, as determined using the two fitting curves with $I = 1{\times}10^{17}$ Wcm^{-2}

We have seen that in the regime of intense laser-plasma interactions when the plasma is transparent, the defocusing of the laser pulse can affect the variation of the beam radius and consequently the scaling of the beam divergence. This is sensitive to changes in plasma density, where collimation is obtained for high intensity values. The difference obtained is primarily due to the two different fitting functions used, mainly because we provided different initial values based on the specific data and the characteristics of the Gaussian curve we wanted to fit. With the OGF we automatically estimated the starting point coefficients for the fit via the predefined behavior of the function based on the data provided, thus measuring the overall transverse radius of the beam. By contrast, using the APGF the initial guesses in the fitting function were defined manually based on the understanding of the data, aming to identify the peak of a dataset and subsequently employing a Gaussian function to model the observed distribution around this peak. At higher density values, the choice of the fitting function becomes crucial and must align with the underlying model that best represents the data. Therefore, as we have seen the accuracy of these initial guesses have significant impact on the convergence and reliability of the fitting algorithm. Another distinction pertains to the varying intensity values of the laser pulse, where we have seen how for lower intensity values (10^{17} Wcm^{-2}) the laser pulse does not appear to undergo significant variations during propagation, since the laser is not intense enough to sufficiently perturb the plasma and induce a density change. Consequently, there is no refractive index variation leading to the absence of focusing effects.

All these simulations were performed with the focal spot diameter matched to the experimental measured focal spot size. As previously mentioned in chapter 3, the parabola used during the experiment enables a minimum spot size with F-number, F/1.6. In reality beam aberrations affecting the focal spot quality, modifying the divergence of the collimated beam need to be considered. This leads to a larger Gaussian intensity distribution close to 5 μm of FWHM, used in previous simulations. In the next section we will try to match experimental F-number, F/1.6, which corresponds to a smaller Gaussian intensity distribution, 1.26 μm (of FWHM).

5.5.6 Defocusing effect in transparency regime for a slab uniform plasma with smaller focal spot

In previous simulations, the ascertained focal spot size of the beam when it interacts with the plasma is ~ 9 μm. To maintain congruity with this focal spot size, we determined through the Gaussian beam equation the focal distance, which defines the variation of the radius that propagates in a vacuum, given its minimum value $r_{0,min}$, its wavelength λ and the Rayleigh distance $X_{0,min}$ (consistent with the definition provided in EPOCH). This is described in the following equation:

$$r(x) = r_{0,min}\sqrt{1 + \left(\frac{x}{X_{0,min}}\right)^2} \tag{5.10}$$

and rearranging the equation the defocus distance is reduced to $x_{foc} = 30$ μm from the front surface of the target. Therefore simulations were performed keeping the same laser and plasma parameters as before, but with the laser pulse focused 30 μm before the slab plasma and with $\phi_L = 1.26$ μm rather than 9 μm as before.

The results from these simulations showed edges of the preceding wavefront inside the plasma parallel to the main pulse, and as in the previous simulations with a bigger F-number, these appear in the vacuum case, where the beam wavefronts tend to curve as it propagates away from the best focus, and diverge over the remainder of the simulation. This behaviour is illustrated by the intensity beam profiles as a function of time, as depicted in figure 5.28, where at low densities, already from $0.3n_c$ filamentary structures begin to appear mainly in the main lobe of the pulse and become more pronounced towards higher density values, see figures 5.28 from (c) to (h). Note, these filaments also further perturb the plasma density, as depicted in figure 5.29. With smaller FWHM the Gaussian fitting functions agree with each other for very low density plasma, $0.01n_c$ and $0.03n_c$. As shown in figure 5.30 (a) and (b), as the plasma density increases the respective peaks of the Gaussian fitting functions differ slightly. As we have seen before, this difference primarily stems from the use of the two distinct fitting functions, with the OGF function that matches the overall beam whereas the APGF function fits the the peak filament, leading to a small difference in the size of the beam, which increases already from $0.05n_c$ case and then decreases as the plasma density increases at $0.08\mathrm{n}_c$. This behaviour is repeated again for higher density values, the variation of the radius increases to $0.09n_c$, there is a maximum difference of over 6 μm, and then reduces to the highest density value $0.1n_c$, as shown in figure 5.31 (a). These differences also show up clearly in terms of divergence, as shown in figure 5.31 (b), and as already stated, this discrepancy is due to the different fitting function used.

The results of these simulations show once again a convergence of the laser pulse with a larger angle than in the previous case, as we expected. Due to the smaller focal spot, the divergence is reduced in all cases of plasma density, some differences are obtained as the plasma becomes denser, but as stated this is due to the two fitting functions.

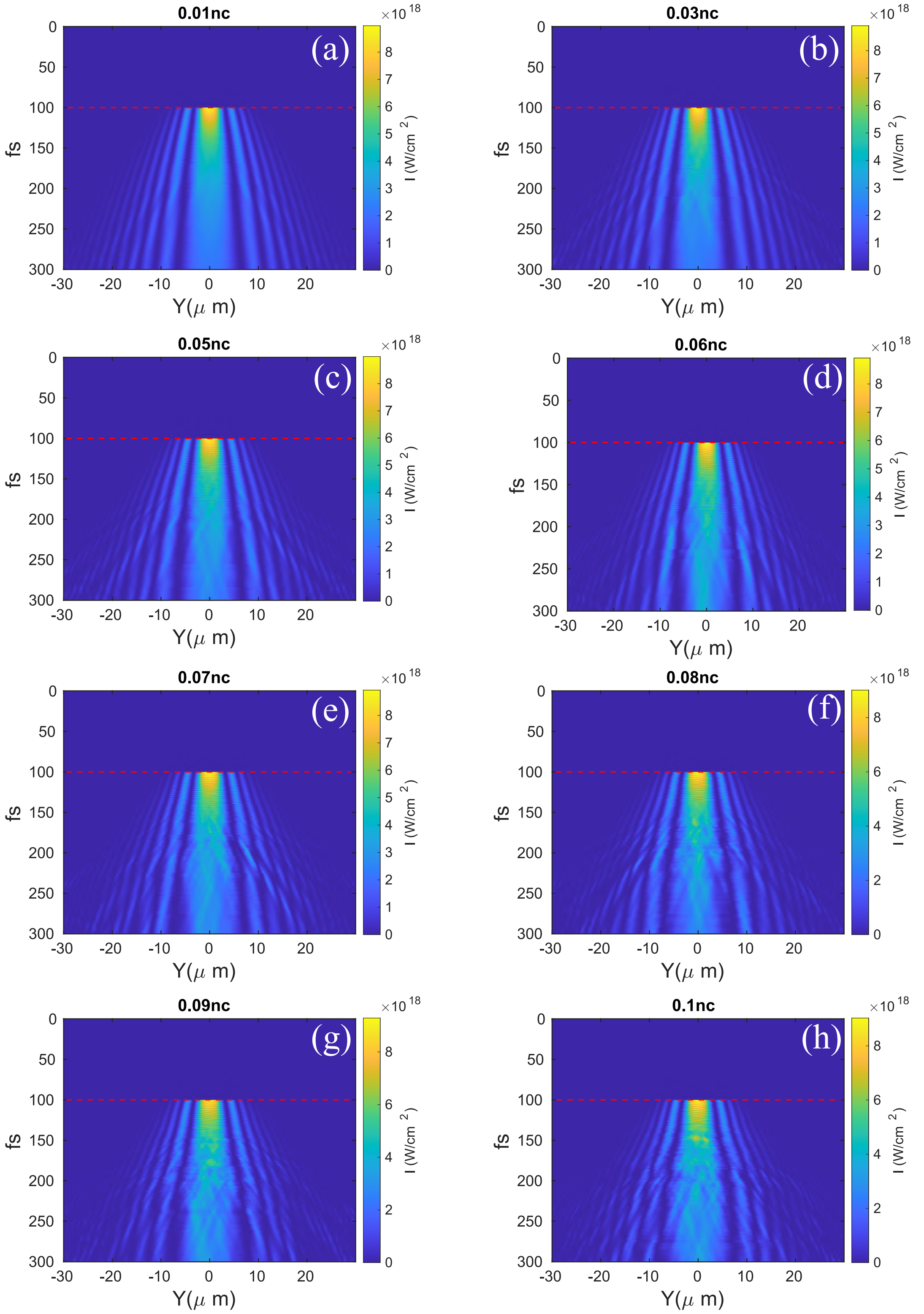

Figure 5.28: Evolution of the intensity profiles as a function of time, with the beam focused 30 μm before the front surface of the target, with $I = 1\times10^{19}$ Wcm^{-2} at the initial density shown above each plot.

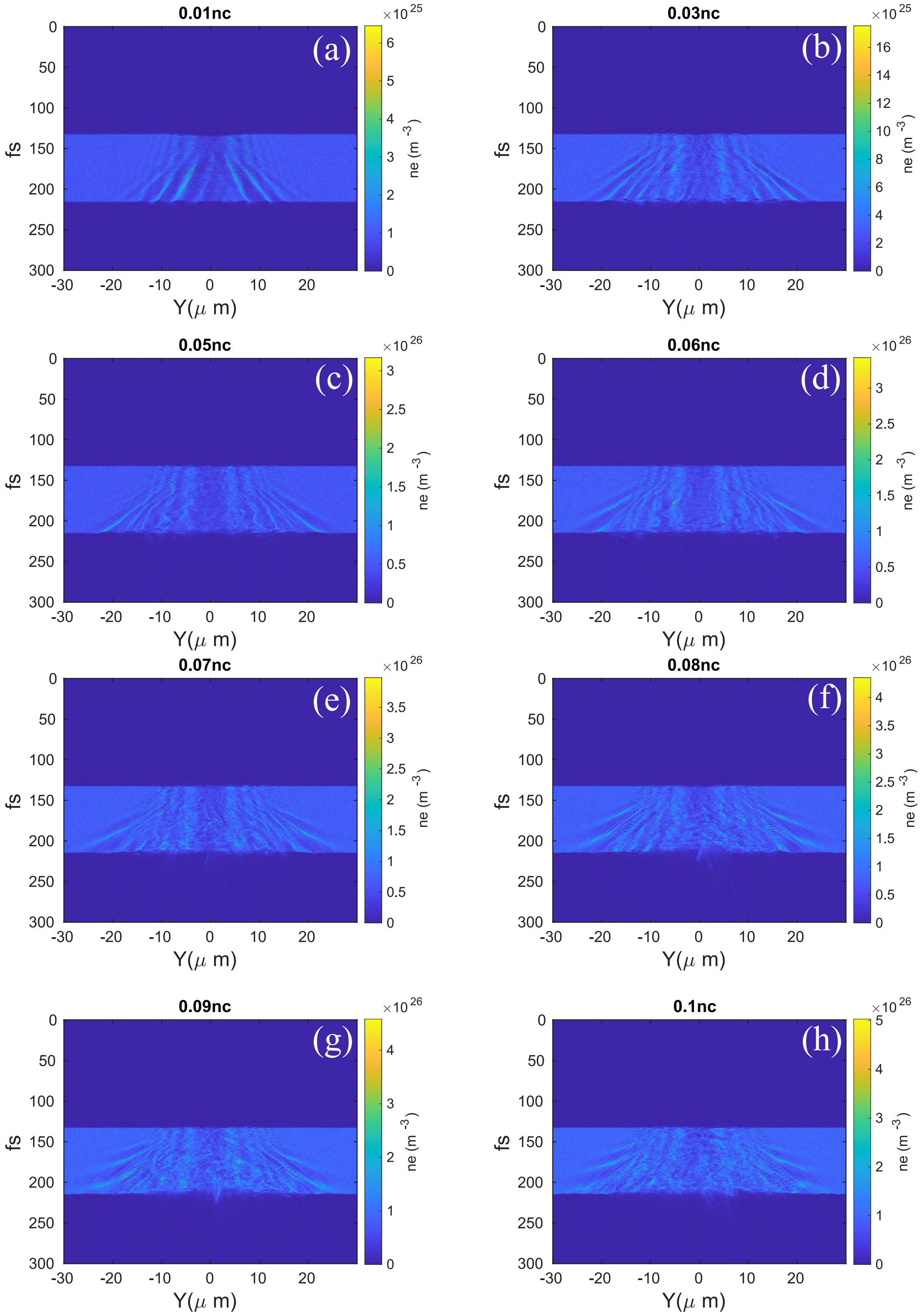

Figure 5.29: Evolution of density profiles as a function of time, with the beam focused 30 μm before the front surface of the target, with $I = 1{\times}10^{19}$ Wcm^{-2} at the initial density shown above each plot.

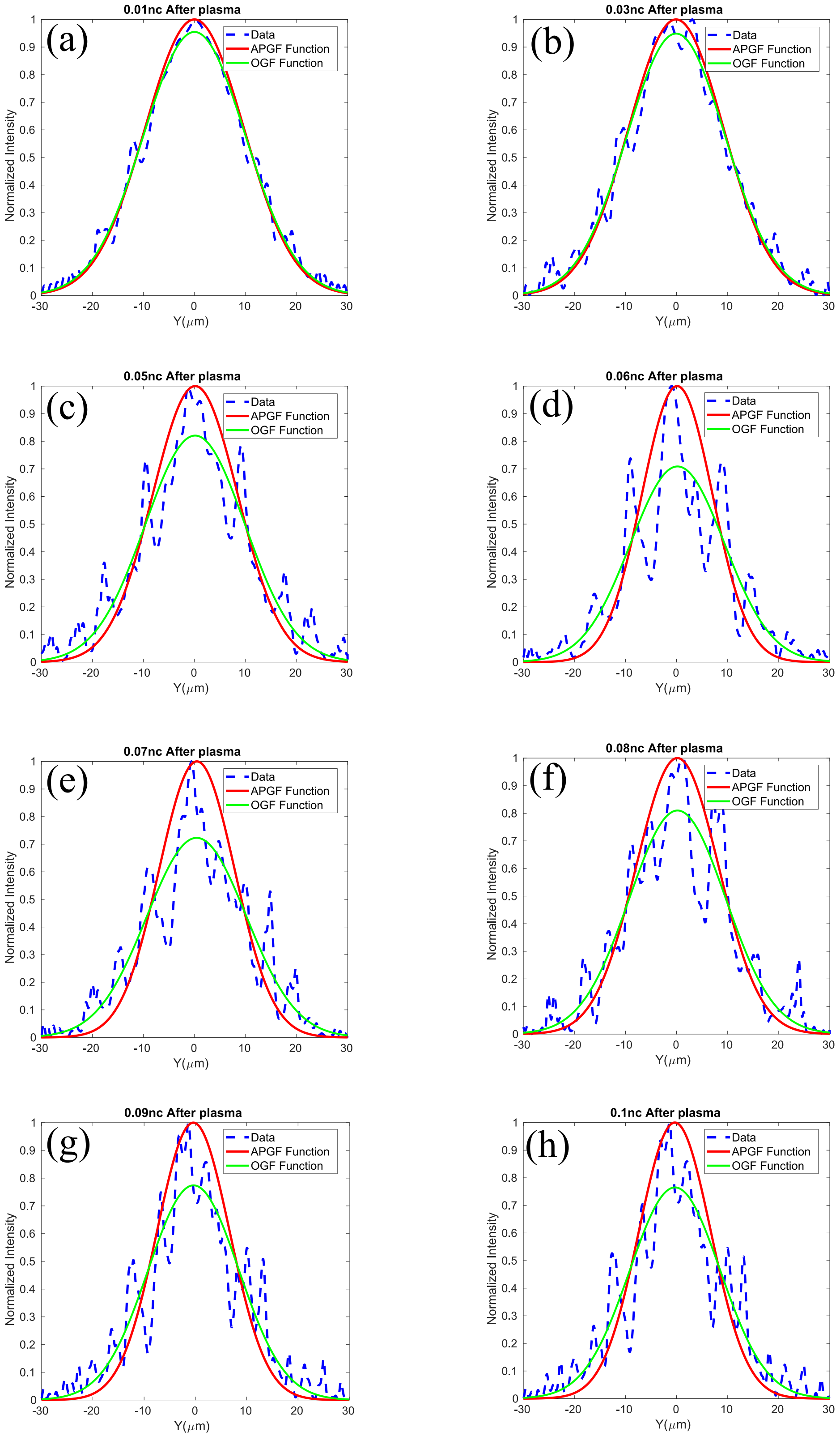

Figure 5.30: Comparing the fitting curves as the beam, with $I = 1\times10^{19}$ Wcm^{-2}, leaves the plasma for different initial plasma density, as shown above each plot: the dashed blue line represents the simulation results, the solid red line is the APGF function and the green line is the OGF function.

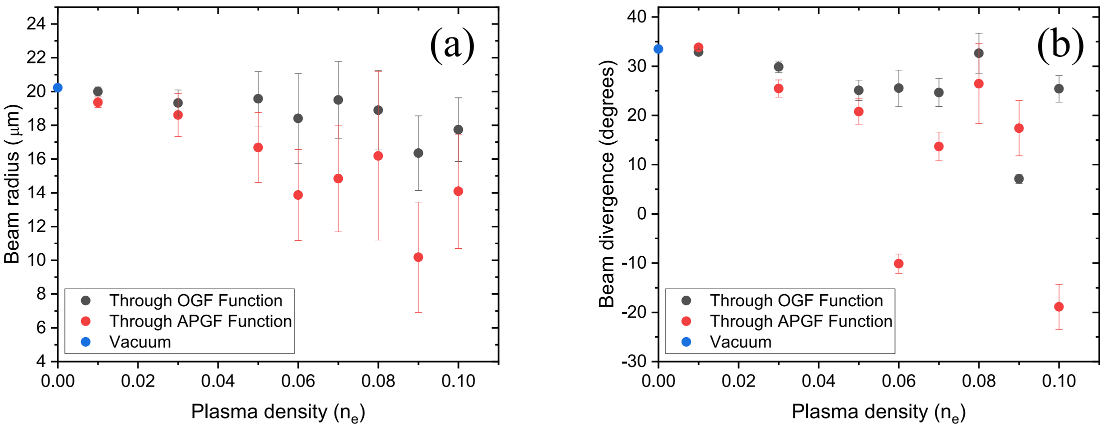

Figure 5.31: (a) Beam radius as the laser pulse leaves the plasma as a function of initial plasma density and (b) the divergence angle through the two fitting curves with $I = 1\times10^{19}$ Wcm^{-2} as a function of initial plasma density.

Given the difficulty in determining the outcome of the beam divergence during the interaction of the laser pulse with the plasma, different approaches were employed using the moving window method, as detailed in the following section.

5.5.7 Exploring defocusing in the regime for an expanded plasma scenario

The simulations in the previous sections showed reduced divergence for an initially defocused laser pulse interacting with an underdense plasma as it leaves the plasma. In order to explore this further, much larger simulations were required in order to verify if this behaviour was consistent at distances far from the plasma. The required larger simulations were achieved using the UK National Supercomputing service, ARCHER2, using a moving window scheme. A fixed empty box 144 μm × 180 μm was initialised with 14400 × 18000 computational mesh cells, inside which the laser pulse was injected and once centred in the box the window starts to move as the beam propagates for 2 ps. In this way, it was possible to conduct higher resolution simulations, with plasma density up to $0.3n_c$ and performed for longer distances.

In order to investigate higher intensities inside the plasma, the laser pulse with $I = 1\times10^{19}$ Wcm^{-2} and $\tau = 100$ fs, was focused 60 μm prior to a 30 μm thick uniform density plasma at densities varied from $0.01n_c$ to $0.3n_c$. A schematic of this method is illustrated in figure 5.32

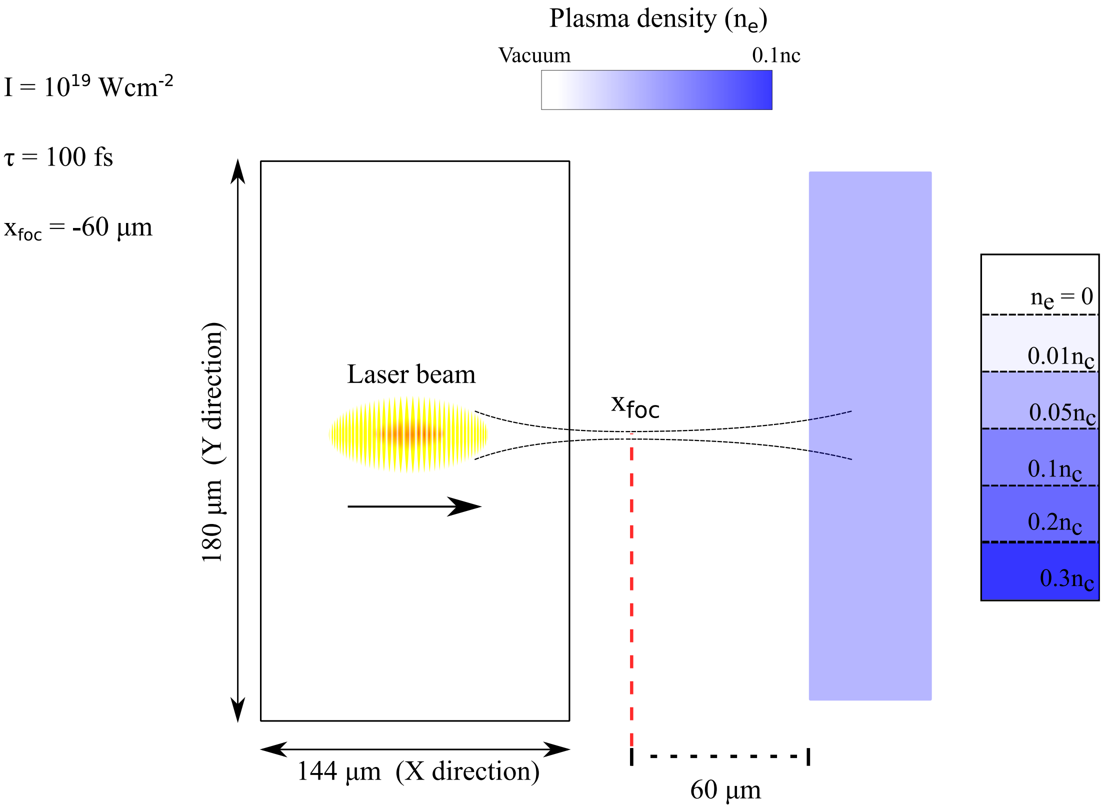

Figure 5.32: Schematic of a laser pulse focused 60 μm prior to a 30 μm thick uniform density plasma for various peak densities, from $0.01n_c$ to $0.3n_c$. The rectangular box is the moving window inside which the laser pulse is centred and moves as the beam propagates. In the example n_e was set to $0.02n_c$.

Figure 5.33 shows the 2D intensity time-space profiles for multiple initial peak where the intensity was determined by integrating along longitudinal dimension (X direction) to derive the transverse profile and normalised at each output time step of 50 fs. As can be seen for relatively low plasma densities, the propagating laser pulse shows a constant divergence that reduces with increasing initial peak plasma density. As the density is increased beyond $0.1n_c$, as shown in figure 5.33 (d), the laser pulse starts to show a formation of multiple filamentary structures, which diverge together with the overall profile of the laser pulse, with each filament becoming thinner for higher density values.

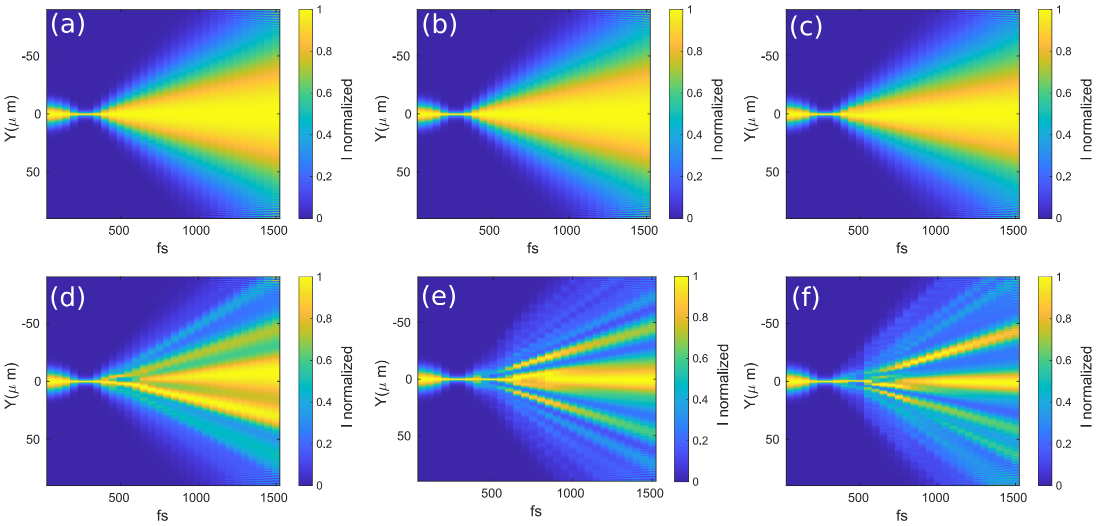

Figure 5.33: 2D intensity time-space plots for differential initial peak density. (a) vacuum ($0n_c$); (b) $0.01n_c$; (c) $0.05n_c$; (d) $0.1n_c$; (e) $0.2n_c$ and (f) $0.3n_c$

To measure the divergence angle the same curve fitting methods were used, and given the minimal disparities observed in the results between the two fitting functions employed, we opted to retain the APGF function for all ensuing simulations. For the higher density cases, there is a more prevalent filament formation which would alter the measurement of the beam width and so consequently the divergence angle. To counter this, a threshold to the intensity measurement was applied with lower intensity values below that threshold set to zero. A value of 50% of the peak intensity was chosen as the threshold for each simulation, because it was the minimum that allowed to calculate the correct dimension of the beam by adapting the Gaussian curve to the data of all the cases analysed.

As can be seen from figure 5.34, for the case of vacuum, the divergence angle values between the analytical and the Gaussian model agree each other, while as the initial peak density increases the beam collimates and the divergence angle becomes smaller, reaching a minimum at $0.2n_c$, to then grow back at higher densities. These results indicate that there is a narrow density range in which the divergence of the beam can be expected to be small enough to obtain a quite high collimation.

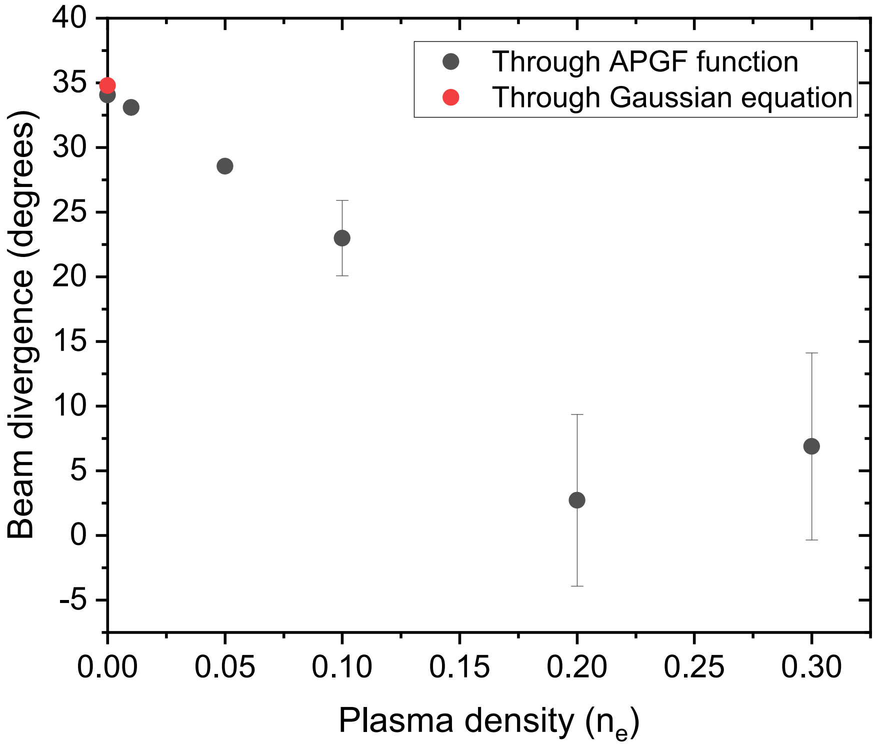

Figure 5.34: Divergence angle as a function of the initial peak plasma density. The results are compared with the vacuum case and the expected divergence from the Gaussian beam equation depicted by the red dot.

Further analysis was done on the propagation of the laser pulse for the initial peak plasma density for which the beam appears to have the minimum divergence ($0.2n_c$), by varying the initial focal position, x_{foc} from -60 μm to 30 μm. To begin, analysis was done on the interaction of the beam focused to the Gaussian plasma before the density peak, x_{foc} = -30 μm. Compared to the furthest case, x_{foc} = -60 μm, there is no generation of strong filaments, see the difference in figure 5.35 (a) and (b), and the intensity profile presents a constant trend in terms of divergence, showing a divergence angle much bigger than 20 degrees, as shown in figure 5.36. Subsequently we analysed the laser pulse variation focusing on the peak density, x_{foc} = 0 μm, and in this case, as can already be seen from the 2D time-space plots (figure 5.35 (c)), the intensity profile shows a smaller divergence with an angle of 15°, and slight appearance of filaments that diverge alongside the main pulse. While, employing a negative defocus, x_{foc} = 30 μm, the behaviour of the laser pulse shows a fork divergence, as shown in figure 5.35 (d), immediately after the focusing point the laser pulse is divided mainly into two strong filaments, one either size of the propagation axis. In 3D, this may approximate to a hollowed (or ring-like) beam.

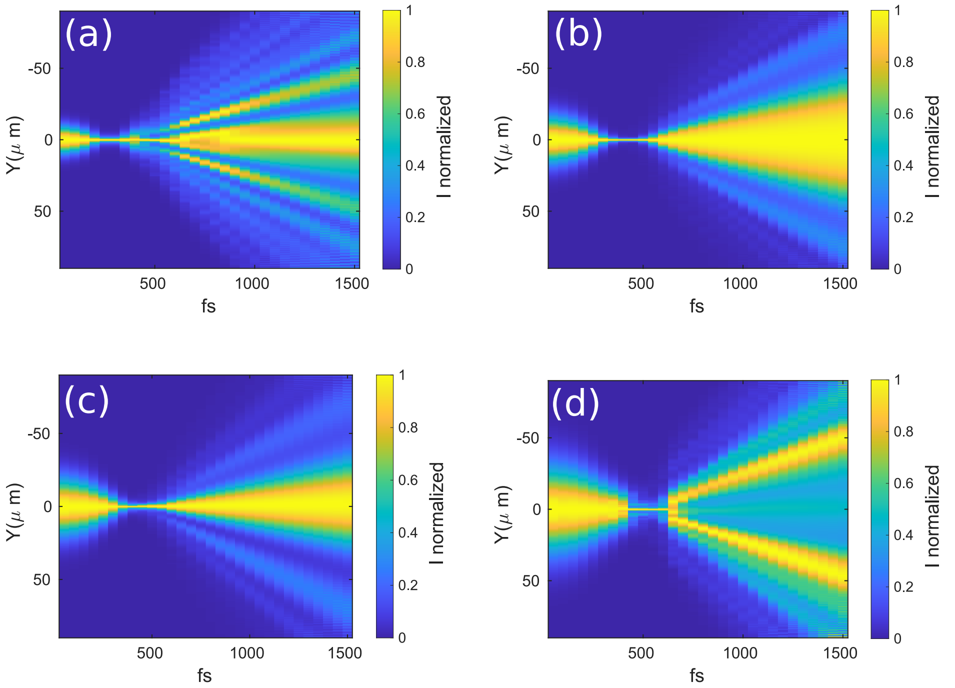

Figure 5.35: 2D intensity time-space plots at different focus distance, with $0.2n_c$ of initial peak plasma density. (a) x_{foc} = -60 μm, (b) x_{foc} = -30 μm, (c) x_{foc} = 0 μm and (d) x_{foc} = 30 μm.

This occurrence is likely attributed to the wavefronts of the beam that are moving faster where the edges of the laser pulse are curved so much that the beam self-focuses and produces a hollowed distribution downstream. In the 2D simulation results, the correspond two 'filaments' begin to diverge almost symmetrically, 8 and 11 degrees for the upper and lower filaments, respectively, as showed in figure 5.36.

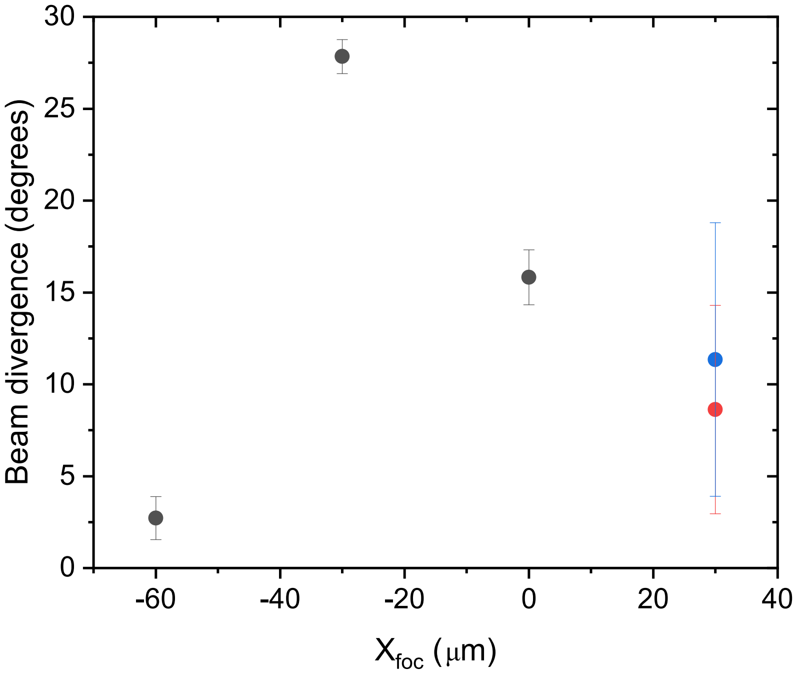

Figure 5.36: Divergence angle as a function of focus distance. The red and the blue points are the angles respectively for top and bottom filaments for the x_{foc} = 30 μm case, corresponding to negative defocus.

We extended our inquiry through additional simulations employing shorter laser pulse duration (τ = 40 fs) across a range of initial peak plasma densities from $0.1n_c$ to $0.3n_c$, maintaining a focal point at x_{foc} = -60 μm. A comparative analysis of intensity profiles between 100 fs and 40 fs revealed a distinct absence of filaments in the case of the shorter pulse duration, as depicted in figure 5.37 (a) to (c), where the laser pulse has less divergence as the initial peak plasma density increases.

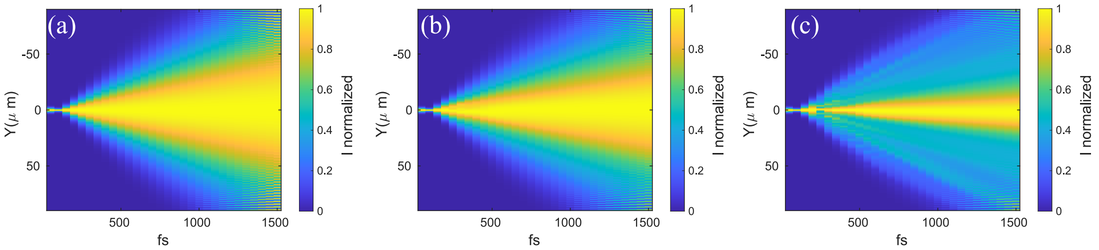

Figure 5.37: Laser pulse intensity as a function of time (with τ = 40 fs) in 2D intensity time-space plots at different initial peak plasma density. (a) vacuum case ($0n_c$); (b) $0.1n_c$; (c) $0.3n_c$

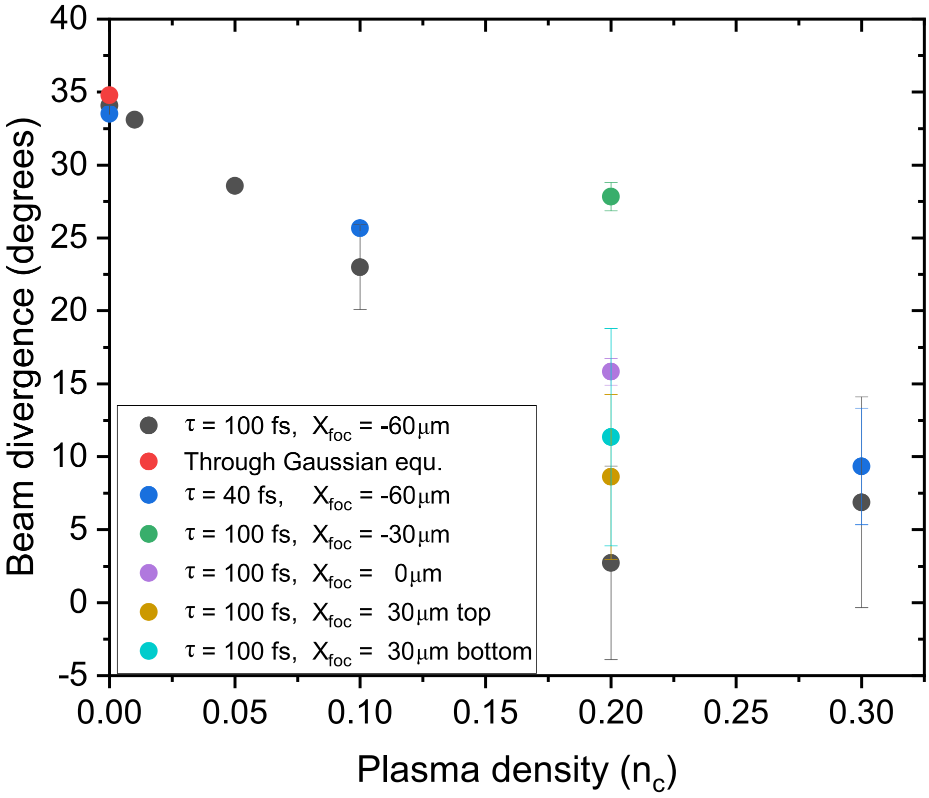

Figure 5.38: Divergence angle as a function of initial peak plasma density.

Comparing the results it is observed that the variation of the beam divergence appears to have the same trend for both the 40 fs and 100 fs laser pulse durations.

To investigate the interplay between an expanded plasma and the focal position of the laser pulse, simulations were performed varying the focal position and expansion profile for a longitudinally expanded plasma with a 1D Gaussian profile. The peak density was varied from $0.03n_c$ to $0.1n_c$ with a corresponding change to the expansion FWHM from 207 μm to 62 μm respectively, to maintain an areal density of the equivalent of a 10 nm solid density Al target. The laser pulse was defined with $I = 1{\times}10^{19}$ Wcm^{-2} and $\tau = 100$ fs, and focused at different positions, from x_{foc} = -50 μm to x_{foc} = 50 μm, measuring the beam size at $t_1 = 1000$ fs, and $t_2 = 1250$ fs which corresponds to 75 μm of propagation in vacuum. A schematic of this method is illustrated in figure 5.39.

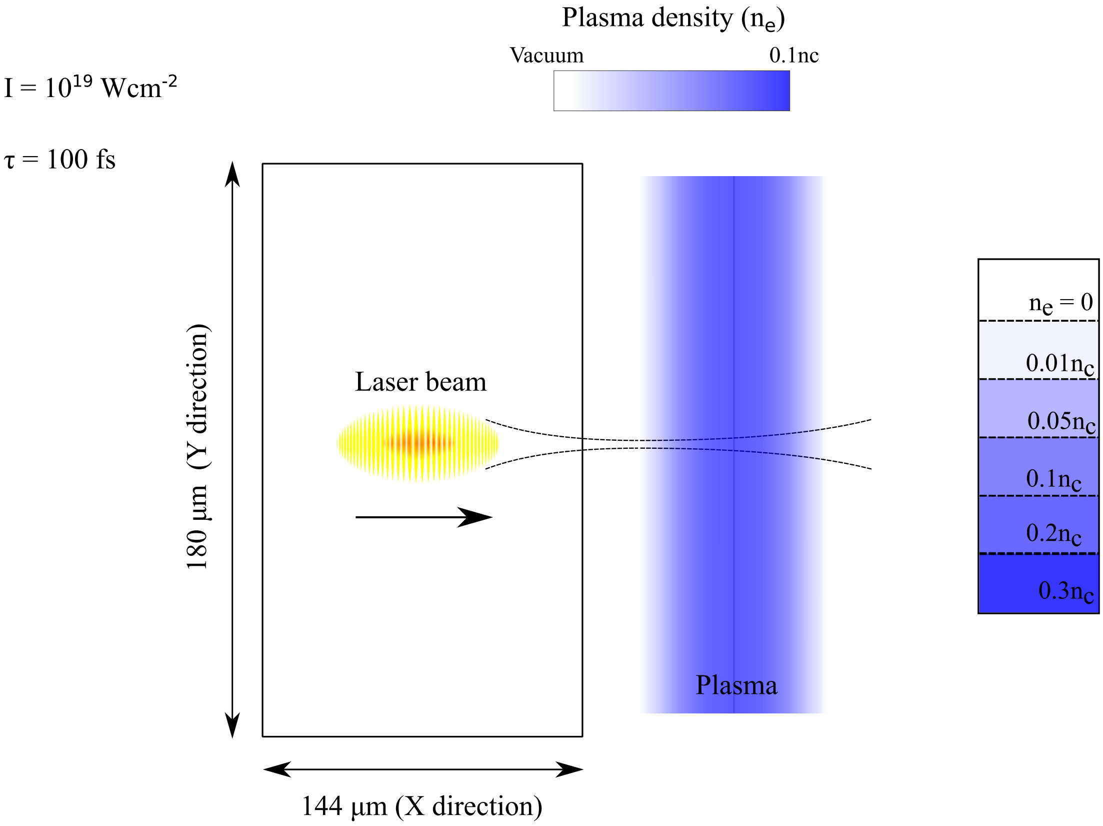

Figure 5.39: Schematic of a laser pulse focused 30 μm before the peak of the Gaussian density plasma for various peak densities, from $0.01 n_c$ to $0.3 n_c$. In the example n_e was set to $0.02 n_c$.

In measuring the divergence the beam size was determined by integrating across the transverse size for 152 μm (along y direction) in the box simulation since the reflection of the laser pulse would alter the measurements of the beam size, keeping the threshold set to 50% to the intensity profile as before. Figure 5.40 (a) illustrates the divergence angle variation, while (b) displays the transmitted energy variation of the laser pulse as a function of plasma density within the 0.03-0.1n_c range, each for different x_{foc}.

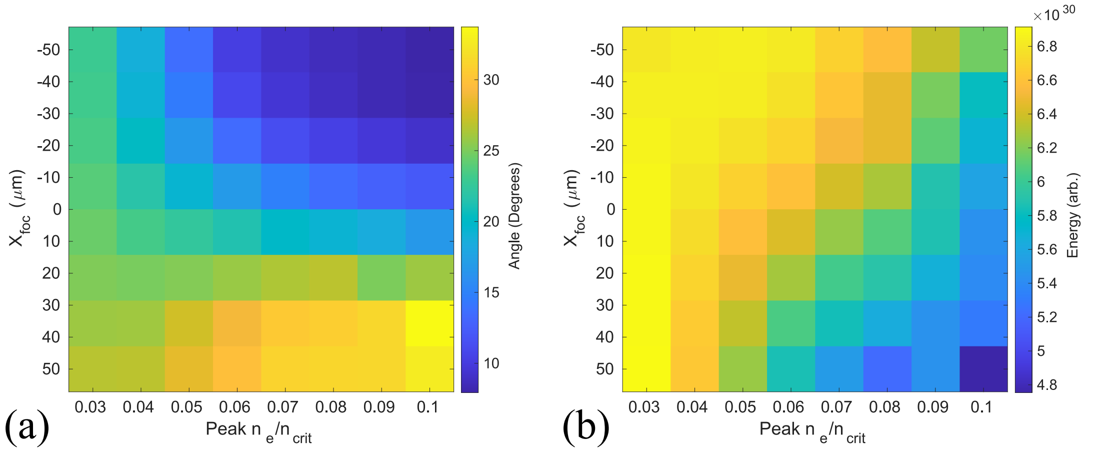

Figure 5.40: (a) Divergence angle and (b) transmitted energy as a function focal position x_{foc}, and initial peak plasma density

Examining figure 5.40 (a), it is noteworthy to observe that, at every plasma density value, the laser pulse exhibits a distinctive divergence pattern delineating two discernible regions of interest. When the laser pulse is focused before and close to the plasma, as the density of the plasma increases, the beam collimates resulting in a notable reduction in the divergence angle which is particularly pronounced at x_{foc} = -50 μm, where the divergence angle reaches a minimum of 8°. By contrast, when the laser pulse is focused beyond the plasma (towards x_{foc} = 50 μm) as the plasma density increases, the divergence undergoes a progressive increase, reaching a maximum of 27°. Furthermore, an intriguing observation arises regarding the change in divergence in response to plasma density variations. It becomes apparent that the divergence manifests a more rapid and pronounced variation under conditions of high initial peak plasma density when compared to the scenarios with the lowest plasma density.

Nevertheless, looking at figure 5.40 (b) as the laser pulse is focused near the plasma and close to x_{foc} = 50 μm the transmitted residual laser energy decreases due to increased absorption by the plasma and with increasing density this absorption effect is further accentuated, resulting in a progressive diminishment of the remaining (transmitted) laser energy. These results were compared with the vacuum case along with an increased simulation box size in the transverse direction (from 192 to 384 μm along y direction) for some select cases. This was to test if the beam was cropped due to the large divergence angles which could affect the energy measurements and potentially the beam divergence measurements.

Figure 5.41 (a), shows the angle variation as a function of focal position. There are no differences in the variation of divergence for larger transverse simulation size, with only a slight difference of about 2° observed for the highest plasma density in positive defocus case. However, there should theoretically be no energy change in the vacuum scenario, but as the figure 5.41 (b) shows, there is a noticeable change in the vacuum case. In plasma, the phenomenon of self-focusing redirects the laser pulse away from the simulation box edges, and indeed, there is a similarity in trends, unlike in vacuum, where the situation is notably different due to cropping effects. This means that when the laser pulse is focused earlier, the beam diverges sufficiently that some of the laser pulse is lost out of the simulation boundary which results in erroneous absorption results. The simulations were repeated for $0.05n_c$ and $0.1n_c$ at the same defocus distances, and both of them present a drop in energy as the laser pulse is focused after the plasma. In terms of divergence, (see figure 5.41 (a)), there is minimal impact in both cases with plasma and vacuum, except for instances of extreme defocusing in the vacuum scenario (x_{foc} = -50 μm) where the divergence is typically largest.

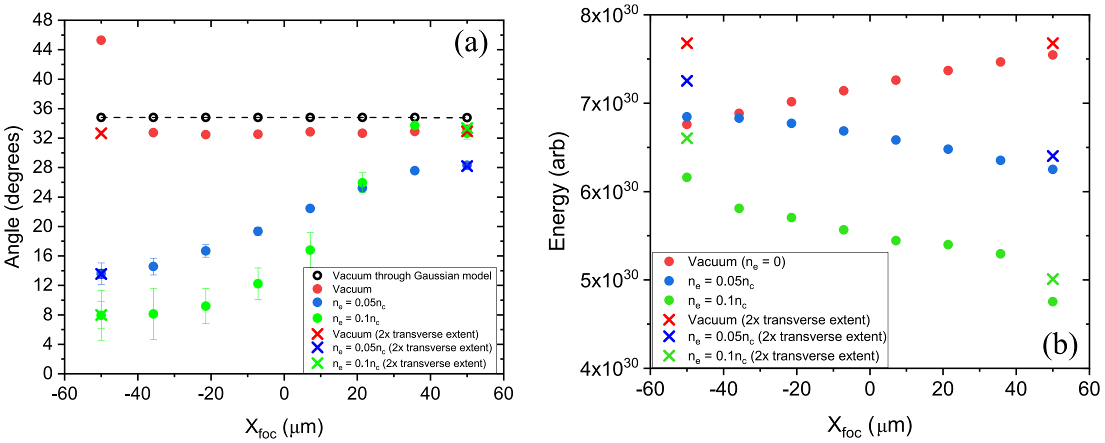

Figure 5.41: Comparing (a) divergence angle and (b) the transmitted energy variation of the laser pulse as a function of focal position x_{foc}, in vacuum, at $0.05n_c$ and $0.1n_c$. The cross symbols represent the simulation with longer box size in y direction

To further understand the plasma dynamics and the associated affect on the laser pulse for specific cases from the moving window simulations, it is necessary to first examine the spatial profile of the electron density and laser pulse as it propagates at various points in time, shown in figure 5.42. In the optimal scenario with the lowest divergence, x_{foc} = -50 μm at $0.1n_c$, a noticeable depletion of the electron density close to the focal position can be observed in figure 5.42 (b).

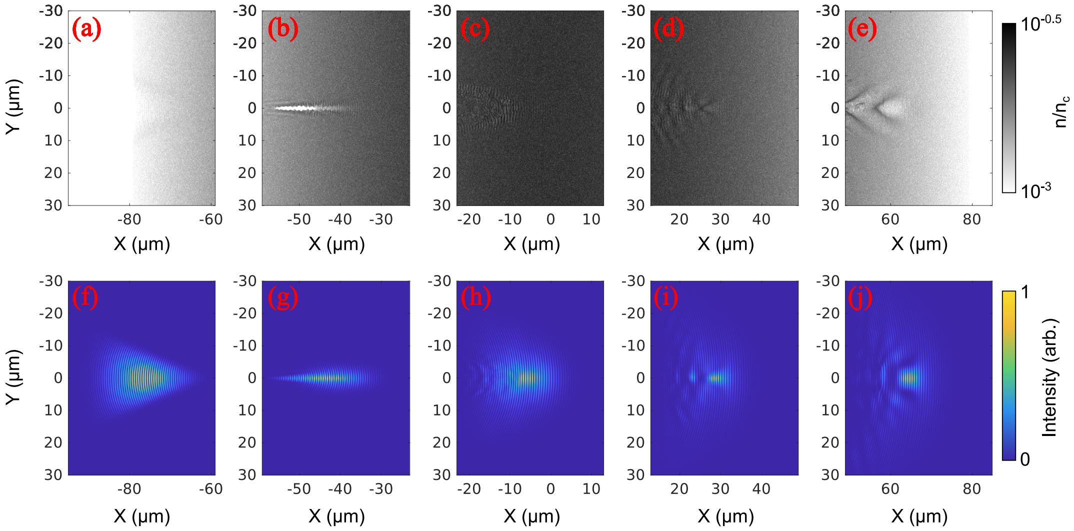

Figure 5.42: Temporal evolution for 5 time steps of plasma density and laser intensity for initial peak density of $0.1n_c$ and x_{foc} = -50 μm.

As the intense laser pulse propagates into the plasma, illustrated in the figures 5.42 (c), (d) and (e), instead of the continued formation of a well-defined channel, there is a perturbation of the plasma by the laser pulse, which actually generates in its wake a plasma wave, consequently influencing the spatial profile of the laser pulse, as shown in figures 5.42 (h), (i), and (j), resulting in a laser pulse characterised by a prominent central filament and lobes at the sides, consistent with observations from previous simulations. This plasma channelling effect resembles similarities with the laser-driven wakefield phenomenon [119] but operates under different conditions characterised by higher plasma densities and shorter interaction distances, typically occurring over tens of microns. In contrast, laser-driven wakefields extend much further, often spanning distances measured in millimetres and for significantly lower peak plasma densities.

When focusing the laser pulse nearer to the peak plasma density, $x_{foc} = 7$ μm, observations from figures 5.43 (a) and (b) show that the density of the plasma remains relatively unperturbed during the propagation of the laser pulse up until the point of focus, as illustrated in figure 5.43 (c). Note that self-focusing effects results in a shift in the focal position to $\sim$ -5 μm.

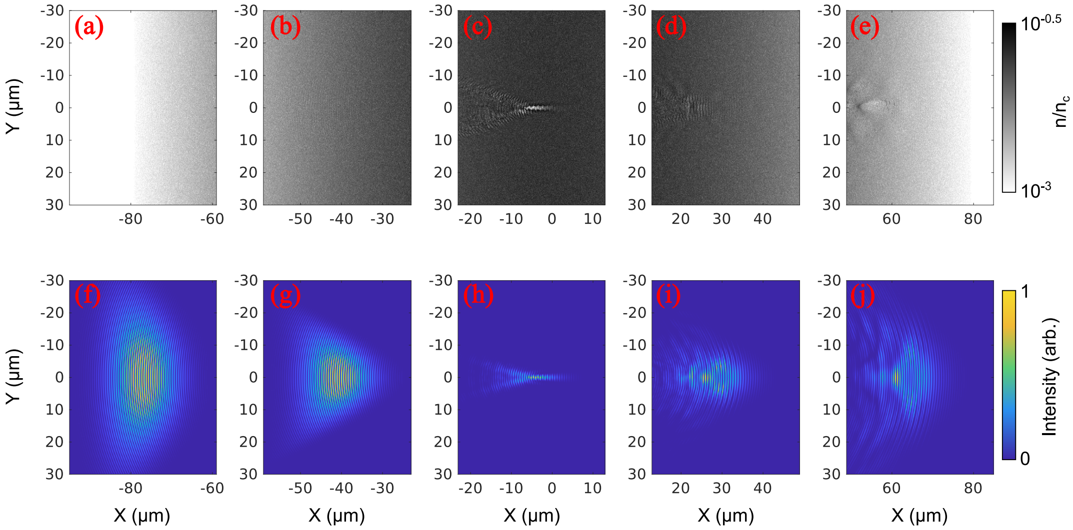

Figure 5.43: Temporal evolution for 5 time steps of plasma density and laser intensity for initial peak density of $0.1n_c$ and $x_{foc} = 7$ μm.

Subsequently, there is a delayed and less pronounced formation of a wake structure compared to previous instance (x_{foc} = -50 μm) with effects observed primarily at the rear of the laser pulse, as shown in figure 5.43 (j).

Finally, when focusing the laser pulse beyond the peak plasma density, $x_{foc} = 50$ μm, similar to the previous scenario ($x_{foc} = 7$ μm), there is minimal perturbation observed in the plasma, as shown in figures 5.44 from (a) to (c), until the laser pulse reaches the focal position, which again is shifted due to self-focusing effects to X $\approx$ 30 μm, as illustrated in figure 5.44 (d).

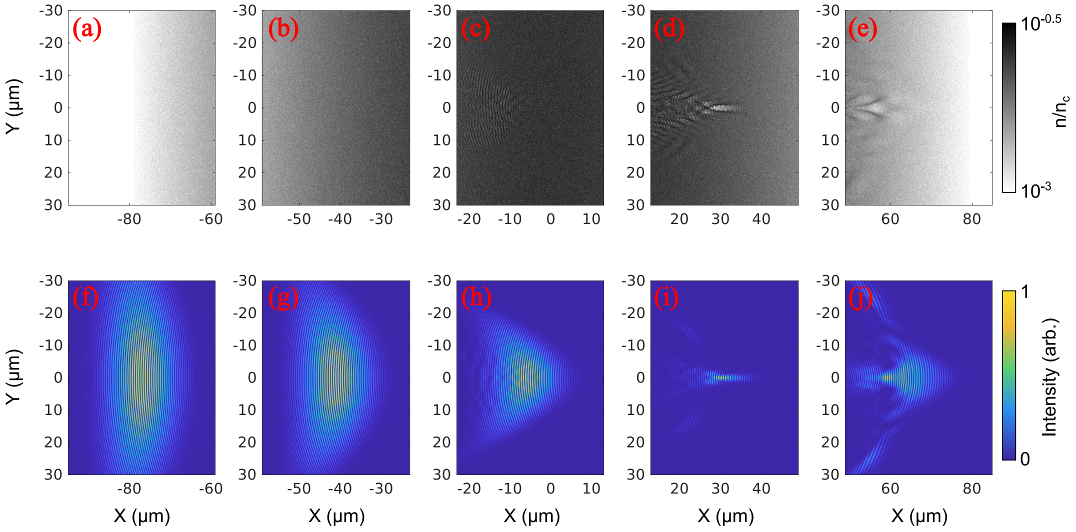

Figure 5.44: Temporal evolution for 5 time steps of plasma density and laser intensity for initial peak density of $0.1n_c$ and x_{foc} = 50 μm.

Once again, a structural evolution is evident in the laser pulse, exerting influence primarily further towards the rear of the pulse, as shown in figure 5.44 (j), similar to the previous instance.

At the end of the simulation, we can see in figure 5.45 a comprehensive depiction revealing the intricate spatial profile of the laser pulse within the simulated 2D space domain far from the plasma. As illustrated in figure 5.45 (a-d) for increasing peak plasma density for x_{foc} = -50 μm, a well-defined Gaussian profile is discernible at the low plasma density of $0.03n_c$. This profile undergoes a transformation as the plasma density increases, resulting in the emergence of a spatially modulated laser pulse. However, for a fixed peak density of 0.1 n_c and varying x_{foc}, as depicted in the figure 5.45 (e-h), when the laser pulse is focused near and beyond the peak plasma density, the modulations tend to appear closer to the rear of the laser pulse longitudinal profile.

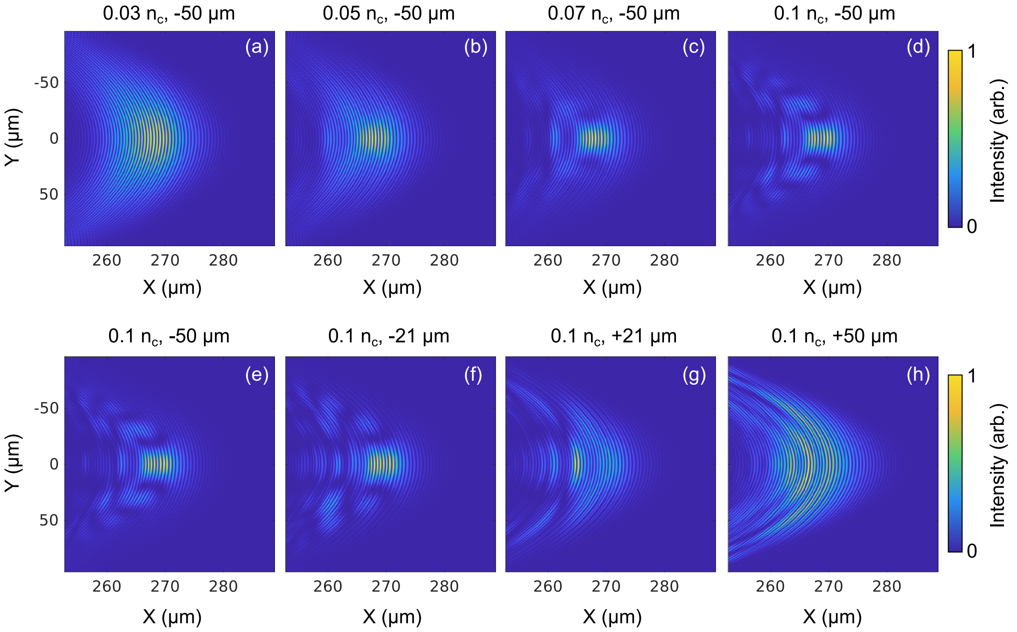

Figure 5.45: 2D intensity profile, varying the peak plasma density with x_{foc} = -50 μm: (a) 0.03n_c; (b) 0.05n_c; (c) 0.07n_c; (d) 0.1n_c (Top row). Bottom row: Same for fixed initial plasma density equal to 0.1n_c, for: (e) x_{foc} = -50 μm; (f) x_{foc} = -21 μm; (g) x_{foc} = 21 μm; (h) x_{foc} = 50 μm;

Examining the transverse intensity profiles of the laser pulse, determined at the final time step of the simulation for x_{foc} = -50 μm, the effect of the plasma on the laser pulse can be observed in figure 5.46 (a). For lower peak plasma densities, the transverse intensity profile exhibits a typical Gaussian profile. However, as the initial peak plasma density increases, a distinct central lobe forms at the centre in addition to emerging side lobes, whilst still maintaining an overall Gaussian profile. This may be indicative of interference induced by the localised modulation of the laser wavefronts as they pass through the formed plasma modulations, observed in figure 5.42.

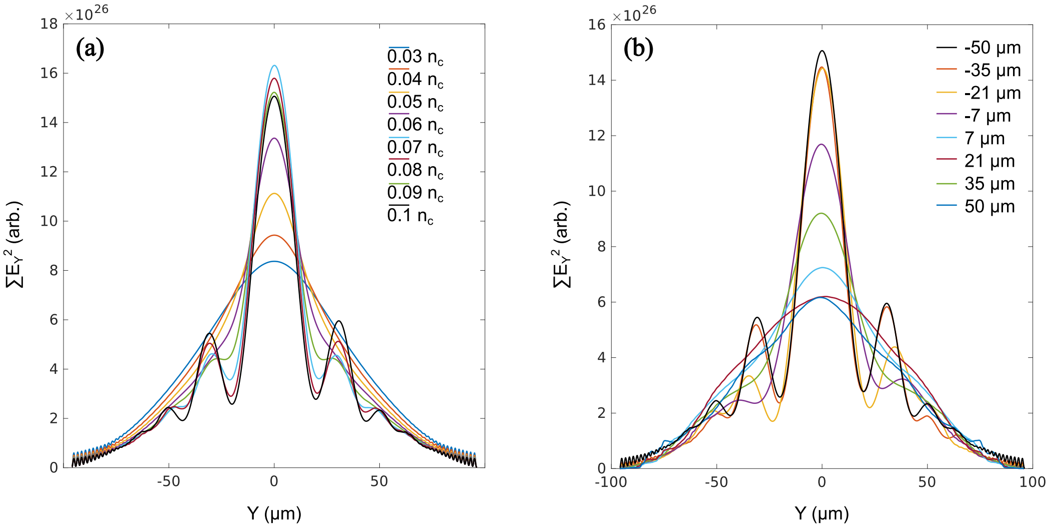

Figure 5.46: (a) Transverse laser pulse profiles, with x_{foc} = -50 μm for varying peak plasma density at X = 250 μm. (b) Transverse laser pulse profiles with $0.1n_c$ for varying focal position at X = 250 μm.

At a peak plasma density of $0.1n_c$, variations in the transverse spatial profile of the laser intensity becomes evident across different focal positions, as illustrated in figure 5.46 (b). As the focal point approaches the peak plasma density, there is a discernible transition back towards a more Gaussian distribution in the transverse spatial profile. This trend persists even as the laser pulse is focused beyond the peak plasma density however, perturbations in the transverse profile can still be observed. This may be due to the spatial modulations occurring towards the rear of the longitudinal profile of the pulse, as shown in figure 5.44, resulting in less of an effect on the overall transverse intensity profile.

To further investigate this, it is possible to examine the temporal profile of the central feature by plotting the longitudinal profile along the laser axis, as illustrated in figure 5.47 for changes in peak plasma density and focal position. Figure 5.47 (a) displays the temporal profiles of the laser pulse, at x_{foc} = -50 μm for the lowest, $0.03n_c$, and the highest peak plasma density, $0.1n_c$, along the laser axis. An increase in peak intensity and a slight reduction in the duration of the laser pulse can be observed at the higher peak density with increased temporal modulations towards the rear of the pulse. For low plasma density, $0.03n_c$, the temporal profile exhibits an approximately Gaussian shape similar to an unperturbed pulse.

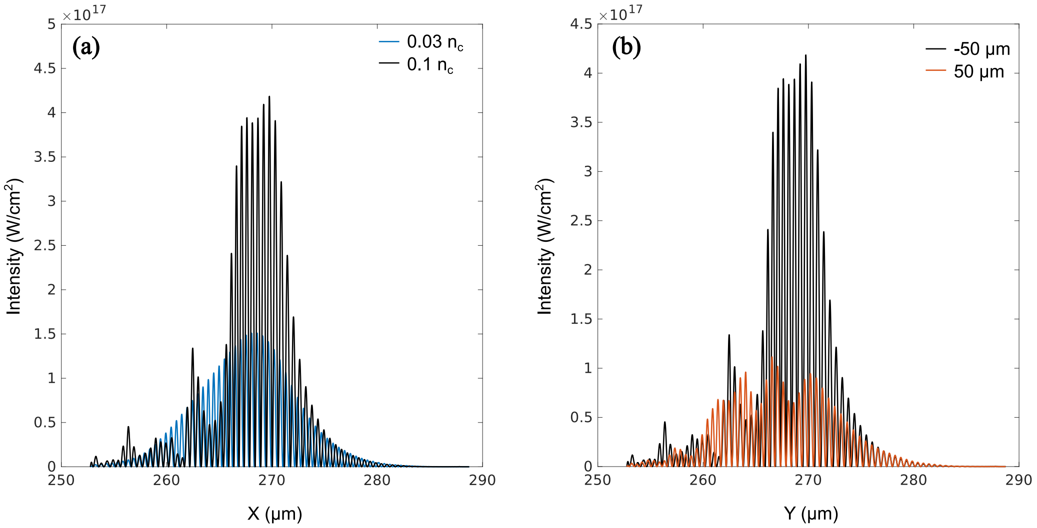

Figure 5.47: (a) Longitudinal laser pulse profile along laser axis, Y = 0, at x_{foc} = -50 μm varying peak plasma density at X = 250 μm. (b) Longitudinal laser pulse profile along laser axis, Y = 0, at $0.1n_c$ for varying focal position at X = 250 μm.

Similar phenomena is observed when changing the focal position, as shown in the figure 5.47 (b) at a constant peak plasma density, $0.1n_c$ from x_{foc} = -50 μm to x_{foc} = 50 μm. When the laser pulse is significantly focused after the peak plasma density, x_{foc} = 50 μm, the temporal profile displays follows a Gaussian profile up to the peak intensity before exhibiting sharp spikes or irregularities but still with an overall Gaussian profile.

Due to the variation in temporal profiles observed, it is useful to also investigate the spectral properties of laser pulse, as illustrated in Figure 5.48 (a), for varying peak densities for a fixed x_{foc} = -50 μm. These spectral profiles were measured utilising the spatial Fourier transform of the laser pulse electric field along the laser propagation axis, integrated across Y and normalised to the laser wavenumber. It can be observed that as the plasma density increases, there is a noticeable broadening of the spectrum signal at the laser wavenumber likely attributed to the shorter duration of the pulse. However, the strength of the spectral signals for the other harmonics of the laser light reduce with increasing peak density whilst maintaining their width. Comparable spectra are depicted in figure 5.48 (b), illustrating the laser spectra profiles for various focal positions for a fixed peak plasma density of $0.1n_c$. As the laser pulse focal position is moved through the plasma, the spectrum signal at the laser wavenumber remains broad, however the harmonic signals also begin to increase and broaden.

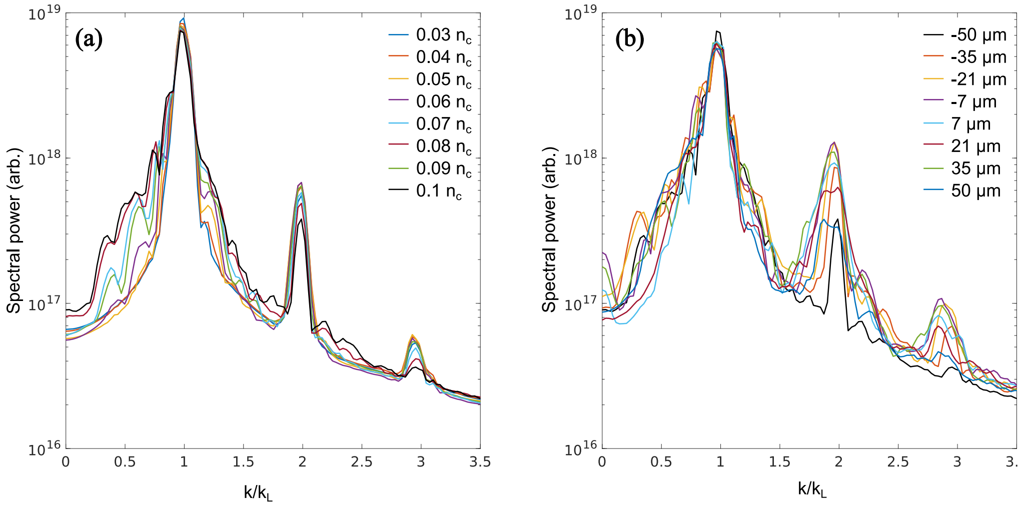

Figure 5.48: (a) Integrated laser pulse spectrum along laser axis, Y = 0, at x_{foc} = -50 μm for varying peak plasma density at X = 250 μm. (b) Integrated laser pulse spectrum along laser axis, Y = 0, at $0.1n_c$ for varying focal position at X = 250 μm.

The results indicate a subtle interplay of factors influencing the divergence, the spatial and temporal profile and laser energy absorption in the context of laser propagation through expanded ultrathin targets, highlighting the importance of initial focal position. Moreover, the influence of the degree of plasma expansion and resultant peak electron density on these phenomena adds an additional layer of complexity. Specifically, we can discern two distinct regions: when the laser pulse is focused before the plasma and when the pulse is focused after the plasma. When the focus is before the plasma, there is a notable reduction in divergence as the peak plasma density increases, and thus expansion decreases. This may be due to the fact that focusing the laser pulse earlier results in an early density depletion close to the focal position, influencing the expansion of the pulse resulting in modulations in the plasma to produce variation in the laser wavefronts that yields a strong central filament and sidelobes. The higher peak plasma density is likely required to produce perturbations with a localised density that will have an appreciable change in refractive index across the wavefronts. This, in turn, produces a laser pulse characterised by reduced divergence of the central lobe, as we have seen in the previous simulations, which could explain the reduced laser size measured on the transmission screen during the experiment (as detailed in the previous chapter). Conversely, focusing the laser pulse after the centre of the expanded plasma yields a more substantial increase in divergence, akin to its behaviour in a vacuum. The 2D intensity profile at the end of the moving window simulation showed that the front of the pulse behaves similar to that of a typical expanding Gaussian beam, however plasma modulations do still appear to affect the rear of the pulse. Spectral analysis demonstrated a broadening of the laser wavenumber with increased density and focal position, as well as influencing the spectral characteristics of the generated harmonics. For the case of the focusing before the centre of the plasma, temporal analysis of the laser pulse, indicates a potential shortening of the laser pulse duration with rising plasma density whilst this effect is lessened when focal position is after the centre of the plasma. Therefore, the precise location of the focal point introduces significant variations in divergence and laser energy absorption along with changes to the temporal and spectral properties for targets expanded into the underdense regime.

5.5.8 Conclusions

In conclusion, in the relativistically underdense plasma regime, it was found that the two most important factors that influence the behaviour of the propagating laser pulse are the focal position of the pulse and the expansion and peak density of the plasma. Starting with a 1D analytical model to identify key parameters for self-focusing in the regime where the relativistic self-focusing depends on the plasma density and the power of the laser, we advanced our study through PIC simulations with increasing complexity by investigating the underlying physics and developing different analysis methods. To begin, the influence of underdense to near-critical density plasma on the laser pulse propagation was considered. Both the ponderomotive expulsion and relativistic self-focusing becomes significantly stronger at higher densities leading to plasma depletion and thus a reduction in plasma frequency along the propagation axis. Notably, the laser pulse exhibits a discernible self-focusing phenomenon, with the degree of self-focusing intensifying for higher plasma densities. Examining a more realistic scenario with Gaussian plasma density profile, the laser pulse still exhibits pronounced self-focusing as it progresses toward the initial focal point, with filaments starting to form due to diffraction. While in simulations where the laser pulse is focused before a plasma of uniform density, it was observed that the beam radius increases near the peak plasma density. In this scenario, the plasma acting as a lens, causes the pulse to refocus and results in a reduction in pulse radius during propagation. As a result, the laser pulse appears highly collimated towards the end of the propagation. This convergence continues at higher density values, leading to strong self-focusing and notable divergence, where the interaction causes the laser beam to break into numerous filaments, a phenomenon accentuated with higher plasma density, significantly influencing the overall behaviour of the laser pulse propagation. The outcomes with a smaller focal spot reaffirm the convergence of the laser pulse at a larger angle compared to the previous case. As anticipated, the divergence is reduced in all cases of plasma density.

Performing the moving window simulations for longer distance propagation through a target expanded to various peak densities, the findings indicate that there exists a nuanced interplay of factors governing the divergence and absorption of laser energy within the complex plasma dynamics. The critical role of focal position is emphasised, with a distinction between negative and positive defocus yielding notable differences in divergence, absorption, temporal profile and spectral properties. The results underscore that the focal position and significant target expansion before the arrival the main pulse could lead to significant reduction in divergence angle such as to explain the smaller beam size measured on the transmission screen that compromised the functioning of the integrating sphere used to measure the absorbed energy in RSIT regime. Such expansion of the target may arise through significant pre-pulses or changes to the temporal intensity contrast. This nuanced understanding is crucial for investigations in such scenarios, requiring careful measurement of target expansion prior to the main pulse along with any variation in the focal position. It may also be possible to utilise these findings to deliberately tune the laser properties by inducing the expansion and setting an appropriate focal position. The resultant pulse could then be further applied to other applications.

Chapter 6

Conclusions & future work

The research presented in this thesis focuses on experimental and numerical investigations exploring the interplay between high-intensity laser pulses (exceeding 10^{19} Wcm^{-2}) and ultra-thin foils at micro and nanoscales thicknesses, particularly focusing on the RSIT regime. This was achieved firstly through diagnostic techniques to characterise the degree of laser energy coupling to overdense and relativistically transparent plasmas. Specifically, an integrating sphere and diffuse scatter screens were employed to evaluate the energy components of laser light not absorbed in the target plasma. In addition, PIC simulations have played an important role in this investigation providing complementary insights into the intricate processes occurring during the interaction, revealing a complex interplay between the variation of laser focal position and target expansion that influences the divergence and residual absorption of laser energy in plasma dynamics. This final chapter provides a summary of the key findings and conclusions of these studies, while also discussing possible future research directions.

6.1 Effect of RSIT on laser absorption in ultra-intense laser-solid interactions

In chapter 4 an experimental investigation to examine the use of diagnostics such as an integrating sphere and scatter screen, to diagnose the effect of RSIT on absorption of the laser energy into the plasma is presented. Specifically, the results of the experimental investigation into the total absorbed laser energy are initially delineated for relatively thick (micron-scale) targets, remaining opaque throughout the interaction. Subsequently, the focus shifts to relatively thinner (nanometer-scale) targets experiencing RSIT during the interaction. In good agreement with previous experiments presented in Refs. [37, 108, 109], the findings indicate that for thick targets that remain opaque during the interaction the absorption scales with higher intensities (by varying the input laser energy) giving confidence in the diagnostic approach used. In the next stage, for the investigations relating to the transparency regime, by using ultra-thin nm-scale foils, the total laser energy absorption was calculated by additionally considering the transmitted laser component using a scatter screen to measure this. Comparing the total absorption measurements with the experimental and simulation results presented in Ref. [113], differences in the absorption scaling with target thickness were observed. In contrast to the results reported by Williamson *et al.* [113], where a decrease in absorption is expected for ultrathin targets due to the early onset of transparency, our present results show a less pronounced decrease. To address this inconsistency, a comparison was conducted between the energy values measured both from the sphere and on the transmission screen for same target thicknesses, revealing a discrepancy in the measurement for the thinnest targets. The energy detected by the sphere appeared to be lower than the energy on the transmission screen, which cannot be the case because the energy within the sphere is the sum of scattered and transmitted energy. Exploring several potential sources of this disparity, and analysing the spatial dimensions of the transmitted laser pulse it was found that the divergence of the laser pulse after focus is altered as it propagates through the relativistically transparent plasma, becoming more collimated. Consequently, an increase in intensity led to the breakdown of the diffuse scattering coating on the integrating sphere, rendering it incapable of accurately diagnosing the contained energy. Considering the unmeasured energy, better agreement was observed with the outcomes presented in Ref. [113], highlighting a decreasing in absorption as the targets become very thin.

In spite of the challenges faced, particularly evident in situations involving ultra-thin targets, the utilisation of the integrating sphere, coupled with other diagnostic tools such as the diffuse scatter screens, enabled the successful attainment of accurate measurements of laser energy absorption. These results carry significant implications for the essential comprehension of the RSIT regime with the approach to experiments involving lasers and overdense plasma. Numerous aspects of the interaction between lasers and solid-density plasma remain incompletely understood, particularly concerning the applications discussed in Chapter 1, such as in the mechanisms by which ions are accelerated from solid targets. Additionally, these results are important for fields reliant on diagnostic tools to guarantee accuracy and standardisation in optical and lighting applications. The challenges posed by ultra-thin targets and the need for precise measurements of laser energy absorption underscore the critical role played by integrating spheres in ensuring accuracy and standardisation. As we explore the intricate complexities of laser-plasma interactions, these diagnostic tools prove indispensable, not only for providing reliable measurements but also for facilitating advancements in scientific research, industrial applications, and broader research endeavours. Moving forward, continuous improvements in integrating sphere technology, coupled with advancements in design, materials, and methodologies, promise to further enhance their capabilities and contribute significantly to the evolving of laser-plasma interaction studies.

As a further development of this work, a major advancement should be enhancing better diagnostics such as for the integrating sphere optimising its design involving the size and geometry. The increased dimensions would make the integrating sphere more adaptable to various laser systems with different power levels and beam characteristics maximising light collection efficiency and making it a versatile tool for laser-plasma research. If enlarging the size poses challenges due to potential complexities in the setup such as spatial limitations based constraints imposed by specific experimental requirements, an alternative could be consider an aperture to manage and allowed the incident laser light to be transmitted without damaging the internal surfaces. Another way to enhance the integrating sphere, is to add a tube to the sphere on the surface, in the direction of the transmitted light, that the intense transmitted light could propagate through for a larger distance before interaction with the walls without damaging the sphere. This approach would help to manage high collimation and transmission while avoiding the need to add an additional aperture, as too many in the sphere could compromise its function as an integrating sphere. Additionally, a real-time monitoring features within the sphere may be another valuable enhancement. This would allow for immediate feedback on the laser-plasma interaction, facilitating adjustments and optimisations as needed. Exploring these alternative approaches would improve the accuracy in the absorbed energy measurements especially in a regime where there is a high degree of transparency.

6.2 Ultrathin targets to control the divergence of High-Power laser pulse in underdense plasma

Expanding upon the investigation presented in chapter 4, a numerical investigation into the role that laser and plasma parameters play in laser propagation behaviour during a laser-ultra thin target interaction is presented in chapter 5. In the transition to the RSIT regime, the plasma electron density evolves in response to the propagating laser pulse, creating a dynamic spatial-intensity profile of the plasma refractive index. The expulsion of electrons reduces the plasma density, creating a spatial variation in the refractive index that increases along the laser axis and decreases radially. Thus the plasma acting as a positive lens focuses the laser pulse as it propagates through relativistically transparent plasma resulting in a variation of the pulse divergence. To comprehend and analyse this process, along with its effects on dynamics in a laser-solid interaction experiencing relativistic transparency, several PIC simulations with varying analysis methods were conducted.

The PIC simulation results demonstrate that the primary factors influencing the beam behaviour are the focal position (in longitudinal direction) of the pulse and the expansion of the plasma. Exploring the impact of underdense to near-critical density plasma on beam propagation, the ponderomotive expulsion and relativistic self-focusing were found to strengthen at higher densities. This variation leads to changes in refractive index, which in turn influence the propagation of the laser pulse through the plasma. Particularly, self-focusing of the laser pulse intensified with higher plasma densities, accompanied by the formation of filaments due to diffraction with a Gaussian plasma density profile. Simulations with a laser pulse focused before the plasma (diverging onto the target) revealed that the beam radius continued to increase up to the centre of the plasma, where the plasma then acted as a lens, causing pulse refocusing and a reduction in pulse radius during the continued propagation. This results in a highly collimated laser pulse outside the plasma, with stronger self-focusing and significant divergence at higher density values. Higher plasma density causes the laser beam to break into numerous filaments, significantly impacting overall beam behaviour. Extending simulations for longer distances (in longitudinal direction) using a moving simulation window for various degrees of expansion of an ultrathin 10 nm Al target revealed a nuanced interplay of factors governing divergence and absorption of laser energy within the dynamic plasma. The divergence of the laser pulse exhibits a complicated response, dependent on specific circumstances of plasma expansion and focal position. After significant propagation into vacuum after the interaction with the plasma, it was possible to observe the intricate spatial profile of the laser pulse within the simulated 2D space. A clearly defined Gaussian profile is evident at the low plasma densities similar to that of a pulse propagating in vacuum. This particular profile undergoes a noticeable change as the plasma density increases, giving rise to a shorter modulated laser pulse with a noticeable central peak and the appearance of side lobes. As the laser pulse focal position is moved forwards and beyond the peak plasma density, it progressively becomes less complex on the laser pulse rising edge with the central peak and sidelobes reducing and the overall spatial profile gradually returning to a Gaussian distribution. There is still evidence of modulation at the rear of the pulse but this has reduced impact on the overall spatial distribution. This characteristic aligns with the temporal profile, wherein the temporal features exhibit an approximate

Gaussian distribution at lower densities and indicate a degree of compression at higher densities resulting in the emergence of modulations in the trailing edge of the pulse. Similar behaviour occurs on the trailing edge when the focal point nears the peak plasma density and extends beyond but the rising edge and peak of the pulse is relatively unperturbed, similar to the low density cases. Moreover, distinctions in spectral characteristics corresponding to varying densities are revealed, showing a noticeable broadening of the spectrum signal at the fundamental laser wavenumber with increased plasma density. This broadening also occurs when the laser pulse is focused near and beyond the plasma. There is also evidence of spectral broadening of the generated harmonics with changes to the focal position that may warrant further investigation in future work.

These findings provide valuable insights into how to keep a high-energy laser beam collimated over a long distance after passing through dense plasma and represent a important new understanding in the realm of laser-plasma interactions. Control of the plasma profile and laser focal position may aide in tuning the beam divergence and spatial profile along with the temporal and spectral properties. It is also important to mitigate energy loss during beam propagation which is affected by the peak plasma density, in order to optimise the efficiency and efficacy of these interactions.

This topic may be considered in future research, as it promises to advance high-energy physics through direct laser acceleration (DLA). This could lead to an improvement in both the maximum energy achieved and the number of escaping electrons, particularly in thin targets that undergo RSIT. Therefore, in order to control the process to generate the desired beam qualities, an effective strategy could be to extend the simulations to longer distances and times to capture the nuanced interplay of factors governing the divergence and absorption of the laser energy. This can reveal potential stability issues that may not be evident in shorter simulations reflecting experimental scenarios. Furthermore, increasing the spatial and temporal resolution of the simulations would allow for a more detailed representation of the evolution of plasma dynamics, in particular during the intricate processes of self-focusing and filament formation.

Additionally, moving from 2D to three-dimensional (3D) interaction simulations could advance our understanding of the complex physical phenomena, such as enhanced spatial accuracy, better representation of temporal evolution, the ability to study interactions with complex geometries and a more detailed exploration of angular dependencies. This evolution would allow for a more realistic representation of real-world scenarios, crucial for optimising experimental setups and gaining deeper insights into a broad spectrum of applications. As a result of these factors however, simulating laser-plasma interactions in 3D would involve a trade-off between accuracy and computational cost where high-performance computing resources with sufficient spatial and temporal resolutions are required. Despite these challenges, the advantages of 3D simulations could prove invaluable in gaining a deeper understanding of these complex laser-plasma interaction phenomena.

6.3 Concluding remarks

The research presented in this thesis contributes to our comprehension of the fundamental physics governing ultra-intense laser-solid interactions, particularly in the relativistic transparency regime. The realm of intense laser-solid interaction studies has undergone substantial maturation in recent years, driven by the anticipation of envisioned applications. This anticipation has, in turn, stimulated numerous investigations aimed at understanding the intricate dependencies and controllability inherent in these interactions. The motivations driving these studies are multifaceted, encompassing both a desire to unlock the scientific principles at play and to explore potential practical uses of laser-solid interactions. As we have seen, the results reported in this thesis contribute to our understanding of the fundamental physics in ultra-high-intensity laser-solid interactions and also have implications for future applications. The trade-off highlighted in this study underscores the importance of meticulous experimental design to balance the benefits of reduced divergence with the potential challenges posed to measurement instruments. The evolving landscape of this field continues to inspire rigorous exploration and experimentation, driven by the prospect of advancements that could have transformative implications across various scientific and cutting-edge domains.

Bibliography

[1] T. H. Maiman. Stimulated Optical Radiation in Ruby. *Nature*, 187(4736):493–494, 1960.

[2] F. J. McClung and R. W. Hellwarth. Giant Optical Pulsations from Ruby. *Journal of Applied Physics*, 33(3):828–829, 2004.

[3] L. E. Hargrove, R. L. Fork, and M. A. Pollack. Locking of He-Ne Laser Modes Induced by Synchronous Intracavity Modulation. *Applied Physics Letters*, 5(1):4–5, 2004.

[4] D. Strickland and G. Mourou. Compression of amplified chirped optical pulses. *Optics Communications*, 56(3):219–221, 1985.

[5] K. Weichman, A. P. L. Robinson, M. Murakami, and A. V. Arefiev. Strong surface magnetic field generation in relativistic short pulse laserâplasma interaction with an applied seed magnetic field. *New Journal of Physics*, 22(11):113009, 2020.

[6] J. Colgan, J. Abdallah, A. Ya. Faenov, S. A. Pikuz, E. Wagenaars, N. Booth, O. Culfa, R. J. Dance, R. G. Evans, R. J. Gray, T. Kaempfer, K. L. Lancaster, P. McKenna, A. L. Rossall, I. Yu. Skobelev, K. S. Schulze, I. Uschmann, A. G. Zhidkov, and N. C. Woolsey. Exotic dense-matter states pumped by a relativistic laser plasma in the radiation-dominated regime. *Physics Review Letters*, 110:125001, 2013.

[7] P. A. Norreys, M. Santala, E. Clark, M. Zepf, I. Watts, F. N. Beg, K. Krushelnick, M. Tatarakis, A. E. Dangor, X. Fang, P. Graham, T. McCanny, R. P. Singhal, K. W. D. Ledingham, A. Creswell, D. C. W. Sander-

son, J. Magill, A. Machacek, J. S. Wark, R. Allott, B. Kennedy, and D. Neely. Observation of a highly directional γ-ray beam from ultrashort, ultraintense laser pulse interactions with solids. *Physics of Plasmas*, 6(5):2150–2156, 1999.

[8] M. Roth, D. Jung, K. Falk, N. Guler, O. Deppert, M. Devlin, A. Favalli, J. Fernandez, D. Gautier, M. Geissel, R. Haight, C. E. Hamilton, B. M. Hegelich, R. P. Johnson, F. Merrill, G. Schaumann, K. Schoenberg, M. Schollmeier, T. Shimada, T. Taddeucci, J. L. Tybo, F. Wagner, S. A. Wender, C. H. Wilde, and G. A. Wurden. Bright laser-driven neutron source based on the relativistic transparency of solids. *Physical Review Letters*, 110:044802, 2013.

[9] R. A. Snavely, M. H. Key, S. P. Hatchett, T. E. Cowan, M. Roth, T. W. Phillips, M. A. Stoyer, E. A. Henry, T. C. Sangster, M. S. Singh, S. C. Wilks, A. MacKinnon, A. Offenberger, D. M. Pennington, K. Yasuike, A. B. Langdon, B. F. Lasinski, J. Johnson, M. D. Perry, and E. M. Campbell. Intense high-energy proton beams from petawatt-laser irradiation of solids. *Physical Review Letters*, 85:2945–2948, 2000.

[10] T. Esirkepov, M. Borghesi, S. V. Bulanov, G. Mourou, and T. Tajima. Highly efficient relativistic-ion generation in the laser-piston regime. *Physical Review Letters*, 92:175003, 2004.

[11] B. Qiao, S. Kar, M. Geissler, P. Gibbon, M. Zepf, and M. Borghesi. Dominance of radiation pressure in ion acceleration with linearly polarized pulses at intensities of 10^{21} W cm^{-2}. *Physical Review Letters*, 108:115002, 2012.

[12] A. Macchi, M. Borghesi, and M. Passoni. Ion acceleration by superintense laser-plasma interaction. *Reviews of Modern Physics*, 85:751–793, 2013.

[13] M. Nishiuchi H. Daido and A. S. Pirozhkov. Review of laser-driven ion sources and their applications. *Reports on Progress in Physics*, 75(5):056401, 2012.

[14] O. A. Hurricane, P. K. Patel, R. Betti, D. H. Froula, S. P. Regan, S. A. Slutz, M. R. Gomez, and M. A. Sweeney. Physics principles of inertial confinement fusion and u.s. program overview. *Reviews of Modern Physics*, 95:025005, 2023.

[15] S. Bulanov and V. Khoroshkov. Feasibility of using laser ion accelerators in proton therapy. *Plasma Physics Reports*, 28:453–456, 2002.

[16] T. Ruth. Accelerating production of medical isotopes. *Nature*, 457:536–7, 2009.

[17] V. A. Vshivkov, N. M. Naumova, F. Pegoraro, and S. V. Bulanov. Nonlinear electrodynamics of the interaction of ultra-intense laser pulses with a thin foil. *Physics of Plasmas*, 5(7):2727–2741, 1998.

[18] S.V. Bulanov, T.Zh. Esirkepov, V.S. Khoroshkov, A.V. Kuznetsov, and F. Pegoraro. Oncological hadrontherapy with laser ion accelerators. *Physics Letters A*, 299(2):240–247, 2002.

[19] K. Ledingham, P. Bolton, N. Shikazono, and C.M. Ma. Towards laser driven hadron cancer radiotherapy: A review of progress. *Applied Sciences*, 4(3):402–443, 2014.

[20] K. Zeil, M. Baumann, E. Beyreuther, T. Burris-Mog, T. E. Cowan, W. Enghardt, L. Karsch, S. D. Kraft, L. Laschinsky, J. Metzkes, D. Naumburger, M. Oppelt, C. Richter, R. Sauerbrey, M. Schürer, U. Schramm, and J. Pawelke. Dose-controlled irradiation of cancer cells with laser-accelerated proton pulses. *Applied Physics B: Lasers and Optics*, 110(4):437–444, 2013.

[21] F.E. Kroll, F.and Brack, C. Bernert, S. Bock, E. Bodenstein, K. Brüchner, T. E. Cowan, L. Gaus, R. Gebhardt, U. Helbig, L. Karsch, T. Kluge, S. Kraft, and et al. Tumour irradiation in mice with a laser-accelerated proton beam. *Nature Physics*, 18(3):316–322, 2022.

[22] R. R. Wilson. Radiological use of fast protons. *Radiology*, 47(5):487–491, 1946. PMID: 20274616.

[23] C. A. Tobias, J. H. Lawrence, J. L. Born, R. K. McCombs, J. E. Roberts, H. O. Anger, B. V. A. Low-Beer, and C. B. Huggins. Pituitary Irradiation with High-Energy Proton Beams A Preliminary Report. *Cancer Research*, 18(2):121–134, 1958.

[24] E. Fourkal, I. Velchev, C.M. Ma, and J. Fan. Linear energy transfer of proton clusters. *Physics in Medicine Biology*, 56(10):3123, 2011.

[25] R. Schulte, C. Johnstone, S. Boucher, E. Esarey, C. G. R. Geddes, M. Kravchenko, S. Kutsaev, B. W. Loo, François Méot, Brahim Mustapha, Kei Nakamura, Emilio A. Nanni, Obst-Huebl, and et. Transformative technology for flash radiation therapy. *Applied Sciences*, 13(8), 2023.

[26] H. W. Powell, M. King., R. J. Gray, D. A. MacLellan, B. Gonzalez-Izquierdo, L. C. Stockhausen, G. Hicks, N. P. Dover, D. R. Rusby, D. C. Carroll, H. Padda, R. Torres, S. Kar, R. J. Clarke, I. O. Musgrave, Z. Najmudin, M. Borghesi, D. Neely, and P. McKenna. Proton acceleration enhanced by a plasma jet in expanding foils undergoing relativistic transparency. *New Journal of Physics*, 17(10):103033, 2015.

[27] A. Higginson, R. J. Gray, M. King, R. J. Dance, S. D. R. Williamson, N. M. H. Butler, R. Wilson, R. Capdessus, C. Armstrong, J. S. Green, S. J. Hawkes, P. Martin, W. Q. Wei, S. R. Mirfayzi, X. H. Yuan, S. Kar, M. Borghesi, R. J. Clarke, D. Neely, and P. McKenna. Near-100 MeV protons via a laser-driven transparency-enhanced hybrid acceleration scheme. *Nature Communications*, 9(1):1–9, 2018.

[28] W. L. Kruer. The physics of laser plasma interaction. *Westview Press*, 2003.

[29] P. Gibbon. Short pulse laser interactions with matter. *Imperial College Press*, 2005.

[30] A. Macchi. A superintense laser-plasma interaction theory primer. *Springer Netherlands*, 2013.

[31] J. L. Heilbron and Bernard S. Finn. Electricity in the 17th and 18th Centuries: A Study of Early Modern Physics. *Physics Today*, 33(7):46–46, 1980.

[32] W.N. Cottingham and D.A. Greenwood. Electricity and magnetism. *Cambridge University Press*, 1991.

[33] J. C. Maxwell. Xxv. on physical lines of force. *The London, Edinburgh, and Dublin Philosophical Magazine and Journal of Science*, 21(139):161–175, 1861.

[34] O. Heaviside. Xi. on the forces, stresses, and fluxes of energy in the electromagnetic field. *Philosophical Transactions of the Royal Society of London. (A.)*, 183:423–480, 1892.

[35] J. Hornung, Y. Zobus, P. Boller, C. Brabetz, U. Eisenbarth, T. KÃ¼hl, Zs. Major, J.Â B. Ohland, M. Zepf, B. Zielbauer, and et al. Enhancement of the laser-driven proton source at phelix. *High Power Laser Science and Engineering*, 8:e24, 2020.

[36] S. S. Harilal, R. W. Coons, P. Hough, and A. Hassanein. Influence of spot size on extreme ultraviolet efficiency of laser-produced Sn plasmas. *Applied Physics Letters*, 95(22):221501, 2009.

[37] R. J. Gray, R. Wilson, M King, S. D. R. Williamson, R. J. Dance, C. Armstrong, C. Brabetz, F. Wagner, B. Zielbauer, V. Bagnoud, D. Neely, and P. McKenna. Enhanced laser-energy coupling to dense plasmas driven by recirculating electron currents. *New Journal of Physics*, 20(3):033021, 2018.

[38] I. Langmuir. Oscillations in ionized gases. *Proceedings of the National Academy of Sciences of the United States of America*, 14(8):627–637, 1928.

[39] M. Göppert Mayer. Über elementarakte mit zwei quantensprüngen. *Annalen der Physik*, 401:273 – 294, 2006.

[40] D. Bauer, P. Mulser, and W. H. Steeb. Relativistic ponderomotive force, uphill acceleration, and transition to chaos. *Physical Review Letters*, 75:4622–4625, 1995.

[41] E. A. Startsev and C. J. McKinstrie. Multiple scale derivation of the relativistic ponderomotive force. *Physical Review E*, 55:7527–7535, 1997.

[42] R. J. Gray, D. C. Carroll, X. H. Yuan, C. M. Brenner, M. Burza, M. Coury, K. L. Lancaster, X. X. Lin, Y. T. Li, D. Neely, M. N. Quinn, O. Tresca, C.G. Wahlström, and P. McKenna. Laser pulse propagation and enhanced energy coupling to fast electrons in dense plasma gradients. *New Journal of Physics*, 16(11):113075, 2014.

[43] P. McKenna, D.C. Carroll, O. Lundh, F. NÃ¼rnberg, K. Markey, S. Bandyopadhyay, D. Batani, R.G. Evans, R. Jafer, S. Kar, and et al. Effects of front surface plasma expansion on proton acceleration in ultraintense laser irradiation of foil targets. *Laser and Particle Beams*, 26(4):591–596, 2008.

[44] J. D. Lawson. Some Criteria for a Power Producing Thermonuclear Reactor. *Proceedings of the Physical Society B*, 70(1):6–10, 1957.

[45] P.M. Woodward. A method of calculating the field over a plane aperture required to produce a given polar diagram. *Journal of the Institution of Electrical Engineers - Part IIIA: Radiolocation*, 93:1554–1558(4), 1946.

[46] N. G. Denisov. On a singularity of the field of an electromagnetic wave propagated in an inhomogeneous plasma. *Soviet Physics JETP-USSR*, 1957.

[47] J. P. Freidberg, R. W. Mitchell, R. L. Morse, and L. I. Rudsinski. Resonant absorption of laser light by plasma targets. *Physical Review Letters*, 28:795–799, 1972.

[48] P. Gibbon and A. R. Bell. Collisionless absorption in sharp-edged plasmas. *Physical Review Letters*, 68:1535–1538, 1992.

[49] B. Bezzerides, S. J. Gitomer, and D. W. Forslund. Randomness, maxwellian distributions, and resonance absorption. *Physical Review Letters*, 44:651–654, 1980.

[50] F. N. Beg, A. R. Bell, A. E. Dangor, C. N. Danson, A. P. Fews, M. E. Glinsky, B. A. Hammel, P. Lee, P. A. Norreys, and M. Tatarakis. A study of picosecond laser-solid interactions up to 10^{19} Wcm^{-2}. *Physics of Plasmas*, 4(2):447–457, 1997.

[51] M. G. Haines, M. S. Wei, F. N. Beg, and R. B. Stephens. Hot-electron temperature and laser-light absorption in fast ignition. *Physical Review Letters*, 102:045008, 2009.

[52] S. C. Wilks, W. L. Kruer, M. Tabak, and A. B. Langdon. Absorption of ultra-intense laser pulses. *Physical Review Letters*, 69:1383–1386, 1992.

[53] C. D. Chen, J. A. King, M. H. Key, K. U. Akli, F. N. Beg, H. Chen, R. R. Freeman, A. Link, A. J. Mackinnon, A. G. MacPhee, P. K. Patel, M. Porkolab, R. B. Stephens, and L. D. Van Woerkom. A Bremsstrahlung spectrometer using k-edge and differential filters with image plate dosimetersa). *Review of Scientific Instruments*, 79(10):10E305, 2008.

[54] D. Rusby, R.J. Gray, N. Butler, R. Dance, G. Scott, V. Bagnoud, B. Zielbauer, P. McKenna, and D. Neely. Escaping electrons from intense laser-solid interactions as a function of laser spot size. *EPJ Web of Conferences*, 167:02001, 2018.

[55] J. R. Davies. Alfvén limit in fast ignition. *Phys. Rev. E*, 69:065402, 2004.

[56] K. Quinn, L. Romagnani, B. Ramakrishna, G. Sarri, M. E. Dieckmann, P. A. Wilson, J. Fuchs, L. Lancia, A. Pipahl, T. Toncian, O. Willi, R. J. Clarke, M. Notley, A. Macchi, and M. Borghesi. Weibel-induced filamentation during an ultrafast laser-driven plasma expansion. *Physical Review Letters*, 108:135001, 2012.

[57] A. Macchi, S. Veghini, and F. Pegoraro. "light sail" acceleration reexamined. *Physical Review Letters*, 103:085003, 2009.

[58] A. Henig, D. Kiefer, K. Markey, D. C. Gautier, K. A. Flippo, S. Letzring, R. P. Johnson, T. Shimada, L. Yin, B. J. Albright, K. J. Bowers, J. C. Fernández, S. G. Rykovanov, H.-C. Wu, M. Zepf, D. Jung, V. Kh. Liechtenstein, J. Schreiber, D. Habs, and B. M. Hegelich. Enhanced laser-driven ion acceleration in the relativistic transparency regime. *Physical Review Letters*, 103:045002, 2009.

[59] Q. L. Dong, Z.-M. Sheng, M. Y. Yu, and J. Zhang. Optimization of ion acceleration in the interaction of intense femtosecond laser pulses with ultrathin foils. *Physical Review E*, 68:026408, 2003.

[60] D. J. Stark, C. Bhattacharjee, A. V. Arefiev, T. Toncian, R. D. Hazeltine, and S. M. Mahajan. Relativistic plasma polarizer: Impact of temperature anisotropy on relativistic transparency. *Physical Review Letters*, 115:025002, 2015.

[61] R. Kodama, P. Norreys, K. Mima, A. Dangor, R. Evans, H. Fujita, Y. Kitagawa, K. Krushelnick, T.T. Matsuoka, N. Miyanaga, T. Norimatsu, S. Rose, T. Shozaki, K. Shigemori, A. Sunahara, M. Tampo, K. Tanaka, Y. Toyama, T. Yamanaka, and M. Zepf. Fast heating of ultrahigh-density plasma as a step towards laser fusion ignition. *Nature*, 412:798–802, 2001.

[62] R. B. Stephens, S. P. Hatchett, R. E. Turner, K. A. Tanaka, and R. Kodama. Implosion of indirectly driven reentrant-cone shell target. *Physical Review Letters*, 91:185001, 2003.

[63] V. I. Veksler. The principle of coherent acceleration of charged particles. *The Soviet Journal of Atomic Energy*, 2(5):525–528, 1957.

[64] L. Yin, B. Albright, B. Hegelich, and J. Fernandez. Gev laser ion acceleration from ultrathin targets: The laser break-out afterburner. *Laser and Particle Beams*, 24:291–298, 2006.

[65] L. Yin, B. J. Albright, B. M. Hegelich, K. J. Bowers, K. A. Flippo, T. J. T. Kwan, and J. C. FernÃ¡ndez. Monoenergetic and GeV ion acceleration from the laser breakout afterburner using ultrathin targetsa). *Physics of Plasmas*, 14(5):056706, 2007.

[66] S. P. Hatchett, C. G. Brown, T.E. Cowan, E.A. Henry, J.S. Johnson, M.H. Key, J.A. Koch, A. B. Langdon, B.F. Lasinski, R.W. Lee, A.J. Mackinnon, D.M. Pennington, M.D. Perry, T.W. Phillips, M. Roth, T.C. Sangster, M.S. Singh, R.A. Snavely, M.A. Stoyer, S.C. Wilks, and K. Yasuike. Electron, photon, and ion beams from the relativistic interaction of Petawatt laser pulses with solid targets. *Physics of Plasmas*, 7(5):2076–2082, 2000.

[67] E. L. Clark, K. Krushelnick, J. R. Davies, M. Zepf, M. Tatarakis, F. N. Beg, A. Machacek, P. A. Norreys, M. I. K. Santala, I. Watts, and A. E. Dangor. Measurements of energetic proton transport through magnetized plasma from intense laser interactions with solids. *Physical Review Letters*, 84:670–673, 2000.

[68] S. C. Wilks, A. B. Langdon, T. E. Cowan, M. Roth, M. Singh, S. Hatchett, M. H. Key, D. Pennington, A. MacKinnon, and R. A. Snavely. Energetic proton generation in ultra-intense laserâsolid interactions. *Physics of Plasmas*, 8(2):542–549, 2001.

[69] Y. Sentoku, T. E. Cowan, A. Kemp, and H. Ruhl. High energy proton acceleration in interaction of short laser pulse with dense plasma target. *Physics of Plasmas*, 10(5):2009–2015, 2003.

[70] A. J. Mackinnon, Y. Sentoku, P. K. Patel, D. W. Price, S. Hatchett, M. H. Key, C. Andersen, R. Snavely, and R. R. Freeman. Enhancement of proton acceleration by hot-electron recirculation in thin foils irradiated by ultraintense laser pulses. *Physical Review Letters*, 88:215006, 2002.

[71] T. E. Cowan, J. Fuchs, H. Ruhl, A. Kemp, P. Audebert, M. Roth, R. Stephens, I. Barton, A. Blazevic, E. Brambrink, J. Cobble, J. Fernández,

J.-C. Gauthier, M. Geissel, M. Hegelich, J. Kaae, S. Karsch, G. P. Le Sage, S. Letzring, M. Manclossi, S. Meyroneinc, A. Newkirk, H. Pépin, and N. Renard-LeGalloudec. Ultralow emittance, multi-mev proton beams from a laser virtual-cathode plasma accelerator. *Physical Review Letters*, 92:204801, 2004.

[72] O. Tresca, D. C. Carroll, X. H. Yuan, B. Aurand, V. Bagnoud, C. M. Brenner, M. Coury, J. Fils, R. J. Gray, T. Kühl, C. Li, Y. T. Li, X. X. Lin, M. N. Quinn, R. G. Evans, B. Zielbauer, M. Roth, D. Neely, and P. McKenna. Controlling the properties of ultraintense laserâproton sources using transverse refluxing of hot electrons in shaped mass-limited targets. *Plasma Physics and Controlled Fusion*, 53(10):105008, 2011.

[73] P. McKenna, D. C. Carroll, R. J. Clarke, R. G. Evans, K. W. D. Ledingham, F. Lindau, O. Lundh, T. McCanny, D. Neely, A. P. L. Robinson, L. Robson, P. T. Simpson, C.-G. Wahlström, and M. Zepf. Lateral electron transport in high-intensity laser-irradiated foils diagnosed by ion emission. *Physical Review Letters*, 98:145001, 2007.

[74] M. Hegelich, S. Karsch, G. Pretzler, D. Habs, K. Witte, W. Guenther, M. Allen, A. Blazevic, J. Fuchs, J. C. Gauthier, M. Geissel, P. Audebert, T. Cowan, and M. Roth. Mev ion jets from short-pulse-laser interaction with thin foils. *Physical Review Letters*, 89:085002, 2002.

[75] A. Măgureanu, L. Dincă, C. Jalbă, R. F. Andrei, I. Burducea, D. G. Ghiţă, V. Nastasa, M. Gugiu, T. Asavei, O. Budrigă, D. Ticoş, V. Crăciun, B. Diaconescu, and C. M. Ticoş. Target characteristics used in laser-plasma acceleration of protons based on the tnsa mechanism. *Frontiers in Physics*, 10, 2022.

[76] J. Fuchs, P. Antici, E. D'Humières, E. Lefebvre, M. Borghesi, E. Brambrink, C. A. Cecchetti, M. Kaluza, V. Malka, M. Manclossi, S. Meyroneinc, P. Mora, J. Schreiber, T. Toncian, H. Pépin, and P. Audebert. Laser-driven

proton scaling laws and new paths towards energy increase. *Nature Physics*, 2(1):48–54, 2006.

[77] L Robson, PT Simpson, RJ Clarke, KWD Ledingham, F Lindau, Olle Lundh, Thomas Mccanny, Paola Mora, D Neely, Claes-Göran Wahlström, Matt Zepf, and Paul McKenna. Scaling of proton acceleration driven by petawatt-laser-plasma interactions. *Nature Physics*, 3, 2006.

[78] A. P. L. Robinson, M. Zepf, S. Kar, R. G. Evans, and C. Bellei. Radiation pressure acceleration of thin foils with circularly polarized laser pulses. *New Journal of Physics*, 10(1):013021, 2008.

[79] A. Macchi, S. Veghini, T. V. Liseykina, and F. Pegoraro. Radiation pressure acceleration of ultrathin foils. *New Journal of Physics*, 12(4):045013, 2010.

[80] A. Macchi and C. Benedetti. Ion acceleration by radiation pressure in thin and thick targets. *Nuclear Instruments and Methods in Physics Research Section A: Accelerators, Spectrometers, Detectors and Associated Equipment*, 620(1):41–45, 2010. COULOMB09.

[81] B. Gonzalez-Izquierdo, R. Capdessus, M. King, R. J. Gray, R. Wilson, R. J. Dance, J. McCreadie, N. M. H. Butler, S. J. Hawkes, J. S. Green, N. Booth, M. Borghesi, D. Neely, and P. McKenna. Radiation pressure-driven plasma surface dynamics in ultra-intense laser pulse interactions with ultra-thin foils. *Applied Sciences*, 8(3), 2018.

[82] C.N. Danson, C. Haefner, J. Bromage, T. J. Butcher, C.F. Chanteloup, E.A. Chowdhury, A. Galvanauskas, L.A. Gizzi, J. Hein, D.I. Hillier, and et al. Petawatt and exawatt class lasers worldwide. *High Power Laser Science and Engineering*, 7:e54, 2019.

[83] A. J. DeMaria, D. A. Stetser, and H. Heynau. Self mode–locking of lasers with saturable absorbers. *Applied Physics Letters*, 8(7):174–176, 2004.

[84] M. Grishin, V. Gulbinas, and A. Michailovas. Dynamics of high repetition rate regenerative amplifiers. *Optics Express*, 15(15):9434–9443, 2007.

[85] M. Kaluza, J. Schreiber, M. I. K. Santala, G. D. Tsakiris, K. Eidmann, J. Meyer-ter Vehn, and K. J. Witte. Influence of the laser prepulse on proton acceleration in thin-foil experiments. *Physical Review Letters*, 93:045003, 2004.

[86] A. Flacco, F. Sylla, M. Veltcheva, M. Carrié, R. Nuter, E. Lefebvre, D. Batani, and V. Malka. Dependence on pulse duration and foil thickness in high-contrast-laser proton acceleration. *Physical Review E*, 81:036405, 2010.

[87] I.N. Ross, P. Matousek, M. Towrie, A.J. Langley, and J.L. Collier. The prospects for ultrashort pulse duration and ultrahigh intensity using optical parametric chirped pulse amplifiers. *Optics Communications*, 144(1):125–133, 1997.

[88] C. Thaury, F. Quere, J. Geindre, A. Levy, T. Ceccotti, P. Monot, M. Bougeard, F. Reau, P. D'Oliveira, P. Audebert, R. Marjoribanks, and P. Martin. Plasma mirrors for ultrahigh-intensity optics. *Nature Physics*, 3:424–429, 2007.

[89] A. Blazevic S. Borneis C. Bruske B. Ecker U. Eisenbarth J. Fils A. Frank E. Gaul S. Goette C. Haefner T. Hahn K. Harres H.-M. Heuck D. Hochhaus D. H. H. Hoffmann D. Javorkov H.-J. Kluge T. Kuehl S. Kunzer M. Kreutz T. Merz-Mantwill P. Neumayer E. Onkels D. Reemts O. Rosmej M. Roth T. Stoehlker A. Tauschwitz B. Zielbauer D. Zimmer V. Bagnoud, B. Aurand and K. Witte. Commissioning and early experiments of the phelix facility. *Applied Physics B*, 100:137–150, 2010.

[90] B. Zielbauer, T. Kuehl, B. Aurand, V. Bagnoud, B. Ecker, U. Eisenbarth, D. C. Hochhaus, P. Neumayer, D. Zimmer, K. Cassou, S. Daboussi, O. Guilbaud, J. Habib, S. Kazamias, D. Ros, J. Seres, and C. Spielmann. X-ray laser developments at phelix. *Springer Proceedings in Physics*, pages 31–38, 2011.

[91] S. Holler, J.C. Auger, B. Stout, Y. Pan, J. R. Bottiger, R.K. Chang, and G. Videen. Observations and calculations of light scattering from clusters of spheres. *Applied Optics*, 39(36):6873–6887, 2000.

[92] J Yan, H Liu, W Zhao, and Y Su. Led filament standard lamp for total luminous flux with uniform spatial distribution. *Journal of Physics: Conference Series*, 1345(3):032046, 2019.

[93] O. Hamdy and H. Mohammed. Investigating the transmission profiles of 808 nm laser through different regions of the rat head. *Lasers in Medical Science*, 2021.

[94] R. Kristal. Surface plasma absorption in an integrating sphere at high optical flux levels. *Applied Optics*, 21(11):1885–1887, 1982.

[95] M. Borghesi, A. J. Mackinnon, R. Gaillard, O. Willi, and D. Riley. Absorption of subpicosecond uv laser pulses during interaction with solid targets. *Physical Review E*, 60:7374–7381, 1999.

[96] I.P. Shkarofsky, T.W. Johnston, and M.P. Bachynski. *The Particle Kinetics of the Plasmas.* Addison-Wesley Publishing Company, 1966.

[97] E.M. Lifschitz and L.P. Pitajewski. *Physical kinetics.* 1983.

[98] Y. L. Klimontovich. Relativistic transport equations for a plasma 1. *Soviet Physics JETP*, 10(3):524–530, 1960.

[99] A.B. Langdon B.K. Birdsall. *Plasma Physics via Computer Simulation.* CRC Press, 2017.

[100] K. Yee. Numerical solution of initial boundary value problems involving maxwell's equations in isotropic media. *IEEE Transactions on Antennas and Propagation*, 14(3):302–307, 1966.

[101] J. P. Boris. Relativistic plasma simulation-optimization of a hybrid code. *Proceeding of Fourth Conference on Numerical Simulations of Plasmas*, November 1970.

[102] H. Nishimura, H. Azechi, K. Yamada, A. Tamura, Y. Inada, F. Matsuoka, M. Hamada, Y. Suzuki, S. Nakai, and C. Yamanaka. Experimental study of wavelength dependences of laser-plasma coupling, transport, and ablation processes. *Physical Review A*, 23:2011–2019, 1981.

[103] T. Nakamura, S. Kato, H. Nagatomo, and K. Mima. Surface-magnetic-field and fast-electron current-layer formation by ultraintense laser irradiation. *Phys. Rev. Lett.*, 93:265002, 2004.

[104] P.K. Singh, Y.Q. Cui, A. Adak, A.D. Lad, G. Chatterjee, P. Brijesh, Z.M. Sheng, and G.R. Kumar. Contrasting levels of absorption of intense femtosecond laser pulses by solids. *Scientific Reports*, 9:17870, 2015.

[105] T. Ma, H. Sawada, P. K. Patel, C. D. Chen, L. Divol, D. P. Higginson, A. J. Kemp, M. H. Key, D. J. Larson, S. Le Pape, A. Link, A. G. MacPhee, H. S. McLean, Y. Ping, R. B. Stephens, S. C. Wilks, and F. N Beg. Hot electron temperature and coupling efficiency scaling with prepulse for cone-guided fast ignition. *Physical Review Letters*, 108:115004, 2012.

[106] D. F. Price, R. M. More, R. S. Walling, G. Guethlein, R. L. Shepherd, R. E. Stewart, and W. E. White. Absorption of ultrashort laser pulses by solid targets heated rapidly to temperatures 1–1000 eV. *Physical Review Letters*, 75:252–255, 1995.

[107] E. T. Gumbrell, R. A. Smith, T. Ditmire, A. Djaoui, S. J. Rose, and M. H. R. Hutchinson. Picosecond optical probing of ultrafast energy transport in short pulse laser solid target interaction experiments. *Physics of Plasmas*, 5(10):3714–3721, 1998.

[108] Y. Ping, R. Shepherd, B. F. Lasinski, M. Tabak, H. Chen, H. K. Chung, K. B. Fournier, S. B. Hansen, A. Kemp, D. A. Liedahl, K. Widmann, S. C. Wilks, W. Rozmus, and M. Sherlock. Absorption of short laser pulses on solid targets in the ultrarelativistic regime. *Physical Review Letters*, 100:085004, 2008.

[109] J. R. Davies. Laser absorption by overdense plasmas in the relativistic regime. *Plasma Physics and Controlled Fusion*, 51(1):014006, 2008.

[110] M. C. Levy, S. C. Wilks, M. Tabak, S. B. Libby, and M. G. Baring. Petawatt laser absorption bounded. *Nature Communications*, 5(10):4149, 2014.

[111] E. Lefebvre and G. Bonnaud. Transparency/opacity of a solid target illuminated by an ultrahigh-intensity laser pulse. *Physical Review Letters*, 74:2002–2005, 1995.

[112] E. Lefebvre and G. Bonnaud. Nonlinear electron heating in ultrahigh-intensity-laser–plasma interaction. *Physical Review E*, 55:1011–1014, 1997.

[113] S. D. R. Williamson, R. J. Gray, M. King, R. Wilson, R. J. Dance, C. Armstrong, D. R. Rusby, C. Brabetz, F. Wagner, B. Zielbauer, V. Bagnoud, D. Neely, and P. McKenna. Energy absorption and coupling to electrons in the transition from surface- to volume-dominant intense laserâplasma interaction regimes. *New Journal of Physics*, 22(5):053044, 2020.

[114] R. Fedosejevs, X. F. Wang, and G. D. Tsakiris. Onset of relativistic self-focusing in high density gas jet targets. *Physical Review E*, 56:4615–4639, 1997.

[115] E.E. Fill. Focusing limits of ultrashort laser pulses: analytical theory. *Journal of the Optical Society of America B*, 11(11):2241–2245, 1994.

[116] J.C. Solem, T.S. Luk, K. Boyer, and C.K. Rhodes. Prospects for x-ray amplification with charge-displacement self-channeling. *IEEE Journal of Quantum Electronics*, 25(12):2423–2430, 1989.

[117] T. D. Arber, K. Bennett, C. S. Brady, A. L. Douglas, M. G. Ramsay, N. J. Sircombe, P. Gillies, R. G. Evans, H. Schmitz, A. R. Bell, and C. P. Ridgers. Contemporary particle-in-cell approach to laser-plasma modelling. *Plasma Physics and Controlled Fusion*, 57(11):113001, 2015.

[118] M. Capitelli, A. Casavola, G. Colonna, and A. De Giacomo. Laser-induced plasma expansion: theoretical and experimental aspects. *Spectrochimica Acta Part B: Atomic Spectroscopy*, 59(3):271–289, 2004.

[119] B. Cros. Laser-driven plasma wakefield: Propagation effects. *CERN Yellow Reports*, pages 207–230, 2016.